UNIVERSITÀ DI PARMA

DEPARTMENT OF MATHEMATICAL, PHYSICAL AND COMPUTER SCIENCES

PhD IN PHYSICS

XXX CYCLE

Improvements in CdTe- and CIGS-based thin-film solar cells and investigation on new materials for photovoltaic applications.

Coordinator:
Prof. Cristiano Viappiani

Supervisor:
Prof. Alessio Bosio

Candidate
Greta Rosa
260679

2014 / 2017

CONTACT INFORMATION

Greta Rosa

Email	greta.rosa@difest.unipr.it
Address	Department of Mathematical, Physical and Computer Sciences
	Università di Parma
	Parco Area delle Scienze 7/A
	43124, Parma - Italy

To my family,
for their advice, their patience, and their love,
because they have always supported my choices.
Thank you!

Contents

List of Figures

List of Tables

Acronyms

A	Electron Acceptor Material
ABX_3	General Formula of Perovskite Compound
AC	Alternating Current
AIST	Japanese National Institute of Advanced Industrial Science and Technology
AM	Air Mass
(ap)	Aperture Area
a-Si	Amorphous Silicon
at.%	Atomic Percentage
a.u.	Arbitrary Unit
AZO	Aluminum-Doped Zinc Oxide
BIPV	Building-Integrated Photovoltaic
boe	Barrel of Oil Equivalent
BOS	Balance of System
BRICS	Brazil, Russian Federation, India, China and South Africa
BSF	Back Surface Field
Btu	British Thermal Units
Btu/ft^3	British Thermal Units per Cubic Foot
cal	Calorie
CB	Conduction Band
CBD	Chemical Bath Deposition
Cd	Cadmium
$CdCl_2$	Cadmium Dichloride

CdS Cadmium-Sulphide

CdTe Cadmium-Telluride

CGS Copper Gallium Diselenide ($CuGaSe_2$)

CH_4 Methane

CHF_2Cl Chlorodifluoromethane

χ Electron Affinity

χ_s Electron Affinity of a Semiconductor

CIGS Copper Indium Gallium Diselenide ($CuInGaSe_2$)

CIS Copper Indium Diselenide ($CuInSe_2$)

CMVB Chemical Modulation of the Valence Band

CNR National Research Council

CO_2 Carbon Dioxide

COP 21 2015 United Nations Climate Change Conference

cps Counts Per Second

CPV Concentrator Photovoltaic

c-Si Crystalline Silicon

CSP Concentrating Solar Power

CSS Close-Spaced Sublimation

CVD Chemical Vapour Deposition

CZTS Copper Zinc Tin Sulphide (Cu_2ZnSnS_4)

CZTSe Copper Zinc Tin Selenide ($Cu_2ZnSnSe_4$)

CZTSSe Copper Zinc Tin Sulphide Selenide ($Cu_2ZnSn(S,Se)_4$)

D Electron Donor Material

(da) Designated Illumination Area

DC Direct Current

DSSC Dye-Sensitized Solar Cell

E_{BOS} Energy Requirement of Balance of System Components

E_{CB} Energy of the Bottom Edge of the Conduction Band

EFG	Edge-Defined-Film-Fed-Growth
E_F	Quasi-Fermi Level
E_{Fn}	Quasi-Fermi Level of Electrons
E_{Fp}	Quasi-Fermi Level of Hole
E_g	Energy Band Gap
e.g.	Exempli Gratia
EIA	U.S. Energy Information Administration
E_{input}	Primary Energy Input of the Photovoltaic Module
EJ	Exa Joule (10^{18} Joule)
E_{output}	Annual Power Generation by the Photovoltaic Module
EPBT	Energy Pay-Back Time
EVA	Ethyl Vinyl Acetate
E_{VB}	Energy of the Top Edge of the Valence Band
E_0	Energy of the Vacuum Level
FF	Fill Factor
FhG-ISE	Fraunhofer Institut für Solare Energie systeme
FTO	Fluorine Doped Tin Oxide
GaAs	Gallium Arsenide
GDP	Gross Domestic Product
Ge	Germanium
GHG	Greenhouse Gases
GJ	Giga Joule (10^9 Joule)
GW	Gigawatt (10^9 Watt)
h	Planck Constant
HOMO	Highest Occupied Molecular Orbitals
IBC	Interdigitated Back Contact
IEA	International Energy Agency
IEA PVPS	International Energy Agency Photovoltaic Power System Programme

IMEM Institute of Materials for Electronics and Magnetism

IR Infra-Red

IRENA International Renewable Energy Agency

I_{SC} Short-Circuit Current

ISO International Organization for Standardization

IT International Table

ITO Indium Tin Oxide

J Joule

J_D Dark Current Density

J_M Maximum Current Density

J_{Ph} Photogenerated Current Density

J_{SC} Short-Circuit Current Density

J_0 Reverse Saturation Current Density

k_B Boltzmann's Constant

kcal Kilo-Calorie

KRICT Korea Research Institute of Chemical Technology

kWh Kilowatt-Hour

LCA Life Cycle Assessment

LPE Liquid Phase Epitaxy

LUMO Lowest Unoccupied Molecular Orbitals

MBE Molecular Beam Epitaxy

MBtu Millions of British Thermal Units

mc-Si Multi-Crystalline Silicon

Mo Molybdenum

MOCVD Metallorganic Chemical Vapour Deposition

μc-Si Micro-Morph Silicon

NBE Near Band Edge

η Efficiency

NREL	National Renewable Energy Laboratory
ν	Frequency
OECD	Organisation for Economic Co-operation and Development
Ω	Ohm
Ω_{abs}	Absorption Solid Angle
Ω_{emit}	Emission Solid Angle
OPV	Organic Photovoltaic
p.a.	Per Annum
P1	Laser Scribing Step Process 1
P2	Laser Scribing Step Process 2
P3	Laser Scribing Step Process 3
φ	Work Function
φ_m	Work Function of a Metal
φ_s	Work Function of a Semiconductor
PPP	Purchasing Power Parity
PSCs	Perovskite Solar Cell
PV	Photovoltaic
q	Electronic Charge
R-22	Chlorodifluoromethane
$R_{Cd/Te}$	Cadmium/Tellurium Ratio
rf	Radio Frequency
R_L	Load Resistance
R_S	Series Resistance
R_{Sh}	Shunt Resistance
RTI	Research Triangle Institute
sc-Si	Single-Crystalline Silicon
σ	Electrical Conductivity
Si	Silicon

SLG	Soda-Lime Glass
S-Q	Shockley and Queisser
STC	Standard Test Condition
(t)	Total Area
T	Temperature
T_c	Solar Cell Temperature
tce	Metric Tonne of Coal Equivalent
TCO	Transparent Conducting Oxide
Te	Tellurium
ton	Metric Tonne
T_s	Sun Temperature
UNIST	Ulsan National Institute of Science and Technology
UNSW	University of New South Wales
USD	United States Dollar
UV	Ultraviolet
V_B	Breakdown Voltage
VB	Valence Band
V_M	Maximum Voltage
V_{OC}	Open-Circuit Voltage
Wh	Watt-Hour
Wt.%	Weight Percentage
XRD	X-Ray Diffraction
ZnO	Zinc Oxide
ZSW	Zentrum für Sonnenenergie- und Wasserstoff-Forschung

Foreword

Currently, thin-film solar cells are one of the most promising technologies for low-cost renewable energy production. CdTe- and $CuInGaSe_2$-based cells, which achieved record efficiencies of 22.1% and 22.6% respectively, are the most attractive among thin-film solar cells. These high efficiencies have had a huge influence in making them highly competitive in the photovoltaic market, with an estimated final cost per module lower than US $ 0.50 per peak-watt.

At the Thin Film Laboratory of the University of Parma, a fully scalable process able to produce high-efficiency CdTe- and CIGS-based solar cells has been developed. The only deposition techniques the production process require are: close-spaced sublimation and sputtering for CdTe, sputtering and selenisation for CIGS. Our choice, justified by its great flexibility, was sputtering as core deposition technique: it can be used to deposit a wide variety of materials, such as insulators, semiconductors, conductors, alloys and composites. At the same time, we have chosen close-spaced sublimation for making CdTe films because it is one of the simplest approaches to physical vapour deposition and it offers high deposition rates.

In the wider context of implementing these technologies, my PhD research project has privileged three main aspects:

1. Implementation of high-performance CdTe-based devices fabricated by using close-spaced sublimation and sputtering in an attempt to improve both grain boundary passivation and back-contact ohmicity.

2. Implementation of high-efficiency ($> 16\%$) CIGS-based devices with the aim of exporting the fabrication process developed for soda-lime glass and ceramic substrates to flexible substrates, such as thin metal foils.

3. Investigation of sputter-deposited copper-based delafossites as novel transparent conducting oxides for photovoltaic and electronic applications.

In this PhD thesis, I will present the results I achieved while pursuing the previous three objectives.

The first part of my PhD thesis is a general overview of photovoltaic energy and it is composed of two chapters. In the first chapter, I will focus on the analysis of the role that photovoltaic renewable technologies are playing and are going to play in current world energy demand and consumption. The second chapter will be a review of the theoretical and technological aspects of photovoltaic systems.

In the second part, I will describe the deposition techniques that were employed in our laboratory to produce all the samples used for this study. Chapter 3 will also briefly mention the characterisation techniques used to analyse both thin film and solar cells.

The final part will be a description of the experimental results I obtained and it will include their interpretation. This part includes three chapters, each of which refers to the three main objectives mentioned above.
In particular, Chapter 4 will deal with the development of an innovative process, which reduces the thickness of the CdTe absorber layer and incorporates a barrier-free back contact, suitable for the production of high-efficiency solar cells.
Chapter 5 will focus on the identification of the main process requirements that are needed for preparing high-efficiency CIGS devices, making use of scalable techniques such as sputtering and selenisation. These results have been used to extend this process, which is an established one for soda-lime glass and ceramic substrates, to flexible thin metal foil substrates. I will also address the new technological challenges introduced by this type of substrate. These include the problem of film adhesion and the necessity of a barrier layer between the metallic substrates and the active layer to prevent the diffusion of impurities and to provide electrical insulation between the metal substrate and the monolithically interconnected solar cells.
Chapter 6 will report on the successful sputtering-based preparation of $CuGaO_2$ and $CuBO_2$ delafossite thin films suitable to use as transparent back contacts in bifacial CIGS- and CdTe-based solar cells.

I will finish by providing a summary of the main conclusion of my PhD project and some future perspectives.

Chapter

1

Analysis of global energy consumption

In this chapter, a summary of the current state of the art in regard to global energy consumption is given. I will report on the present global energy demand and provide relevant predictions for the coming years, discussing on how this demand may be satisfied. I will focus on the role of renewable energies sources and, in particular, of photovoltaic energy.

1.1 Analysis of world energy demand

Energy is essential for our everyday life. This obvious fact raises a key question: what is the current global energy demand and what are the future expectations? To answer these questions, we need to take a closer look at the main parameters that influence the world energy demand. There are various factors which contribute to the increase in energy request, but the two main parameters are: global population and Gross Domestic Product (GDP[1]) per capita [1]. This connection is made evident by the following equation, which gives a rough but reasonable estimate of energy needs from world population and life standards:

$$People \quad \times \quad Living \quad standards \quad = \quad Energy \quad needs \tag{1.1}$$

According to this equation, we now review each of these variables, in order to understand how important the photovoltaic energy might be in the coming years.

[1] **GDP** (Gross domestic product) is the monetary value of all the finished goods and services produced within a country's borders in a specific time period.

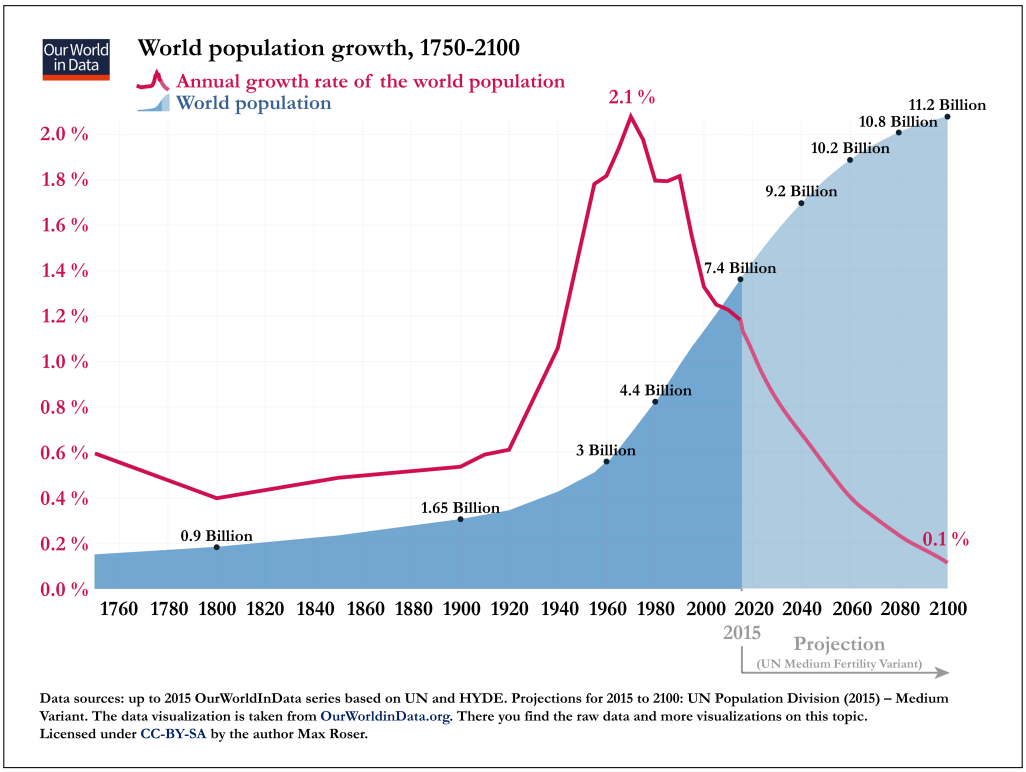

Figure 1.1: The annual population growth rate (red curve) superimposed on the total world population (blue area) for the period 1750 - 2015, and the probabilistic projection for the period 2016 - 2100, adapted from [3].

1.1.1 Analysis of growth prospects of world population and economy

The increase in world population witnessed from 1900 to 2000 has been three times grater than the one experienced in entire history of mankind before then. The population has increased from 1.5 to 6.1 billion in just 100 years [2]. The number of people in the world is currently still growing, although it should be stressed that this growth is taking place at a slower rate than in the recent past. The growth rate has in fact decreased from last decade's 1.24%/y to today's 1.18%/y. Approximately, the world population is projected to increase by more than one billion people in the next 15 years (it will be 8.5 billion units in 2030) [3]. Statistical estimations predict an increase to 9.7 billion in 2050, and a further one to 11.2 billion in 2100, as shown in Figure 1.1. These projections, released the United Nations Department of Economic and Social Affairs, are based on the statistical forecasts of total fertility and life expectancy at birth.

The population growth, however significant, is not the only factor. Economic prospects play an equally important role in determining the outlook for energy consumption [4]. Let us now observe the headline rate of growth in GDP (as shown in Figure 1.2). This economic outlook shows that the world economy is likely to double its output in the next 20 years, with an average growth of 3.4%/y (at the same exchange rate of purchasing power).

The combination of these two trends, the increase in population and the expansion of the global market, will inevitably lead, as per Equation (1.1), to a definite increase in world energy consumption. However, it is important to underline that the way in which the future growth in economic activity translates into demand for energy is heavily dependent on policies and on structural changes in the economies.

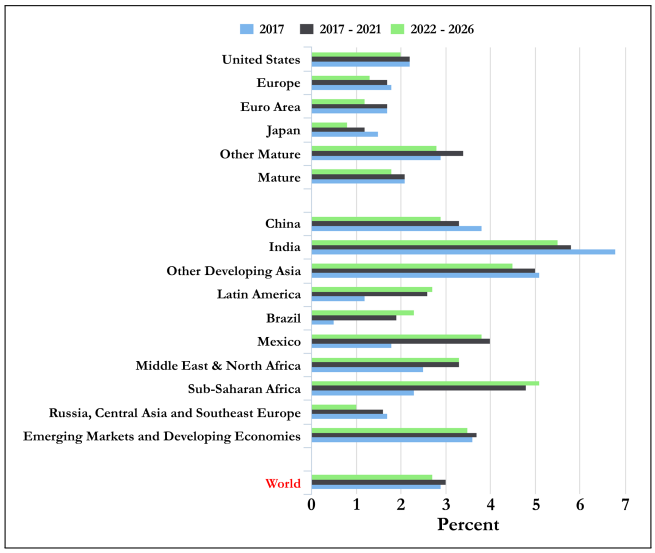

Figure 1.2: The growth of GPD for geographical area, reprinted from [6].

1.1.2 Outlook for energy demand

In its latest international energy outlook [5], the U.S. Energy Information Administration (EIA) has foreseen a significant growth in worldwide energy demand from 2012 to 2040. As shown in Figure 1.3, the data on total world energy consumption show a steady increase from 549×10^{15} British thermal units (Btu - shown Appendix A - Energy units) in 2012 to 629×10^{15} Btu in 2020 and to 815×10^{15} Btu in 2040, with an increase of 48% from 2012 to 2040.
It is clear from these data, that the global increase in energy demand will mostly occur among non-OECD[2] developing countries. A 71% rise in energy demand has been forecast for these countries in the period from 2012 to 2040. This is in contrast to predictions for OECD members, whose increase will only amount to 18% in the same period.

What are the primary energy sources with which the world's energy needs are satisfied?
Figure 1.3 shows that fossil fuels will still be providing most of the world's energy in the next decades. In particular, liquid fuels, coal and natural gas are estimated to provide 78% of the total world energy consumption in 2040. Oil and other liquid fuels will retain their traditional role as primary sources of energy, although their use will slowly decline from 33% in 2012 to 30% in 2040. Liquid fuel consumption dominates in transportation, industry and commerce sector, but is decreasing in the residential and electric power sectors.
Predictions also highlight that coal is currently the second most used energy source, with an estimated average increase in use of 0.6%/y from 2012 to 2040. This rate is considerably slower than the 2.2%/y that has been recorded in the past 30 years. A marked decline in its use is expected everywhere in the world over the next 30 years. The most significant counteraction will be taken by China, traditionally a heavy user of this source, which is currently implementing measures to reduce the growth in coal consumption from an annual 6% to just 0.3%.

[2] **OECD** (Organisation for Economic Co-operation and Development) is an intergovernmental economic organisation with 35 member countries, founded in 1960 to stimulate economic progress and world trade. The 35 countries are: Australia, Austria, Belgium, Canada, Chile, Czech Republic, Denmark, Estonia, Finland, France, Germany, Greece, Hungary, Iceland, Ireland, Israël, Italy, Japan, Korea, Latvia, Luxembourg, Mexico, Netherlands, New Zealand, Norway, Poland, Portugal, Slovak Republic, Slovenia, Spain, Sweden, Switzerland, Turkey, United Kingdom, United States.

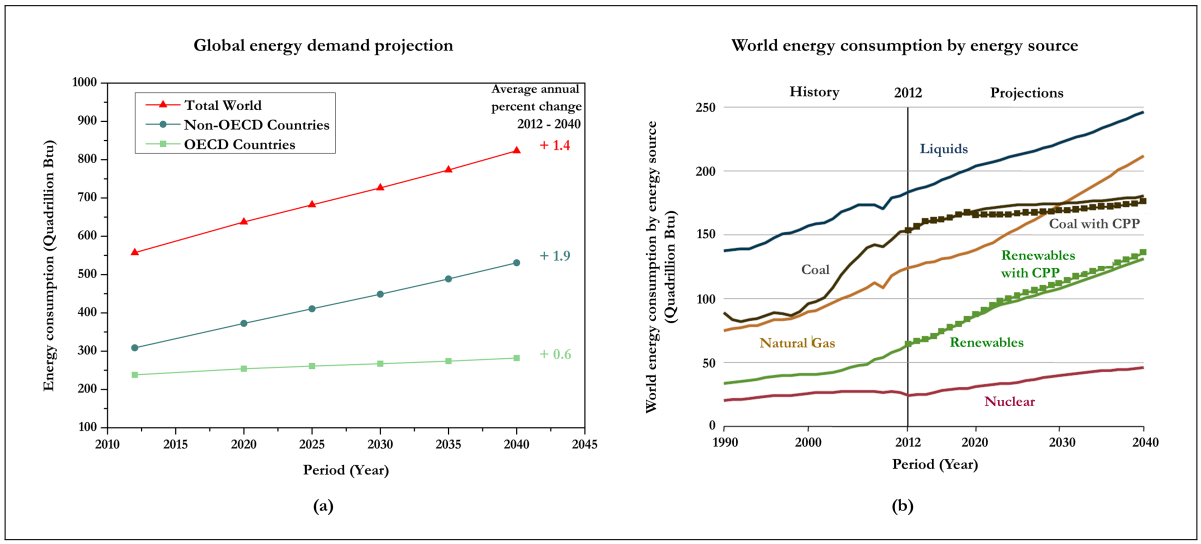

Figure 1.3: **(a)** Bottom to top: energy demand estimations in the OECD area, in non-OECD countries and in the whole world, respectively. Adapted from [5].
(b) The energy consumption estimations from all sources, redrawn from [5]. In the case of coal and renewable energies, dotted lines show projected effects of the U.S. Clean Power Plan.

The third most used energy source is the natural gas, with an average increase of 1.9%/y in the period 2012 - 2040. Natural gas consumption has the largest increment in the electric power generation and in the industrial sector. These data reveal one last important trend; renewable energy is the world's fastest-growing source of energy, with an average increase of 2.6%/y from 2012 to 2040. This increase has been made possible thanks to far-sighted government policies incentivising the use of non-fossil energy sources in many countries.

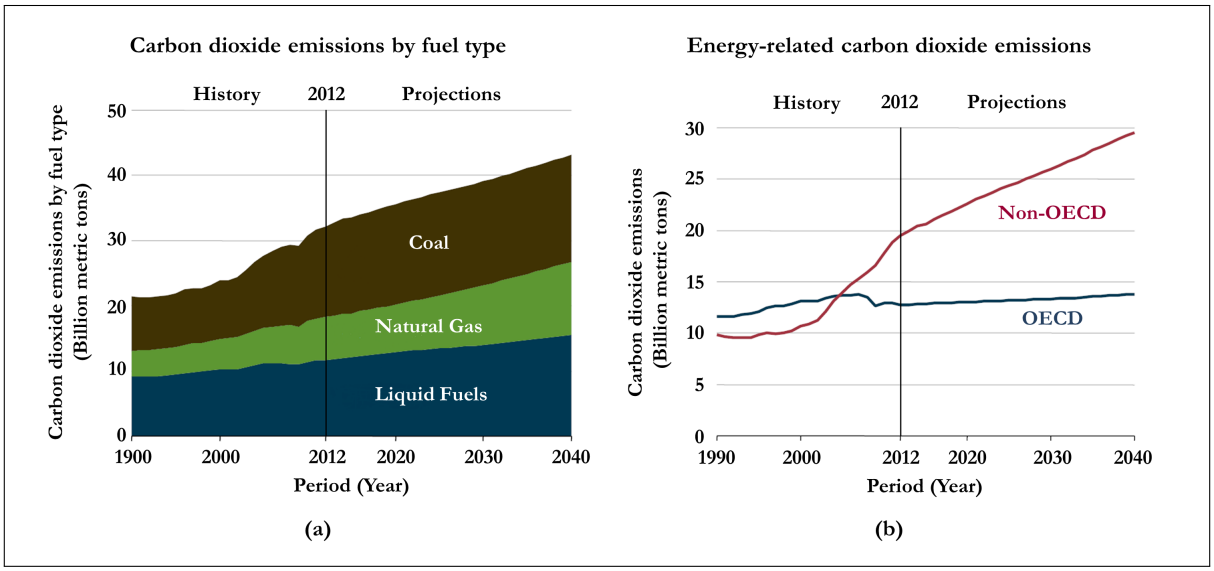

Figure 1.4: **(a)** World energy-related carbon dioxide (CO_2) emissions by fuel type, for the period 1990 – 2040, redrawn from [5].
(b) The energy-related (CO_2) emissions projections for OECD and non-OECD countries, adapted from [5].

1.1.3 Environmental consequences of the increase in energy demand

All the incentives, introduced to promote the use of renewable energy sources, have been created in order to mitigate the highly detrimental effects that a growing economy based on fossil fuels would ultimately have on the health of the planet.

One such effect is the release of carbon dioxide (CO_2), a greenhouse gas. It is generally accepted today, that CO_2 emissions primarily result from the combustion of fossil fuels (see Figure 1.4). Predictions suggest that the amount of global energy produced by burning fuel will likely increase to 35.6 billion metric tons in 2020 and to 43.2 billion metric tons in 2040 (it was 32.3 billion metric tons in 2012). Details also show that emissions will be larger for non-OECD countries. These will see an increase of 51% in their emission from 2012 to 2040. By contrast, the OECD area will experience a slower, 8% rise in the same period [5].

Everywhere in the world, experts are trying to find a compromise between the economic need of efficient energy generation and the environmental need of clean, low-emission technologies. Renewable energy has been proposed by many specialists as a viable, realistic solution to this challenge as it combines a clean, inexhaustible supply of energy with the promise of higher efficiency.

1.2 Renewable energy sources: state of the art and future prospects

Energy can be obtained from a number of different sources, but these are not all equivalent. The usual way of drawing a distinction between them is to describe them as either renewable or non-renewable. It is very important to understand the definition and the difference between these two terms [7].

By definition, non-renewable energy sources are those sources based on Earth's finite mineral resources. Energy is obtained from static stores of energy that remain underground unless released by human interaction. First examples of non-renewable energy sources include fossil fuels (coal, oil and natural gas) and nuclear power.

This is in contrast to renewable energy which is by definition energy obtained from naturally repetitive and persistent flows of energy occurring in the local environment. This includes sunlight, geothermal heat, wind, tides, water, and various forms of biomass fuels. This kind of energy cannot be exhausted and is constantly renewed.

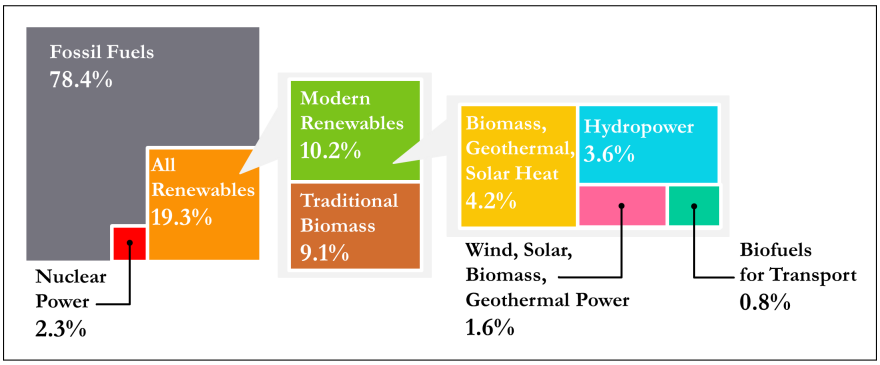

Figure 1.5: Global renewable energy consumed in 2015, reprinted from [8].

Years of supportive policies, declining costs and rapid technical progress have allowed renewable

technologies to experience a period of unprecedented growth in global investment during the last 10 years.

1.2.1 Current consumption of renewable energy

In 2015, renewable energy contributed to approximately 19.3% of global final energy consumption (as shown in Figure 1.5) [8]. However, renewable energy comes in many different individual forms.

The largest contributor is traditional biomass, which is mainly used for heating in the rural areas of developing countries, and represents about 9.1% of the global consumption of renewable energy. The remaining 10.2% comes from modern renewable sources of energy and they break down as follows:

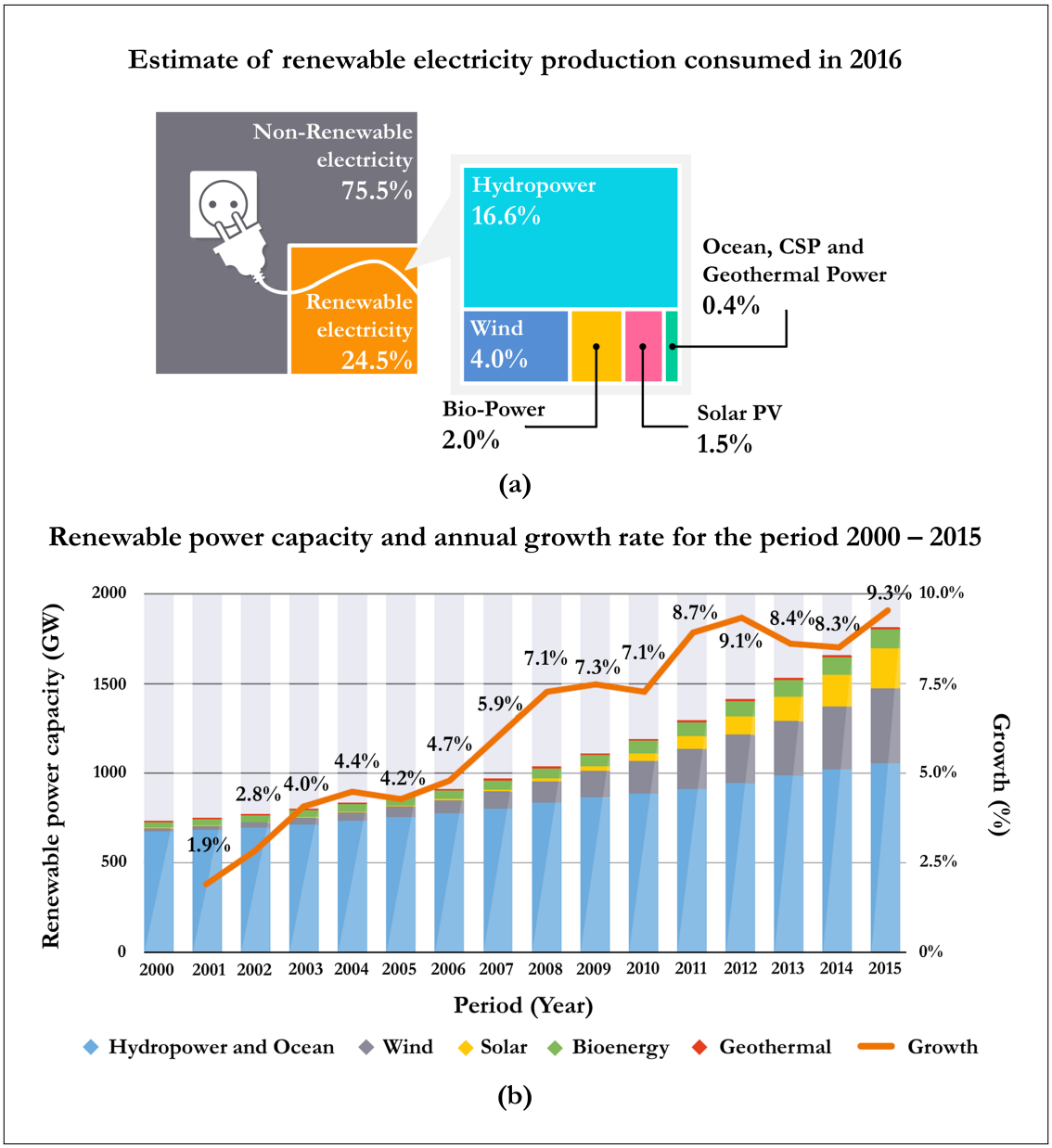

Figure 1.6: **(a)** The estimate of renewable electricity production consumed at the end of 2016, adapted from [8]. **(b)** The renewable power capacity (GW) and annual growth rate for the period 2000 - 2015, reprinted from [1].

- 4.2% modern biomass, geothermal and solar heat for heat energy sector;

- 3.6% hydro-power;
- 1.6% wind, solar, biomass and geothermal power for power energy sector;
- 0.8% bio-fuels for transport sector.

The main contribution of all renewable energy sources to the global energy demand is in the electricity sector (24.5% of total production). This sector grew by 9.3% between 2014 and 2015 [1], with an estimated added capacity of 161 GW.

This significant increase has been driven mainly by wind, by solar photovoltaic (PV) and by hydroelectric power (see Figure 1.6). In 2016, 47% of new installed renewable power capacity came from photovoltaics, 34% from wind power and the remaining 15.5% from hydro-plants.
Today solar PV and wind power have reached a state of development enabling them to contend against fossil fuels in an increasing number of locations. This is due in part to the reduction in the price of system components and to improvements in energy generation efficiency.

China, the United States, Brazil, Germany and Canada remain the top countries for installed renewable electric capacity at the end of 2016. China alone produces more than a quarter of the world's renewable power capacity (approximately 564 GW, of which around 305 GW from hydro-power).

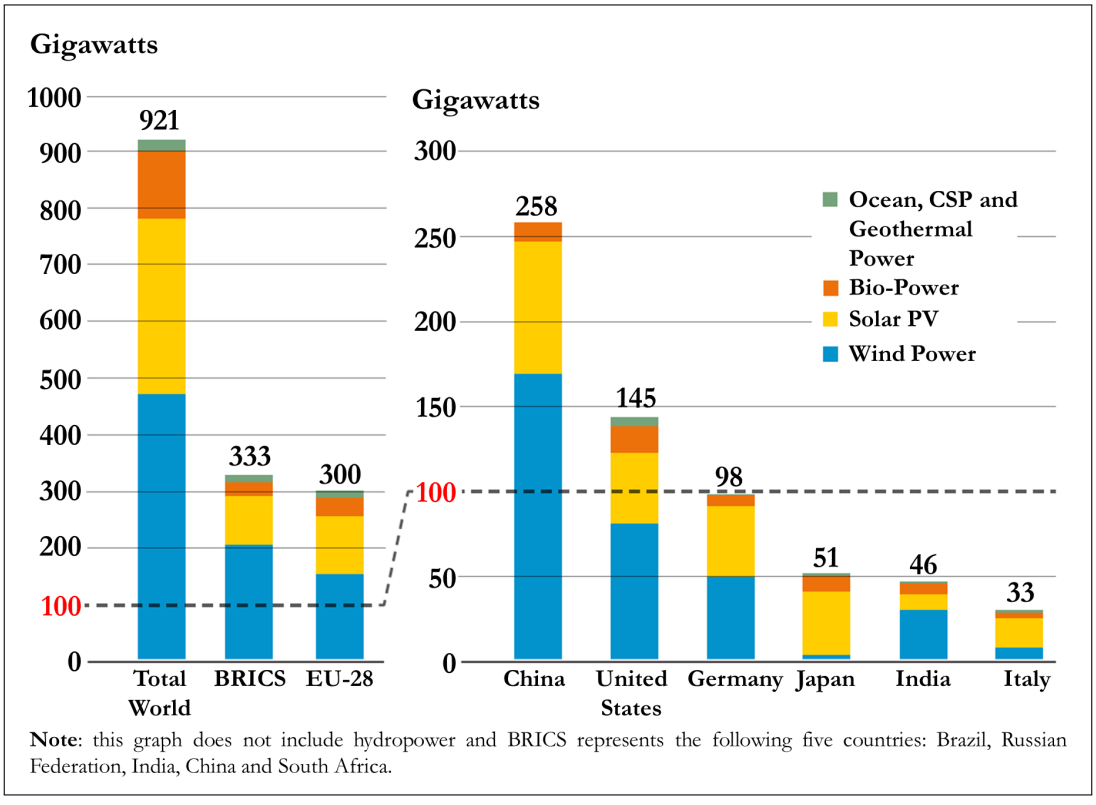

Figure 1.7: On the left: renewable power capacity around the world; data are also shown in aggregate form for BRICS and EU-28 blocs. On the right: renewable power capacity for the six largest investors in 2016. Adapted from [8].

If we exclude hydro-power capacity, the biggest investors in renewable technologies in 2016 were China, the United States and Germany. These were followed by Japan, India and finally Italy (Figure 1.7).

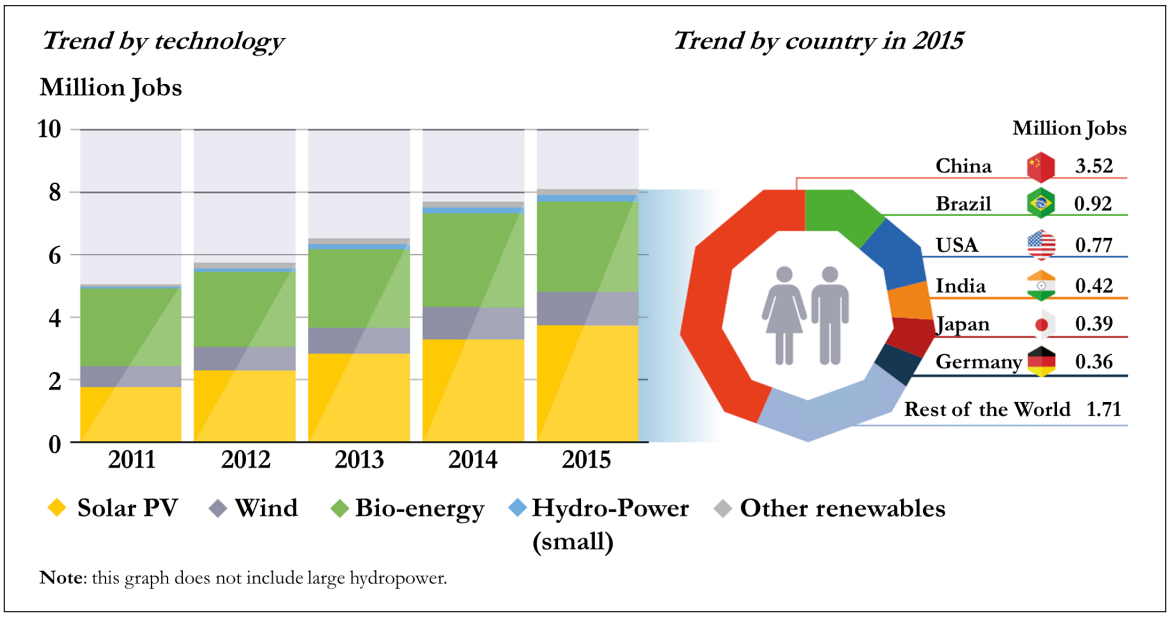

Figure 1.8: Global employment in renewable energy between 2011 and 2015 and, the 2015 jobs trend divided by country, reprinted from [1].

Hydro-power, which is the largest contributor to renewable power capacity, could overshadow more important developments in other renewable technologies, and that is why it was excluded. Iceland, Denmark, Sweden and Germany are the main countries for non-hydro power capacity per inhabitant. Renewable energy consumption is increasing worldwide, but there is another kind of demand that countries are considering, the social one.

1.2.2 Job opportunities in renewable energy sources

Besides bringing major benefits to the environment, a rapid development of renewable energy sources could also be a wise investment in human capital [8, 9]. This sector has in fact become a significant source of new employment around the world. If we consider all the direct and indirect positions involved in the development, manufacture and distribution of renewable energy, the number of people employed in this sector amounted to 9.8 million in 2016, with an increase of 1.1% over 2015. If we exclude hydro-power, these figures become 8.8 million workers in 2016, with an increase of 2.8% over 2015. Moreover, predictions seem to suggest that global renewable-oriented employment will keep rising thanks to falling prices and favourable policies in several countries.
In 2015, solar PV was the largest single renewable energy employer, followed by bio-fuels, wind energy, small-scale hydro-power and solar heating and cooling. Figure 1.8 shows how China has a leading position in renewable industry employment with 3.52 million of jobs in 2015. Within the Chinese renewable energy labour market, the main source of new jobs is solar PV. On the other hand, the number of positions in other renewable sectors such as thermal heating, small-scale hydro-power and bio-energy is reported to be decreasing.
The second major employer was Brazil with 0.92 million new jobs in 2015. Unfortunately, data reveal that there has been a reduction in this number as a consequence of increased mechanisation in the bio-fuel sector, and lower investment in the wind power and the solar water heating industries.

The United States is the third largest employer with 0.77 million new jobs in 2015. It is important to underline that the United States experienced an expansion in the number of jobs during the same year, which was encouraged by growing solar PV and wind power sectors (up 16%) under a regime of extended federal tax credits.
These countries are followed by India, Japan and finally Germany, the fist European country on this list. Germany remained the European leader in renewable energy employment with 0.36 million of new positions in 2015 even if, the number of jobs declined by approximately 6% in the same year.
Renewable energy employment has increased in several other countries worldwide, particularly in Asia. For instance, the number of solar PV jobs has risen by 10% in Bangladesh thanks to mini-grids growing and solar water pumps sector. Another example is Malaysia, which employed 95,500 people in its renewable energy industry in 2015, with about 27,900 jobs (a significant 46% increase) in the solar PV sector alone.

As for the exact nature of these occupations, it involves every segment of the renewable energy life-cycle, i.e. production, installation, feedstock supply, operation, maintenance, decommissioning and disposal or recycling. All these segments will require the training of a global, highly-qualified workforce bringing in a wide array of very different specialists, such as:

- Construction workers and technical personnel;
- Environment and geotechnical experts;
- Engineers for project planning, installation and grid connection;
- Logistic experts and quality control specialists;
- Financial analysts;
- Health and safety experts;
- Legal, energy regulation and taxation experts.

1.2.3 Future prospects of renewable energy sources

In this section we will describe the future prospects of renewable energy sources [1, 10]. We have already shown how renewable energies will play a key role in the future demand for energy, and how they can significantly contribute to a sustainable development of modern energy access. We have explained that these technologies can provide a solution to a number of concerns such as the high energy demand required by our fast-paced economy, or the air pollution caused by the use of environmentally unfriendly energy sources. Another pressing issue is the need to reduce the world's temperature increase below 2 °C, as noted at the 2015 United Nations Climate Change Conference (COP 21).

In order to solve these problems, the renewable share of world energy consumption (currently 18%) must at least double by 2030. However, the International Renewable Energy Agency (IRENA) has warned that this share will increase only slightly in the next 15 years - from 18.3% in 2014 to 21% in 2030 - if current national plans and policies are observed (as shown in Figure 1.9). Thus, a twofold increase in renewable energy will only be possible if all the signatories comply with the United Nations COP21 initiative.

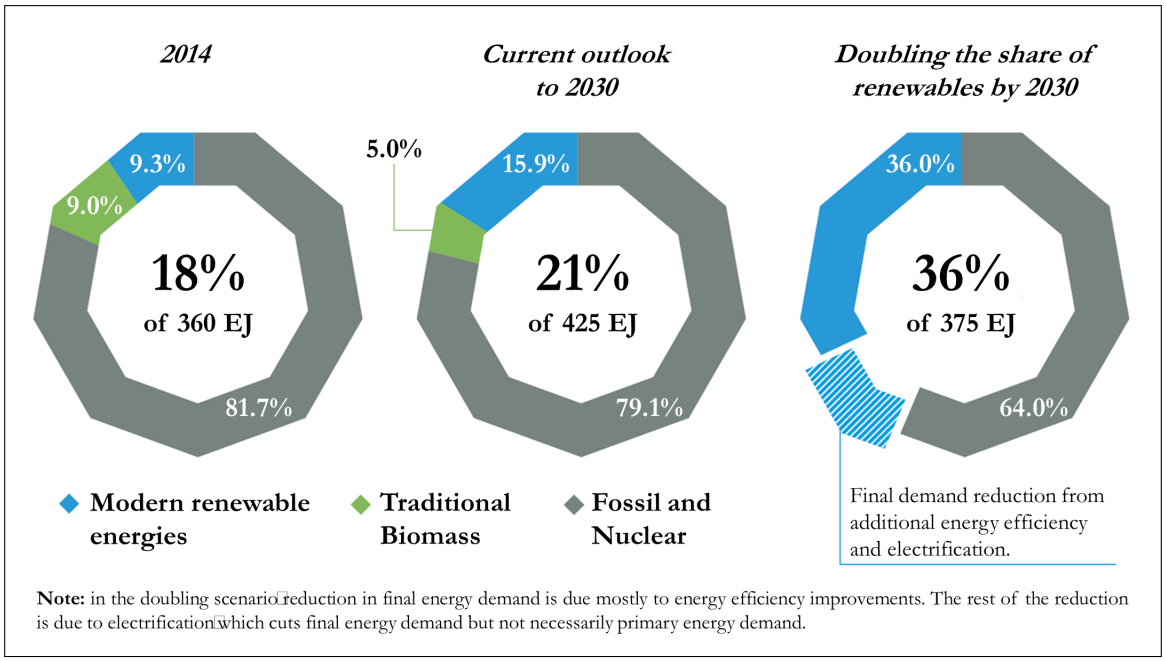

Figure 1.9: Renewable share of total energy consumption in 2014, and two projections of it for 2030 based on the current IRENA outlook and a twofold increase scenario, respectively. Adapted from [1].

IRENA's projections also suggest that doubling the renewable share of world energy may increase GDP by 1.1%, improve welfare by 3.7% and generate jobs for over 24 million people. It may also reduce air pollution enough to save up to about 4 million lives per year (see Figure 1.10).

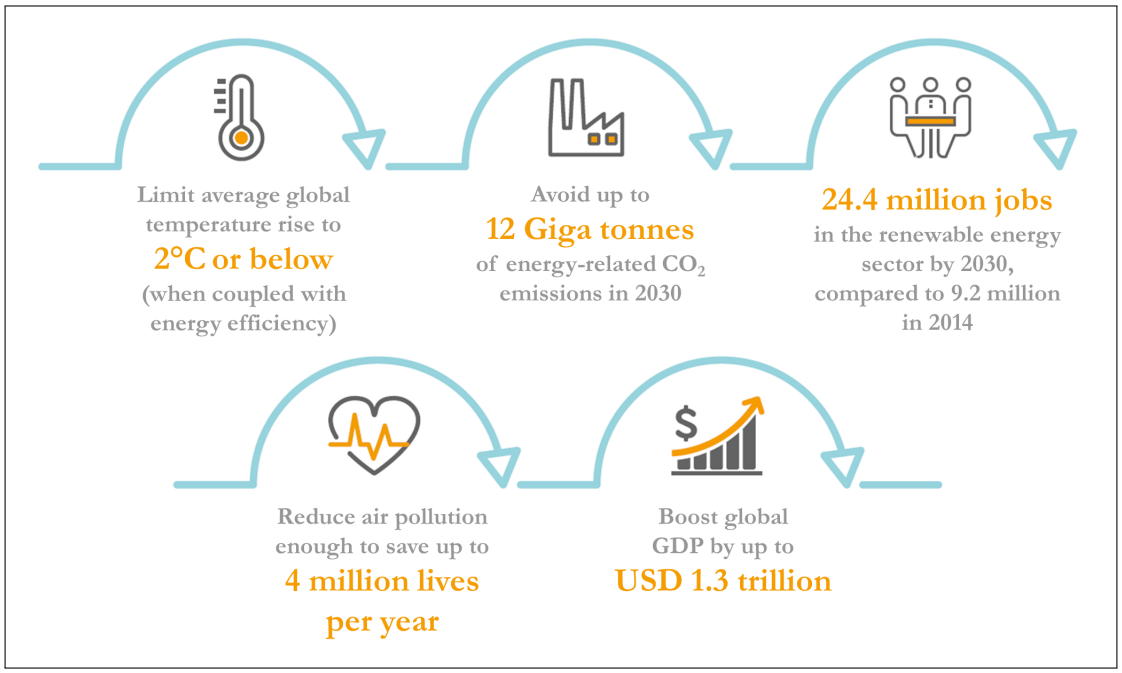

Figure 1.10: List of benefits that IRENA's roadmap envisages in case of a twofold increase in the renewable share of energy consumption. Redrawn from [10].

It is important to emphasize that to double this share, an annual investment of over USD 500 billion will be needed between 2015 and 2020, and another USD 900 billion between 2021 and 2030. The power

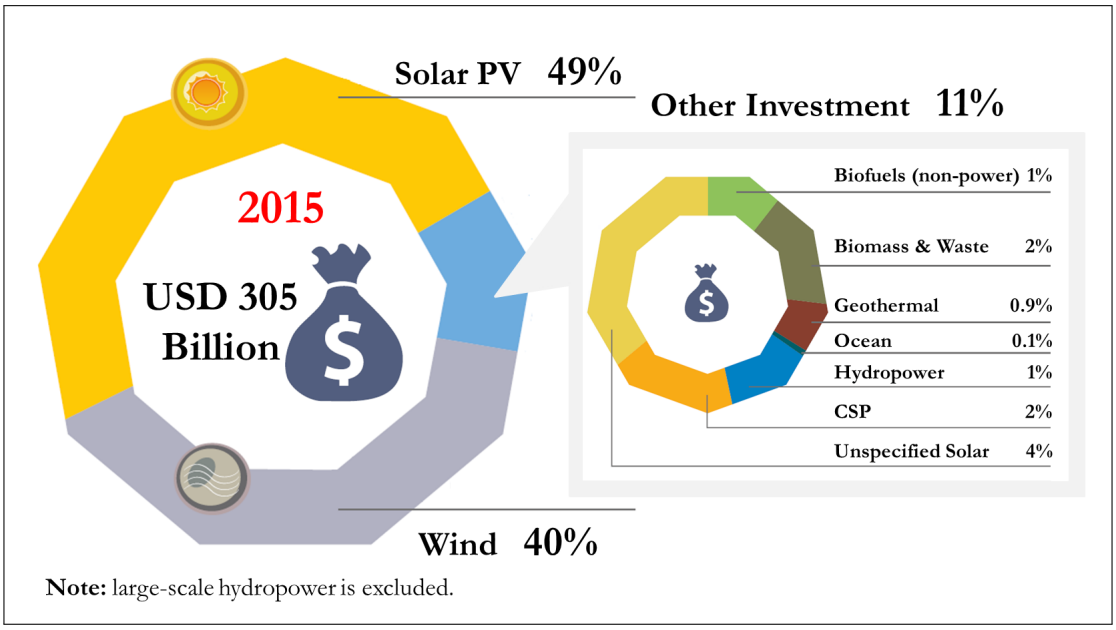

Figure 1.11: Percentage of global investment in renewable energy by technology in 2015, adapted from [1].

sector will be the main beneficiary of this investment with an estimated allocation of almost 80% of the incoming funds, but other areas will have to be funded as well, particularly transport and building thermal performance solutions.

The global investment in renewable energy reached USD 305 billion in 2015 and the level of funding has substantially increased over the past decade – it was less than USD 50 billion in 2004. From the point of view of international commitment, China alone supplied one third of the required total investment in 2015. The largest contributors after China were Japan, India, Europe (with USD 52 billion) and the United States (with USD 51 billion).
As was to be expected, about 90% of global investment in renewable energy was aimed at solar PV and wind power (see Figure 1.11). This particular choice of investment reveals a distinct lack of interest in diversifying the mix of renewable energies. But the most serious concern at present is the huge gap separating the actual amount of investment that countries have made so far from the missing amount that is still needed to achieve the aforementioned climate goals.

Thus, if we really want to achieve these goals, we have to combine a strong presence of renewable sources with a significant increase in energy efficiency [11, 12]. As a matter of fact, these two requirements are commonly defined as the 'twin pillars' of the future sustainable energy. True synergy will be achieved when either pillar supports the other and, this synergy exist across several sectors, such as buildings, industry, transport and finance.

Renewable energy systems and energy-efficient improvements can work together to reduce both the environmental and economic costs of the energy production. For example, they can help manage peak electricity demands on the grid, distribute energy sources more uniformly and efficiently and, at the same time, reduce transportation and transmission losses. The interaction between these two pillars can also promote the development of applications that might not be technically or economically viable otherwise.

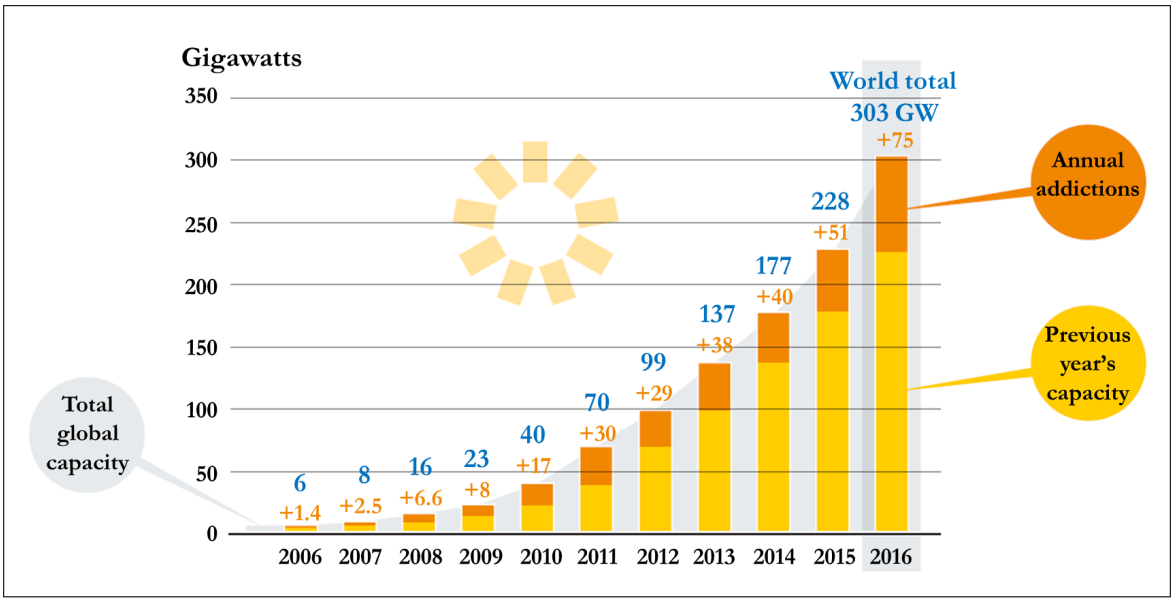

Figure 1.12: Total world capacity of solar PV in GW during the period 2006 - 2016. The orange part of the blocks represents the annual addictions, reprinted from [8].

1.3 A snapshot of total world photovoltaic market

Now, we will focus our attention on the present and the future trend of global PV market [8, 13, 14, 15, 16].

The COP21 agreement in Paris officially recognized photovoltaic energy as a major player against climate change, especially in keeping global warming below the critical 2 °C threshold (namely 2 °C above pre-industrial levels). At that time, an International Solar Alliance was created, in which 120 Countries have pledged to make solar energy a core energy source. Current estimates indicate that global installed solar power may reach nearly 1 TW by 2021.

The year 2016 will be remembered as a breaking point in the history of renewable energy as PV market broke several records. The global PV capacity reached 303 GW(DC)[3] at the end of 2016, with an increase of 75 GW (up 48%) over 2015. This is roughly equivalent to more than 31,000 solar panels installed every hour during last year. This impressive result is good news showing a return to a rapid expansion, after a period between 2014 and 2015 (up 25%) when the PV market grew rather slowly (see Figure 1.12).

Asia again eclipsed all other PV markets accommodating around two thirds of the newly installed global capacity. China, the United States, Japan, India and the United Kingdom were the top five markets and their combined effort amounted to about 85% of total installations in 2016 (Table 1.1). In contrast, the top five countries for cumulative installed capacity were China, Japan, Germany, the United States and, on a smaller scale, Italy (as shown in Figure 1.13 and Table 1.1). Interestingly, ranking in order of solar PV capacity per inhabitant shows Germany (first) 511 W per capita, Japan (second) 336 W per

[3]**GW(DC)** The capacity of a solar PV panel is evaluated with the output of direct current (DC). But in most cases, this output has to be converted by inverters to alternating current (AC), in order to supply the everyday electricity uses. Unfortunately, there are not a single equation to convert DC data into AC data, because the conversion depends on many factors, such as: inverters used, shading, dust build-up, line losses and temperature effects on conversion efficiency. Thus, this PhD thesis reports all solar PV capacity data as DC output, where data are provided in AC, this is indicated.

Table 1.1: Top 10 countries for newly installed capacity and for total installed capacity, respectively. Adapted from [14].

Top 10 countries for annual capacity added in 2016			Top 10 countries for cumulative capacity in 2016		
Position	**Country**	**Installed capacity (GW)**	**Position**	**Country**	**Installed capacity (GW)**
1	China	34.5	1	China	78.1
2	United States	14.8	2	Japan	42.8
3	Japan	8.6	3	Germany	41.2
4	India	4.1	4	United States	40.3
5	United Kingdom	2.0	5	Italy	19.3
6	Germany	1.5	6	United Kingdom	11.6
7	Korea	0.9	7	India	9.0
8	Australia	0.9	8	France	7.1
9	Philippines	0.8	9	Australia	5.9
10	Chile	0.7	10	Spain	5.5

capita and Italy (third) 322 W per capita.

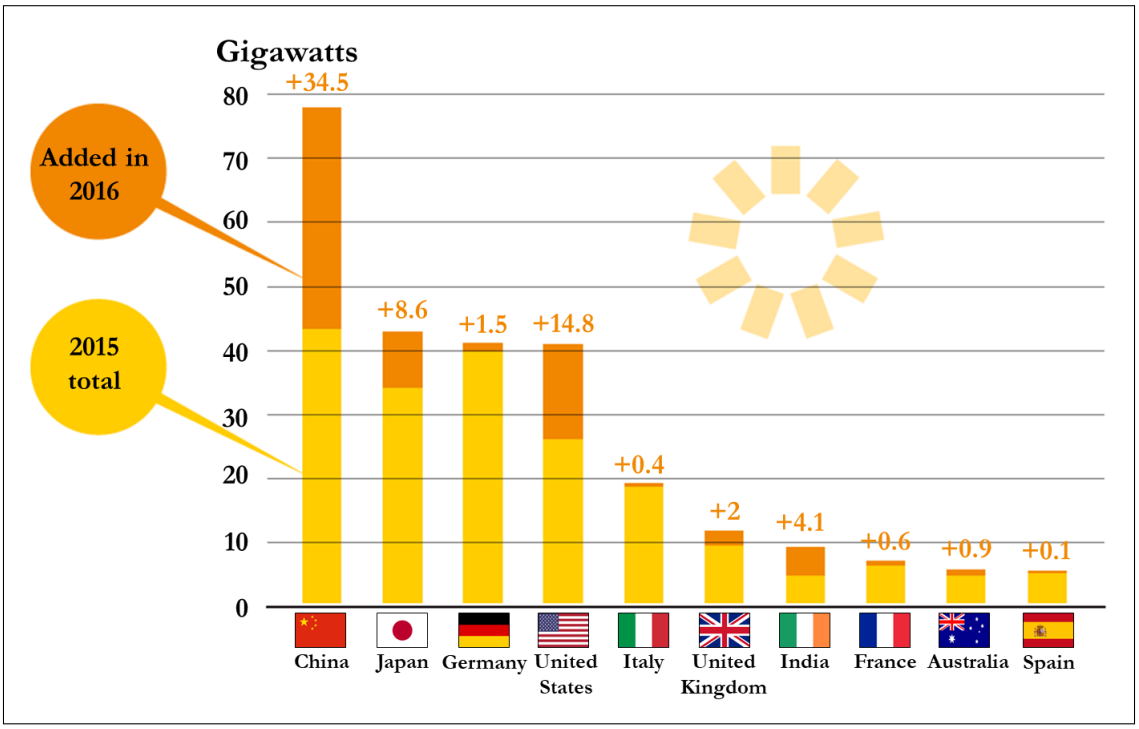

Figure 1.13: Cumulative and newly installed PV capacity of the top ten countries, redrawn from [8].

The main reason for this growth in the global number of installations is that PV becoming more competitive, which is made possible by reducing production costs and enhancing module efficiency. As a result, PV is closing its competitiveness gap with fossil fuels and even with onshore wind power. The cheapest contract price for solar energy agreed on in 2016 was 2.44 US cent/kWh. Even if this contract was awarded under very advantageous circumstances - namely stable political framework, very conve-

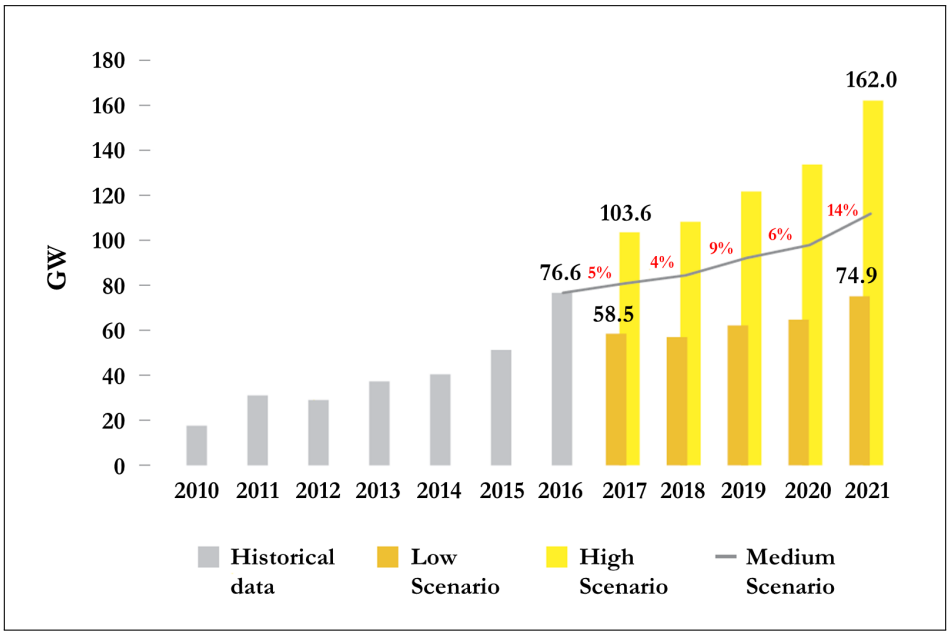

Figure 1.14: World annual PV growth rate and three different scenarios for the period 2017 - 2021. Adapted from [17].

nient financing environment and high irradiation - it is a model of hope for the future reduction of PV costs. It should be mentioned that the different incentive mechanisms such as: traditional feed-in tariffs or power purchase agreements are still in place, driving the market demand. This is of great importance as a lower price of PV modules alone has already been proved to be not sufficient to sustain the solar energy market. For instance, solar demand quickly became negligible in Spain after incentives were removed, and the same is true for the United Kingdom, where the government has chosen to subsidize new nuclear power indeed solar energy.

Another important matter concerns the global market prospects for the 2017 - 2021 period. Solar Power Europe, in its latest outlook [17], has shown three different scenarios for the future prospects of solar power. These are called: Low, Medium and High Scenario, and they are displayed in Figure 1.14. All three scenarios imply that there will be a more moderate growth rate in 2017 compared to 2016, but of course there are some differences between them:

- The Low Scenario assumes that government incentives will be removed and, as a consequence, PV demand will drastically fall to 58.5 GW in 2017. Fortunately, this is very unlikely to happen, because early year data on new solar installations already show a better trend than the one envisaged in this scenario.
- The Medium Scenario estimates a growth rate for newly installed PV of about 5% compared to 2016. This would mean an increase of about 80.5 GW for 2017.
- The High Scenario is very ambitious. It predicts an annual growth of about 103.6 GW. This value is quite optimistic, and nobody had originally forecast an annual 50% growth for 2016 when it actually happened.

The solar Power Europe scenarios also predict that the growth rate will subsequently increase between 2018 and 2021 as a result of further cost reduction, new markets and new market players. In

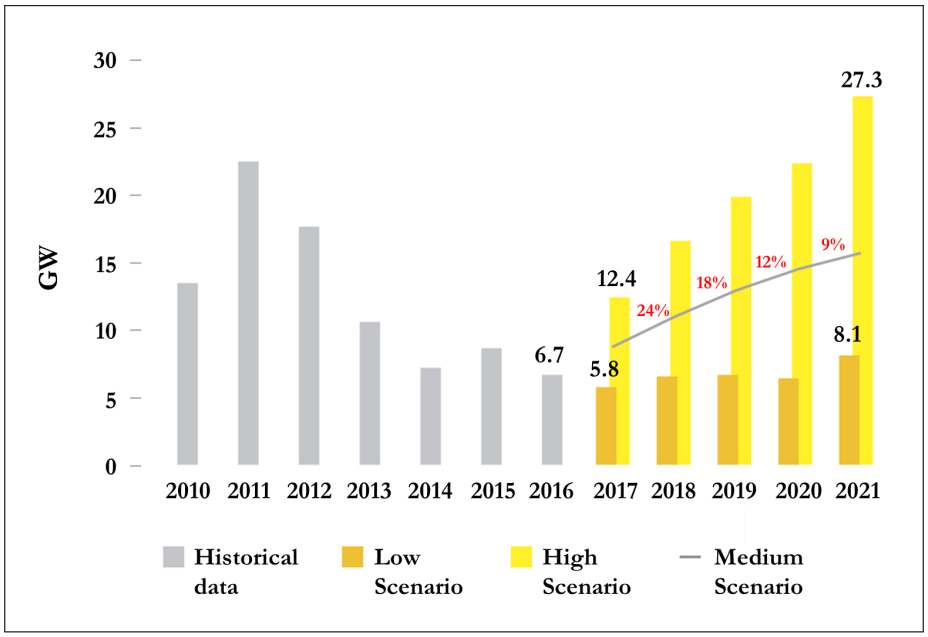

Figure 1.15: European annual PV growth rate and three different scenarios for the period 2017 - 2021, reprinted from [17].

particular, the Medium Scenario highlights that the world installed PV capacity will go over the level of 400 GW in 2018, 500 GW in 2019, 600 GW in 2020 and 700 GW in 2021. Going over these scenarios, Asia will keep a dominating position in the PV market with at least two thirds of total installations in the near future.

1.3.1 European photovoltaic market

In European PV market, there are some conflicting aspects, as well [16, 17]. Although Europe passed the 100 GW milestone of installed PV capacity in 2016 and still represents a principal provider of world solar energy installation, its contribution to PV energy is slowly decreasing. New installed capacity was a rather disappointing 6.7 GW, and the European solar market declined by 22% compared to the previous year.

Data from 2016 show that the United Kingdom was the European leading solar market, with around 2 GW of new installations, but unfortunately the government decided to withdraw its support to solar energy at the end of the first quarter of 2016.

Germany was once again the second European solar market leader. Its delivery of solar energy was stable with an increase of 1.5 GW. The Netherlands', Switzerland's and Austria's commitment was also quite stable but it provided a limited number of new installations (525 MW, 250 MW and 150 MW, respectively).

France was the most surprising disappointment. It froze its number of installations to below 0.6 GW, which means a decrease of 38% in its PV market compared to the previous year.

Italy radically reduced its PV market as well, installing only 373 MW of new PV systems. This reduction is common to all the countries, in which the feed-in tariffs were phased out. Finally, countries such as the Czech Republic, Greece, Romania and Bulgaria persisted in their tendency to install very little solar power systems.

The 2016 solar energy reports suggest that there are no major changes in the European solar picture, with Germany (39.4%) and Italy (18.2%) remaining the bulk of total solar capacity on the continent.

For the European PV market in the 2017 - 2021 period (Figure 1.15), the spread between High and Low Scenarios could be very large in the coming years, depending on Brussels' and single countries' future policies.

If most of the European countries removed any trade barriers to solar energy (High Scenario), the annual PV increase could reach the level of 27 GW in 2021 and Europe would be able to almost double its cumulative PV capacity from 104.3 GW installed in 2016 to 202.9 GW by the end of 2021.

On the contrary, if all the European countries failed to see the potential of solar energy and its benefits, the Low Scenario is what would happen. The annual increase in PV capacity would only reach the level of 8.1 GW in 2021 and Europe's solar power capacity would only rise as high as 137.9 GW by the end of that year.

Unfortunately, prospects of continued government support for solar energy are not as promising as expected for the next years in Europe. It is estimated that the top three solar market in Europe will be Germany, France and Turkey by 2021. These will be followed by the Netherlands and Italy. Surprisingly, the United Kingdom, a three years' leader in this sector (2014 - 2016), is not expected to retain its position among the top five nations.

References

[1] Irena. *Rethinking energy 2017: Accelerating the global energy transformation.* In International Renewable Energy Agency, Abu Dhabi, 2017.

[2] United Nations Department Of Economic, Social Affairs and Population Division. *World population prospects: The 2015 revision, key findings and advance tables.* Working Paper, No. ESA/P/WP. 241, 2015.

[3] M. Roser and E. Ortiz-Ospina. *World population growth.* 2017 (Accessed May 22, 2017).
https://ourworldindata.org

[4] International Energy Agency. *World energy outlook 2016.* Chapter 1. 2016 (Accessed May 25, 2017).
https://www.iea.org

[5] Eia. *International energy outlook 2016. With projections to 2040.* May 2016. DOE: EIA-0484(2016) (Accessed May 25, 2017).
https://www.eia.gov

[6] The Conference Board, Trusted Insights for Business Worldwide. *The conference board global economic outlook 2017.* May 2017. (Accessed May 25, 2017).
https://www.conference-board.org

[7] J. Twidell and T. Weir. *Renewable energy resources.* Routledge. 2015.

[8] Ren21. *Renewables 2017. Global status report.* ISBN 978-3-9818107-6-9. Paris, 2017 (Accessed June 09, 2017).
http://www.ren21.net

[9] Ren21. *Renewables global futures report: Great debates towards 100% renewable energy.* ISBN 978-3-9818107-4-5. Paris, 2017 (Accessed June 09, 2017).
http://www.ren21.net

[10] Irena. *Unlocking renewable energy investment: The role of risk mitigation and structured finance.* ISBN 978-92-95111-92-9. In International Renewable Energy Agency, Abu Dhabi, 2016.

[11] Ren21. *Renewables 2012 global status report.* Paris, 2012 (Accessed June 27, 2017).
http://www.ren21.net

[12] Ren21. *Renewables 2015 global status report.* ISBN 978-3-9815934-6-4. Paris, 2015 (Accessed June 27, 2017).
http://www.ren21.net

[13] Solar Power Europe. *Global market outlook. For solar power / 2015 - 2019.* Euoropean Photovoltaic Industry Association, Bruxelles, Tech. Rep. 2015 (Accessed June 27, 2017).
http://www.solarpowereurope.org

[14] Pvps and Iea. *Snapshot of global photovoltaic markets.* IEA Photovoltaic Power Systems Programme Report T1-29. 2016 (Accessed July 20, 2017).
http://http://www.iea-pvps.org

[15] Solar Power Europe. *Solar market report & Membership directory.* Brüssel. 2016 (Accessed June 27, 2017).
http://www.solarpowereurope.org

[16] Solar Power Europe. *Global market outlook. For solar power / 2016 - 2020.* 2016 (Accessed July 27, 2017).
http://www.solarpowereurope.org

[17] Solar Power Europe. *Global market outlook. For solar power / 2017 - 2021.* 2017 (Accessed July 27, 2017).
http://www.solarpowereurope.org

Chapter

2

An introduction to photovoltaic energy

In this chapter, a summary of the state of the art concerning photovoltaic solar energy is given. I will focus on the theoretical and technological aspects of photovoltaic systems. I will also report on the structure of photovoltaic cells and on their life-cycle assessment.

2.1 Solar photovoltaic basics

Before analysing the state of the art in PV technology, I will give a clear definition of it [1, 2, 3]. Therefore, the first question we need to answer is, 'what is photovoltaic solar energy?'. The term 'photovoltaic' is the union of two words:

- Photo: Greek word for 'light';
- Voltaic: word that means electricity. The Volt is the SI unit of the electric potential.

In other words, a PV system is a system, which converts sunlight directly into electricity. This conversion process is based on the photoelectric effect, discovered by Alexander Bequerel in 1839. The photoelectric effect is responsible for the emission of negative charge carriers when light strikes the surface of a solid material [4].

It is well known that all materials can be divided into three groups based on their electrical properties - namely, conductors, semiconductors and insulators. Electrical conductivity (σ) and the energy band gap (E_g) are the two main properties that can be used to classify materials (see Table 2.1), but it should be underlined that there is no clear border between these classes [5].

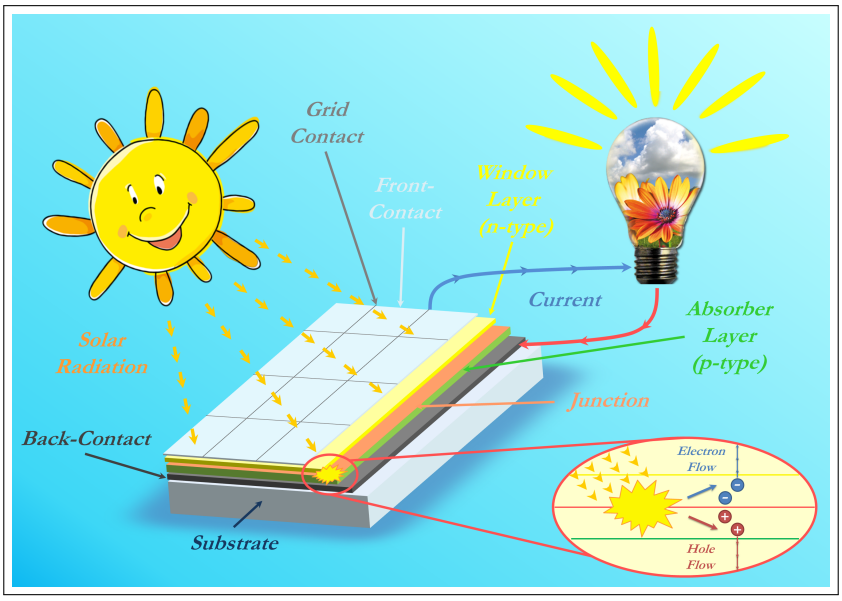

Figure 2.1: Schematic representation of the photovoltaic effect.

Table 2.1: Typical values of electrical conductivity and energy band gap for the three different classes of electronic materials, adapted from [5].

Parameter	Conductors	Semiconductors	Insulators
σ $(\Omega\ \mathrm{cm})^{-1}$	$\sim 10^{8} - 10^{1}$	$\sim 10^{1} - 10^{-8}$	$\sim 10^{-8} - 10^{-20}$
E_g (eV)	~ 0.3 or negative value	$\sim 0.3 - 4.0$	$\sim 4.0 - 10.0$

Most PV devices are composed of different sequences of semiconducting materials. Their central part is made of two layers. One must be a *p*-type semiconductor, characterised by an excess of positively charged carriers, i.e. holes; the other one must be a *n*-type material, doped with an excess of negatively charged carriers, i.e. electrons. These two layers constitute the so-called *p*-*n* junction.
At the junction interface, the difference in work functions between the *p*- and *n*-type region results in an electrical potential barrier. This potential means an internal electric field, which is responsible for separating the charge carriers when they are released by light.

What follows is a simple description of the PV effect (see Figure 2.1):

1. Absorption of photons and creation of charge carriers
   The absorption of light with appropriate energy promotes the electrons from the lower-energy valence band (VB) to the higher-energy conduction band (CB).

2. Separation of photo-generated carriers before their recombination
   Thanks to the junction electric field, the electrons in CB flow from the *p*-type to the *n*-type side of the junction, and the photo-generated holes in the VB flow in the opposite direction. The light absorption and the electric field generate a steady motion of the charge carriers.

3. Collection of charge carriers
   These electric charges can finally be collected through metal contacts and they can therefore be extracted from the device to supply power to an external load.

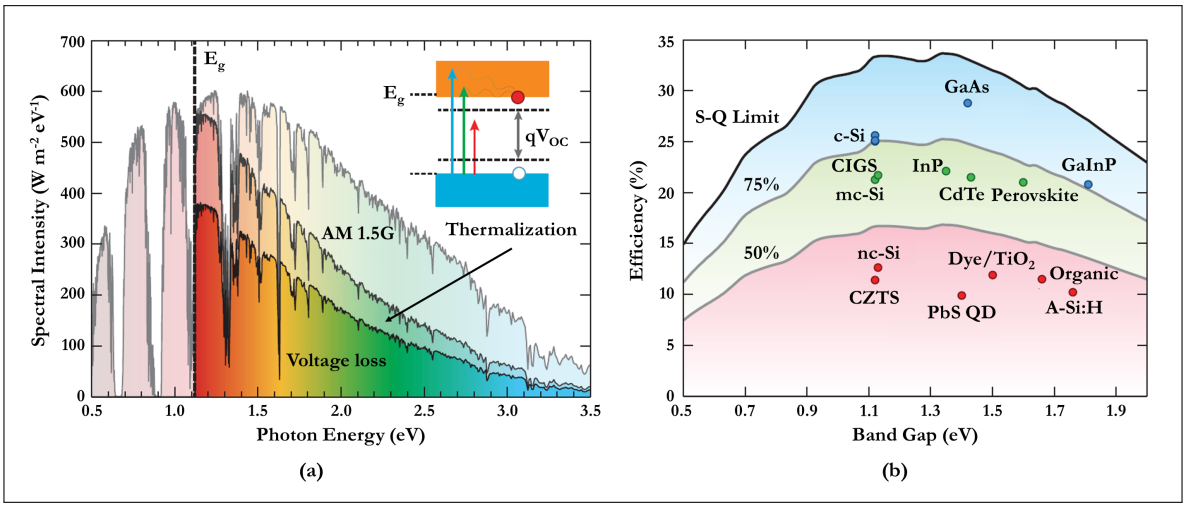

Figure 2.2: (a) Solar spectrum at AM 1.5, adapted from [7]. The E_g dashed black line refers to the E_g of silicon. The effects of thermalisation and voltage loss are highlighted. In the upper right corner, a diagram of the electronic band structure illustrates the separation in energy between quasi-Fermi levels.
(b) The black line represents the theoretical S-Q limit as a function of E_g. The two grey lines drawn below this limit mark 75% and 50% of the limit itself, respectively. Redrawn from [7]. World record efficiency of different single-junction solar cells are plotted at the corresponding values of energy band gaps (these data are referred to April 2016).

2.1.1 Limit of efficiency of *p-n* junction solar cells

As a consequence of the PV effect, the amount of electrical power that each PV cell can generate is determined by the incoming light intensity.

Solar energy is the most abundant energy resource on our planet and it is a very convenient way to satisfy world energy demand. It is well known that each square meter of land on Earth has the potential of generating an average 1,700 kWh of energy every year. In principle, the amount of solar radiation that reaches the Earth's surface could provide 10,000 times the energy which is currently globally required.

Unfortunately, only a small part of the solar irradiation can be utilised to generate electricity with PV devices [6, 7, 8]. Shockley and Queisser (S-Q) developed a theoretical framework for determining the efficiency limit of a solar cell in 1961. The Shockley–Queisser limit (S-Q limit), also known as detailed balance limit, is outlined for a single-junction solar cell in Figure 2.2. The maximum solar conversion efficiency was found to be around 33.7% for a semiconductor with an energy band gap of 1.34 eV (using Air Mass (AM) 1.5[1] filter). Of the total amount of sunlight that illuminates an ideal solar cell (about 1000 W/m^2), only 33.7% can be turned into electricity (about 337 W/m^2).

In determining the detailed balance limit of efficiency, Shockley and Queisser have calculated the efficiency of a solar cell considering the usual definition - namely, the ratio between the maximum electrical power generated by the solar cell under a working load and the incident solar power that

[1] **Air mass coefficient** (AM) defines the optical path passing through the Earth's atmosphere in a fixed moment in time and space. It quantifies the reduction in the power of light when it passes through the atmosphere and is absorbed by air. Air Mass is expressed as:

$$Air\ Mass = \frac{1}{\cos\theta_z} \tag{2.1}$$

where θ_z is the angle between the light ray and the vertical (zenith angle). The standard spectrum used to facilitate an accurate comparison between solar cells is AM 1.5 (ϑ_z = 48.6°), normalized to a total power density of 1 kW/m^2.

impinges on the cell. For these calculations, they considered only the following three variables:

1. Sun temperature (T_s):
$$k\,T_s \;=\; q\,V_s \tag{2.2}$$

2. Solar cell temperature (T_c):
$$k\,T_c \;=\; q\,V_c \tag{2.3}$$

3. Energy band gap of the semiconductor acting as the photovoltaic absorber (E_g):
$$E_g \;=\; h\,\nu_g \;=\; q\,V_g \tag{2.4}$$

where k is Boltzmann's constant, q = |q| is the electronic charge, and h is Planck's constant. Furthermore, the three basic assumptions of S-Q limit can be summarised as follows:

a. If the incoming photons have an energy (E_{Ph}) below E_g, they will not be absorbed and they will not contribute for generating energy. On the other hand, if the incoming photons have an energy $E_{Ph} = h\nu \geqslant E_g$, the generation of a single electron-hole pair in the absorber material has a probability equal to one.

b. The collection probability for all photo-generated carrier pairs is equal to one.

c. The only loss mechanism is spontaneous emission of photons by radiative recombination of electron-hole pairs.

Hirst and Ekins-Daukes deduced the following approximate relation between the energy band gap of a PV solar cell and its voltage at maximum power point (V_M) from the detailed balance limit principle [9, 10]:
$$q\,V_M \;\approx\; E_g\left(1 \;-\; \frac{T_c}{T_s}\right) \;-\; k\,T_c\,\ln\!\left(\frac{\Omega_{emit}}{\Omega_{abs}}\right) \tag{2.5}$$

where Ω_{emit} and Ω_{abs} are the emission and absorption solid angles, respectively. The two terms on the right-hand side of the Equation (2.5) represent, respectively:

1. The Carnot efficiency. It expresses the need of evacuating the incoming entropy.

2. The voltage loss due to the spectral mismatch between the incident radiation and the absorption in the cell. The maximum of the solar spectrum does not meet the energy band gap of the absorber (Figure 2.2b).

Figure 2.3 shows the loss mechanisms corresponding to the effects previously mentioned in the case of an ideal *p-n* junction solar cell. These two types of loss are linked to the spectral mismatch of the energy distribution of photons in the solar spectrum and to the energy band gap of the absorber materials. In the figure, they appear as 'below E_g loss' and 'thermalisation loss', respectively. The last three losses are related to the balance between absorption and emission rate and they are also called balance losses. It should be underlined that these three losses stem from the same physical mechanism, i.e. radiative recombination, but we can separate them:

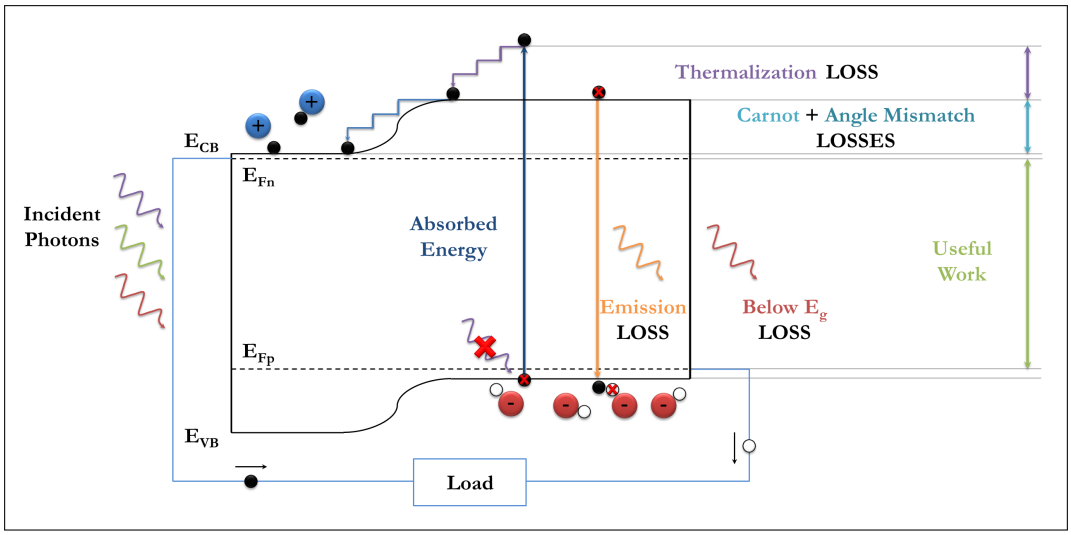

Figure 2.3: Fundamental loss mechanisms for a solar cell. E_{CB} and E_{VB} represent the energies of the bottom edge of the CB and the top edge of the VB, respectively. Instead, E_{Fn} and E_{Fp} represent the quasi-Fermi levels of electrons and holes, respectively. This schematic representation is similar to that in [9].

1. Emission Loss that represents a limit to the current of solar cell and it corresponds to the photons emitted energy at the maximum power point due to recombination.

2. Carnot and Angle Mismatch Losses that represent the voltage losses associated with the emission process. These losses occur at the junction or more generally where the charges are separated.

Furthermore, it should be mentioned that the radiative emission increase with temperature of solar cell. As a consequence, there is an increase of the equilibrium carrier concentration and also an increase of the recombination rate. This shows why the maximum efficiency of PV device decreases with the temperature.

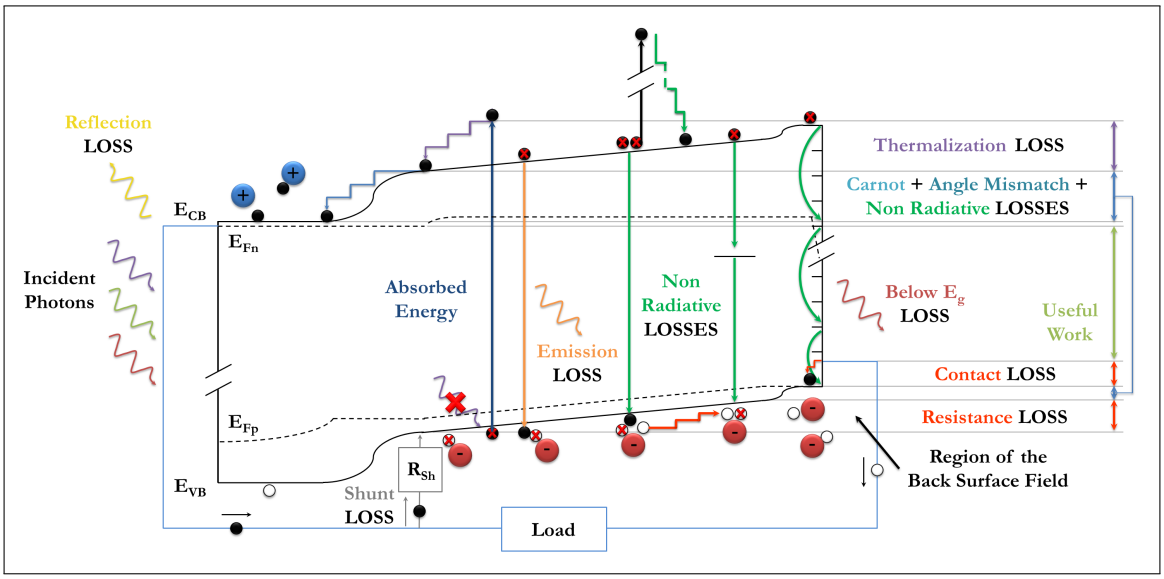

Figure 2.4: Conversion loss mechanisms of a real *p-n* junction solar cell. This schematic representation is similar to that in [9].

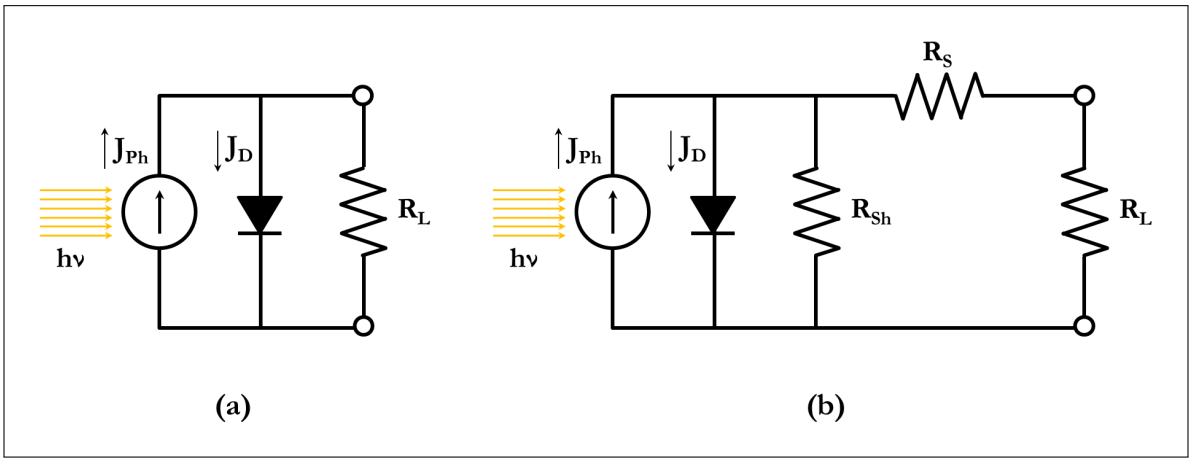

Figure 2.5: Comparison between the equivalent circuit of an ideal solar cell (a) and a real solar cell (b).

Unfortunately, currently commercial PV devices show efficiencies considerably lower than the S-Q limit. The main additional losses that limit real PV solar cell performances are summarised in Figure 2.4. The non-radiative recombinations represent the main losses and the most important process are: Shockley Read Hall[2], Auger[3] and surface[4] recombination. There are also other losses that need to be highlighted, such as: reflection loss at the front contact of the solar cell, electrical shunt, non perfect contacts and the finite mobilities of carriers. Finally, Figure 2.4 does not shows the case of photons with sufficient energy that are not absorbed, i.e. the transmission loss. This loss can causes a reduction of efficiency in case of thin-film solar cells with non sufficient light trapping. In summary, the combination of all the above factors leads to a substantially lower efficiency than the S-Q limit.

2.2 Equivalent circuit of solar cells

From an electrical point of view, a PV cell can be represented as a diode connected in parallel with an ideal current generator (Figure 2.5a). The current generator corresponds to the process of photo-excitation while the *p-n* junction (diode) supplies the internal electric field necessary for driving the photo-excited carriers through the external circuit [11, 12].

A solar cell is activated by light. When this is provided, it develops electrical power. The term open-circuit voltage (V_{OC}) refers to the voltage developed when the terminals are isolated, or equivalently connected to an infinite resistance load (R_L). The term short-circuit current (I_{SC}) refers to the current flowing through the circuit when the terminals are directly connected one to each other. Because the current itself is roughly proportional to the illuminated area it is useful to consider the short-circuit current density (J_{SC}).

[2]**Shockley Read Hall recombination** consider only two particles (an electron and a hole) and a two step process by which an excited carrier recombines trough a defect state in the forbidden energy band gap. These defects can either be unintentionally introduced (such as: crystalline defects) or deliberately added to the material (such as: dopants).

[3]**Auger recombination** is a process where three particles are involved: two of them in the process of generation or recombination, and the third that takes or gives some energy. These process does not depend on the presence of defects, but on the local concentration of carriers in the CB and VB.

[4]**Surface recombination**. Surfaces and interfaces are regions where the lattice structure presents a huge quantity of defects. Furthermore, it should be underlined that the impurities tend to gather in these regions. Thus, the energy band gap is filled with defect states and recombinations happen extremely fast.

The overall current-voltage response of a solar cell can be approximated to the sum of two terms:

1. The current generated by light;

2. The current flowing in the dark, when a voltage is applied.

This assumption is known as superposition approximation. If we assume this, the current density (J) that flows in an ideal solar cell when photo-excitation occurs can be written as:

$$J = J_{SC} - J_0 \left(e^{(qV/k_B T)} - 1 \right) \tag{2.6}$$

The second term on the right-hand side of the Equation (2.6) represents the forward current driven by the voltage V (i.e. dark current density, (J_D)). The constant J_0 is often called reverse saturation current, k_B is the Boltzmann constant and T is the temperature in Kelvin.

When the contacts are isolated, namely in open-circuit condition, J = 0 and the solution of the Equation (2.6) becomes:

$$V_{OC} = \frac{kT}{q} \ln \left(\frac{J_{SC}}{J_0} + 1 \right) \tag{2.7}$$

This equation shows that V_{OC} increases logarithmically by increasing the light intensity. The operational regime of a solar cell, the interval in which it delivers power, is the range from 0 to V_{OC}. The power density of a solar cell is the product of current density and voltage:

$$P = J \times V \tag{2.8}$$

The maximum power point (P_M), which corresponds to the product of current density (J_M) and voltage (V_M), is (Figure 2.6):

$$P_M = J_M \times V_M \tag{2.9}$$

The efficiency (η) of a solar cell can be expressed as:

$$\eta = \frac{P_M}{P_{Inc}} = \frac{J_M \times V_M}{P_{Inc}} = FF \times \frac{J_{SC} \times V_{OC}}{P_{Inc}} \tag{2.10}$$

where P_{Inc} is the total incident light power striking the cell. The FF is defined as the ratio:

$$FF = \frac{J_M \times V_M}{J_{SC} \times V_{OC}} \tag{2.11}$$

and it is a measure of the 'squareness' of J-V curve.

J_{SC}, V_{OC}, FF and η are the four key quantities for assessing the performance of a solar cell. The Standard Test Condition (STC) for solar cells corresponds to an incident power density of 1000 W/m^2 and a temperature of 298.15 K, under AM 1.5 filtered solar light spectrum.

2.2.1 Equivalent circuit of a real solar cell

When we consider a real device, some degree of power losses will need to be taken into account. Major losses are associated with light absorption and with the recombination of charge carriers. For

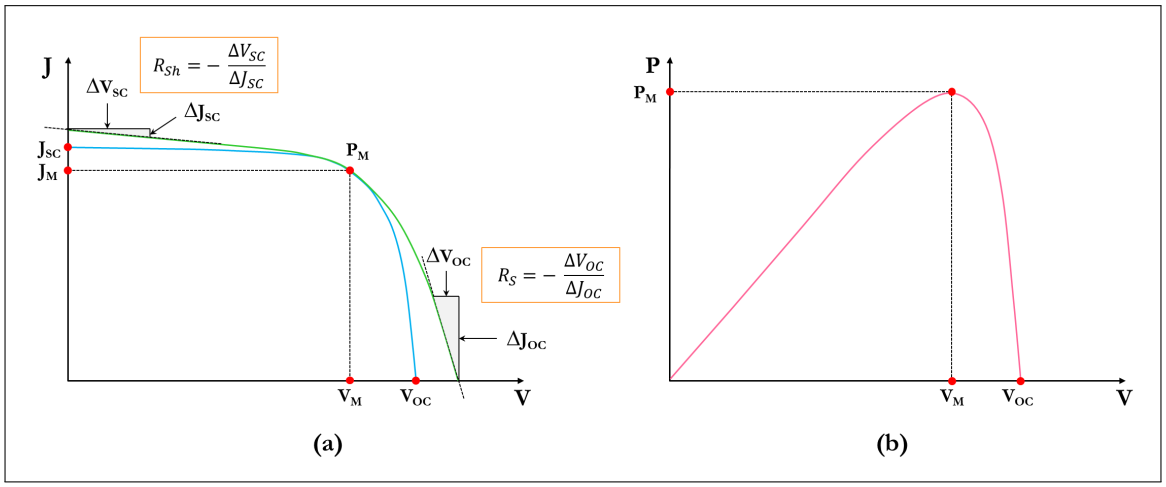

Figure 2.6: (a) Comparison between the J-V characteristics of a cell with shunt and series resistances (green curve) and a standard cell without any resistance issues (blue curve).
(b) P-V characteristic of a standard PV solar cell.

this reason, the equivalent circuit of a real solar cell has two additional parasitic resistances: the shunt resistance (R_{Sh}) and the series resistance (R_s), both shown in Figure 2.5b. Typical values of R_{Sh} and R_S for a good silicon solar cell are at least 500 Ω cm^2 and less than 0.5 Ω cm^2, respectively.

R_{Sh} represents the effects of recombination currents and leakage currents around the edge of devices. A big R_{Sh} value corresponds to a high solar cell efficiency, since it means that the leakage currents are reduced. On the contrary, a small R_{Sh} will cause power losses, and will reduce both the amount of current flowing through the *p-n* junction and the photovoltage. The effect of a small shunt resistance is more evident on the behaviour of a solar cell, at low light levels since is smaller its effect on photovoltage.

R_S represents the effects of total Ohmic resistance of the solar cell, which essentially corresponds to the poor ohmicity of the electrical contacts. A smaller R_S value coincides with increased solar cell efficiency. A high value, on the other hand, will cause a reduction of the short-circuit current, and therefore of the fill factor.

The effects of series and parallel resistances on the general J-V characteristic are presented in Figure 2.6. The corresponding diode equation then becomes:

$$J = J_{SC} - J_0 \left(e^{(q(V + JAR_S)/k_B T)} - 1 \right) - \frac{V + JAR_S}{R_{Sh}} \tag{2.12}$$

2.3 The main PV technologies

In general, solar cells are categorised according to their light absorbing material, which can be effectively considered the main component of the device given its key role in absorbing photons and generating free charge carriers via the photovoltaic effect. Nowadays, there are many different light absorbing materials, and correspondingly many different PV cell technologies available on the market [2, 13]. PV technologies are usually subdivided into three generations. This division depends mainly on the type of the absorber and on the commercial maturity of the device:

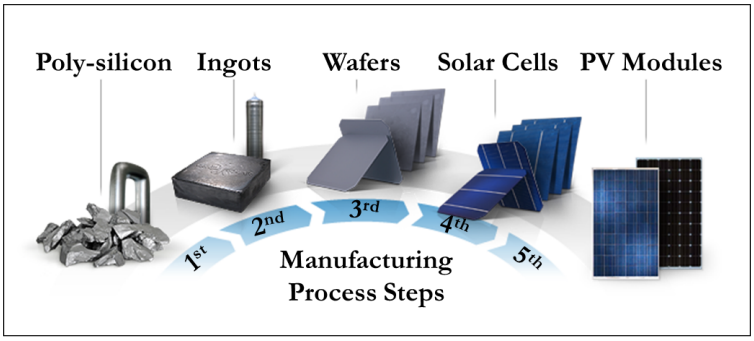

Figure 2.7: Manufacturing process of wafer-based silicon PV modules, reprinted from [15].

- First generation
  This technology is based on crystalline silicon (c-Si), either single-crystalline (sc-Si) or multi-crystalline (mc-Si). Currently, first-generation solar cells are fully commercialised.

- Second generation
  This technology is based on thin-film structures and can be further split into four broad families:

  1. Amorphous silicon (a-Si) and micro-morph silicon (μc-Si);
  2. Cadmium-telluride (CdTe);
  3. Copper indium diselenide ($CuInSe_2$ - CIS) and copper indium gallium diselenide ($CuInGaSe_2$ - CIGS);
  4. Copper zinc tin sulphide (Cu_2ZnSnS_4 - CZTS), copper zinc tin selenide ($Cu_2ZnSnSe_4$ - CZTSe) and sulphur-selenium alloy ($Cu_2ZnSn(S,Se)_4$ - CZTSSe).

- Third generation
  This group include technologies that are still under early development or have not been commercialised yet, such as concentrating PV (CPV) or organic PV.

In order to present a comprehensive overview on the current level of PV efficiency, a list of cell parameters, confirmed and updated to January 2017, is reported in Tables 2.2 and 2.3 for single cells and whole modules, respectively [14]. In the next sections, we will focus in more detail on each of the three generations of PV solar cells.

2.3.1 First generation: crystalline silicon cells

It is a well-known fact that silicon is the most abundant element in the Earth's crust, second only to oxygen. It is also renowned as a suitable semiconductor material for PV applications, having an energy band gap of 1.1 eV.

Silicon-based technology is considered fully mature as it successfully capitalised on the previous extensive knowledge accumulated from the electronics industry. This easily explains why the PV market is currently dominated by silicon-based modules.

The manufacturing process of wafer-based silicon PV modules can be summarised in the following five steps (see Figure 2.7):

Table 2.2: Confirmed efficiencies of terrestrial PV cells, mini-modules and sub-modules, measured under the global AM 1.5 spectrum (1000 W/m^2) at 298.15 K. Adapted from [14].

Classification	Efficiency (%)	Area (cm^2)	V_{OC} (V)	I_{SC} (A)	FF (%)	Description
Silicon						
c-Si	26.7 ± 0.5	79.0 (da)	0.738	42.65	84.9	Kaneka, *n*-type rear IBC
mc-Si	21.9 ± 0.4	4.0003 (t)	0.673	40.76	79.7	FhG-ISE, *n*-type
Si*	21.2 ± 0.4	239.7 (ap)	0.687	38.50	80.3	Solexel (35 µm thick)
Si**	10.5 ± 0.3	94.0 (ap)	0.492	29.70	72.1	CSG Solar (<2 µm on glass)
III-V cells						
Thin-film GaAs	28.8 ± 0.9	0.9927 (ap)	1.122	29.68	86.5	Alta Devices
mc-GaAs	18.4 ± 0.5	4.011 (t)	0.994	23.20	79.7	RTI, Ge substrate
c-InP	24.2 ± 0.5	1.008 (ap)	0.939	31.15	82.6	NREL
Chalcogenide						
Thin-film CIGS	21.7 ± 0.5	1.044 (da)	0.718	40.70	74.3	Solar Frontier
Thin-film CdTe	21.0 ± 0.4	1.0623 (ap)	0.876	30.25	79.4	First Solar, on glass
Thin-film CZTS	10.0 ± 0.2	1.113 (da)	0.708	21.77	65.1	UNSW
a/mc-Silicon						
a-Si	10.2 ± 0.3	1.001 (da)	0.896	16.36	69.8	AIST
mc-Si	11.9 ± 0.3	1.044 (da)	0.550	28.72	75.0	AIST
Perovskite						
Perovskite	19.7 ± 0.6	0.9917 (da)	1.104	24.67	72.3	KRICT/UNIST
Perovskite**	16.0 ± 0.4	16.29 (ap)	1.029	19.51	76.1	Microquanta, 6 serial cells
Dye sensitised						
Dye	11.9 ± 0.4	1.005 (da)	0.744	22.47	71.2	Sharp
Dye**	10.7 ± 0.4	26.55 (da)	0.754	20.19	69.9	Sharp, 7 serial cells
Dye***	8.8 ± 0.3	398.8 (da)	0.697	18.42	68.7	Sharp, 26 serial cells
Organic						
Organic	11.2 ± 0.3	0.992 (da)	0.780	19.30	74.2	Toshiba
Organic**	9.7 ± 0.3	26.14 (da)	0.806	16.47	73.2	Toshiba, 8 series cells

Abbreviation:
(ap): Aperture area;
(t): Total area;
(da): Designated illumination area.

Note:
* Thin transfer sub-module;
** Mini-module;
*** Sub-module.

Table 2.3: Confirmed efficiencies of terrestrial PV modules, measured under the global AM 1.5 spectrum (1000 W/m^2) at a cell temperature of 298.15 K. Adapted from [14].

Classification	**Efficiency (%)**	**Area (cm^2)**	**V_{OC} (V)**	**I_{SC} (A)**	**FF (%)**	**Description**
c-Si	24.4 ± 0.5	13177 (da)	79.50	5.040	80.1	Kaneka, 108 cells
mc-Si	19.9 ± 0.4	15143 (ap)	78.87	4.795	79.5	Trina Solar, 120 cells
Thin-film GaAs	24.8 ± 0.5	865.3 (ap)	11.07	2.288	84.7	Alta Devices
CIGS (Cd Free)	19.2 ± 0.5	841 (da)	48.00	0.456	73.7	Solar Frontier, 70 cells
CIGS (Large)	15.7 ± 0.5	9703 (ap)	28.24	7.254	72.5	Miasole
CdTe (thin-film)	18.6 ± 0.6	7038.8 (ap)	110.60	1.533	74.2	First Solar, monolithic
a-Si/nc-Si (tandem)	12.3 ± 0.3	14322 (t)	280.10	0.902	69.9	TEL Solar, Trubbach Labs
Organic	8.7 ± 0.3	802 (da)	17.47	0.569	70.4	Toshiba
InGaP/GaAs/InGaAs	31.2 ± 1.2	968 (da)	23.95	1.506	83.6	Sharp, 32 cells

Abbreviation:
(ap): Aperture area;
(t): Total area;
(da): Designated illumination area.

1. Poly-silicon purification

   The first stage in the production of silicon PV solar cells is the conversion of metallurgical silicon (MG-silicon) into high-purity poly-silicon also known as solar-grade silicon (SoG-silicon) [16].
   MG-silicon is commercially produced by reducing silicon oxide (naturally found in the form of quartz) with carbon (in the form of coal) inside submerged arc furnaces ((1800 ÷ 2300) K). An idealised reaction for the process can be written as:

$$\mathrm{SiO_2} \; + \; 2\,\mathrm{C} \; \longrightarrow \; \mathrm{Si} \; + \; 2\,\mathrm{CO} \tag{2.13}$$

   MG-silicon is used in the metallurgical industry and it exhibits purity levels typically ranging from 98.5% to 99.5%. It contains impurities such as Fe, Al, Ti, Mn, C, Ca, Mg, B and P. The nature and concentration of impurities have important effects on the structure of silicon solar cells. For example, small amounts ((10 ^{13} ÷ 10^{20}) atom/cm^3) of boron and phosphorus are highly beneficial to the formation of the *p-n* junction. Other impurities, on the contrary, can lead to the formation of defects (e.g. dislocations) which can damage both the mechanical and electrical properties of the resulting solar cells.
   This is why the MG-silicon needs to be purified into SoG-silicon. This purification process is referred to the Siemens process, which consists of three steps: gasification of metallurgical-grade silicon, distillation and deposition of ultra-pure silicon. The standard version of the Siemens process takes place in a reactor chamber, and it involves the reaction of trichlorosilane ($SiHCl_3$) and hydrogen (H_2) gases at (1400 ÷ 1500) K. However, SoG-silicon is currently obtained using a different, modified Siemens process; this employs highly volatile silane (SiH_4) instead of $SiHCl_3$ in the decomposition stage, and requires gases to be heated to only about 1100 K. As a result, the

modified Siemens process allows for more efficient energy use. At present, industrial processes can produce poly-silicon with a purity of 99.99999%.

2. Ingot production

   The second stage is ingots casting, for which there are several techniques. The two most common crystallisation methods are: the Czochralski process[5], which yields single-crystal ingots, and the Bridgman method[6], which results in multi-crystalline silicon ingots. The type of wafer that will be obtained is highly dependent on the production process. Monocrystalline wafers have a regular, perfectly ordered crystal structure, while multi-crystalline wafers consist in a whole distribution of differently orientated crystals. This structural difference directly affects carrier transport into the solar cell.

3. Wafer sawing

   In the third stage, silicon ingots are cut into slices with a cross-sectional area equal to the wafer intended size. Material wastage is quite significant during this step, i.e. about 25% for mono-Si wafers and about 15% for multi-Si wafers. Usually, mono-Si wafers have a size of 156×156 mm^2 (243×10^{-4} m^2) and a thickness of (180 ÷ 270) µm. As a comparison, the thickness of a multi-Si wafer is (180 ÷ 240) µm.

4. Cell production

   The next stage involves the conversion of wafers into actual PV solar cells. These are the key steps:

   - Surface etching (wafer are placed into chemical baths to remove swarf and other debris from the sawing stage).
   - Doping (intrinsic Si in the wafer is selectively doped to create a *p*-*n* junction).
   - Screen printing of the external electrical contact (in order to collect the carriers).
   - Anti-reflection coating (additional deposition step for minimizing the reflection loss, in order to improve the device efficiency).
   - Testing (solar cell electrical characteristics and efficiency are evaluated).

   Figure 2.8 illustrates the basic structure of a silicon solar cell. Crystalline silicon cells are typically classified into three main types, based on how the corresponding initial wafer was made (as shown previously). The three classes are:

   a. Mono-crystalline also called single crystalline silicon cells (wafers made using the Czochralski process).

[5]The **Czochralski process** consists in the slow extraction of a growing single crystal directly from the melting. Poly-silicon is first melted under vacuum in a non-reacting crucible and is subsequently solidified starting from a monocrystalline seed dipped into the molten silicon. The crystal that forms around the seed is then slowly pulled upwards while being simultaneously rotated. This results in the extraction of a cylindrical ingot. Pull rate and temperature profile determine the final diameter of the ingot.

[6]The **Bridgman process** is a method for casting multi-crystalline ingots. It is characterised by the use of directional solidification; the melt is progressively translated from a hot zone in the furnace to a colder one to achieve continuous solidification. To obtain a high-quality crystalline structure, strict control of temperature gradient and growth rate parameters is required.

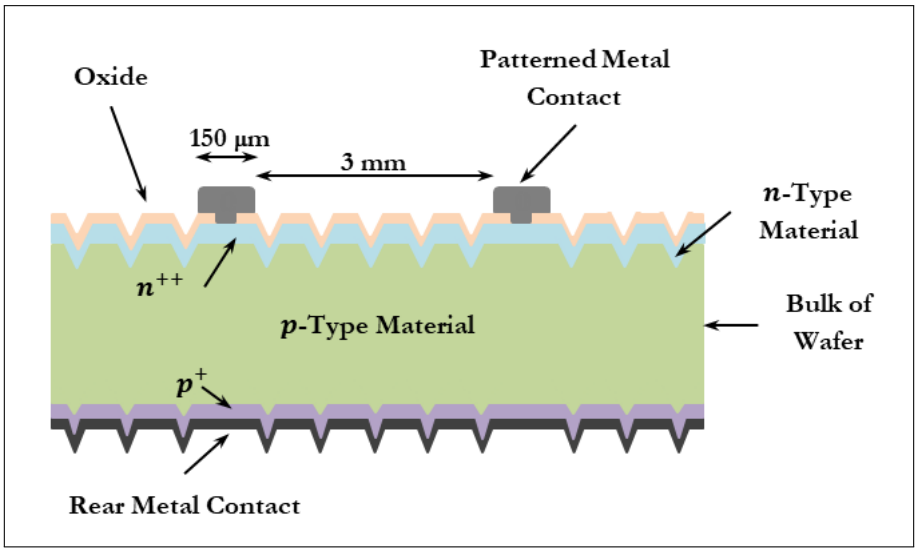

Figure 2.8: Basic structure of a silicon solar cell.

b. Polycrystalline also referred to multi-crystalline silicon cells (wafers made using the Bridgman process).

c. Edge-defined Film-fed Growth (EFG) ribbon solar cell (wafers are ribbon growing using EFG process).

5. Module assembly

The last production step consists in interconnecting several different PV cells together and encasing the resulting assembly in a coating in order to form a complete module [17].

PV module assemblage is usually performed by soldering together individual solar cells to increase the power of the ensemble. Typically, a 36-cell string is produced. The interconnection process of wafer-based silicon solar cells involves the use of infrared (IR) soldering. This process can be divided into two separate steps: tabbing and bussing. Tabbing is the act of joining solar cells together into strings. The Bussing is the act of assembling these strings together to form a PV module. The typical structure that results from interconnecting separate tabbing ribbons in series to form the final layout of a crystalline silicon solar cell is outlined in Figure 2.9a.

A protective material is placed on either face of each PV string in order to safeguard the functional component from damage and environmental agents. Transparent glass is commonly used as front-protective material and a thin polymer sheet (usually Tedlar) is used as the rear layer. The rear layer also needs to have low thermal resistance and to be weatherproof.

An encapsulant polymeric material is used to improve the adhesion between the cell and the front and rear protective sheets. The encapsulant need to be stable at high temperatures and withstand high ultraviolet (UV) exposure. It also need to be optically transparent and to have a low thermal resistance. The most widespread encapsulant species is ethyl vinyl acetate (EVA). After the encapsulant has been inserted between the cell and the protective layers, it is necessary to heat the whole assembly to about 400 K to polymerise EVA and bond the module layers together.

Every PV module is then finished by adding a frame, typically made of aluminium. In Figure 2.9b, the final structure of a conventional PV module is shown.

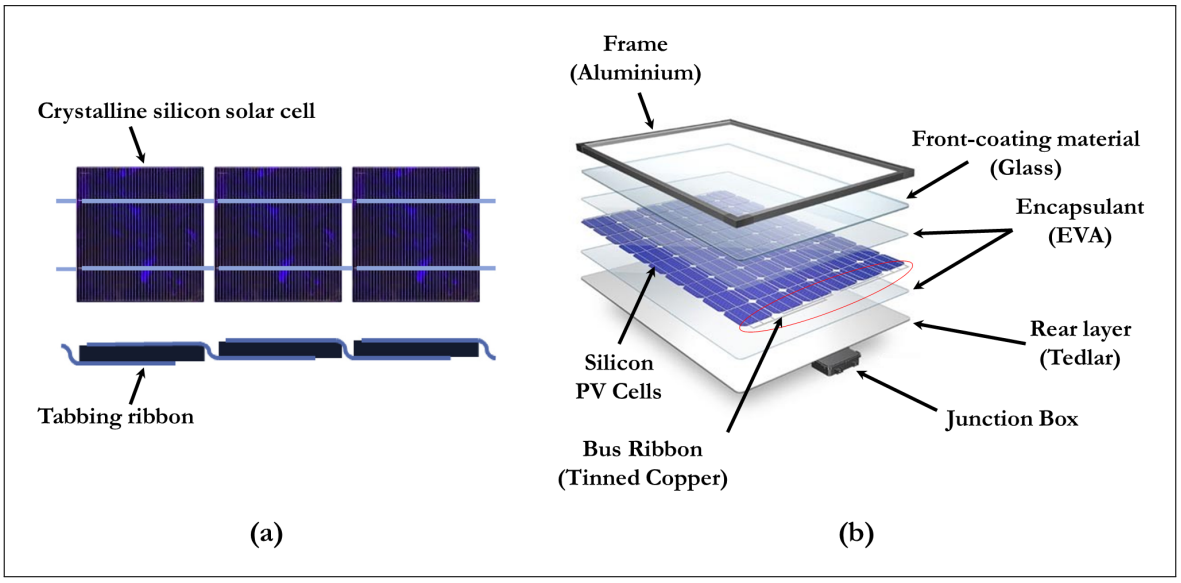

Figure 2.9: (a) Tabbing ribbons are interconnected in series to form the final structure of a crystalline silicon solar cell. Reprinted from [17]. (b) The structure of a conventional PV module [18].

2.3.2 Second generation: thin-film solar cells

Compared with first-generation solar cells, thin-film solar cells have the potential of providing cheaper electricity. Because they require less material, this would result in lower production costs, without any sacrifice in terms of device lifetime [2, 19]. Crystalline silicon is an indirect energy band gap material and this implies that:

- wafers require a thickness of at least 100 μm for an optimal absorption of incident radiation;
- wafers need to be sandwiched between glass panels to create modules.

Thin-film cells, on the other hand, are created by depositing extremely thin layers of active materials directly on low-cost substrate such as glass, stainless steel or plastic. Film thickness varies from a few nanometers (nm) to few microns (μm). Usually, the absorber layer is made of a direct energy band gap material and thus only a few microns are required for absorbing the incident radiation. The main requirements for obtaining an efficient thin-film solar cell are:

- an absorbing layer allowing the absorption of a large fraction of the incident solar radiation;
- an efficient collection of both photo-generated electrons and holes;
- a *p-n* junction with a built-in potential of the order of 1 V;
- a low R_S (smaller than 0.5 Ω cm^2).

In the case of thin-film modules, the interconnection between the separate cells is made by laser scribing. In addition, the choice of depositing the functional materials directly on thin stainless steel foil or plastic makes it possible to create flexible solar cells. This in turn paves the way for solar cell integra-

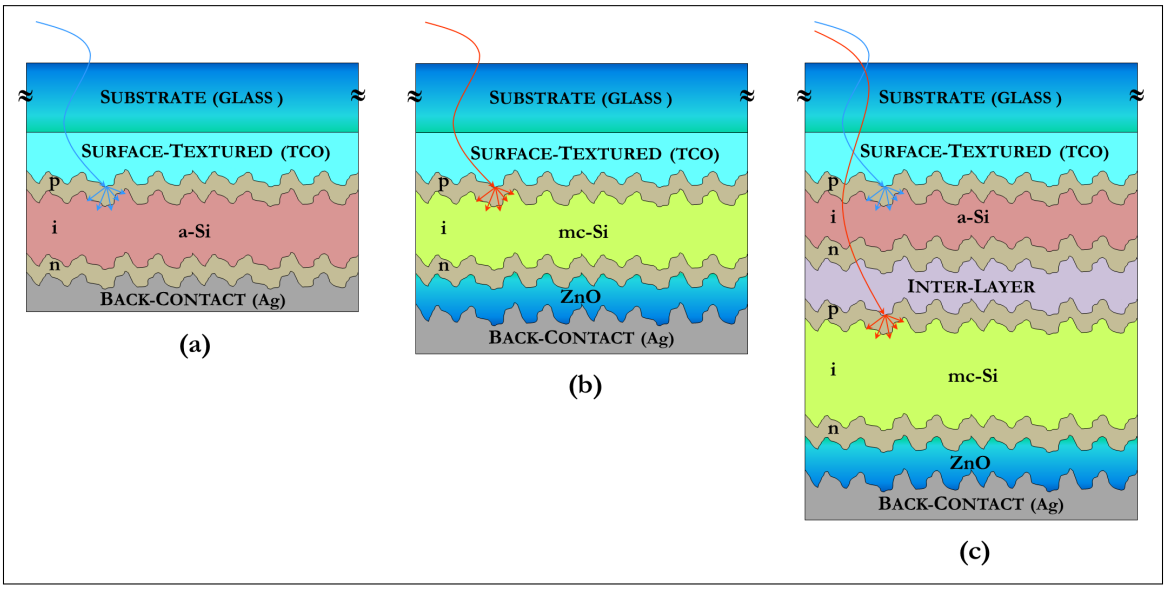

Figure 2.10: Comparison between the basic structures of (a) a-Si, (b) mc-Si and (c) multi-junction a-Si/mc-Si solar cells.

tion into building components or even customized technology devices. The following is a list of the main types of thin-film solar cells:

- Amorphous silicon (a-Si)
  Amorphous silicon is one of the earliest and most common thin-film technologies (Figure 2.10a). It was reported for the first time by Carlson and Wronski in 1976 [20, 21]. Unlike crystalline silicon, where atoms are arranged in an ordered structure, atoms in a-Si are positioned at random distances between each other. Consequently, there are the presence of some dangling bonds and lattice defects. This amorphous structure has a decisive effect on the electronic properties. a-Si has a higher direct energy band gap (1.7 eV) compared with crystalline silicon indirect energy band gap (1.1 eV). As a consequence of this larger energy band gap, a-Si can absorb the visible portion of the solar spectrum more strongly than IR part of the spectrum. Moreover, the absorption coefficient of a-Si is higher than crystalline Si, and this allows for a reduction in the amount of material to be used. The typical thickness of the absorbing layer is around 1 µm.
  However, a-Si solar cells are also characterised by a poorer flow of photo-generated charges and this leads to a lower performance. The efficiency of these thin-film solar cells is currently in the range of $(4 \div 8)\%$.
  At present, it is possible to deposit the absorber material onto very large substrate (up to an area of 5.7 m^2 on glass), and this can obviously reduce production costs. For this reason, a growing number of companies are now developing new variants based on this technology, such as depositing on flexible substrates or experimenting with tandem, double or even triple junctions.

- Multi-junction thin silicon film (a-Si/mc-Si)
  As we have already shown, a-Si solar cells have a lower efficiency than first-generation silicon devices and, in particular, the a-Si modules suffer from degradation after being exposed to sunlight, leading to efficiency stabilising at levels around $(4 \div 8)\%$. This degradation is due to the Stae-

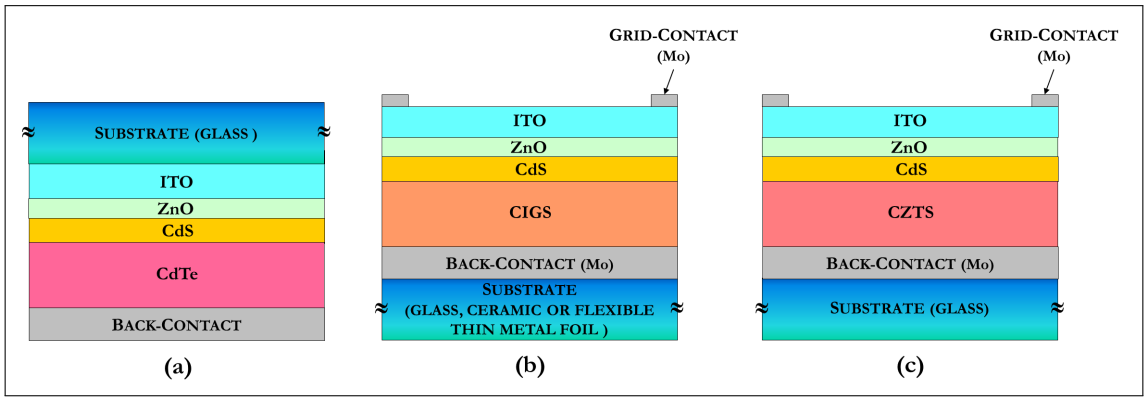

Figure 2.11: Structure of (a) CdTe, (b) CIGS and (c) CZTS-based solar cells.

bler–Wronski effect, which describes light-induced changes in the properties of hydrogenated a-Si.

One way to improve efficiency and eliminate the degradation problems is to create a multi-junction solar cell. This consists in an a-Si cell complemented by an additional multi-crystalline silicon (mc-Si) layer (Figure 2.10c). Thus, it is possible to capture more different wavelengths from solar irradiation: the red and near-infrared part of the light spectrum thanks to mc-Si and the shorter wavelengths of the visible solar spectrum thanks to a-Si. This can effectively increase the efficiency up to 10%, depending on layers structure and thickness.

Currently, it is possible to produce stable tandem amorphous-Si and multi-crystalline-Si solar cell on substrates with an area up to 1.4 m^2.

- Cadmium telluride (CdTe)

  The cadmium telluride solar cell is one of the most promising thin-film cell because of its high efficiency, low production costs and high scalability at the industrial level (Figure 2.11a). The current record efficiency for CdTe solar cells was established by First Solar in 2016, and stands at 22.1% [22].

  CdTe shows outstanding qualities as an absorber layer for PV solar cells. It has a direct energy band gap of 1.49 eV (very close to the S-Q limits) and it can be easily fabricated in form of thin film through highly scalable industrial techniques, such as sputtering, electrodeposition and close-spaced sublimation (CSS). Furthermore, its absorption coefficient is on the order of 10^4 cm^{-1}, which means that 1 µm thick layer is enough to absorb about 90% of the incident radiation.

  In CdTe thin-film solar cells, the two main starting elements are cadmium and tellurium, both are by-products of other processes. In particular, cadmium is a by-product of zinc extraction and tellurium is a by-product of copper refining. Two main problems in the use of Cd and Te are:

  - Te is produced in far smaller amounts than Cd and its availability in the long-term depends on copper industry.
  - Cd is considered a toxic element and this may limit its use.

  In Chapter 4, we will discuss the state of the art of this type of solar cell in greater detail.

- Copper indium gallium di-selenide (CIGS)

CIGS- and CIS-based solar cells are the main alternative to silicon-based devices for large-scale applications (Figure 2.11b). The current record efficiency for CIGS solar cells was set by Zentrum für Sonnenenergie- und Wasserstoff-Forschung (ZSF) in 2016 and stands at 22.6% [22]. Several companies have also confirmed a module efficiency exceeding 16%.
Also CIGS displays excellent qualities as an absorber material for PV solar cells. It is a I-III-VI_2 semiconductor material and can be represented by the chemical formula $CuIn_xGa_{(1-x)}Se_2$, where the value of x can vary from 1 (pure copper indium selenide, CIS) to 0 (pure copper gallium selenide, CGS). CIGS direct energy band gap can vary directly with x. It ranges from 1.0 eV for CIS to 1.7 eV for CGS. As well as for CdTe 1 μm thick layer of CIGS is enough to absorb about 90% of the incident radiation.
There are no long-term availability issues for selenium or copper, though indium and gallium may suffer from limited supply. Indium price, in particular, is expected to rise in the coming years because a number of different industries are competing for this resource (the liquid crystal display industry alone currently accounts for 85% of indium demand).
More details on the state of the art of CIGS solar cells will be given in Chapter 5.

- Copper zinc tin sulphide (CZTS)
  As already mentioned, CdTe and CIGS solar cells have achieved remarkable efficiencies at laboratory scale, but some of their constituents are rare elements (such as, indium and tellurium) while others are quite toxic (such as, cadmium). For these reasons, earth-abundant copper-zinc-tin-chalcogenide kesterites - with formula $Cu(Zn,Sn)(S,Se)_2$ - have attracted great interest in recent years as a potential alternative to CdTe and CIGS (Figure 2.11c) [23, 24]. The CZTS absorbing layer is structurally very similar to CIGS, a part that indium is replaced by zinc and gallium is replaced by tin.
  CZTS can crystallise either into a kesterite crystal structure or into a stannite crystal structure. Kesterite, however, is preferred for PV applications. As well as for CIGS, CZTS has an absorption coefficient of the order of 10^4 cm^{-1} and its energy band gap can be tuned over a wide range from 1.0 eV to 1.6 eV, which is very close to the optimal energy band gap for single-junction solar devices. Unfortunately, it is very difficult to grow pure CZTS because its thermodynamic stability window is quite narrow. Sn compounds are generally volatile and CZTS breaks down at high temperatures. This leads to the formation of many different secondary phases (such as: ZnS and Cu_2SnS_3) and to the presence of large compositional non-uniformity. This explains why the highest efficiency ever reached by CZTS-based solar cells is only 12.6% [22], significantly lower than CIGS- and CdTe-based solar cells. In conclusion, the success of this technology and the ability to overcome its stability problems will depend on a better understanding of the mechanisms, which are behind defect formation and on a more careful engineering of the device fabrication process.

2.3.2.1 Thin-film solar cells manufacturing processes

The basic manufacturing process of a thin-film solar cell involves a sequential deposition of different thin films on a large-area substrate. It can be split into six steps, as shown Figure 2.12. The following

[7] **Super-strate configuration**: layers are deposited on glass. During cell operation, light will be required to enter the cell

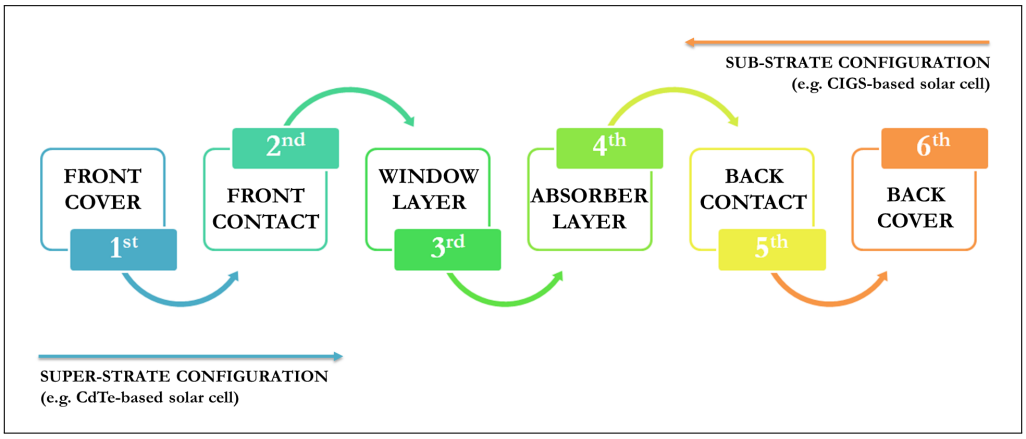

Figure 2.12: Main steps of the manufacturing process of thin-film solar modules.

base sequence describes the process in the case of super-strate configuration[7]; the order would need to be reversed for sub-strate configuration[8] cells, since the process is inverse.

1. Substrate fabrication and cleaning
   Substrates are typically made of soda-lime glass (SLG), even though other materials, such as ceramics, flexible steel, plastics or aluminium, can be used only in sub-strate configuration. In addition, thorough surface cleaning is required to avoid any film adhesion problems.

2. Transparent conducting layer deposition
   After its surface is cleaned, the substrate is coated with a transparent conducting oxide (TCO) layer. Indium tin oxide (ITO) and SnO_2(F) (FTO) are the most widely used.

3. Window layer deposition
   In a *p*-*n* junction, the window layer represents the *n*-part of the junction. Typically, a layer of cadmium sulphide (CdS) is used, which is an *n*-type semiconductor, with an energy band gap of 2.42 eV.

4. Absorber layer deposition
   The absorber layer represents the *p*-part of *p*-*n* junction, and it can be deposited using several different techniques, such as chemical and physical vapour deposition.

5. Back-contact deposition
   After the absorber layer has been deposited, the cell is coated with metal to form a contact. Molybdenum and Cu-doped graphite paste are the two more widely used metal contact.

6. Back-cover
   The PV module is enclosed in a glass-polymer casing and is finished by installing electrical connections and a frame.

through this glass layer.

[8] **Sub-strate configuration**: layers are deposited on an economical substrate that is no longer required to be transparent to light. This offers new options in terms of substrate choice, e.g. ceramic materials and flexible thin metal foil. Light will enter the cell through the TCO and the window layer, which are both located on the opposite side of the cell.

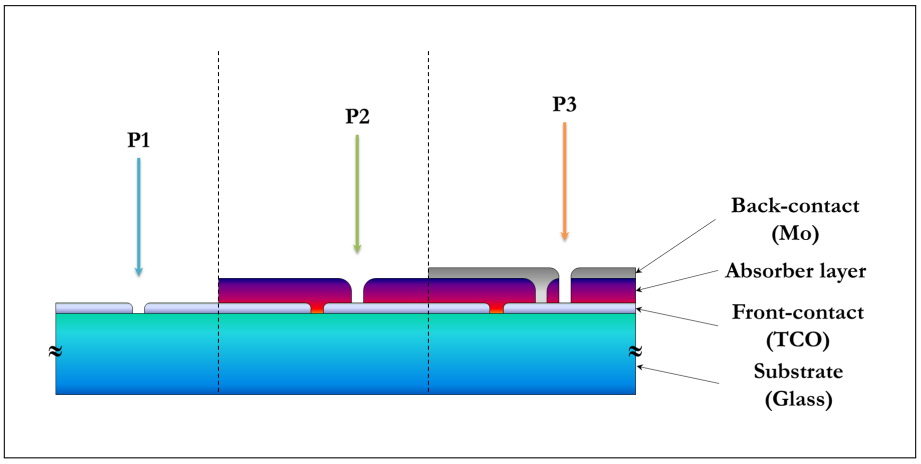

Figure 2.13: Outline of a basic monolithic series connection in a super-strate configuration.

It should be emphasised that a great advantage of thin-film PV modules over crystalline Si PV panels lies in having a monolithically integrated structure [25, 26]. A monolithically integrated series connection can be made using laser scribing, which is a process that significantly reduces operating cost by removing the wafer connection stage present in the fabrication of crystalline Si PV modules. Laser scribing process also allows to maximise the effective area of each panel.

The laser scribing process is a technique that involve laser-induced vaporisation and sublimation of the thin-film layers. In order to achieve sublimation, it is necessary to use laser pulses, with a pulse length in the range of nano-second. The choice of which specific laser beam source (i.e. laser wavelength) should be used, depends on the absorption characteristics and the damage threshold of the material that needs to be scribed.

Typically, three steps of laser scribing (also called P1, P2 and P3) are required in the production of a thin-film panel. With reference to Figure 2.13, the three stages of a typical monolithic series connections are:

1. Laser scribing P1
   This first step refers to the scribing of molybdenum (back-contact) and TCO (front-contact), in sub-strate and in super-strate configuration, respectively. The back/front contact of the module is subdivided into thin strips electrically insulated one from each other.

2. Laser scribing P2
   This second step refers to the selective ablation of the active layers, performed without damaging the previously scribed molybdenum or TCO coating. This creates a series connection between neighbouring PV cells.

3. Laser scribing P3
   This third step consists in the selective ablation of the absorber layer and newly deposited front/back contact and it spares the initial molybdenum/TCO coating, respectively. This last step is necessary to open the short-circuited path between neighbouring cells.

2.3.3 Third generation solar cells

Several new photovoltaic technologies have been studied in recent years in an effort to find an alternative to first-generation solar cells. These studies are aimed at creating new PV devices with higher efficiency and lower costs per Watt of electricity produced. The term 'third generation technology' is somewhat ambiguous as it includes a variety of very different technologies, such as tandem/multi-junction cells, hot-carrier cells, dye-sensitised solar cells (also called 'Grätzel cell'), organic solar cells, polymer solar cells, perovskite solar cells, quantum dot solar cells and so on.

In the following subsections, we will examine a few, most notable examples of third-generation solar cells.

2.3.3.1 Gallium arsenide solar cells

Gallium arsenide (GaAs) is a III-V compound, which is commonly used to realize the highest conversion efficiency solar cell based on single or multi-junction structure [11, 27, 28, 29, 30]. III-V semiconductor compounds offer several advantages for PV applications, such as an easy energy band gap engineering and the possibility to absorb 97% of solar radiation within a thickness of about 2 μm. GaAs, in particular, has a direct energy band gap of 1.42 eV, close to the optimum value indicated by S-Q limit for solar conversion.

Furthermore, GaAs solar cells can operate at a higher temperature than Si solar cells and they are expected to be more radiation resistant. Currently, GaAs solar cell has achieved the record efficiency as single-junction with a value of 28.8% [22].

Despite their great promise, the prohibitive cost of III-V solar cells has restricted their use in spatial or concentrated PV applications. The two most significant factors behind the total cost of these devices are:

1. The high cost of the starting substrate, typically germanium (Ge) and GaAs single crystals. Currently, the use of Si is under evaluation. This would bring several advantages, such as high mechanical robustness, good thermal conductivity, large areas and low cost. Unfortunately, the lattice mismatch between GaAs and Si is quite high, and this is a main obstacle in achieving high-quality GaAs solar cells.

2. The deposition techniques required to fabricate the cell. Layers in GaAs solar cells are deposited using expensive techniques, such as liquid phase epitaxy (LPE), chemical vapour deposition (CVD), metalorganic chemical vapour depositon (MOCVD) or molecular beam epitaxy (MBE).

For these reasons, III-V solar cells are traditionally used in niche markets that require high efficiency over a small area (e.g. space applications). Furthermore, because of the use of arsenic (a notoriously toxic element), encapsulation and recycling are especially important steps during the lifetime of GaAs modules.

As mentioned above, the GaAs-based solar cells can be divided into two categories:

1. Single-junction solar cells

   Figure 2.14a illustrates the typical structure of a GaAs cell. This is constructed by stacking different layers on top of an *n*-type GaAs substrate: first, a *n*-type GaAs buffer layer for high crystal

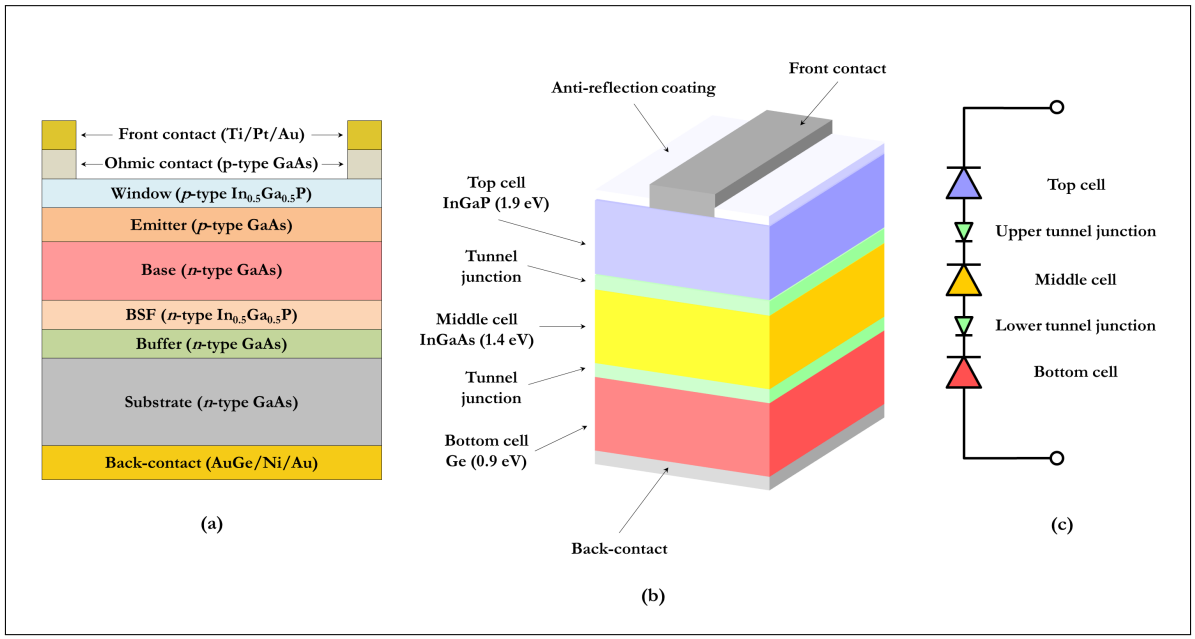

Figure 2.14: (a) Schematic structure of a GaAs single-junction solar cell. (b) Physical scheme of triple-junction (InGaP/InGaAs/Ge) solar cell. (c) Equivalent electrical circuit of the triple-junction solar cell in (b).

quality; secondly, an *n*-type InGaP back surface field (BSF) layer; then an *n*-type GaAs base layer, followed by a *p*-type GaAs emitter layer and a *p*-type InGaP window layer; finally a *p*-type GaAs cap layer for ohmic contact.

InGaP is utilised as a window layer, thanks to the difference between its refractive index and the refractive index of air. In fact, more than 30% of incident light can be reflected away from the surface of the solar cells. An anti-reflecting coating is also necessary to further improve the conversion efficiency of the device.

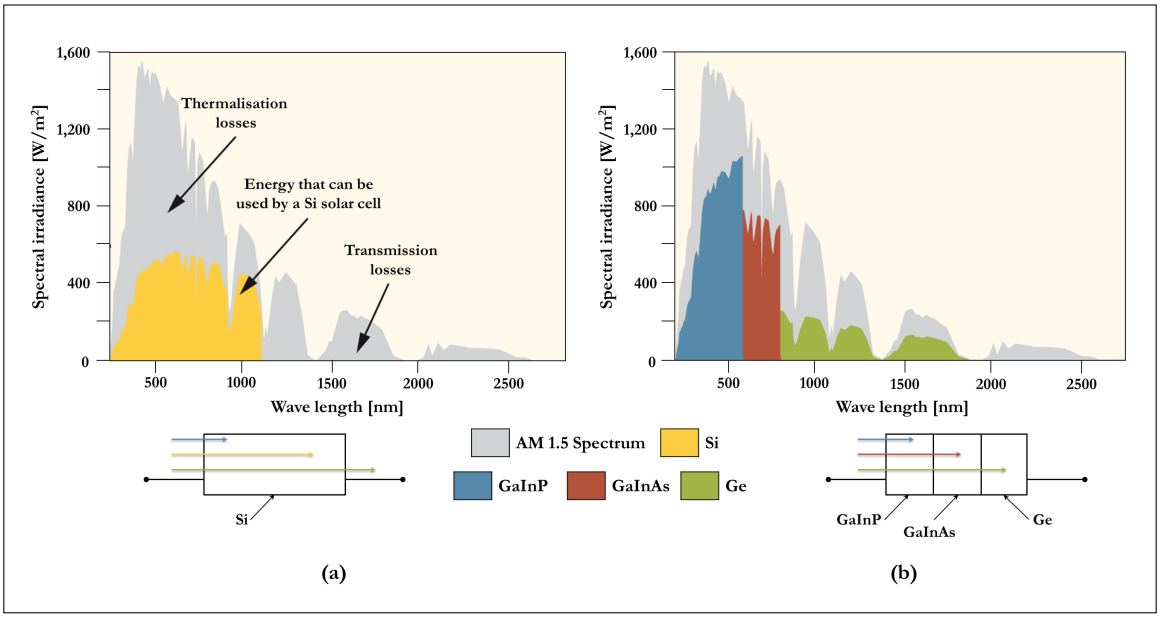

Figure 2.15: Comparison between the energy that can be used by a Si solar cell (a) and by a multi-junction solar cell (b), reprinted from [31].

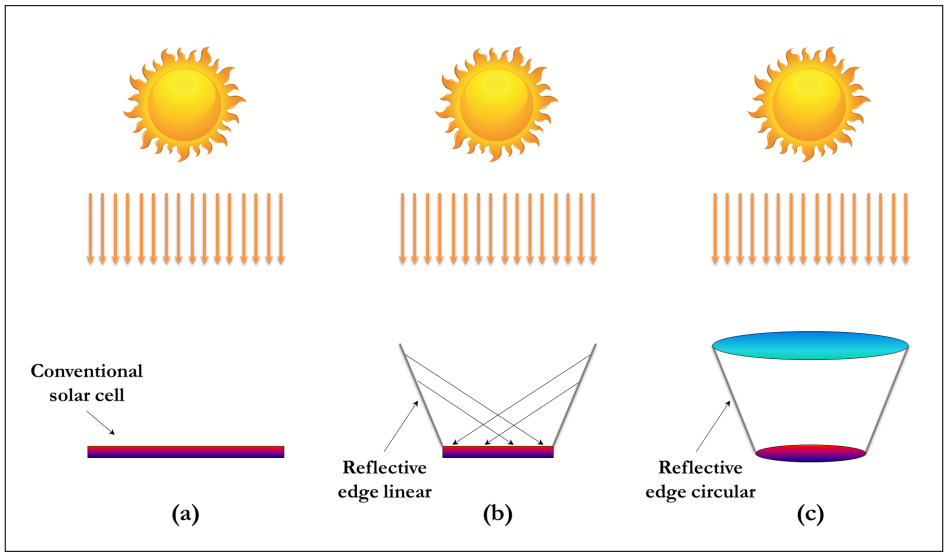

Figure 2.16: (a) A conventional, flat solar cell. (b) Linear reflective edge arrangement: the solar cell receives radiation directly and through reflection from the lateral edges. (c) Circular reflective edge arrangement.

2. Multi-junction solar cells

   Multi-junction (or tandem) solar cells have the potential to exceed an efficiency of 50%. In fact, the fundamental concept behind multi-junction solar cells is to improve conversion efficiency by using two or more solar cells consisting of absorber materials with different energy band gaps (see Figure 2.15). In particular, the higher-energy solar radiation is absorbed by the top solar cell, which has an absorber layer of larger energy band gap, and the residual lower-energy solar radiation is absorbed by the bottom solar cell, which has an absorber layer of smaller energy band gap.

   Figure 2.14b shows the structure of a typical multi-junction solar cell. This is effectively equivalent to a sequence of three absorbers:

   - InGaP (with an energy band gap of 1.9 eV);
   - InGaAs (with an energy band gap of 1.4 eV);
   - Ge: (with an energy band gap of 0.67 eV).

   These junctions are formed on a substrate using epitaxial growth techniques in order to produce a series-connected multi-junction solar cell.

2.3.3.2 Concentrator photovoltaic

Concentrator photovoltaic (CPV) is based on the concentration of sunlight [32, 33]. Optical lenses, such as Fresnel lenses, and mirrors are common devices to concentrate sunlight onto a very small solar cell area. It is possible to make use of these components in several different arrangements to increase the density of incident photons on the solar cell surface. Two simple examples of effective arrangements are shown in Figure 2.16. A CPV system can be divided into three main parts:

1. The focusing optics for concentrating sunlight on the receiver.

2. The solar tracker, which is a device that tracks the path of the Sun across the sky, is used for optimising the amount of incident radiation as CPV systems requires to be facing their light source directly.

3. The receiver consists in triple-junction solar cells in most CPV modules.

CPV performance greatly depends on how effectively each of these three parts performs individually and on how effectively the whole assembly performs collectively.

CPV can classified into three groups depending on its concentration factor (usually indicated with the letter X, which is the multiplying factor) and on the type of tracking system:

- Low concentration CPV: X between 2 and 100, and 1-axis sun tracker;
- Medium concentration: X between 100 and 300, and 2-axes sun tracker;
- High concentration: X between 300 and <1000, and 2-axes sun tracker.

The main advantages and disadvantages of CPV solar cells are summarised below:

- Advantages:
  - A reduction in the total area of the solar cell, and consequently a cost reduction due to using smaller amounts of expensive PV materials.
  - A higher device efficiency.
  - Thanks to the tracking system, electricity production can begin earlier and extend later during the day.
- Disadvantages:
  - Because the operation temperature of a solar cell increases when sunlight is concentrated, CPV devices need a cooling system.
  - CPV solar cells require an accurate sun tracking system and this increases the cost of the final device.

We can conclude that CPV system could play an important role in the future of renewable energies.

2.3.3.3 Organic solar cells

Organic solar cells (OPV), also known as 'excitonic' solar cells, are a promising alternative option for overcoming the high-cost issue that affects current inorganic solar cells [34, 35, 36, 37, 38]. Organic materials were introduced for the first time as absorber materials for solar cells by A. Pochettino in 1906. The great potential of OPV solar cells lies in the possibility of manufacturing them on large-area flexible substrates using a low-temperature, vacuum-free, roll-to-roll process.

The main organic materials for PV applications are hydrocarbon compounds with a backbone of alternating C–C and C=C bonds. The basic structure of an OPV solar cell is a bilayer device. A bilayer device is composed of two laminated films of organic semiconductor material: one with high hole affinity, called electron donor (D), and the other with high electron affinity, referred to as electron

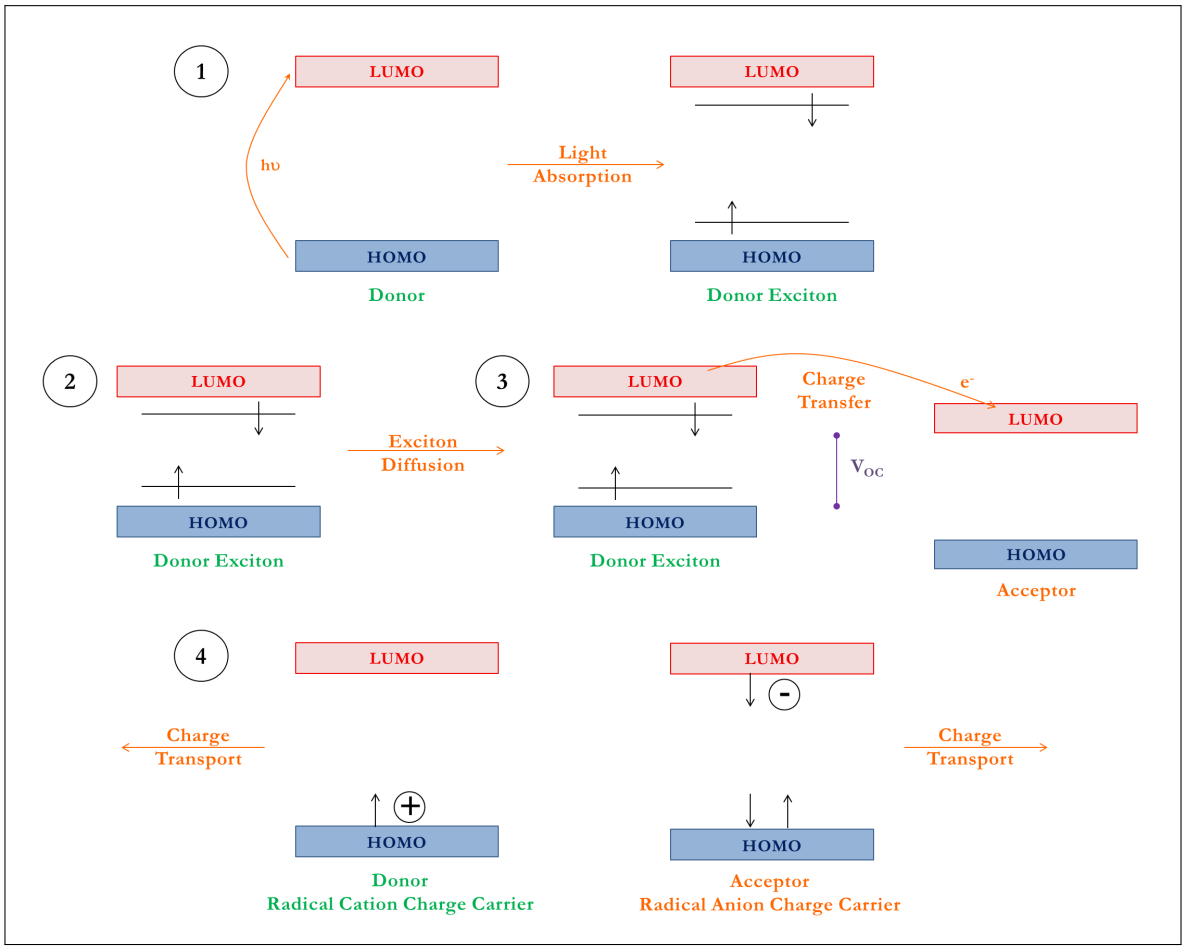

Figure 2.17: Overview of the mechanisms involved in OPV solar cell photo-energy conversion, adapted from [38].

acceptor (A). These two active layers are sandwiched between two electrodes, one of which needs to be transparent (typically ITO) to enable active layer photo-excitation.

One of the main differences between inorganic and organic PV solar cells is the charge generation mechanism. In organic semiconductor materials, there are no spatially separated electron-hole pairs, but rather short-lived bound species called excitons. This is precisely why organic cells are sometimes referred to as 'excitonic' solar cells. When sunlight photons are absorbed inside an OPV solar cell, excitons are created. Due to the concentration gradient, these excitons start to diffuse to the donor/acceptor interface and thus there is the charge separation (free holes and electrons). Then, the separated charges are transported by the internal field to the corresponding electrodes.

Figure 2.17 shows how the process of converting light into electrical energy can be described in four fundamental steps:

1. Absorption of light inside the OPV device and subsequent generation of Coulomb correlated electron-hole pairs (excitons). An absorber layer of a few hundred nanometers is sufficient to absorb the incident light, given its high absorption coefficient (typically higher than 10^5 cm^{-1}). The photo-excitation of the donor can be express by the equation:

$$D + A \rightleftharpoons D^* + A \quad (h\nu) \tag{2.14}$$

2. Exciton diffusion to the donor–acceptor interface. It should be underlined that all excitons should reach a dissociation site, ideally. Unfortunately, the decay and recombination processes are in competition with the hole-electron generation, because of the short exciton diffusion length (between 1 and 20 nm). In other words, covering a distance longer than the maximum diffusion length is likely to result in exciton relaxation, and consequently in a limitation of the solar cell efficiency.
   Exciton diffusion can be described as:

$$D^* + A \rightleftharpoons [D^*, A] \tag{2.15}$$

3. Exciton dissociation at the donor-acceptor interface and subsequent formation of the geminate pair:

$$[D^*, A] \rightleftharpoons [D^{+\bullet}, A^{-\bullet}] \tag{2.16}$$

4. Free charge transport to the corresponding electrode (electrons to the cathode and holes to the anode) and collection. The transport efficiency of the free charges can be limited by the recombination occurring before reaching the electrode or by interaction with other atoms. Furthermore, an efficient collection of the charges requires that each charge overcomes the potential barrier at the organic/metal interface, which is actually the main obstacle.
   Charge separation can be indicated as:

$$[D^{+\bullet}, A^{-\bullet}] \rightleftharpoons D^{+\bullet} + A^{-\bullet} \tag{2.17}$$

The process in the case of an excited acceptor is analogous.

It should also be underlined that the donor and acceptor components need to have an interface with the largest possible area so that the formed excitons can quickly reach the interface for dissociation. Another important requirement is that electrons and holes can move rapidly towards the electrode, which can be achieved by using a highly ordered material. Furthermore, V_{OC} is directly linked to energy difference between the lowest unoccupied molecular orbital (LUMO) level of the acceptor and the highest occupied molecular orbitals (HOMO) level of donor, in order to provide the primary driving force for the separation of charge. Thus, it is necessary a high difference between these two levels, in order to obtain high values of both V_{OC} and J_{SC}.

The main advantages of this type of PV devices can be identified as:

- Low manufacturing cost compared to current inorganic PV devices. OPV can be made using the roll-to-roll process.
- The possibility of fabricating thin, semi-transparent and flexible PV solar cells.
- Easy integration into new market products, e.g. wearable PV.
- Short energy payback time.
- Low environmental impact during both manufacturing, operation and maintenance of the PV system.

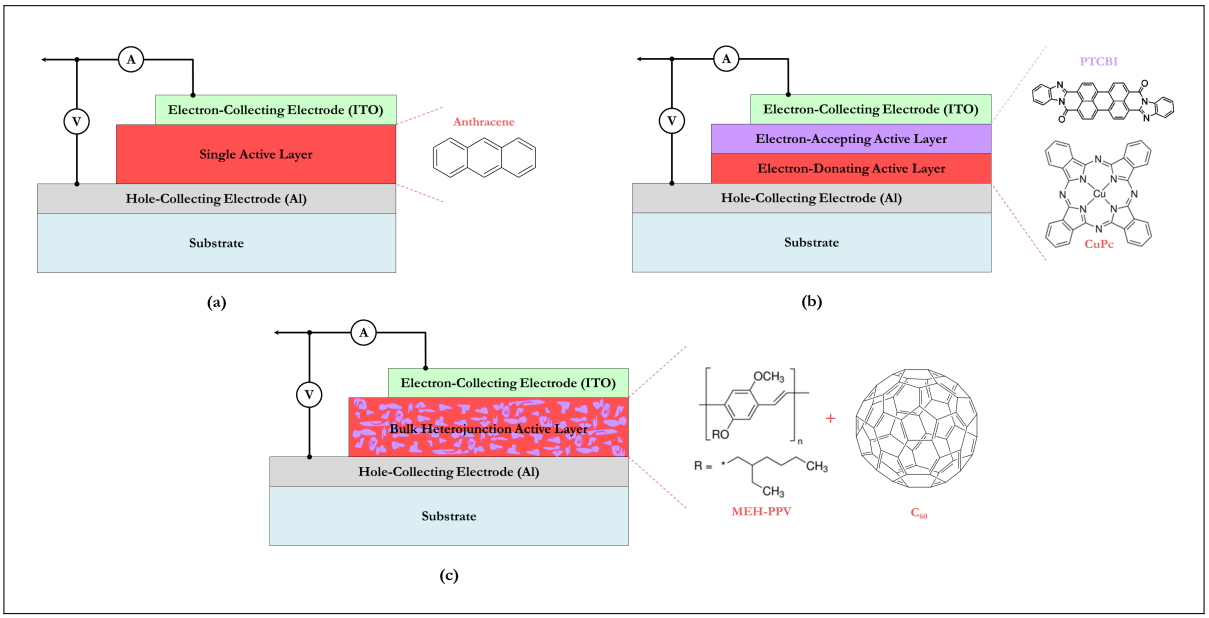

Figure 2.18: Schematic representation of the structure of: (a) single active-layer solar cell, (b) double active-layer solar cell and (c) bulk hetero-junction structure solar cell, adapted from [35].

However, OPV solar cells have two main disadvantages: low efficiency (between 10% and 14%) and high degradation rate (only few year of operation lifetime).

Finally, OPV solar cells can currently be divided into two categories:

1. Polymeric solar cell

   There are three basic structures for the polymeric solar cell (see Figure 2.18) [35, 39, 40]:

   - Single active-layer structure

     This is the simplest structure: a thin-film organic absorber layer is sandwiched between two electrodes. Typically, one electrode is made of TCO (a material with a high work function) and the other is made of Ag, Al, Mg or Ca (materials with a low work function). The difference in work function between these two electrodes generates an electric field that triggers the separation of the hole-electron pair. Unfortunately, this type of device has intrinsically poor efficiency because a single active layer is not enough to absorb light.

   - Double active-layer structure

     In order to favour charge separation, a double active-layer structure has been introduced. Unfortunately, there is a limitation in this case, as well: poor charge transport inside *p*-type and *n*-type layers, respectively.

   - Bulk hetero-junction structure

     In this structure, the active layer is a polymer blend, namely a mixing of the donor and the acceptor materials. This can remove the two previous limitations (charge separation and transport). If the thickness of the polymer blend is comparable to the exciton diffusion length, most of the excitons will be able to reach the interface. If so, a more efficient collection of the charge carriers will be possible.

     The most common bulk hetero-junction solar cell is the polymer-fullerene solar cell, where

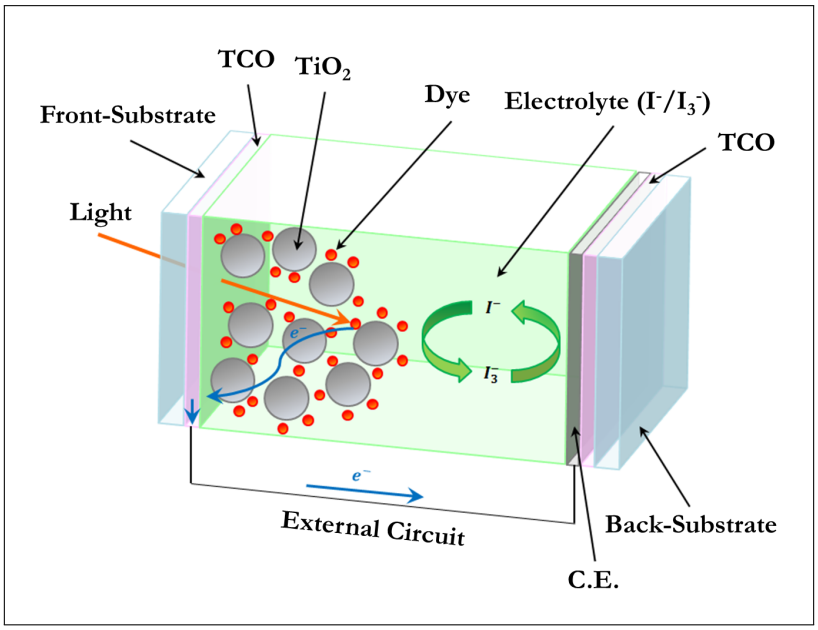

Figure 2.19: Schematic representation of a dye-sensitised solar cell.

a conjugated polymer represents the *p*-type material while a fullerene derivative represents the *n*-type material.

To maximize the efficiency of the polymeric solar cell, it is also possible to create a tandem structure.

2. DYE-SENSITISED SOLAR CELL

Dye-sensitised solar cells (DSSC) were invented by M. Grätzel and B. O'Regan in 1991 and they are also called Gräetzel cells or photo-electrochemical solar cells [41, 42, 43, 44]. The basic structure of DSSC solar cells consists in two electrode immersed in an electrolyte containing suitable redox couples (as shown in Figure 2.19). These two different electrode are:

(a) A photo-active semiconductor working electrode. Typically, TCO covered with a mesoporous oxide layer composed of nanometer-sized particles, which are sintered together to make electronic conduction possible. Common oxides with these characteristics are TiO_2, ZnO and Nb_2O_5.

(b) A counter electrode, which is typically made of either metal (e.g. platinum) or semiconductor material.

The main difference between the photo-electrochemical solar cells and the conventional devices is the separation of the light-absorbing function from the charge carrier transport function. The operation process of a DSSC can be summarised in the following way:

(a) Excitation process.
When the interface between the semiconductor and the electrolyte is illuminated with light of higher energy than the semiconductor energy band gap, dye molecules are excited from HOMO to LUMO states:

$$S + Photon \rightarrow S^* \tag{2.18}$$

(b) Injection process.
If we assume TiO_2 is the *n*-type material used, after a photon has been absorbed by the dye electrolyte, an electron is injected into the conduction band of TiO_2, which oxidises the dye molecule:

$$S^* \ + \ TiO_2 \ \rightarrow \ e^-_{(TiO_2)} \ + \ S^+ \tag{2.19}$$

(c) Energy generation.
The injected electrons are then transferred to the counter electrode via a load:

$$e^-_{(TiO_2)} \ + \ C.E. \ \rightarrow \ TiO_2 \ + e^-_{(C.E.)} \ + \ \text{Electrical Energy} \tag{2.20}$$

where C.E. stands for counter electrode.

(d) Regeneration of the dye molecule.
The electrolyte contains I^-/I_3^- red-ox ions and, as consequence, the oxidised dye molecules can be regenerated by the transfer of an electron from these I^- ion red-ox mediators. At the same time, these ions are oxidised to I_3^-. The dye molecule regeneration can be represented by:

$$S^+ \ + \ \frac{3}{2} \, I^- \ \rightarrow \ S \ + \ \frac{1}{2} \, I_3^- \tag{2.21}$$

(e) Electron recapture reaction.
I_3^- replaces the internally donated electron with an electron from the external load. This allows I_3^- to be reduced back to I^-. This process is represented by:

$$\frac{1}{2} \, I_3^- \ + \ e^-_{(C.E.)} \ \rightarrow \ \frac{3}{2} \, I^- \ + \ C.E. \tag{2.22}$$

It should also be mentioned that the energy generation in dye-sensitised solar cell does not cause any permanent chemical change or transformation.

2.3.3.4 Perovskite solar cell

We can conclude this review of the main types of solar cells with perovskite solar cells (PSCs) [45, 46, 47, 48, 49]. Their rapid improvement in recent few years has made them a rising star in the photovoltaic field. PSCs are the solar cells that showed the fastest increase in power conversion efficiency, reaching a record level of 22.1% in KRICT laboratory [22].

PSCs can be considered an example of hybrid organic-inorganic solar cells. By definition, the term 'perovskite' indicates a calcium titanium oxide mineral composed of calcium titanate ($CaTiO_3$). This was first discovered in the Russian Ural Mountains in 1839 and was named after Lev Perovski (a Russian mineralogist).
With the term 'perovskite structure', we indicate any compound that shows the same structure as the perovskite mineral. The general formula of perovskite is ABX_3, where A and B are cations that occupy the corner and the body-center sites of a pseudo-cubic unit cell respectively, and X is an anion that sits in the face-center sites (Figure 2.20). Obviously, there are hundreds of different compounds with this crystal structure and each material can show different optoelectronic properties. Currently, the best known perovskite compound for PV applications is the one in which:

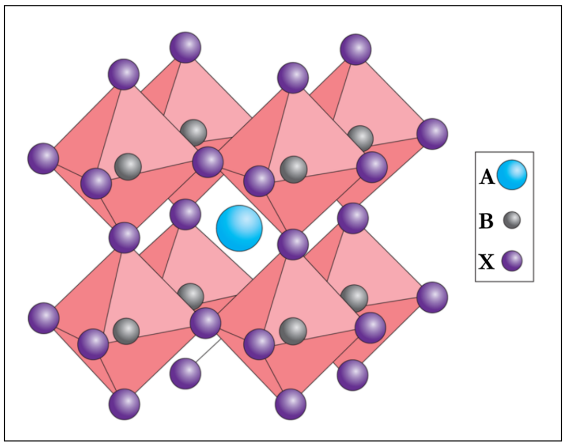

Figure 2.20: Perovskite structure, adapted from [50].

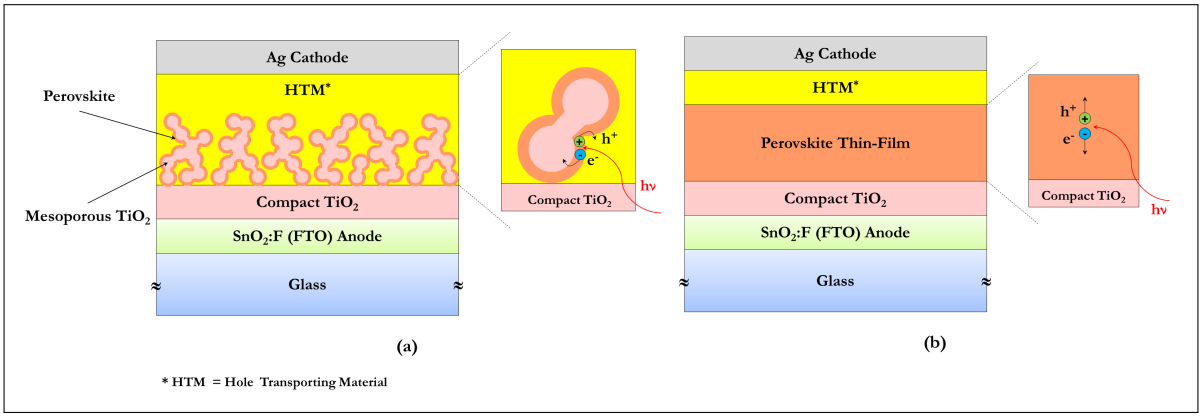

Figure 2.21: Comparison between (a) mesoporous and (b) thin-film planar structure of PSCs.

- A = methylammonium $(CH_3NH_3)^+$ - an organic cation;
- B = Pb^{2+} - an inorganic cation;
- X_3 = Br^-, Cl^- or I^- - a halogen anion.

$CH_3NH_3PbX_3$ (X = Br, Cl or I) has several ideal properties as PV absorber layer, such as:

- high absorption over the whole visible light spectrum;
- high electron and hole mobilities and diffusion lengths;
- high tolerance to structural defects;
- low surface recombination rate.

Usually, PSCs follow the same production structure as DSSC devices. There are two typical architectures available for manufacturing PSCs: mesoporous framework (Figure 2.20a) or planar configuration (Figure 2.20b).

Traditionally, perovskites are fabricated by either one-step or two-step sequential deposition methods. The most common production techniques are based on solution processing, vacuum deposition, or

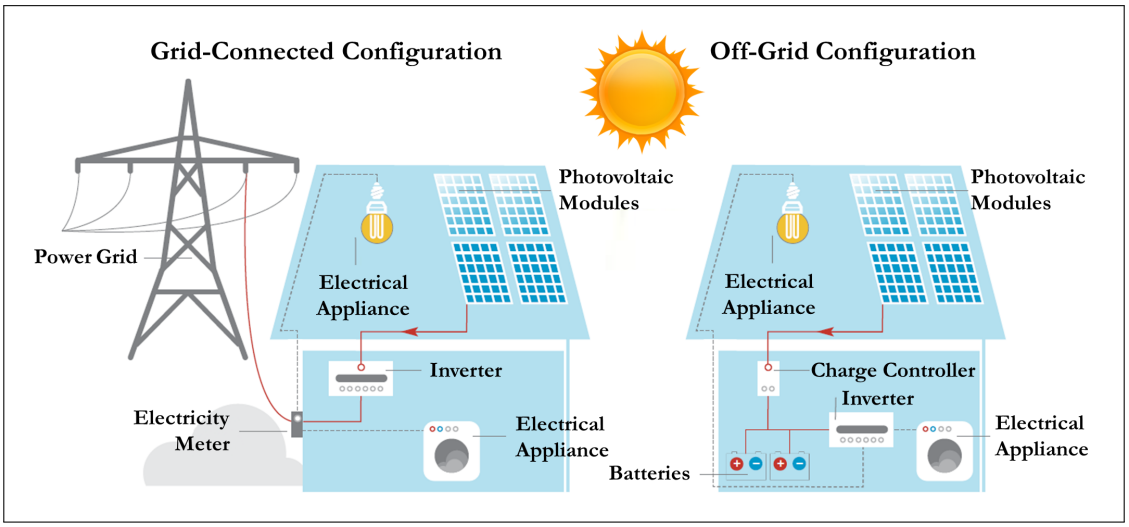

Figure 2.22: Schematic representation of grid-connected and off-grid PV configurations, adapted from [2].

vapour-assisted solution processing, which are methods where the processing conditions (e.g. starting material ratio or growth temperature) directly affect the optoelectronic properties of the absorber layer.

Despite its promise, the major challenge in PSC technology is its over-time degradation. Because of this, the efficiency of this type of solar cells decreases very rapidly, which makes this technology still unprepared for today's standard requirements. The main causes of degradation can be traced to moisture, thermal stress or oxygen exposure. Future research will have to focus on the study of new perovskite materials and processes ensuring the production of devices with long-term stability.

2.4 Structure of photovoltaic technologies

PV systems can be described in general as the union of the following parts [1, 2]:

- PV Cell: the basic building block that is responsible for collecting sunlight.
- PV Module: formed by a number of PV cells, which are interconnected together in a sealed, protective and weatherproof package. A series of PV modules are assembled in a panel and a block of panels form a PV array, which is a complete power-generating unit.
- Inverter: it converts the electricity generated by the PV module (direct current - DC) into a form suitable for our everyday use (alternating current - AC).
- Components for Stand-Alone PV systems: a set of batteries for energy storage for future use.

PV systems are commonly classified into three different configurations: grid-connected, off-grid and hybrid systems.
The most common type of configuration is the grid-connected configuration, in which the solar PV system is connected to a local electricity network. In this case, any power excess produced by the PV system is sold to the public grid and its supplier is paid in conformity with national tariffs and regulations. During night-time or when the solar energy is not available, electricity is imported from the network. An inverter is necessary in grid-connected configuration. Figure 2.22 shows a schematic

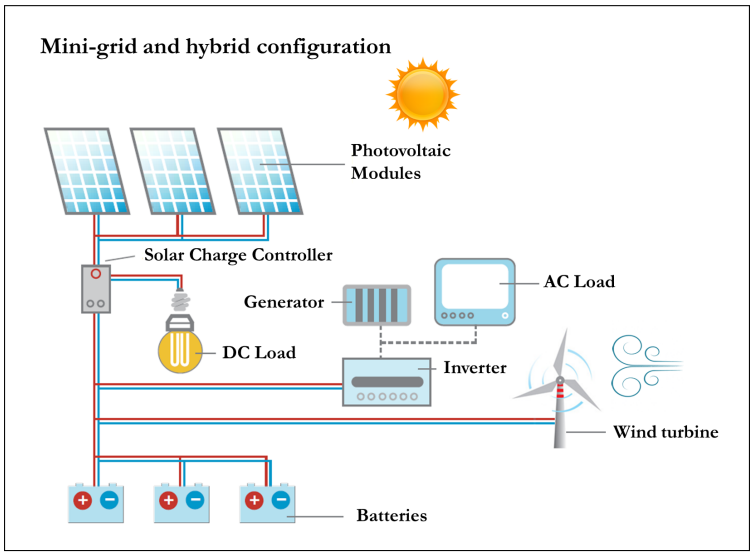

Figure 2.23: An example of mini-grid and hybrid system, reprinted from [2].

representation of this type of system.

By definition, off-grid configuration is a system completely independent of the local electricity grid. This class of systems needs to be equipped with batteries for storing electricity and supplying it during night-time or when solar irradiation is low. An inverter is also needed to convert DC into AC power and use commercial equipment, as shown in Figure 2.22. The three main applications for the off-grid configuration are:

- INDUSTRIAL APPLICATIONS. Off-grid industrial applications are used in remote areas. Some examples of these are: repeater stations for mobile phones, marine navigational aids, remote lighting and so on.

- ELECTRIFICATION OF RURAL AREAS. These installations are used to supply rural areas, off-shore islands or developing countries with electricity. This means small domestic systems, which cover basic electricity needs, or solar mini-grids, which provide energy for a small community.

- CONSUMER GOODS. Currently, PV solar cells can be found in many everyday devices, such as watches, calculators and even embedded in bags and clothes.

Finally, hybrid systems are the combination of solar PV systems with complementary power sources, such as wind, biomass or diesel fuel (see Figure 2.23). Both grid-connected and off-grid systems are possible in this case but, in general, sophisticated control systems are required in order to regulate the interplay between the different sources. For example, in the case of a PV-diesel hybrid system,the diesel generator needs to start energy production as soon as the battery reaches a given discharge level and must deactivate after the battery reaches an adequate level of charge.

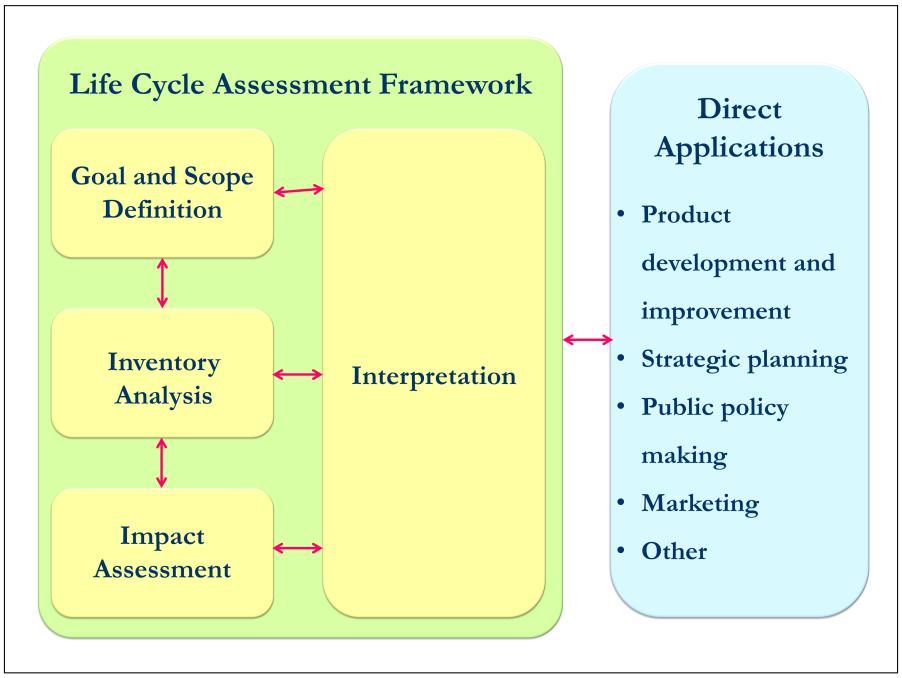

Figure 2.24: Scheme of LCA methodology.

2.5 Life-cycle assessment and energy pay-back time of photovoltaic modules

PV technologies convert solar energy into electricity without fossil energy consumption and greenhouse gases (GHG) emissions during their routine operation. However, they consume energy and emit some GHG at some stage of their life cycle, namely during the manufacturing process, module assembly, system installation and system disposal or recycling.

Life-cycle assessment (LCA) is a methodology to accurately evaluate the environmental impact of PV devices during their life cycle. Energy pay-back time (EPBT) and GHG emission rates can also be used to assess the sustainability and environmental performance of PV systems. As we have seen before, commercial PV materials include multi-crystalline silicon, mono-crystalline silicon and thin-film technologies. These PV materials have different physical and chemical properties, and consequently a different environmental impact. In this section, we will show the principal differences in the EPBT and GHG emission rate of the two largest PV module families.

First of all, it is important to have clear the definition of life-cycle assessment. It is an evaluation of the environmental impact of products, processes or services, through their production, usage and disposal [51, 52, 53, 54]. The evaluation is based on an estimation of the energy requirements and CO_2 emissions throughout the whole life of the PV modules. These results can be used for related environmental assessment. The research and analysis framework for LCA usually consists of four steps (shown in Figure 2.24):

1. Goal and scope definition
   Their function is to determine the research objective and the system's boundaries.

2. Inventory analysis

The inventory analysis mainly focuses on analysing and recording the movements of pollutants, materials and resources throughout the life-cycle.

3. Impact assessment
   In this stage, the energy and resource consumption is categorised and cumulated for different environmental problems, such as global warming potential, acidification potential, ozone layer depletion, ecotoxicity and so on.

4. Interpretation
   The final conclusions of LCA for the specific product will be drawn at this step.

Evaluation indices are fixed for each LCA study and their choice is based on the purpose of the research. In relation to PV systems, EPBT and the CO_2 emission rate can be evaluated.

The EPBT indicator is defined as the time (in years) required for a PV system to generate an amount of energy (converted into equivalent primary energy) as large as the energy required to create, install, maintain and ultimately dismantle it. In other words, it is the time after which the system supplies full compensation for the energy consumed over its life, including energy requirements in PV modules manufacturing, assembly, transportation, system installation, maintenance and recycling. The numeric equation of EPBT can be written as:

$$EPBT = \frac{E_{input} + E_{BOS}}{E_{output}} \; [years] \tag{2.23}$$

where E_{input} is the primary energy input of a PV module during its life cycle, which includes the energy requirement for module manufacturing, transportation, installation, etc.; E_{BOS} is the energy requirement for balance of system (BOS) components, which include support structures, electrical components, inverters, etc; E_{output} is the annual power generated by the PV module.

The CO_2 emission rate is a useful index for determining how effective a PV system is in terms of the fight against global warming. This index is used for comparison between different power generation technologies. Numerically, the CO_2 emission rate can be described as:

$$CO_2 \; emission \; rate = \frac{Total \; CO_2 \; emission \; during \; life \, cycle}{Annual \; power \; generation \times Lifetime} \left[\frac{g\,CO_2}{kWh}\right] \tag{2.24}$$

2.5.1 System boundary of PV modules

The life-cycle of PV modules involves a sequence of different steps (shown in Figure 2.25) [53, 55]. The main ones are:

- Production of raw materials;
- Processing and purification;
- Manufacture of modules;
- Distribution, installation and use of the PV system;
- Decommissioning and disposal or recycling.

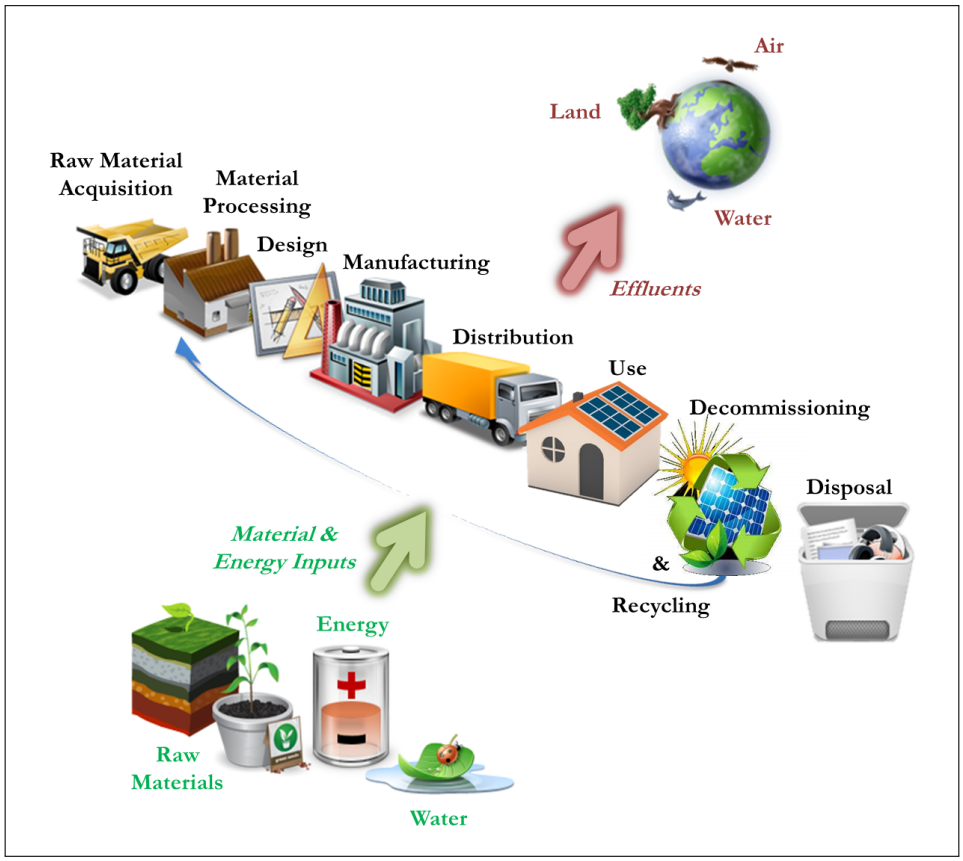

Figure 2.25: Life-cycle steps, energy and material inputs and effluents for PV modules.

The life-cycle steps of PV modules involve products and service related to item's life-cycle. The details of the product vary in each single case and this is important to fit PV modules life-cycle definition to the purpose of the product. For example, type of PV module, efficiency, installation and operation method should be identified to build a suitable system. The indirect factors should also be considered as much as possible.

2.5.2 Methodological LCA guidelines for PV systems

The ISO 14040 and ISO 14044 standards provide a LCA framework. However, there are individual practitioner with a range of choices that can affect the results and the conclusions of a LCA study [53, 56]. For this reason, the International Energy Agency (IEA) has developed the "Methodology Guidelines on Life Cycle Assessment of Photovoltaic Electricity" (published by International Energy Agency Photovoltaic Power System Programme (IEA PVPS), Task 12, Subtask 20). The major motivation to provide these methodological guidelines is due to the variety of approaches and the need for transparent reporting of assumptions and key choices. The main PV-specific aspects highlighted in the guidelines are the following:

1. Life expectancy
   The life expectancy of PV modules is quite difficult to quantify, because most of PV system are still in operation or were produced in the early stages of the technology's development. The Table 2.4 shows life expectancy for different PV components, recommended by IEA PVPS (Task

12, Subtask 20).

Table 2.4: Life expectancy for different PV components, recommended by IEA PVPS (Task 12, Subtask 20). Adapted from [56].

Module	30 years for mature module technologies (for example: glass-glass or glass-Tedlar encapsulation). Life expectancy may be lower for foil-only encapsulation. This life-time is based on standard PV module warranties (i.e. the efficiency degradation of 20% or less after 25 years).
Inverter	15 years for small plants (for example: residential PV) and 30 years with 10% part replacement every 10 years (parts need to be specified) for medium and large plants (utility scale > 1 MW).
Transformer	30 years.
Structure	30 years for roof-top and façades installations. Between 30 to 60 years for ground-mount installations on metal supports. Sensitivity analysis should be performed.
Cabling	30 years.
Manufacturing plants	The life expectancy may be shorter than 30 years due to the rapid development of technology. These assumptions should be listed.

2. Irradiation

   The irradiation collected by the modules depends on their location (latitude), orientation (azimuth) and tilt (zenith). The IEA PVPS (Task 12, Subtask 20) gives three main recommendations:

   - Analysis of industry average and best case system;
   - Assume for ground system, roof-top and façades installation that the panels are optimally oriented and tilted;
   - Analysis of average systems installed on the grid network.

   A description of irradiance (W/m^2) and irradiation or insolation ($kWh/m^2/yr$) is provided by the International Standard IEC 61724.

3. Performance ratio

   The performance ratio (PR) is one of the most important variables for evaluating the efficiency of every PV plant. PR describes the relationship between the actual and the theoretical energy outputs of the PV plant. Two elements increase the PR:

   (a) Decline in temperature;

   (b) Early monitoring of PV systems to detect and to amend defects.

   For example shading and soiling are negative factors for PR. On the contrary, well-designed, well-ventilated, well-maintained and large scale system are positive factors for PR. The IEA PVPS (Task

12, Subtask 20) recommendation for PR is 75% for roof-top and 80% for ground-mounted utility installations. These default values include degradation caused by aging.

4. Degradation
   Modules reduce efficiency during their lifetime and the guidelines recommend the following degradation rate. For mature module technologies, the IEA PVPS assumes an efficiency linear degradation, declining to 80% of the initial value at the end of the 30-year lifetime.

5. Back-up system
   If a back-up system (like temporal storage, hydroelectric or gas combined cycle power plant) is included, it should be explicitly considered.

2.5.3 Estimates of GHG emissions and EPBT from PV systems

There are many studies that report LCA data for PV systems and unfortunately, these reviews show a wide range of results. The main reasons for this variation in outcomes can be related to:

- Different LCA assumptions;
- Different evaluation of the PV technologies, such as: system design and operation or technology improvements over time.

For this reason, NREL has recently developed this project: *Life Cycle Assessment Harmonization* [57]. This research sought to apply a systematic approach to the revision of LCA literature; therefore, it is possible to estimate and clarify the inconsistent and conflicting data of GHG emissions and EPBT in the published literature. A summary of their results is shown in Figure 2.26. Comparing data for PV systems (c-Si and thin-film) and other power generation technologies, it should be noted that the avarage value of GHG emissions to produce electricity using solar PV is about 50 g CO_2-eq./kWh, very lower than using coal (about 1,000 g CO_2-eq./kWh). Instead, GHG emissions for PV system are very similar to other renewable energy sources and nuclear.

Focusing on the PV technologies, we can analyse the LCA data of the top five commercialised PV systems, i.e. mono-Si, multi-Si, a-Si, CdTe and CIGS solar cells [51]. The Figure 2.27 highlights the main differences between these PV technologies in terms of energy requirement, EPBT and GHG emission rate during whole life cycle.
From this data, it should be deduced that:

- From published literature, mono-Si solar modules show that life cycle energy requirement can vary from 2680 to 5253 MJ/m^2, while the EPBT is in the range between 1.7 and 2.7 years. These high variations in data are mainly due to the estimation of energy required for silicon purification and crystallisation processes.
- Multi-Si and mono-Si show very similar data. Indeed, the estimations for energy requirement and EPBT are between 2699 and 5150 MJ/m^2 and (1.5 ÷ 2.6) years, respectively.
- Thin-film solar cells exhibit a lower life cycle energy requirement compared to first-generation devices (in the range from 710 to 1990 MJ/m^2). a-Si solar cells show the highest EPBT (between

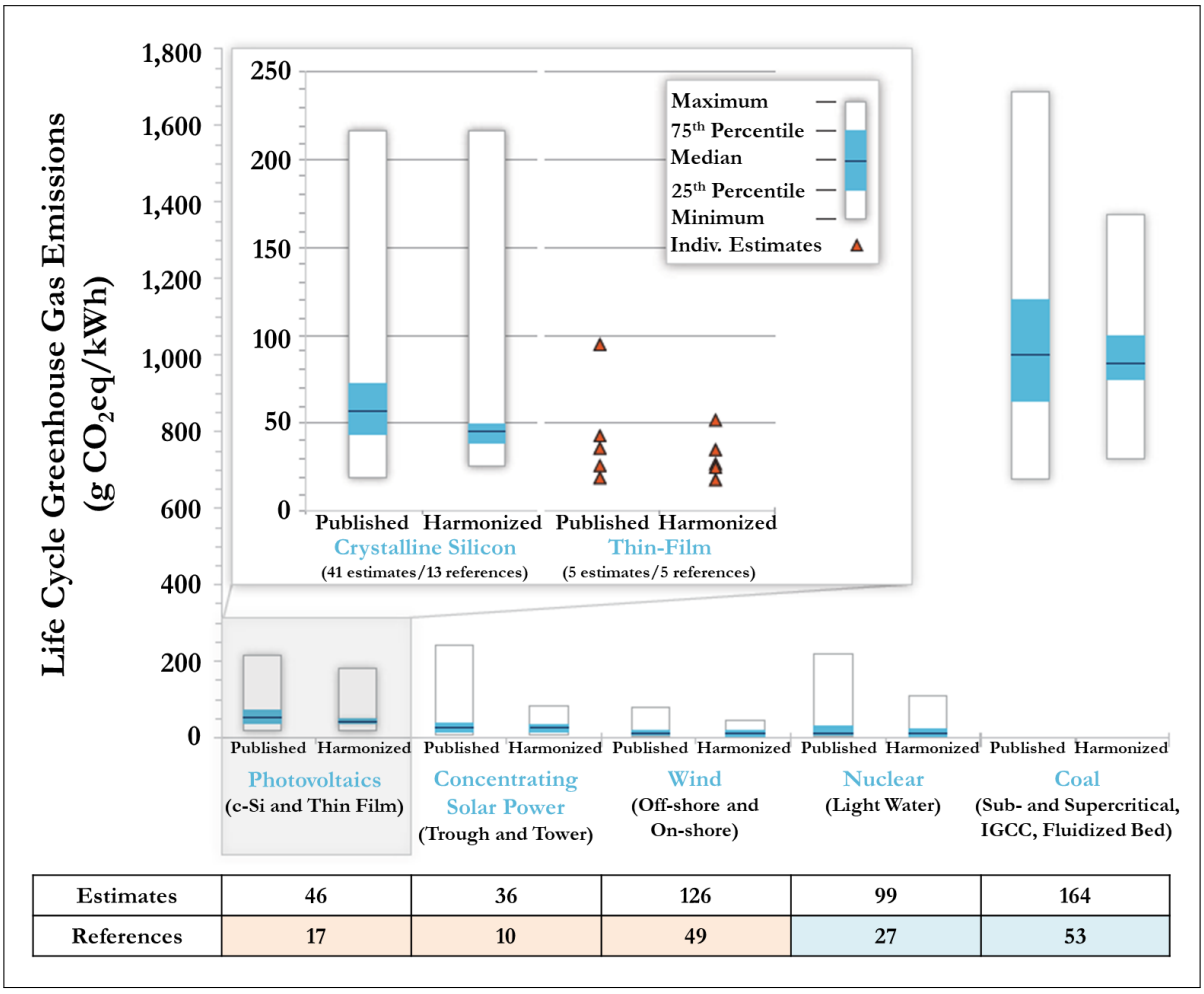

Estimates	46	36	126	99	164
References	17	10	49	27	53

Figure 2.26: Extract of the main results of the NREL Life Cycle Assessment Harmonization Project. Published and harmonized data of estimates of GHG emissions for different electricity generation technologies. Reprinted from [57]

1.8 to 3.5 years), because they have the lowest device efficiency. CIS-based solar cells show a wide range of estimate GHG emission rate, between 10.5 to 46 g CO_2-eq./kWh. As a consequence, it is necessary to make more detailed studies on the LCA of the entire production chain of these devices. Currently, the CdTe-based solar cells evidence the lowest environmental impacts and the shortest EPBT, thanks to their lower energy demand and relatively high efficiency.

It should also be mentioned that there are no differences in GHG emission from ground-mounted and roof-mounted PV systems.

In summary, these LCA data demonstrate that PV technology is a source of sustainable and environmental friendly energy. Currently, CdTe-based solar modules show the best LCA parameters, while silicon-based solar devices highlight the worst environmental benefits, due to their high energy requirements throughout the production process. Finally, it should be underline that there are many factors that can improve the environmental benefits of PV technology, such as new production process, reduction in use of rare materials and advanced recycling techniques. Thus, there are currently many open areas of research in the PV field and during this PhD thesis period I tried to improve some of these aspects, as it will be shown in the next chapters.

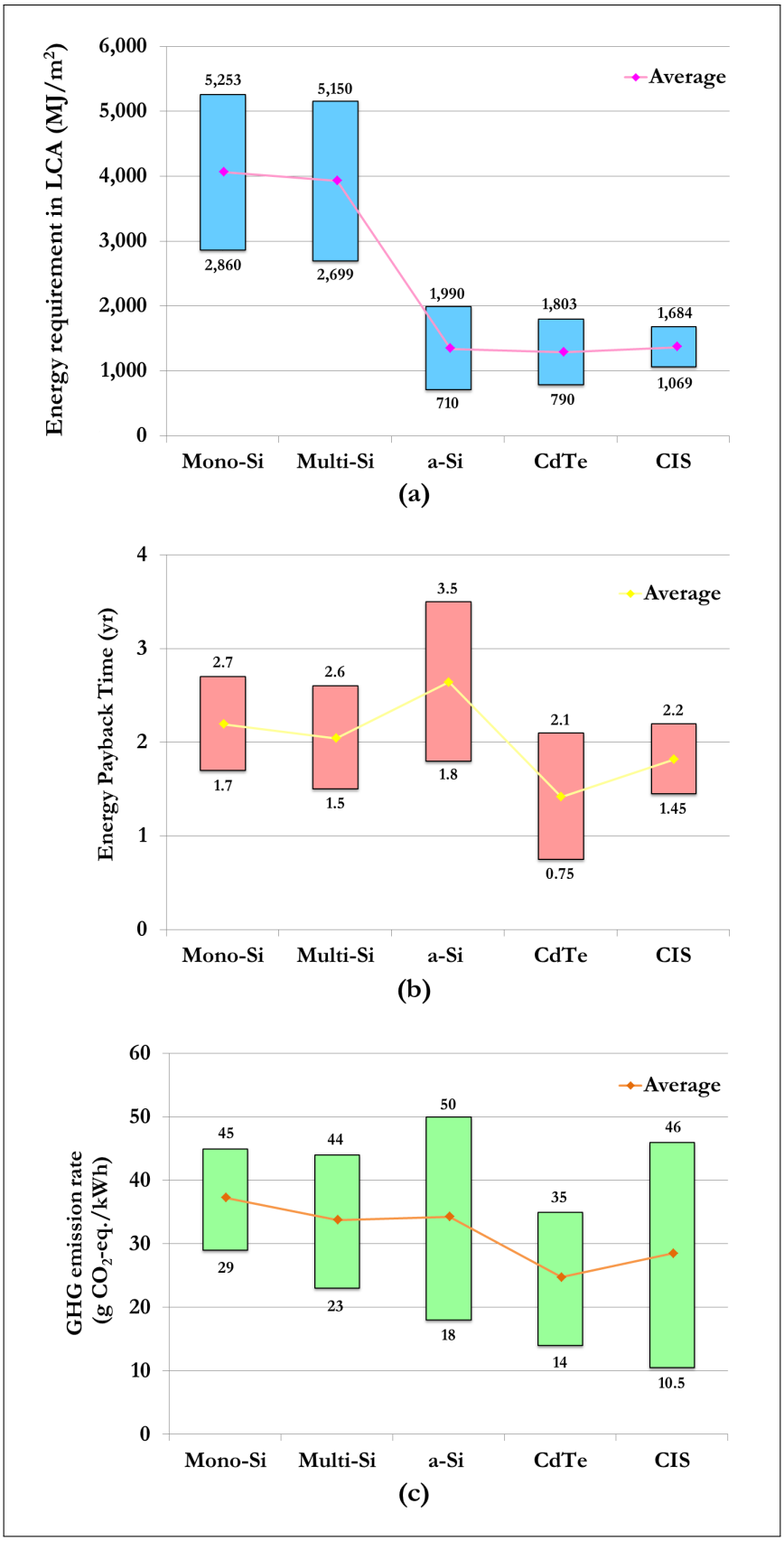

Figure 2.27: Considering the top five commercialised PV systems, the graphics shows a review of: (a) the energy requirements during life cycle, (b) the EPBT and (c) the GHG emission rates, respectively. Data reprinted from [51]

2.6 Pros and cons of photovoltaic technology

We can conclude this broad overview on PV technologies by summarizing their main advantages and drawbacks:

- Main Advantages:
  - Energy comes directly from the Sun, fuel free and completely renewable.
  - This technique does not produce noise and harmful emissions or gases.
  - There are no moving parts.
  - It is proved that it is safety, reliable and each module lasts at least 25 years.
  - PV systems are modular and they are easy and quickly installed everywhere. Furthermore, they have a minimal maintenance requirements.
  - PV modules can be easy incorporated into the architecture of a building, the so-called Building-Integrated Photovoltaic (BIPV).
  - As we will see in the next section, PV devices can be completely recycled at the end of their life.
- Main Drawbacks:
  - Intermittency of the production.
  - Grid connection challenges.
  - Use of rare and in same cases toxic materials.

References

[1] Epia and Greenpeace. *Solar generation. Solar electricity for over one billion people and two million jobs by 2020.* 2006 (Accessed June 27, 2017).
http://www.greenpeace.org

[2] Epia and Greenpeace. *Solar generation 6. Solar photovoltaic electricity empowering the world.* 2011 (Accessed June 27, 2017).
http://www.greenpeace.org

[3] World Energy Council. *World energy resources. 2013 Survey.* ISBN 978 0 946121 29 8. London, 2013 (Accessed June 27, 2017).
http://www.worldenergy.org

[4] M.A. Green. *Photovoltaic principles.* Physica E: Low-dimensional Systems and Nanostructures. Elsevier. 2002, Volume 14, Number 1, Pages: 11-17.

[5] I.M. Dharmadasa. *Advances in thin-film solar cells.* CRC Press. 2012.

[6] W. Shockley and H.J. Queisser. *Detailed balance limit of efficiency of p-n junction solar cells.* Journal of applied physics. AIP. 1961, Volume 32, Number 3, Pages: 510-519. DOI: 10.1063/1.1736034.

[7] A. Polman, M. Knight, E.C. Garnett, B. Ehrler, Bruno and W.C. Sinke. *Photovoltaic materials: Present efficiencies and future challenges.* Science. American Association for the Advancement of Science. 2016, Volume 352, Number 6283, Page: aad4424. DOI: 10.1126/science.aad4424.

[8] U. Rau and J.H. Werner. *Radiative efficiency limits of solar cells with lateral band-gap fluctuations.* Applied Physics Letters. AIP. 2004, Volume 84, Number 19, Pages: 3735-3737.

[9] O. Dupré, R. Vaillon and M.A. Green. *Physics of the temperature coefficients of solar cells.* Solar Energy Materials and Solar Cells. Elsevier. 2015, Volume 140, Pages: 92-100.

[10] L.C. Hirst and N.J. Ekins-Daukes. *Fundamental losses in solar cells.* Progress in Photovoltaics: Research and Applications. Wiley. 2010, Volume 19, Pages: 286–293. DOI: 10.1002/pip.1024.

[11] R.H. Bube. *Photovoltaic materials.* Volume 1, Publisher World Scientific Publishing Company. 1998.

[12] J. Nelson. *The physics of solar cells.* Publisher World Scientific Publishing Co Inc. 2014.

[13] Irena. *Renewable energy technologies: cost analysis series.* June 2012. Volume 1-Power Sector, Issue

4/5 (Accessed June 27, 2017).
https://www.irena.org

[14] M.A. Green, Y. Hishikawa and W. Warta *Solar cell efficiency tables (version 50).* Prog Photovolt Res Appl. 2017, Number 25, Pages: 668–676.

[15] Yingli Solar. (Accessed July 06, 2017).
https://www.twentezon.nl

[16] B.S. Xakalashe and M. Tangstad. *Silicon processing: from quartz to crystalline silicon solar cells.* Southern African Pyrometallurgy. 2011.

[17] Musa T. Zarmai, N.N Ekere, C.F. Oduoza and H.A. Emeka. *A review of interconnection technologies for improved crystalline silicon solar cell photovoltaic module assembly.* Applied Energy. Elsevier. 2015, Volume 154, Pages: 173–182.

[18] DuPont. (Accessed July 11, 2017).
http://www.dupont.com

[19] L. El Chaar, L.A. Lamonta and N.E. Zein. *Review of photovoltaic technologies.* Renewable and sustainable energy reviews. Elsevier. 2011, Volume 15, Number 5, Pages: 2165-2175.

[20] D. Carlson and C.R. Wronski. *Amorphous silicon solar cell.* Applied Physics Letters. AIP. 1976, Volume 28, Number 11, Pages: 671-673.

[21] A. Bahrami, S. Mohammadnejad and S. Soleimaninezhad. *Photovoltaic cells technology: principles and recent developments.* Optical and Quantum Electronics. Springer. 2013, Volume 45, Number 2, Pages: 161-197. DOI: 10.1007/s11082-012-9613-9.

[22] NREL. (Accessed July 31, 2017).
https://www.nrel.gov/pv/assets/images/efficiency-chart.png

[23] E. Kask, T. Raadik, M. Grossberg, R. Josepson and J. Krustok. *Deep defects in Cu_2ZnSnS_4 monograin solar cells.* Energy Procedia. Elsevier. 2011, Volume 10, Pages: 261-265. DOI: 10.1016/j.egypro.2011.10.188.

[24] T.K. Todorov, K.B. Reuter and D.B. Mitzi. *High-efficiency solar cell with earth-abundant liquid-processed absorber.* Advanced materials. Wiley Online Library. 2010, Volume 22, Number 20, Pages: E156-E159. DOI: 10.1002/adma.200904155.

[25] M. Hueske. *High-speed laser processing in thin-film module manufacturing.* Laser Technik Journal. Wiley Online Library. 2010, Volume 7, Number 2, Pages: 64-67.

[26] F. Yang. *Large area a-Si/μc-Si thin film solar cells.* InTech. Chapter: 16, Book: Solar Cells-Thin-Film Technologies. 2011.

[27] Y. Wang, Z. Ren, M. Thway, K. Lee, S.F. Yoon, I.M. Peters, T. Buonassisi, E.A. Fizgerald, C.S. Tan and K.H. Lee. *Fabrication and characterization of single junction GaAs solar cells on Si with*

As-doped Ge buffer. Solar Energy Materials and Solar Cells. Elsevier. 2017, Volume 172, Pages: 140-144.

[28] S. Kim, M.S. Park, D.M. Geum, H. Kim, G. Ryu, H.D. Yang, J.D. Song, C.Z. Kim, and W.J. Choi. *Fabrication and characterization of single junction GaAs solar cell epitaxially grown on Si substrate.* Current Applied Physics. Elsevier. 2015, Volume 15, Pages: 540-543.

[29] K. Kim, H.D. Nguyen, S. Mho and J. Lee. *Enhanced efficiency of GaAs single-junction solar cells with inverted-cone-shaped nanoholes fabricated using anodic aluminum oxide masks.* International Journal of Photoenergy. Hindawi Publishing Corporation. 2013, Volume 2013.

[30] H. Cotal, C. Fetzer, J. Boisvert, G. Kinsey, R. King, P. Hebert, H. Yoon and N. Karam. *III-V multijunction solar cells for concentrating photovoltaics.* Energy & Environmental Science. Royal Society of Chemistry. 2009, Volume 2, Number 2, Pages: 174-192. DOI: 10.1039/b809257e.

[31] G. Hirn. *Energy from a thousand sun. Multi-junction solar cells with concentrator systems utilise a wide solar spectrum.* FIZ Karlsruhe. 2014.

[32] P. Antonini. *Concentrated PhotoVoltaics (CPV): Is it a real opportunity?* EDP Sciences. Book: EPJ Web of Conferences. 2013, Volume 54, Pages: 01015. DOI: 10.1051/epjconf/20135401015.

[33] A. Zahedi. *Review of modelling details in relation to low-concentration solar concentrating photovoltaic.* Renewable and Sustainable Energy Reviews. Elsevier. 2011, Volume 15, Number 3, Pages: 1609-1614. DOI: 10.1016/j.rser.2010.11.051.

[34] B.A. Gregg. *The photoconversion mechanism of excitonic solar cells.* MRS bulletin. Cambridge University Press. 2005, Volume 30, Number 1, Pages: 20-22.

[35] K. Hwajeong, N. Sungho, J. Jaehoon, L. Sooyong, S. Jooyeok, H. Hyemi and K. Youngkyoo. *Organic solar cells based on conjugated polymers: History and recent advances.* Korean Journal of Chemical Engineering. Springer. 2014, Volume 31, Number 7, Pages: 1095-1104.

[36] N. Kaur, M. Singh, D. Pathak, T. Wagner and J.M. Nunzi. *Organic materials for photovoltaic applications: Review and mechanism.* Synthetic Metals. Elsevier. 2014, Volume 190, Pages: 20-26.

[37] B. Savoie, N.E. Jackson, L.X. Chen, T.J. Marks and M.A. Ratner. *Mesoscopic features of charge generation in organic semiconductors.* Accounts of chemical research. ACS Publications. 2014, Volume 47, Number 11, Pages: 3385-3394.

[38] B.C. Thompson and J.M.J. Fréchet. *Polymer-fullerene composite solar cells.* Angewandte chemie international edition. Wiley Online Library. 2008, Volume 47, Number 1, Pages: 58-77.

[39] G. Li, R. Zhu and Y. Yang. *Polymer solar cells.* Nature Photonics. Nature Research. 2012, Volume 6, Number 3, Pages: 153-161.

[40] W. Cai, X. Gong and Y. Cao. *Polymer solar cells: recent development and possible routes for improvement in the performance.* Solar Energy Materials and Solar Cells. Elsevier. 2010, Volume 94, Number 2, Pages: 114-127.

[41] B. O'Regan and M. Grätzel. *A low-cost, high-efficiency solar cell based on dye-sensitized.* Nature. 1991, Volume 353, Number 6346, Pages: 737-740.

[42] D. Wei. *Dye sensitized solar cells.* International journal of molecular sciences. Molecular Diversity Preservation International. 2010, Volume 11, Number 3, Pages: 1103-1113.

[43] M. Grätzel. *Dye-sensitized solar cells.* Journal of Photochemistry and Photobiology C: Photochemistry Reviews. Elsevier. 2003, Volume 4, Number 2, Pages: 145-153.

[44] K.E. Jasim. *Dye sensitized solar cells-working principles, challenges and opportunities.* InTech. Chapter: 8, Book: Solar Cells-Dye-Sensitized Devices. 2011.

[45] H.J. Snaith. *Perovskites: the emergence of a new era for low-cost, high-efficiency solar cells.* The Journal of Physical Chemistry Letters. ACS Publications. 2013, Volume 4, Number 21, Pages: 3623-3630.

[46] S. Prasanthkumar and L. Giribabu. *Recent advances in perovskite-based solar cells.* Current Science. 2016, Volume 111, Number 7, Pages: 1173-1181.

[47] T.B. Song, Q. Chen, H. Zhou, C. Jiang, H.H. Wang, M. Yang, Y. Liu, J. You and Y. Yang. *Perovskite solar cells: film formation and properties.* Journal of Materials Chemistry A. Royal Society of Chemistry. 2015, Volume 3, Number 17, Pages: 9032-9050.

[48] N.K. Elumalai, M.A. Mahmud, D. Wang and A. Uddin. *Perovskite solar cells: Progress and advancements.* Energies. Multidisciplinary Digital Publishing Institute. 2016, Volume 9, Number 11, Page: 861. DOI:10.3390/en9110861.

[49] Ossila. (Accessed August 11, 2017).
`https://www.ossila.com`

[50] M.A. Green, A. Ho-Baillie and H.J. Snaith. *The emergence of perovskite solar cells.* Nature Photonics. Nature Research. 2014, Volume 8, Number 7, Pages: 506-514. DOI:10.3390/en9110861.

[51] J. Peng, L. Lu and H. Yang. *Review on life cycle assessment of energy payback and greenhouse gas emission of solar photovoltaic systems.* Renewable and Sustainable Energy Reviews. 2013, Volume 19, Pages: 255–274.

[52] A. Meijer, M.A.J. Huijbregts, J.J. Schermer and L. Reijnders. *Life-cycle assessment of photovoltaic modules: comparison of mc-Si, InGaP and InGaP/mc-Si solar modules.* Prog. Photovolt: Res. Appl. 2003, Pages: 275–287. DOI: 10.1002/pip.489.

[53] M. Ito. *Life cycle assessment of PV systems.* Crystalline Silicon – Properties and Uses. 2011, Chapter 13, Pages: 297–312.

[54] M. Held and R. Ilg. *Update of environmental indicators and energy payback time of CdTe PV systems in Europe.* Prog. Photovolt: Res. Appl. 2011, Pages: 614–626. DOI: 10.1002/pip.1068.

[55] V.M. Fthenakis and H.C. Kim. *Photovoltaics: Life-cycle analyses.* Solar Energy. Elsevier. 2011, Volume 85, Number 8, Pages: 1609–1628.

[56] R. Frischknecht, G. Heath, M. Raugei, P. Sinha and M. Wild-Scholten. *Methodology guidelines on life cycle. Assessment of photovoltaic electricity 3rd Edition.* IEA PVPS Task 12, Subtask 2.0, LCA. (January 2016).

[57] NREL. *Life cycle greenhouse gas emissions from solar photovoltaics.* November 2012. https://www.nrel.gov

Chapter

3

Thin-film solar cells: deposition and characterisation techniques

The aim of my PhD research project was to provide an implementation of CdTe- and CIGS-based thin-film solar cells techniques.
In this chapter, a summary of the deposition techniques used to produce thin-film solar devices in our Thin Film Laboratory (ThiFiLab) at the University of Parma is reported. I will focus on the principal advantages and on the main problems typical of these deposition methods. I will also briefly report on the experimental techniques that are used to characterise both the thin films and the final solar cells.

3.1 An introduction to thin-film deposition techniques

Thin-films are by definition layers of material having a thickness that can vary from fractions of a nanometer to few microns and they need to be deposited on a suitable substrate [1].

The materials that can be deposited in the form of thin films may vary in terms of conductive properties. They could be metal, semiconductor or insulating materials. This is part of the reason why thin films can be used in such a wide range of technological applications. Some of the main areas of application are: electronic semiconductor devices, LEDs, optical coatings (e.g. anti-reflective coatings), magnetic recording media, medical and biomedical applications and of course energy generation and storage (e.g. thin-film solar cells and batteries). This wide variety of materials and applications proves the need to use different deposition techniques in order to better satisfy the functionality of the deposited material.

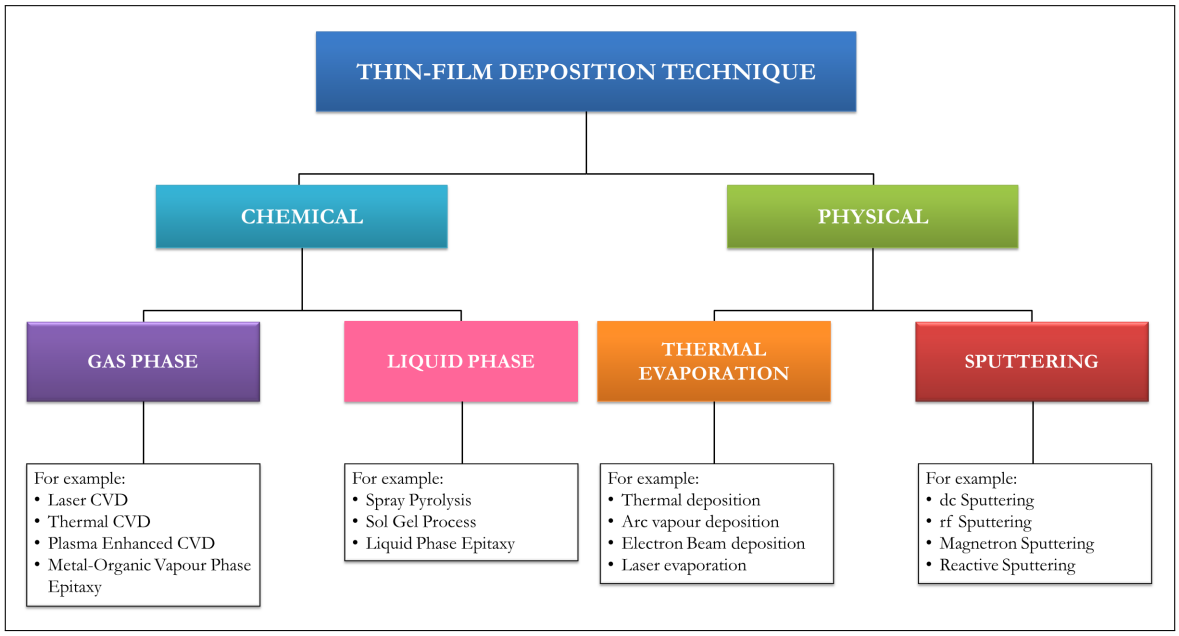

Figure 3.1: Schematic classification of thin-film deposition techniques.

Each deposition process involves three steps:

- Emission of particles from a source.
- Transport of these particles through a medium to the substrate.
- Condensation of particles on the substrate surface.

The deposition techniques can be divided into two broad categories based on how the material is transferred from the source (target) to the destination (substrate):

1. Chemical deposition
   In a chemical vapour deposition (CVD) process, films are deposited through a chemical reaction. They are synthesis techniques (i.e. conduction of one or more chemical reactions) that allow the deposition of a given material that is introduced via a gaseous phase.

2. Physical deposition.
   The techniques in this group are characterised by the evaporation or expulsion of the deposited material out of a solid or a liquid source. Physical methods can be further split into two classes: thermal evaporation and sputtering.

Moreover, there are some processes that combine features from both physical and chemical deposition processes, such as reactive sputtering. These techniques can be categorised as physical-chemical methods. A general overview of the classification of deposition techniques is presented in Figure 3.1.

A key aspect of both PVD and CVD processes is that they are typically conducted in a vacuum environment. The vacuum environment has the following advantages:

- It reduces the particle density of undesirable atoms and molecules (i.e. contaminants). Thus, it also reduces the possibility of interaction between the depositing particles and residual gas atoms or molecules.

- It provides a medium for controlling gas and vapour composition.
- It provides a medium for the process gas control into the deposition chamber.

The nature and quality of the deposited film depends on various process parameters, such as deposition temperature, gaseous environment and deposition rate. In summary, the choice of which technique should be used has to take into account many factors, including:

- Deposition rate.
- Film uniformity.
- The properties of the deposited material.
- The quality requirements of the resulting film, such as: chemical, electrical, mechanical, optical properties. In particular, it is important to control its composition, stoichiometry, film density, texture, grain size, and impurity level.
- Film thickness.
- Nature of the substrate.
- Cost of the deposition process.

In the following sections, we will analyse in detail the PVD deposition techniques we used to produce CdTe- and CIGS-based solar cells in our ThiFiLab laboratory.

3.2 Sputtering

By definition, the word 'sputter' indicates the act of spitting or squirting particles from a source, namely a target. Thus, the term 'sputtering' has come to refer to a physical deposition technique that consists in depositing atoms ejected from the surface of a target onto a substrate [2, 3, 4]. Figure 3.2 shows a greatly simplified scheme of a sputtering system.

In a vacuum chamber (where pressure ranges from 10^{-2} Pa to about 10^{-4} Pa) two holders are typically arranged horizontally: one holds the target and the other one holds the substrate. The two holders face each other. These holders can be equipped with devices to supply heat, cooling, electrical bias or more.

The target is connected to the negative electrode of a voltage supply. This power supply can be either in direct current (dc) or in radio frequency (rf) regime, depending on whether one considers dc or rf sputtering, respectively.

All the cathodic processes depend on a glow discharge or a plasma in order to work. For this reason, a high-purity inert gas – typically argon – is introduced into the chamber and it is called working gas. The purpose of this gas is to provide a medium in which a glow discharge might be generated and maintained.

Once the glow discharge is initiated, the surface of the target is struck by positive ions (Ar^+), which have enough energy to remove atoms from the target surface. During this collision, the target atoms can be ejected thanks to a momentum transfer. The atoms removed from the target have no net charge

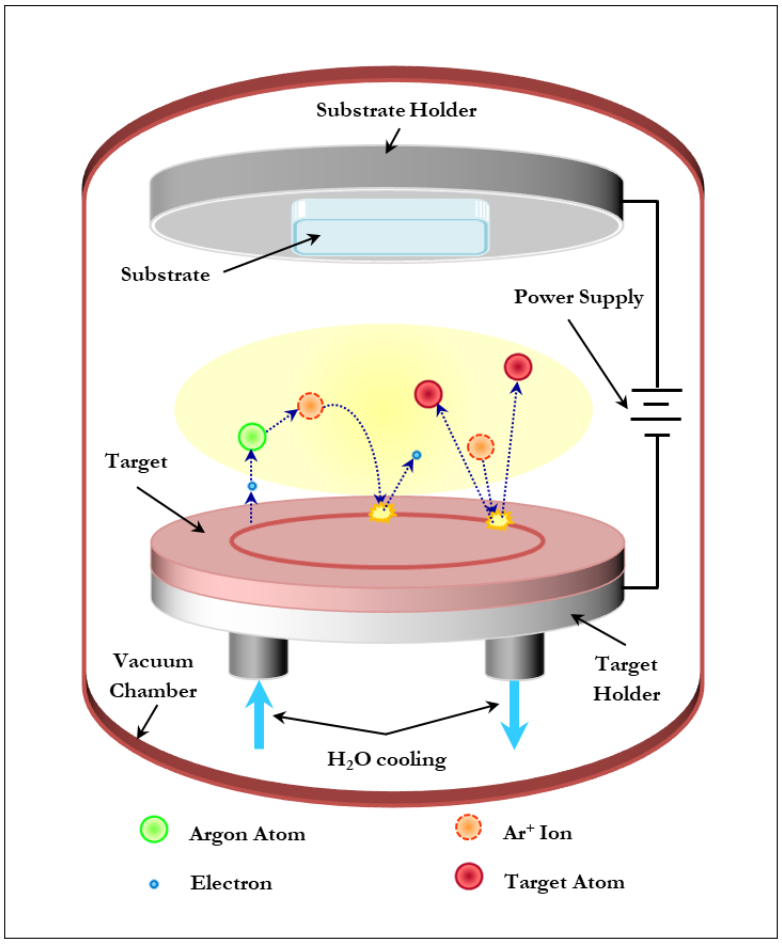

Figure 3.2: Basic cross section of a sputtering system, adapted from [3].

and are, therefore, unaffected by the electric field generated by the discharge. They reach the substrate and condense on its surface in the form of a thin film. The argon ions, on the other hand, are positively charged and they are accelerated towards the target.

It should be underlined that a number of additional events can occur at the target surface during the ion bombardment, such as the emission of secondary electrons or ions, chemical dissociations or reactions, crystallographic changes and back-scattering. These phenomena can greatly influence the properties of the resulting thin films.

The most important parameter of the sputtering process is represented by the sputtering yield (Y_{sp}). The term Y_{sp} refers to the number of atoms that are ejected from a target surface per incident ion. Y_{sp} is a quantity connected to the momentum transfer from high-energy ions to the atoms of the target surface. In this case, the bonding energy threshold of the target constituent atoms is approximately equal to the heat of sublimation.

When the sputtering equipment is operated under typical conditions, the energy of the incoming ions lies between 500 eV and 1000 eV, whereas the energy of the sputtered atoms is in the range of (3 ÷ 10) eV. Thus, a large part (about 95%) of the incoming energy is converted into target heating. For this reason, a target cooling system is necessary to avoid severe damage.

Furthermore, Y_{sp} increases with:

- Energy of the incident ions.

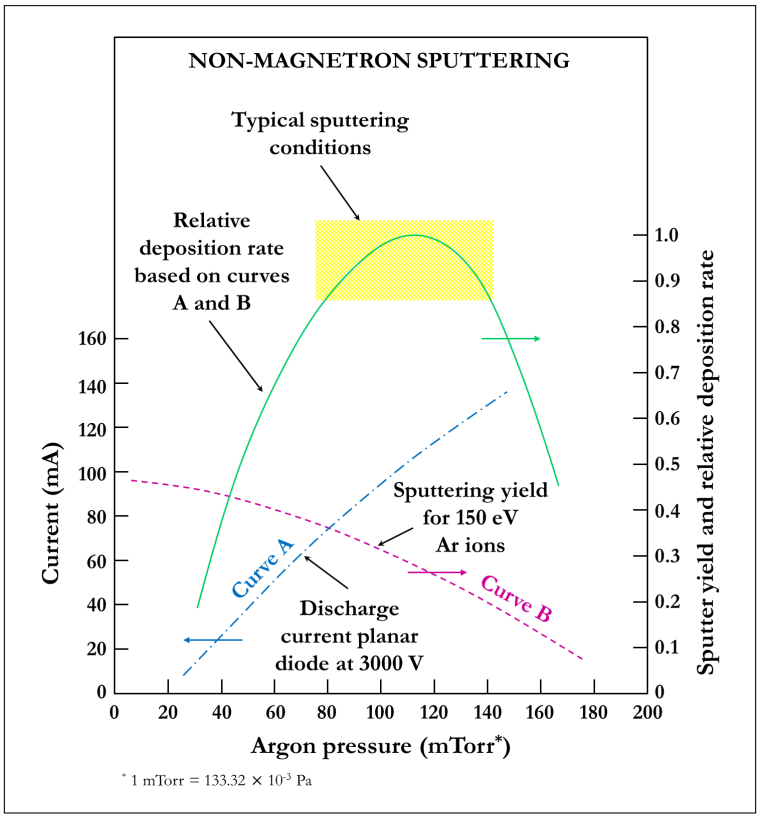

Figure 3.3: Influence of chamber pressure and current on deposition rate for a non-magnetron sputtering with a planar circular geometry (target diameter: 7.62 cm). Reprinted from [2]

- Mass of the incident ions and of the target atoms.
- Binding energy of the atoms in the source.
- Angle of incidence of incoming ions.

Y_{sp} is also associated with erosion rate of the target and with the deposition rate of the film. In order to maximise Y_{sp} and obviously also the deposition rate of the film, the main parameters of the sputtering process that can be operationally optimised are:

- Power applied to the electrodes.
- Substrate temperature.
- Working gas pressure.
- Target-substrate distance.

Among these parameters, the deposition rate dependence on chamber pressure is one of the most critical. The mean free path of the primary electrons is directly proportional to electron energy and is inversely proportional to pressure. In regard to the pressure, we can make the following observations:

- Low chamber pressure (below 1 Pa): ions are produced far from the cathode. Thus, their chances of being lost to the charge walls are high and also many primary electrons hit the anode with high energies, causing a high energy loss. In this case the ionisation efficiency is very low; only

few Ar ions are successful in bombarding the target. It should also be highlighted that the glow discharge cannot be maintained at pressures below about 1.3 Pa.

- High chamber pressure (above 20 Pa): the sputtered atoms have to go through tens of collisions before reaching the substrate. Both the deposition rate and the ion density are reduced in this case. In particular, the deposition rate drops because a large amount of material is wasted on the walls of the chamber, while the ion density drops because too many collisions interfere with ionisation in the first place.

These two facts suggest that there exists an optimum pressure for maximising the deposition rate at a fixed voltage. Figure 3.3 shows the influence of the chamber pressure in the case of a sputtering system with a planar circular geometry.

In summary, the main advantages and disadvantages of the sputtering technique are the following:

- Advantages:
  - Possibility of depositing a wide variety of materials (insulators, semiconductors, conductors, alloys, composites and so on).
  - Replication of target composition in the deposited films.
  - Reproducible deposition process; it is possible to obtain the same film properties for the same process.
  - Possibility of using large area targets for uniform thickness over large substrates. In other words, the sputtering technique is easily scalable at an industrial level.
- Disadvantages:
  - Substrate damage due to ion and electron bombardment.
  - Since most of the incident energy on the target becomes heat, this must be removed using an appropriate target cooling system.
  - Deposition rate of some materials (e.g. oxides) is quite low.

Finally, sputtering system comes in four different variants:

1. dc sputtering;
2. rf sputtering;
3. magnetron Sputtering;
4. reactive Sputtering.

As I will show, these variants can also be combined with each other depending on the material needs. Our ThiFiLab is equipped with all these different sputtering systems and they are regularly used for the production of several layers of CdTe- and CIGS-based solar cells. In the next paragraphs, I will highlight the main differences between the various sputtering systems.

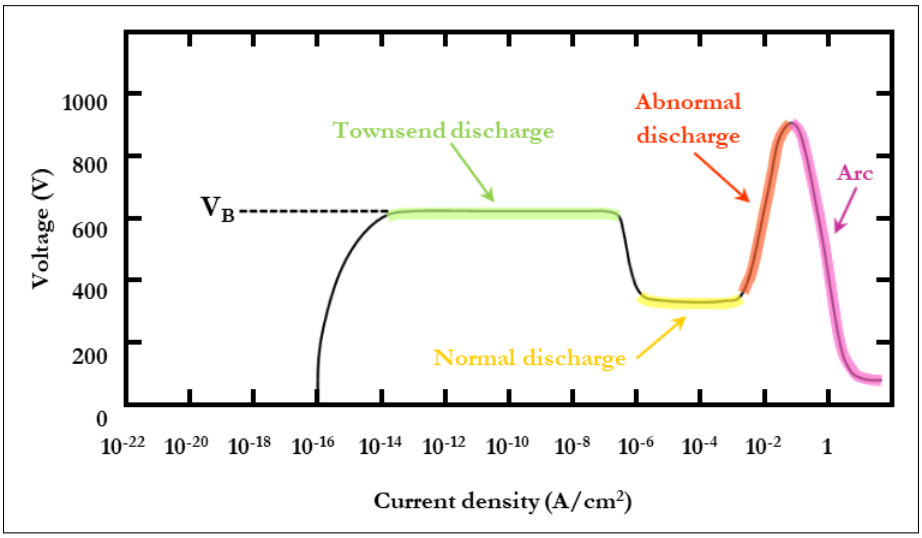

Figure 3.4: Formation of a glow discharge in dc sputtering, adapted from [2].

3.2.1 dc sputtering

In dc sputtering, the target and substrate holders act as a couple of parallel electrodes [2, 4]. By connecting the negative electrode of the power supply to the target (cathode) and the positive one to the substrate holder (anode), a strong continuous potential difference can be generated. As we have shown before, this produces a glow discharge.

Figure 3.4 displays the various steps of glow discharge formation in a chamber at low-pressure gas with a high-impedance dc power supply. As soon as a voltage is applied between the electrodes, a very low current flow. This is due to the presence of a small number of free ions and electrons, which are generated by different sources (such as cosmic radiation). The current is approximately constant initially as all the charges are moving. When the voltage is increased, charged particles acquire more energy and generate more charged particles by colliding with both electrodes (emission of secondary electrons) and neutral gas atoms. This region, which sees an increase in current and on the contrary, a voltage limited by the output impedance of the power supply, is called *Townsend discharge*.

The formation of new ions via consecutive collisions continues until the number of generated electrons is sufficient to produce as many ions as required to regenerate an equal number of electrons. At this point, the discharge becomes self-sustained. This region, which marks the beginning of gas glowing and where the voltage decreases and the current increases sharply, is called *normal discharge*.

At the beginning of this phase, the ionic bombardment of the cathode is not uniform. In particular, it is concentrated around the edges of the cathode or near surface irregularities. To obtain a uniform bombardment, it is necessary to increase the power. This power boost corresponds to an increase of both voltage and current density in the discharge. This region is known as *abnormal discharge*. The abnormal discharge region is normally used in the sputtering technique and in other processes based on a glow discharge.

At this point, the electrodes must be cooled. If the cathode is not cooled, it will become increasingly hotter until the usual emission of secondary electrons is reinforced by a new, thermo-ionic emission of electrons, resulting in a further avalanche. The output impedance of the power supply limits the voltage and the high current induces an *arc discharge*.

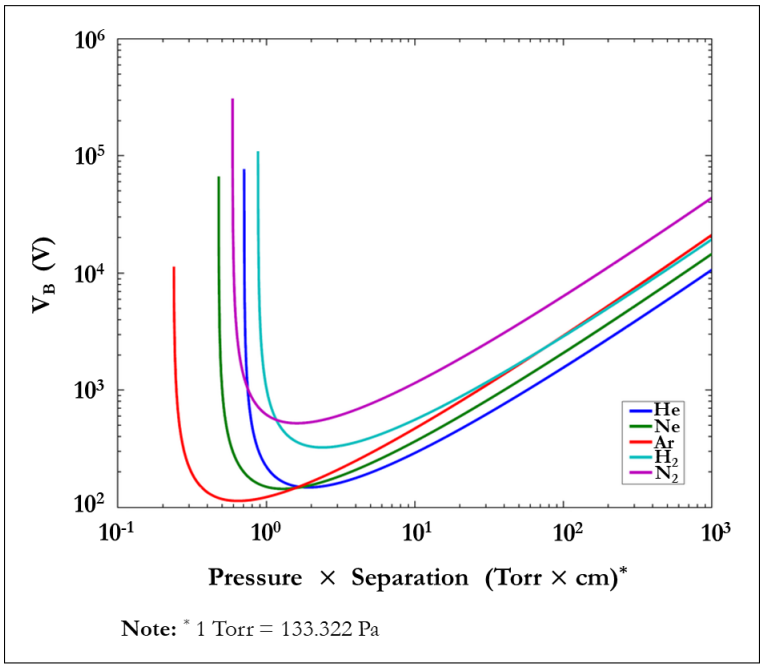

Figure 3.5: Paschen curves for the following gases: helium, neon, argon, hydrogen and nitrogen, adapted from [6].

The determination of the breakdown voltage value (V_B) is crucial to predict the formation of the abnormal discharge. V_B depends on the mean free path of the secondary electrons and on the distance between anode and cathode. Each secondary electron must produce about 10 - 20 ions before the avalanche process can occur. This phenomenon cannot happen if the pressure is too low or if the electrodes are at a short distance from each other. It is possible to estimate the voltage dependence on the pressure-distance product by using the qualitative behaviour of the Paschen's law[1], which is shown in Figure 3.5.

The position of the luminous region of a glow discharge, the voltage distribution and the net spatial charge can be represented as a function of the distance between cathode and anode in a dc sputtering system (Figure 3.6). We can distinguish the following regions between cathode and anode:

1. Aston's dark region
   It is a very thin area where there are both low-energy electrons and high-energy ions, moving in opposite directions.

2. Cathode glow region
   This is the region where incoming discharge ions and cathode ions are neutralised by various processes. It is also the region where the secondary electrons are accelerated away from the cathode. The glow discharge does not only depend on the incident ions but also on the material of which the cathode is made.

[1] **Paschen's law** for the breakdown potential is:

$$V_B = \frac{B_i\, p\, d}{\ln\left(A_i\, p\, d\right) - \ln\left[\ln\left(1 + \frac{1}{\gamma_i}\right)\right]} \tag{3.1}$$

where: A_i and B_i are experimentally determined gas constants, p is the interstitial gas pressure, d is the inter-electrode gap distance and γ_i is the secondary emission coefficient due to ion impact on the cathode surface [5].

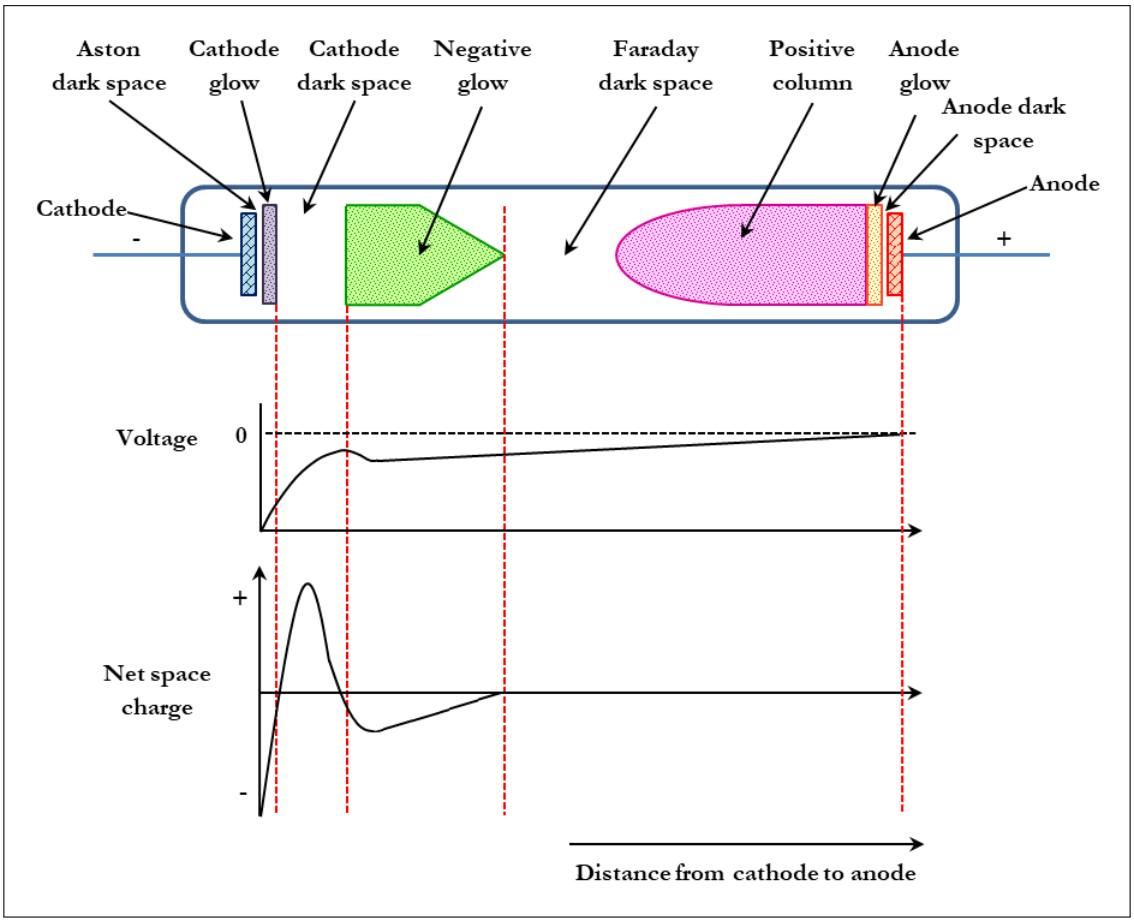

Figure 3.6: Regions within a dc sputtering, corresponding voltage distribution and spatial charge, adapted from [3].

3. Cathode dark region

   The secondary electrons are repelled at high speed by the cathode and begin to collide with the neutral gas atoms, at a distance from the cathode equal to their mean free path. This creates a well-defined dark region, in which all electrons lose their energy very quickly through various collisions and almost all of the applied voltage appears across this dark region. In addition, positive ions are accelerated towards the cathode and, since they have lower mobility than electrons, they predominate in this region.

4. Negative glow region

   In this region, an acceleration of secondary electrons away from the cathode takes place and this effect results in ionising collisions.

5. Faraday dark region and positive column

   These are almost completely free-field regions and their only function is to electrically connect the region of negative glow discharge to the anode. The anode is placed in the negative glow discharge region in most sputtering systems and these two regions are not present.

6. Anode glow discharge and anode dark space regions

   These regions are the area of negative glow discharge, which is exactly symmetrical to the situ-

ation at the cathode.

Finally, only conductive targets can be used with dc sputtering. It is not possible to support the discharge with non-conductive materials since a positive ion charge on the surface of the target is generated. This requirement strongly limits the type of materials that can be deposited with the dc sputtering technique. To overcome this problem, it is possible to use the rf sputtering technique.

3.2.2 rf sputtering

The main difference between dc sputtering and rf sputtering lies in the type of power supply, with the latter running on alternating current [2, 4].

Two relevant phenomena occur in an rf sputtering process:

1. Electrons that oscillate in the discharge region acquire enough energy to create ionising collisions, reducing not only the dependence of discharge on secondary electrons but also its dependence on V_B.

2. Electrodes no longer need to be electrical conductors as rf voltages can be coupled through any impedance.

In principle, it is possible to deposit any kind of material by rf sputtering, even high-resistivity and dielectric materials.

Like dc sputtering, the voltage is developed almost entirely in the dark region close to the two electrodes because the plasma region, which is conductive, is equipotential. The typical frequency of an rf sputtering system is between 5 and 30 MHz, thus most of ions are sufficiently slow to be considered almost unmoving. For this reason, the ion bombardment of the electrodes would be negligible. When one electrode is coupled to the rf power supply through a capacitor connected in series, a negative pulsed potential develops on it. During each rf half-period an inversion of polarisation at the electrodes takes place. This implies that during each half-period one electrode acts as a cathode and it is bombarded by the ions, and the other electrode acts as an anode and it is bombarded by the electrons. Therefore, the average current is zero. If the frequency is sufficiently high, the ions, which are less mobile than the electrons, cannot flow through the plasma region to the electrode as the electrons do. This generates a high electron current that flows to the electrode. The I-V characteristic of a glow discharge is similar to a leaky rectifier (Figure 3.7).

Since the electrode mechanisms are regularly exchanged, it should be evident that the two electrodes come to have a symmetrical role in this system. If so, how can deposition occur? How can the sputtering action be achieved on just a single one of the two electrodes?
To answer this question, we can represent the sputtering system as a circuit formed by two flat, parallel plate capacitors (electrode and plasma) separated by the dark region. By considering A_1 and A_2 the areas and V_1 and V_2 the voltages related to each electrode, respectively. We can write the following equation:

$$\frac{V_1}{V_2} = \left(\frac{A_1}{A_2}\right)^4 \tag{3.2}$$

From this equation, it is evident that it is possible to obtain an asymmetric system, by only acting on the areas of the two electrodes. The target corresponds to the smaller surface electrode and then all

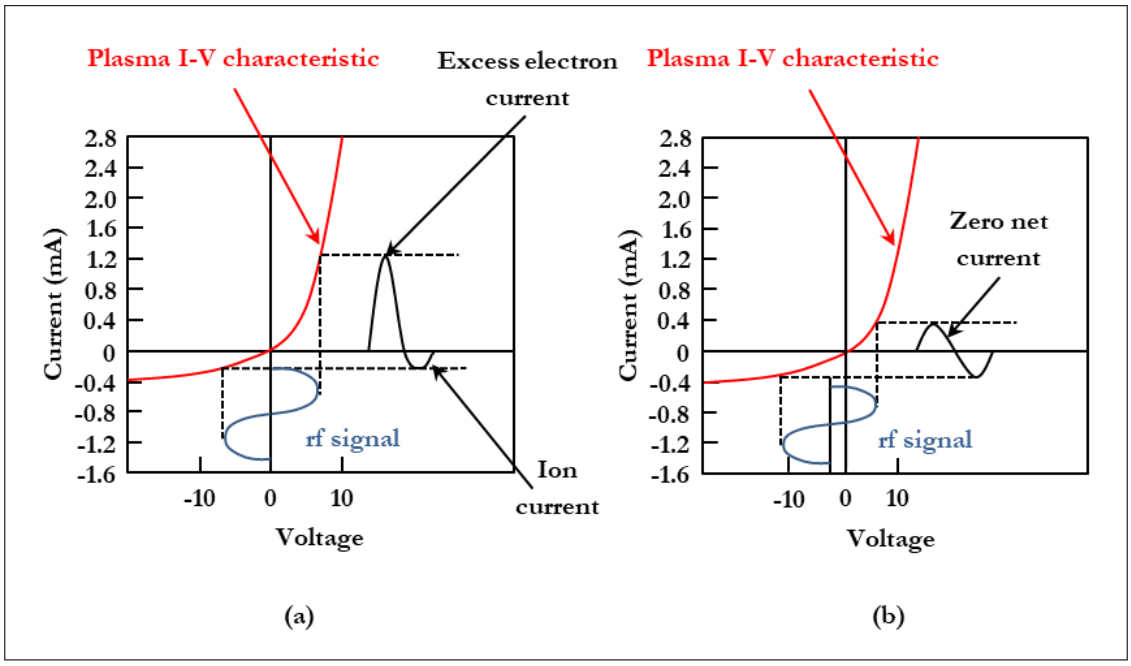

Figure 3.7: I-V characteristics of a glow discharge in the case of: (a) electrodes directly connected to the power supply unit and (b) electrodes decoupled with a capacitor. Reprinted from [2].

the high voltage drops on it. The substrate holder, often electrically connected with all the vacuum chamber, corresponds to the large area electrode and then a small voltage is applied.
In this situation, a constant voltage (of a few kV) appears between the two electrodes, which have to be decoupled from the rf power supply by using a series capacitor in the external circuit between the cathode and the rf generator. Figure 3.8 shows the voltage distribution in case of a real rf sputtering system.

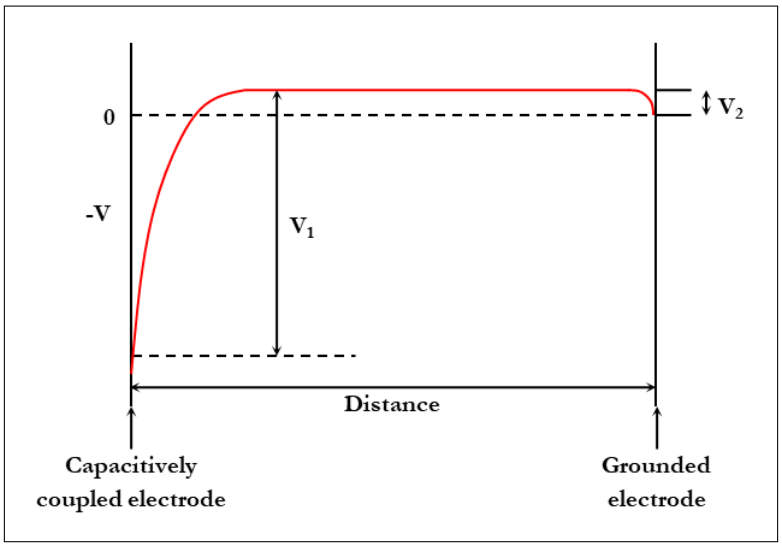

Figure 3.8: Voltage distribution in an rf glow discharge of a real rf sputtering system, adapted from [2].

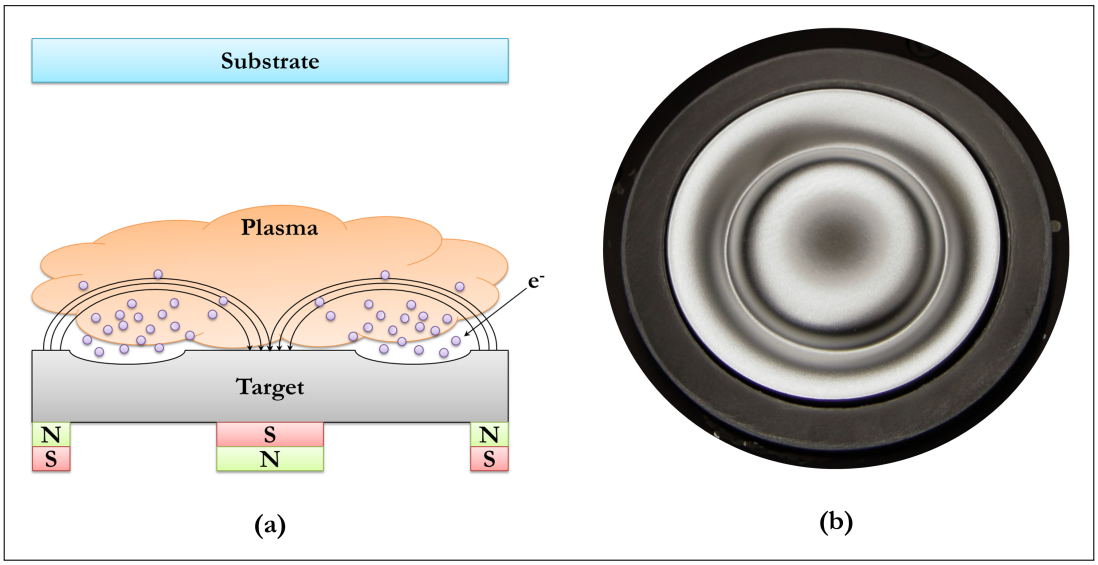

Figure 3.9: (a) Schematic illustration of the electron confinement in the case of magnetron sputtering. (b) An example of non-uniform erosion occurring on target surface.

3.2.3 Magnetron sputtering

The basic dc or rf sputtering processes are successfully employed to deposit a wide variety of materials [7, 8]. However, these processes were found to have the following significant limits:

1. Low deposition rates.
2. Low efficiency of ionisation from the collisions between electrons and gas atoms.
3. Uncontrolled heating of the substrate.

It is possible to overcome these limitations using dc or rf magnetron sputtering.

In a sputtering system, magnets can be used to create a magnetic field close to the target and parallel to its surface. The basic arrangement of the magnets is with one pole positioned on the central axis of the target and the second pole formed by a magnet ring around the outer edge of the target (as shown in Figure 3.9a).
It should be underlined that the presence of the magnetic field causes the confinement of the electron motion near the target surface and therefore increases the collision/ionisation probability. In this way, plasma density increases near the target region and this results in several advantages, which are:

- Increased ion bombardment of the target surface.
- Higher sputtering yield.
- Higher deposition rate.
- The possibility of maintaining the discharge with a lower operating pressure and a lower operating voltage.
- Decreased substrate and target heating.

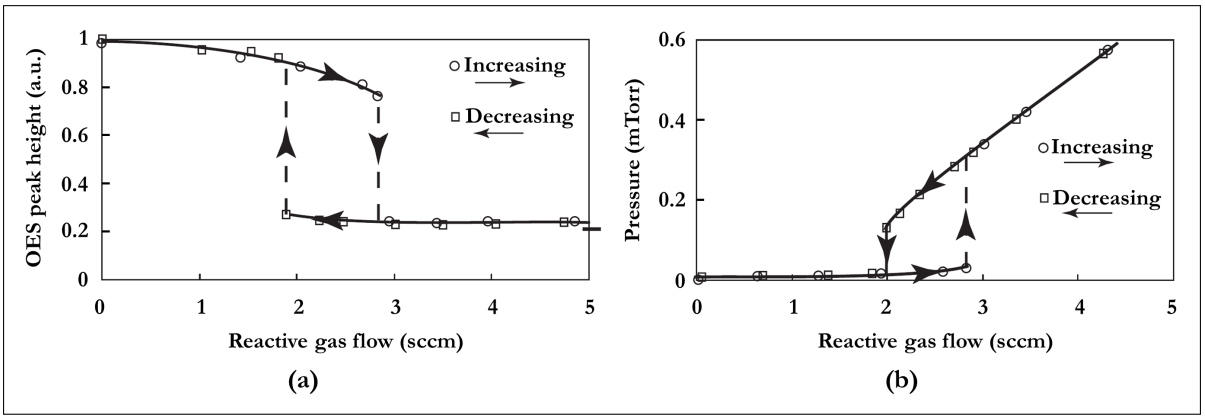

Figure 3.10: In a reactive sputtering process: (a) typical optical emission (OES) from sputtered metal atoms - i.e. the sputter erosion rate - versus reactive gas flow (expressed in standard cubic centimeters per minute (sccm)); (b) partial pressure of the reactive gas from curve (a). These curves are adapted from [9].

However, the plasma density is higher in the target regions where the magnetic field is strongest and this leads to a non-uniform erosion of the target surface (Figure 3.9b). The obvious disadvantage is a poor and inefficient target usage. At industrial level, this problem can be easily overcome by using rotating targets or magnets.

For all these reason, magnetron sputtering is currently the most common deposition technique for large-area coatings.

3.2.4 Reactive sputtering

Reactive sputtering is a widely used coating technique for depositing oxides, nitrides, carbides, silicides and borides in numerous industrial applications [1, 9]. It enables deposition of a wide variety of compounds by simply adding a gas to the working gas, which reacts with the target material during the sputtering process.

Unfortunately, this reaction mechanism suffers from a few drawbacks that cause some stability problems. In general, it is quite difficult to combine the high deposition rate of this technique with the desired film stoichiometry. The main reason for this is that compound formation takes place not only inside the deposited film but also at the target surface. This collateral phenomenon is known as target poisoning. Also obviously, the Y_{sp} value for a compound material is considerably lower than the Y_{sp} of the elemental target material:

$$Y_{sp}[Compound] \ll Y_{sp}[Elemental\,material] \tag{3.3}$$

and as a result the deposition rate is inversely proportional to the partial pressure of the reactive gas.

Film composition and deposition rate stand both in a non-linear and quite complex relationship with reactive gas flow. If we set the current density to a constant value during a reactive sputtering process, the typical experimental plot for the sputter erosion rate versus reactive gas flow is represented in Figure 3.10a. This curve delineates a hysteresis behaviour, i.e. deposition rate follows two different paths upon cycling demonstrating a strong correlation with reactive gas supply. The width of the hysteresis region is defined as the separation between the decrease and the increase path. The partial

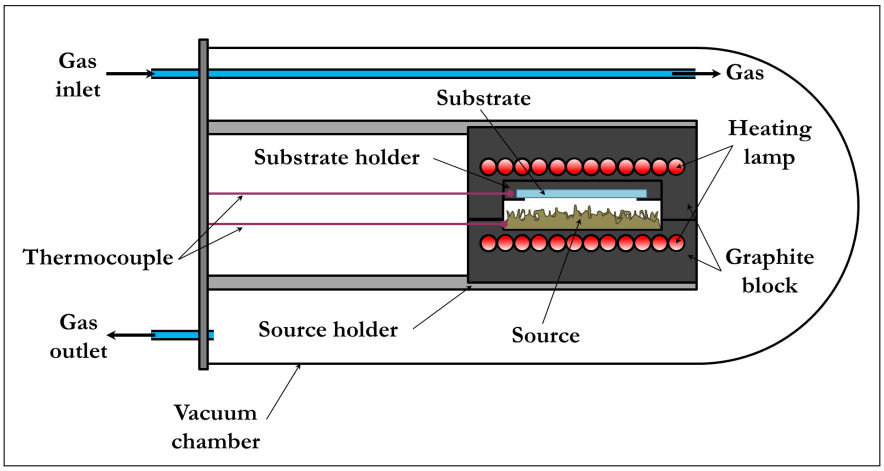

Figure 3.11: Basic chart of a CSS system.

pressure versus reactive gas flow plot also describes a hysteresis behaviour (Figure 3.10b).

Knowledge of this hysteresis effect is of crucial importance in order to control a reactive sputtering process. It should be underlined that this control can be achieved in various ways, such as:

- Feedback control of the reactive gas flow by system parameter monitoring (typically, voltage or pressure).
- Increasing the pumping speed to drive a large part of the reactive gas away rather than into the deposited films.

3.3 Close-spaced sublimation

The close-spaced sublimation (CSS) technique is one of the simplest approaches to physical vapour deposition [6]. This technique has the merit of combining high deposition rates with easy scalability to industrial level, making it particularly attractive for the deposition of CdTe thin films. At ThiFiLab, we recognised the value of CSS and decided to make it our technique for CdTe deposition.

CSS technology exploits the physical principle of sublimation, namely the direct phase transition between a solid and a gaseous state. This process mainly depends on the following three phenomena:

1. A first sublimation process at the source surface.
2. Transport of material in gaseous form from the source to the substrate surface.
3. A second sublimation process at the substrate surface could take place.

An important requirement is the need to minimise the presence of extrinsic impurities in the CSS chamber, which could become incorporated into the deposited film.

Figure 3.11 shows a schematic representation of the CSS apparatus. The substrate is placed at a distance of few millimeters (hence the term 'close-spaced') from the source. Both substrate and source are positioned on suitable holders and they are enclosed in a vacuum chamber with a gas inlet and a gas outlet tube. In this way, the gas atmosphere inside the CSS chamber can be continuously monitored. Furthermore, the required temperature is reached by means of infrared radiation and it is controlled

with two thermocouples placed inside the sample and target holders. In a CSS deposition process, the main parameters to be monitored are:

- Substrate temperature.
- Source temperature.
- Composition of the chamber atmosphere.
- Pressure in the reaction chamber.
- Composition of the source material.

These parameters are intercorrelated and they all affect the deposition rate.
At a fixed source temperature, the sublimation rate is inversely proportional to the chamber pressure. At low chamber pressure (about 100 Pa), the mean free path of the atoms that come into the vapour phase from the target is extended, and the condensation process on the substrate surface is no longer limited by the source-substrate distance.
The composition of the process gas also influences the deposition rate. The parameter that has to be considered is the thermal conductivity of the process gas (in our case, Ar). For example, at a fixed source-substrate distance, a high-thermal conductivity process gas tends to increase the substrate temperature. As a consequence, there is a reduction in the deposition rate of the film.

In Chapter 4, we will examine the CdTe deposition conditions under which a controlled absorber layer suitable for high-efficiency thin-film solar cells is produced.

3.4 Electron beam evaporation technique

Electron beam (e-beam) evaporation is a PVD technique that allows to evaporate materials that are difficult to process using standard thermal evaporation. In particular, it is possible to deposit high-evaporation temperature materials (e.g. molybdenum) or ceramics (e.g. silicon dioxide and alumina).

Figure 3.12 shows a schematic representation of the electron beam evaporation apparatus. Obviously, the core of this equipment is represented by an electron gun that is used for the evaporation process. The electron beam is generated by applying an electric current to a tungsten filament enveloped in a high electric field. Thanks to this electric field, the electrons close to the filament surface gain enough energy to escape the material (thermo-ionic effect). The emitted electrons are then accelerated by a potential of (5 ÷ 10) kV away from the filament and focused by magnets into a beam. This beam is directed towards a crucible, which contains the source material. The kinetic energy of the electron beam is transferred to the material as heat and it can therefore begin to evaporate. The material vapours then travel out of the crucible and coat the substrate.

Since the temperatures of this process are very high (up to 2000 K), a proper cooling system is required. Furthermore, a crucible made of high-melting point materials, such as alumina, Mo, W and graphite is needed. Another important condition is to maintain a high vacuum level in the deposition chamber, which promotes the selective deposition of the evaporated atoms only, avoiding any impurities.

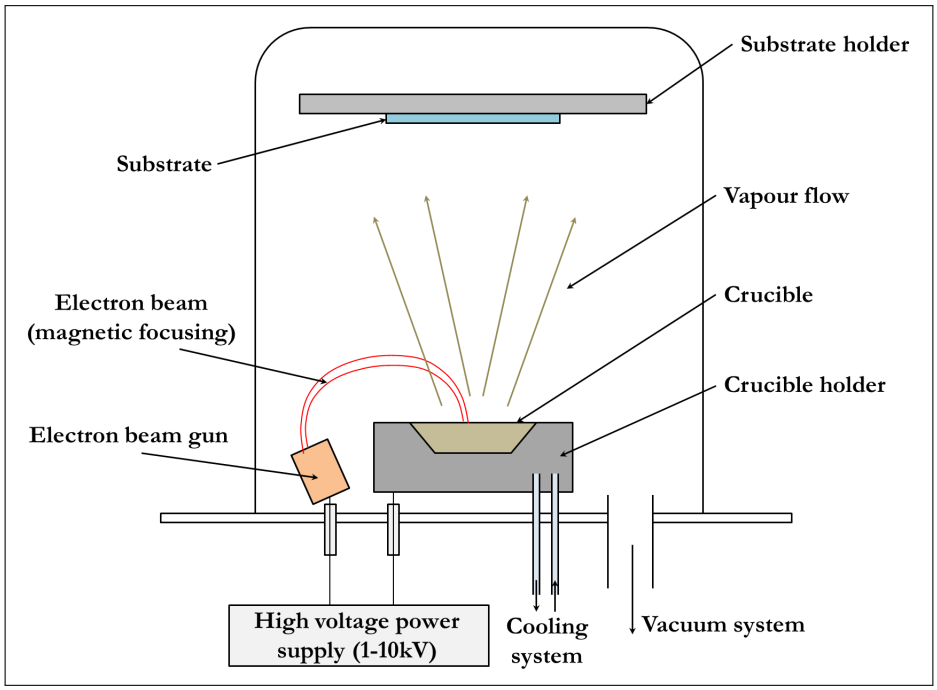

Figure 3.12: Basic chart of an electron beam evaporation system.

The main advantage of this technique is the high deposition rate (as high as 20 μm s^{-1}) and it can also be easily scaled up to an industrial level. The evaporation rate increases exponentially with the source material temperature, making it a crucial parameter to control. During the deposition process, the main physical parameters that have to be monitored are:

- Source material temperature, measurable using a thermocouples.
- Thickness of the deposited film, which can be controlled via a quartz crystal microbalance.
- Current flowing in the electron beam.

It should be highlighted that the evaporation is truly effective only in the highly localised point where the beam hits the evaporating material surface and this allows for a more efficient evaporation compared to heating the whole crucible. On the other hand, the main limitations of this technique are the technical difficulty of achieving well-proportioned alloy compound deposition, and the risk of filament contamination and subsequent reduced lifetime.

3.5 Characterisation

In this section, I will briefly review the different characterisation methods that were used throughout my PhD project. These can be divided into the following two groups based on their scope: analysis of single layers and characterisation of solar cell devices.

3.5.1 Characterisation of single layers

The characterisation of each material layer used in our thin-film solar cells is of great importance for the optimisation of the final device. The thickness, as well as the optical, electrical, morphological

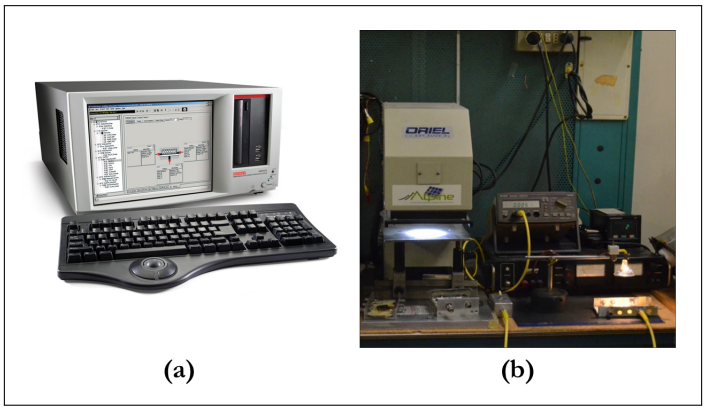

Figure 3.13: (a) The Keithley 4200-SCS instrument. (b) Our Oriel solar simulator.

and structural properties of the films are of course essential for this study. However, it is quite difficult to extract all these data from a finished device, because of the complex layer structure of the solar cells. A useful approach is to deposit and to characterise each single layer separately. This approach has a basic drawback. The properties of thin films depend on both their thickness and the type of substrate on which they are deposited. Because of this, data analysis becomes a sensitive task and experimental values must be interpreted carefully.

During this PhD research, surface investigations were made by using a Tescan scanning electron microscope (SEM) equipped with an Oxford Instruments energy dispersive X-ray (EDX) spectroscopy system to measure the sample composition. In particular, EDS was carried out using an accelerating voltage of 20 kV.
Cross-sectional STEM analysis was performed by using a 300 keV Philips CM 300 transmission electron microscope which is equipped with an Oxford Instruments energy dispersive X-ray system to measure the concentration profiles of the atomic species existing in the sample.
In order to determine the crystalline properties of our films, we used a powder diffractometer operating with $CuK_{\alpha 1}$ (λ = 1.5418 Å) in the theta-2theta configuration.
Finally, the in-depth profile analysis was obtained with secondary ion mass spectroscopy (SIMS).

3.5.2 Device characterisation

The main tool for characterising the electronic properties of a solar cell is the current density-voltage characteristic. The J-V characteristic can be determined both under illumination and in the dark. From the J-V curve under illumination, the solar cell parameters (V_{OC}, J_{SC}, FF and η) can be determined directly. While the dark characteristics is an easy way to assess the quality of a *p-n* junction and to evaluate contact resistances.

Our system for the acquisition of J-V characteristics consists of a continuous Oriel solar simulator, equipped with an A.M. 1.5 filter and with 1 kW/m^2 lighting power density supplied by a 600 W Xe-HgXe lamp. A GaAs/AlGaAs solar cell was used as a reference cell and all the measurements were made at the standard temperature of 298 K. Finally, the J_{SC} values (uncorrected for spectral mismatch) were measured over a calibrated shunt resistance supplied by a Keithley 4200-SCS instrument. Figure 3.13 shows our system for the acquisition of the J-V curves.

References

[1] K. Seshan. *Handbook of thin-film deposition processes and techniques. Principles, methods, equipment and applications.* Noyes Publications - William Andrew Publishing. 2002.

[2] J.L. Vossen and W. Kern. *Thin film processes.* Academic Press, INC. 1978. ISBN: 0-12-728250-5.

[3] A. Bosio, D. Menossi and G. Rosa. *Il fotovoltaico di seconda generazione diventa competitivo.* Aracne Editrice. 2015.

[4] L.I. Maissel and R. Glang. *Handbook of thin film technology.* McGraw-Hill Book Company. 1970. ISBN: 0-07-039742-2.

[5] R. Tirumala. *A mathematical model for the departure from paschen's law at micro meter gaps using ion enhanced field emission.* Ionization and Ion Transport Final Project Paper. 2010.

[6] Wikipedia. (Accessed September 07, 2017). `https://en.wikipedia.org/wiki/Paschen%27s_law#cite_note-Lieberman2005-1`

[7] S. Swann. *Magnetron sputtering.* Physics in technology. IOP Publishing. 1998, Volume 19, Number 2, Page: 67.

[8] P.J. Kelly and R.D. Arnell. *Magnetron sputtering: a review of recent developments and applications.* Vacuum. Elsevier. 2000, Volume 56, Number 3, Pages: 159-172.

[9] S. Berg and T. Nyberg. *Fundamental understanding and modeling of reactive sputtering processes.* Thin solid films. Elsevier. 2005, Volume 476, Number 2, Pages: 215-230.

[10] N. Amin and K.S. Rahman. *Close-spaced sublimation (CSS): A low-cost, high-yield deposition system for cadmium telluride (CdTe) thin film solar cells.* Book: Modern Technologies for Creating the Thin-film Systems and Coatings. Chapter 18. InTech. 2017.

Chapter

4

Improvements in CdTe solar cells

In this chapter, a description of the structure of the CdTe-based solar cells we fabricated using CSS and sputtering at ThiFiLab will be given.
Then I will focus on the two main critical issues of our device: grain boundary passivation and back-contact ohmicity. I will report the main experimental results achieved during my PhD research project, which was aimed at improving both these aspects.

4.1 Experimental details of CdTe-based solar cells structure

The CdS/CdTe solar cell fabricated at ThiFiLab consists of the sequence of layers illustrated in Figure 4.1. As shown, our device is made in superstrate configuration and each layer has a well-defined function. First of all there is the substrate, which is the rigid support; then there is the front contact and the junction formed by the window layer and the absorber material; finally, the back contact. In the next paragraphs, we will examine the different layers that form our solar device and how it is manufactured.

4.1.1 Substrate

The substrate represents the base on which all the solar cell layers are deposited. Therefore, it is extremely important to identify the requirements that the substrate have to meet in order to be suitable for CdS/CdTe solar cells in superstrate configuration. They can be summarised as:

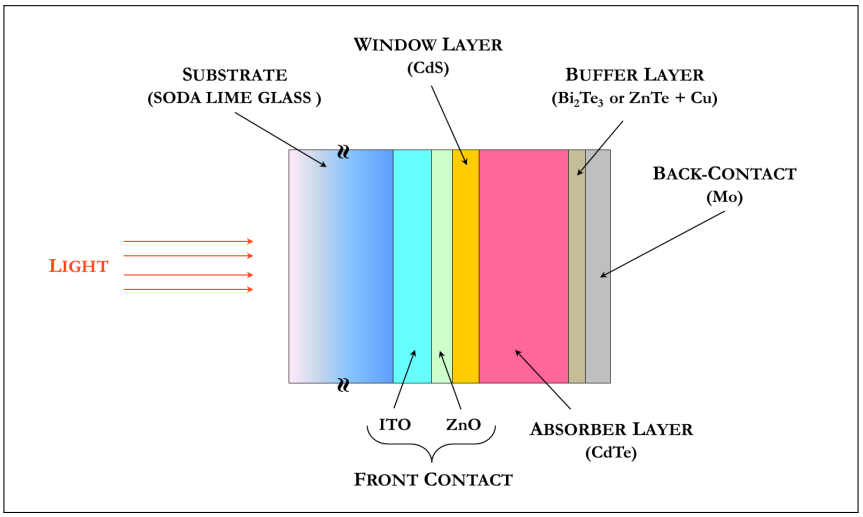

Figure 4.1: Structure of the CdS/CdTe solar cell fabricated at ThiFiLab in superstrate configuration.

1. TRANSPARENCY
   Since in superstrate configuration the sun light has to pass through the substrate, a major requirement is the high transparency in the visible region of the solar spectrum.

2. CHEMICAL STABILITY
   The substrate has to avoid both undesirable reactions with the deposited material and the contamination by diffusion of impurities into the device layers during the deposition steps.

3. MECHANICAL ROBUSTNESS
   The substrate has to withstand all the manufacturing process phases and support the device that is only made of thin films without structural rigidity.

4. LOW LATTICE MISMATCH BETWEEN SUBSTRATE AND DEPOSITED THIN FILM
   This difference should be less than 1% in order to ensure a good film adhesion and a limited concentration of structural defects.

5. LOW COST
   The substrate cost affects the final cost of the device, thus it is necessary to minimize it.

Usually, soda-lime glass (SLG) or borosilicate glass are used as substrates for thin-film CdTe solar cells, because they meet the above-mentioned requirements.

We use SLG in our standard process as it has many advantages including the high softening point (about 840 K), which is lower than the deposition temperatures of the films, and a high transparency in the visible region of the spectrum of electromagnetic radiation (as shown in Figure 4.2). The main physical and chemical properties of SLG are listed in Table 4.1.

It should be highlighted that sodium can diffuse from the soda-lime glass to the absorber layer at process temperatures and this can affect the solar cell performance. To overcome this problem, a ZnO layer can be used against impurities diffusion [2].

Finally, in order to use SLG as a substrate for thin-film solar cells, it has to be cleaned with a well-defined process. Our standard cleaning process is summarised in Appendix B - Cleaning of substrate surface.

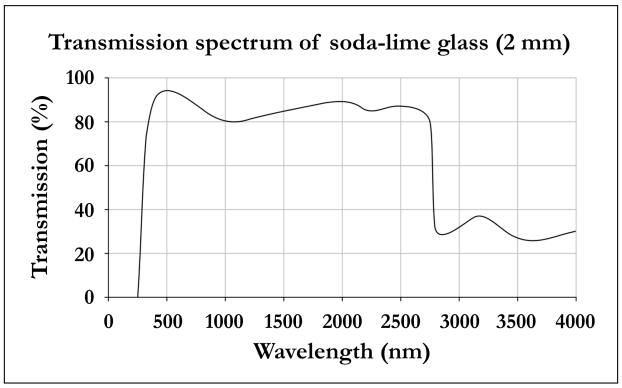

Figure 4.2: Typical transmission spectrum of soda-lime glass, adapted from [1].

Table 4.1: Main physical and chemical properties of soda-lime glass. Data from [1].

Composition	SiO_2 73%, Na_2O 14%, CaO 9%, MgO 3.70%, Fe_2O_3 0.1%, Al_2O_3 0.15%, K_2O 0.03%, TiO_2 0.02%.
Density at 293.15 K	2.53 g/cm^3
Thermal conductivity	0.937 W/(m $\times$ K)
Specific heat	0.88 kJ/(kg $\times$ K)
Softening point	840.15 K
Index of refraction (@ 380-780 nm)	1.5

4.1.2 Front contact

The first layer to be deposited in superstrate CdTe solar cells is the front electrical contact, namely transparent conducting oxide (TCO). Currently, the main TCO thin films are represented by In_2O_3:Sn (ITO), SnO_2:F (FTO) and ZnO:Al (AZO), and they can be deposited with several techniques, such as sputtering, CVD or spray deposition [3, 4]. The predominant properties of these materials are:

1. High transparency in the visible part of the light spectrum (more than 90%).

2. High reflectivity for infrared light.

3. High *n*-type conductivity.

Furthermore, TCO materials are usually nearly degenerate semiconductors with a free carrier concentration in the range of ($10^{18} \div 10^{20}$) cm^{-3}. Finally, for PV applications, TCO thin films need to exhibit also chemical and physical stability.

ITO is the TCO material that was used during this PhD work. ITO thin films are deposited by rf reactive magnetron sputtering starting from a high-density In_2O_3 90% - SnO_2 10% sputtering target and this target is prepared by hot-pressing technique. The deposition is made in an argon plus oxygen atmosphere, typically 20 sccm of Ar + 0.5 sccm of O_2 (chamber pressure around 1 Pa), at a substrate

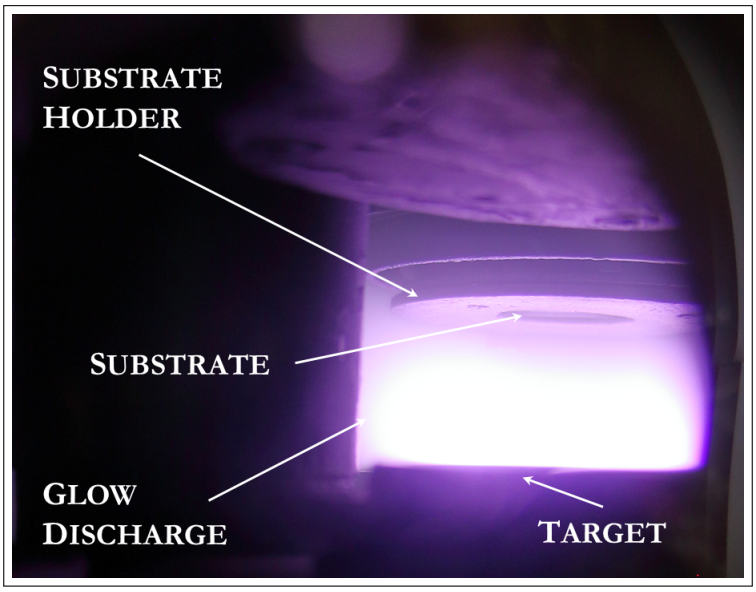

Figure 4.3: Photograph of the glow discharge into the rf reactive magnetron sputtering chamber during the deposition of a ZnO thin film.

temperature of 670 K with a deposition rate of about 6 Å/s. We deposited an ITO thin film with a thickness of 500 nm, exhibiting a sheet resistance of 1 Ω square.

Since we use soda-lime glass as a substrate, sodium diffuses, during thermal treatments, into the layers which constitute the solar cell. To avoid this problem, on top of the ITO layer we deposit 150 nm of ZnO[1] by rf reactive magnetron sputtering (Figure 4.3). The sputtering parameters are the same of ITO deposition. The only variation is represented by the oxygen partial pressure, that is of 30 sccm. Under these sputtering conditions, the ZnO thin film grows with a compact polycrystalline structure and it shows a sheet resistance of 10 Ω square. This ZnO layer is essential for stopping the sodium diffusion, but it acts also as buffer layer for indium and tin contained into the ITO layer, which can diffuse to the junction region. In particular, the deposition of the ZnO layer limits this diffusion process by avoiding the segregation of indium and tin atoms in the grain boundaries of the active materials, and thus, it prevents the formation of shunt paths in the cell.

Furthermore, ZnO and CdS are both II-VI compounds and they grow with the hexagonal wurtzite crystal structure. Their lattice mismatch is very small and at process temperatures, they form a mixed compound which minimises lattice mismatch at the interface.

4.1.3 Window layer

After the deposition of the front contact, it is necessary to deposit the CdS thin film, also known as window layer of the CdTe-based solar cell. CdS is a *n*-type semiconductor with an energy band gap of 2.42 eV hence it is transparent in the visible part of the solar light spectrum. Solar light can therefore pass through the CdS layer and penetrate into the *p*-type CdTe layer, giving rise to the PV effect.

Since the interaction between *n*-type CdS and the *p*-type CdTe is a key aspect in order to form an efficient *p*-*n* junction (as we will shown in the following section 4.1.4), the deposition technique used

[1]The **ZnO** is a II-VI semiconductor with a direct energy band gap of 3.3 eV. It exhibits a transparency in the visible and NIR part of the light spectrum and it grows with hexagonal wurtzite crystal structure.

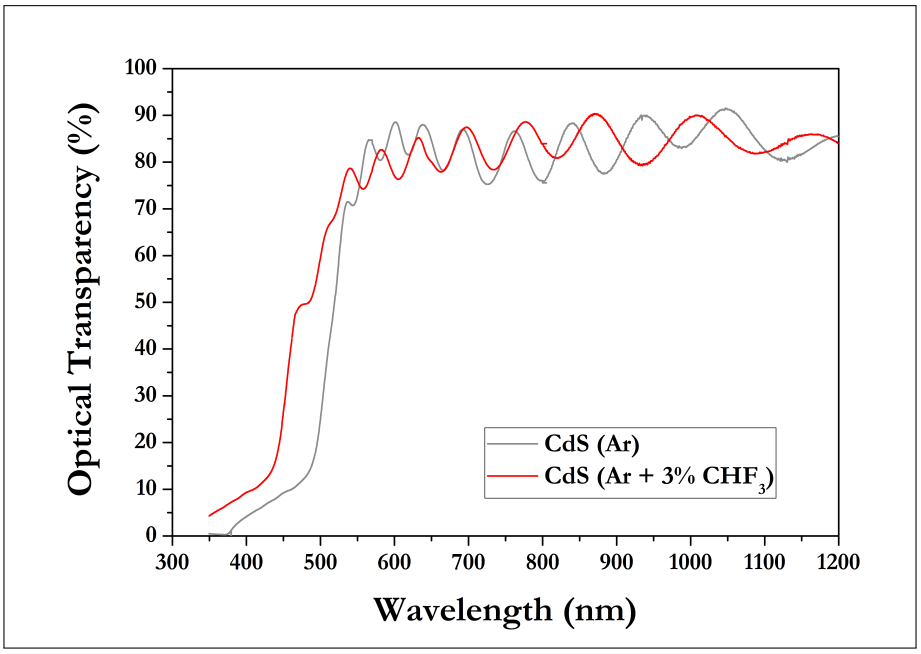

Figure 4.4: Comparison between transmission spectrum of 80 nm-thick CdS thin film deposited by sputtering in pure Ar (grey line), in Ar + 3% CHF_3 (red line). Adapted from [4].

to produce these layers becomes crucial. Currently, the most suitable techniques for the deposition of a CdS layer are: rf sputtering, CSS and CBD.

CdS layers are deposited by rf reactive magnetron sputtering starting from a CdS vacuum cold-pressed target with a purity of 99.995%. The deposition is made by introducing in the sputtering chamber argon containing 3% fluoroform (CHF_3), at a substrate temperature of about 490 K, with a deposition rate up to 10 Å/s. The typical thickness of our CdS layer is about 100 nm.

The presence of CHF_3 during the deposition is of primary importance, since CHF_3 is decomposed and fluorine, being strongly electronegative is easily ionised in the sputtering discharge setting free F^- ions. These ions are forced to hit the substrate surface (positive electrode for the most part of the rf period) and to bombard the growing film. This phenomenon is also known as back sputtering. In this case, it is useful to remove the stoichiometry defects of Cd and S atoms weakly bonded, which typically behave as light absorbing centres.
CdS films deposited using Ar + 3% CHF_3 show a higher optical transparency and a wider energy band gap than the films deposited using Ar alone (as shown in Figure 4.4). The most likely reason for this improvement is to be in the best crystalline quality and smoothness of the CdS films, that present a smaller concentration of light absorbing centers and then less defects.
It should be highlighted that there are no changes in the resistivity of CdS films with the presence of fluorine into the sputtering chamber. Furthermore, it is possible that fluorine forms with Cd atoms the CdF_2 compound during the deposition. CdF_2 is an insulating material, that segregate into the grain boundaries of the CdS polycrystalline film and passivate them. Unfortunately, it is very complex to measure the presence of CdF_2, because of its small amount and its amorphous nature.

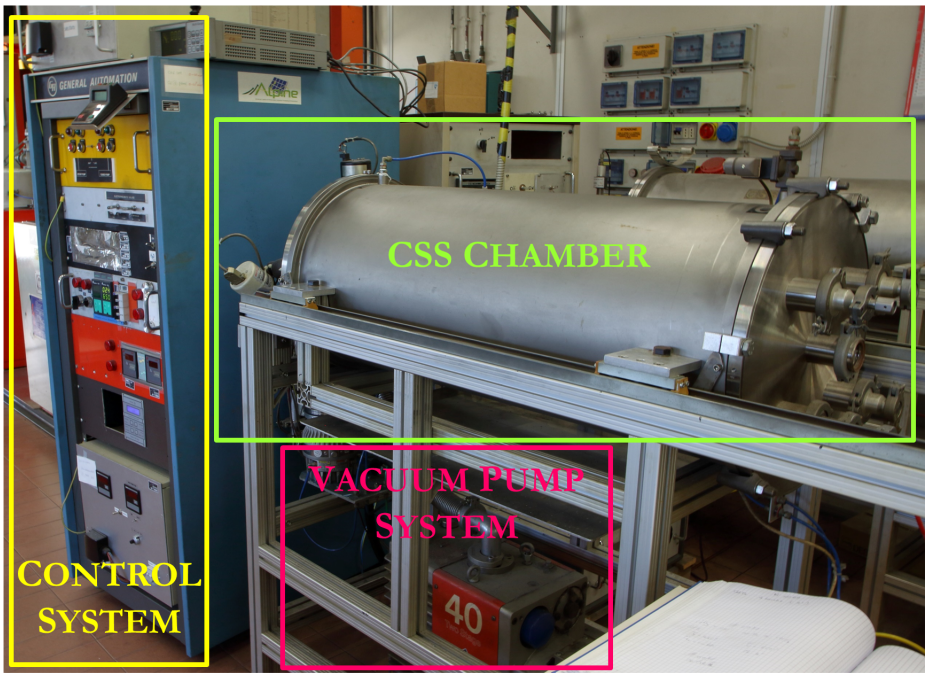

Figure 4.5: Photo of the CSS system used to deposit CdTe layers at ThiFiLab.

4.1.4 Absorber layer

The absorber layer in CdTe-based solar cells is obviously a thin layer of cadmium telluride. CdTe is a II-IV semiconductor that crystallises in the zincblende structure (space group $F\bar{4}3m$ $-T_d{}^2$) [5]. CdTe is a direct energy band gap semiconductor with an energy band gap of about 1.49 eV, which is very close to the S-Q limit. It also has a large optical absorption coefficient on the order of 10^4 cm^{-1}. For this reason, it is a suitable material for thin-film PV applications as an absorber layer [3, 4, 6].

Furthermore, it can be easly doped both *p*-type (for example with: Cu, Ag or group I and V elements) and *n*-type (for example with: B, Al, In and Ga) in the case of single crystal samples. Unfortunately, the doping creates a serious problem in case of polycrystalline thin film. Indeed, the dopant atoms can segregate into the grain boundaries and this effect results in highly electrical conductive phases that can limit the performances of solar cells.

To overcome this problem, it is preferable to grow self-doped CdTe thin film by either cadmium or tellurium vacancies. In particular, Cd vacancies induce a *p*-type behaviour and on the contrary, Te vacancies induce a *n*-type behaviour. As CdTe plays the role of absorber layer, it needs to grow *p*-type (i.e. with cadmium vacancies). This growth is favoured by high temperature ($\geq$ 770 K). Currently, several deposition techniques are used to produce CdTe thin films, such as: CVD, MOCVD, electrodeposition, chemical spray pyrolysis and CSS. Each of these methods can provide a final good quality crystalline thin film but, in order to obtain a low-cost fully automated in-line production process, the most advantageous technique is CSS.

At ThiFiLab, we deposit CdTe by CSS with the following process. The first step in our CSS chamber (Figure 4.5 and 4.6) is to progressively heat up crucible and substrate holders to a temperature of 600 K and 605 K, respectively. Once these temperatures have been reached, the crucible and substrate holders are further heated to a temperature of 905 K and 700 K, respectively. Before this last step, argon (inert

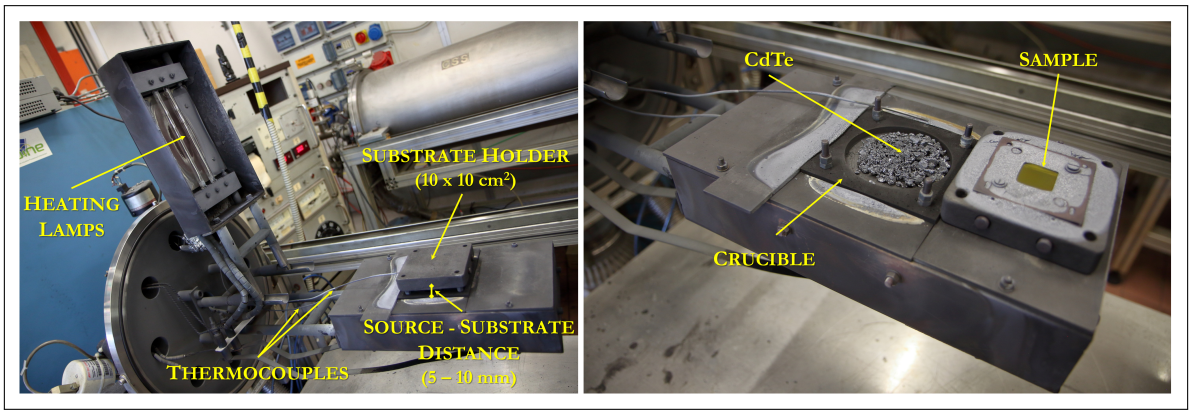

Figure 4.6: Inside of ThiFiLab CSS chamber. It is possible to see the heating lamps, the thermocouples, the substrate holder and the source.

gas) is introduced into the process chamber with a pressure that varies during the process between 100 Pa and 5000 Pa. The role of Ar is to control the sublimation process of CdTe and consequently uniform deposition conditions are strictly required for thermal and structural homogeneity.

It should be highlighted that the deposition by CSS is possible because CdTe dissociates into its two components cadmium (atomic form) and tellurium (molecular form):

$$2\,\mathrm{CdTe}\,(\mathrm{s}) \;\rightleftarrows\; 2\,\mathrm{Cd}\,(\mathrm{g}) \;+\; \mathrm{Te_2}\,(\mathrm{g}) \tag{4.1}$$

They can recombine on the substrate to form the CdTe film.

CdS and CdTe have a high lattice mismatch (9.7%), and then there is a high density of defects at the interface between these two layers that can reduce the solar cells performance [7]. To overcome this problem, it is necessary to create between the two active materials a mixed compound such as CdS_xTe_{1-x}, making it possible to gradually change the lattice mismatch and consequently reducing the number of defects at the interface. For this reason, after the deposition of the CdTe layer an annealing treatment in presence of chlorine is necessary.

4.1.5 Chlorine treatment

The annealing treatment of CdTe films in presence of chlorine is considered a crucial step to produce high-efficiency solar cells, regardless of the technique used for the deposition [8, 9, 10, 11, 12, 13]. Indeed, this treatment is involved in many different aspects, such as the increase of CdTe-film grain size (by re-crystallisation effect), the improvement of the quality of grain boundaries and the enhancement of the intermixing between CdS and CdTe layers at their interface. Furthermore, it also improves the *p*-type doping.

Typically, $CdCl_2$, $MgCl_2$, NaCl, and NH_4Cl salts are used as chlorine suppliers. They are deposited in form of thin film on top of the CdTe layer. These salts can be deposited either by CVD or by drop-casting.

As an example, the classic cadmium dichloride ($CdCl_2$) treatment consists in depositing about 300 nm of the salt on top of the CdTe layer with a subsequent annealing at about 670 K in air or in an inert gas atmosphere. At the temperature process, chlorine diffuses into the grain boundaries and this promotes

the re-crystallisation of CdTe grains with a better-organized CdTe matrix. The more probable reaction on the surface of CdTe films is:

$$\mathrm{CdTe\ (s)\ +\ CdCl_2\ (s)\ \Rightarrow\ Cd\ (g)\ +\ Te\ (g)\ +\ Cl_2\ (g)\ \Rightarrow\ CdTe\ (s)\ +\ CdCl_2\ (s)} \tag{4.2}$$

It is then necessary an acid etching by using a mixture of HNO_3 and HPO_3 or a cleaning in a solution of Br-methanol to remove some oxides, that are formed on the CdTe surface during the annealing.

It should be highlighted that this process shows some disadvantages when it is applied at industrial level and the main critical can be summarised as:

1. $CdCl_2$ has a low evaporation temperature of about 770 K in air. Therefore, it cannot be stored in large quantities as it can release cadmium in the environment in case of fire.

2. $CdCl_2$ is soluble in water and consequently it is required security measures to preserve environmental pollution and health damage.

3. The use of acid etching or Br-Methanol solution implies high security measures to preserve the workers safety and it also implies the problem of their disposal after the treatment.

Consequently, the use of Cd-free salts is preferable, as they have the remarkable advantage to be much more environmentally sustainable than $CdCl_2$.

Possible substitutes can be some halogen carrier gases that can release chlorine or chlorine radicals at the treatment temperature. For example, one can choose the chlorine-based freon family or the chlorine family itself (such as: HCl, Cl_2). In the second case, the more likely reaction on the surface of CdTe films becomes:

$$\mathrm{CdTe\ (s)\ +\ 2\,Cl_2\ (g)\ \Rightarrow\ CdCl_2\ (g)\ +\ TeCl_2\ (g)\ \Rightarrow\ CdTe\ (s)\ +\ 2\,Cl_2\ (g)} \tag{4.3}$$

Unfortunately, these gases are very aggressive and their use can be extremely critical [14].

For these reasons, we have chosen an alternative method that consists in the use of fluorinated hydrocarbons added to chlorine as process gas. The role of fluorine insertion is just to stabilise the reaction between CdTe and chlorine. Indeed, F_2 or F-based species can react with CdTe forming a fluorine compound (such as CdF_2) and some of these compounds are stable materials at the process temperature. On the contrary, they could present a metastable behaviour in presence of chlorine. Then, CdF_2 can promote the growth rate reduction of the chlorine-containing counterparts ($CdCl_2$), decreasing the chlorine aggressiveness. In particular, this is made possible by the use of a control system of the chlorine/fluorine ratio.

Prior to 2010, the method used at ThiFiLab consisted in treating the CdTe film at a temperature around 670 K in an atmosphere composed of $(2 \div 4) \times 10^3$ Pa of chlorodifluoromethane (CHF_2Cl, also known as R-22) and $(3 \div 5) \times 10^4$ Pa of argon. R-22 gas is stable and inert at room temperature and it does not have any toxic action. With this method, it was possible to eliminate the necessity of any chemical etching by substituting it with a vacuum annealing.

The obtained result using this type of treatment is very similar to those obtained using $CdCl_2$. Figure 4.7 shows clearly that the CdTe morphology before and after this treatment changes; it enlarges the grain size and eliminates the small grains. In particular, before the treatment, the grains have non

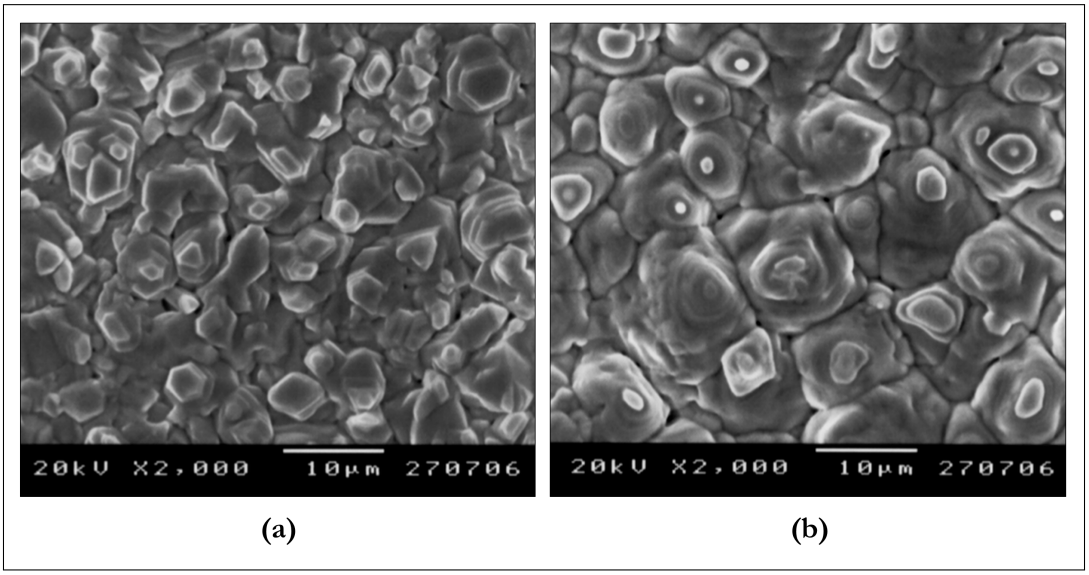

Figure 4.7: Comparison between SEM images of CdTe film morphology before (a) and after (b) the chlorine treatment with Ar + R-22, respectively. Adapted from [15]

homogeneous dimensions and they present a hexagonal structure; on the contrary, after this procedure, they exhibit a more compact structure consisting of hexagonal pyramids.

A further test of good re-crystallisation of the CdTe films after the process is evident from the XRD measurements (Figure 4.8). The CdTe thin film, as expected, presents a zincblende structure but after treatment, it has a more preferential orientation in the crystallographic direction (111) and the peaks due to other orientations tend to decrease (Figure 4.8b).
Moreover, changes in structural properties coincide with differences in cathode-luminescence (CL) spectra (Figure 4.9). Indeed, these spectra show that total luminescence efficiency increases as a function of the freon partial pressure. In particular, the near band edge (NBE) emission peak at 1.57 eV is present in all the samples; on the contrary, a broad CL peak at 1.4 eV appears only in the treated samples with an intensity that increases with the increasing of CHF_2Cl partial pressure. This peak can be linked to the incorporation of Cl or F impurities that can diffuse into CdTe during the treatment and this creates a V_{Cd}-Cl complex, considering the literature results [16]. A last observation from these CL spectra is that the untreated CdTe film shows two peaks centered at 1.34 eV and 1.47 eV, respectively. In particular, the 1.47 eV peak is linked to crystalline defects and the 1.34 eV peak can be assigned to a transition involving impurity-related levels (typically present in the CSS deposition chamber).

Chlorine, through the formation of the V_{Cd}-Cl_{Te} complex, promotes a further *p*-type doping of the CdTe film decreasing its resistivity. Despite the excellent results achieved in terms of grain growth, CdS-CdTe inter-diffusion and therefore the high efficiency of the device, R-22 is no longer used because it is currently considered an ozone-depleting agent and its use is now prohibited.

We have had to change our treatment process for CdTe. The central question then becomes: does another suitable chlorine gas exist? Starting from the observation that CHF_2Cl at 670 K decomposes mainly into HCl and CHF_3, we assumed that it was possible to produce a suitable CdTe treatment combining HCl and CHF_3. In particular, we use Ar containing 4% of HCl at a pressure of $(1 \div 2) \times 10^3$ Pa, as a source of HCl, mixed with CHF_3 at a pressure of $(3 \div 4) \times 10^4$ Pa. We should underlined that, also in this case, the presence of fluorine is fundamental because it decreases the aggressiveness

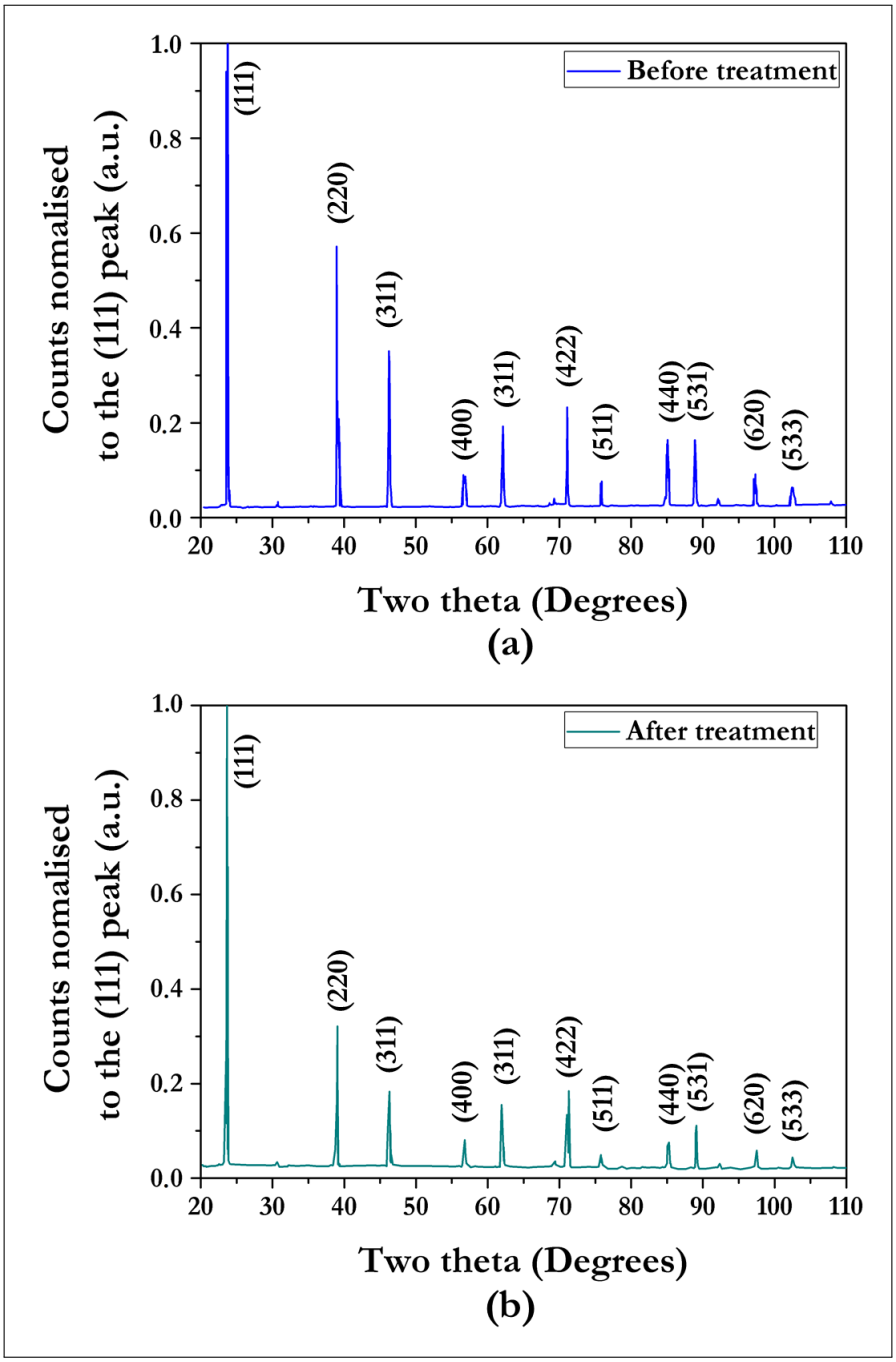

Figure 4.8: Comparison between XRD spectra of CdTe film before (a) and after (b) the chlorine treatment with Ar + R-22, respectively. Data from [8]

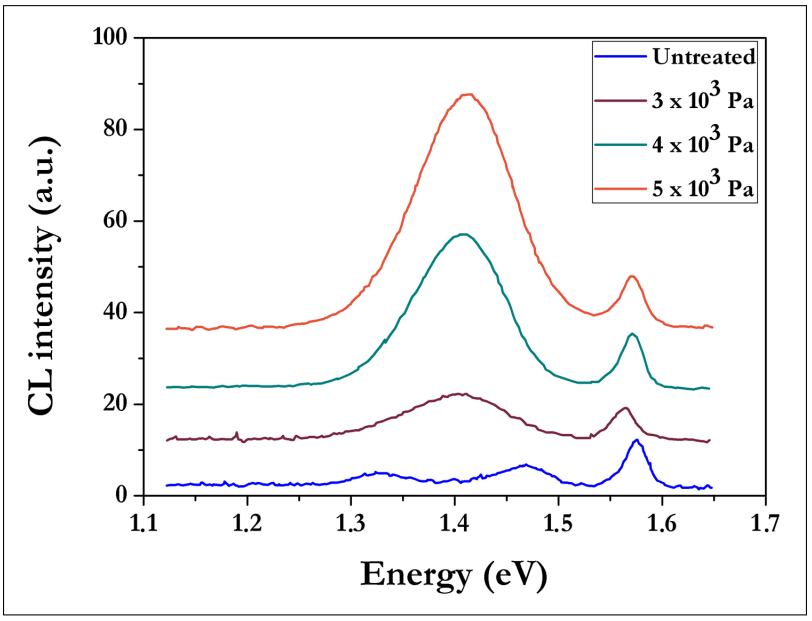

Figure 4.9: Comparison between CL spectra of not treated and treated CdTe film. The treatments are made with an atmosphere of 4×10^4 Pa plus 3×10^3 Pa, 4×10^3 Pa and 5×10^3 Pa of CHF_2Cl. In all these CL analyses are used a temperature of 77 K and beam energy of 25 keV that corresponds to a maximum penetration depth of 2.8 µm. Data from [13]

of HCl, improving the control of the reaction between CdTe and chlorine. Figure 4.10 shows the CdTe morphology before and after this new type of treatment.

4.1.6 Back contact

After the chlorine treatment, the last step for the production of a CdTe-based thin-film solar cell is the deposition of a back contact. It should be underlined that a barrier-free back contact is one of the crucial problem, as it gives stability over time and affects the efficiency of the device. The back contact is deposited on a *p*-type semiconductor layer and then it will not only have to be as much as possible a ohmic behaviour but it will also avoid the diffusion of metallic impurities inside the junction.

The following section 4.2.2 will described the work done during this PhD in order to improve our back contact.

4.2 Research work and experimental results

Starting from a CdTe-based solar cell structured as above, I focused on improving two key aspects of cell operation:

1. Grain boundary passivation.

2. Back-contact ohmicity and stability.

In the following two sections, I will present the main experimental results that were obtained while studying these two aspects.

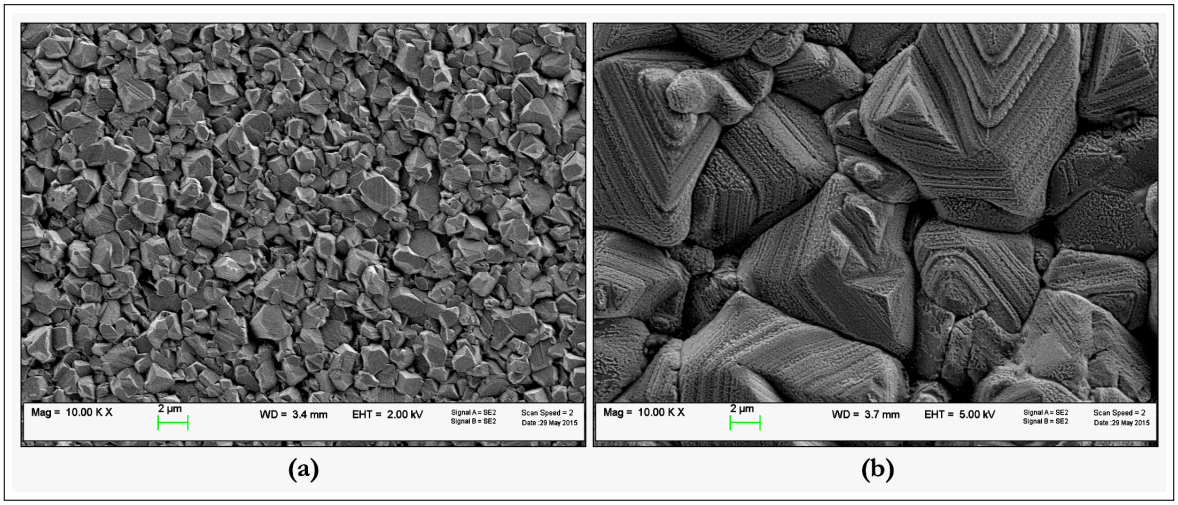

Figure 4.10: Comparison between SEM images of CdTe film morphology before (a) and after (b) the chlorine treatment with Ar containing 4% HCl + CHF_3.

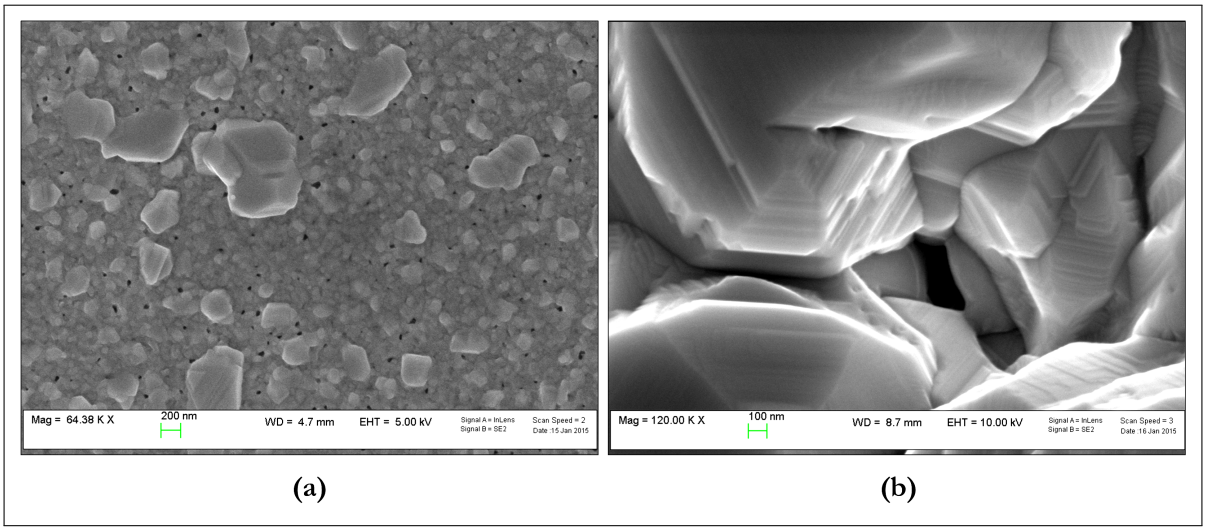

Figure 4.11: SEM images of the 3 µm-thick CSS CdTe film. The black spots in (a) are voids that were probably caused by an incomplete coalescence of the CdTe grains.

4.2.1 Grain boundary passivation

CdTe layers are normally fabricated by using CSS, a technique that can produce compact films only for thicknesses in the range of (6 ÷ 8) µm. By following our standard process, we deposited CdTe films with a thickness of 6 µm and its morphology is shown in Figure 4.10a. Thicker absorber layers can sometimes be employed to avoid pinholes and recombination paths of charge carriers into grain boundaries. However, the thickness of CSS-deposited films is significantly higher than necessary, because the energy band gap of CdTe is 1.49 eV and its absorption coefficient, in the visible part of the solar spectrum, is quite high (> 10^4 cm^{-1}), as illustrated before, a 1 µm-thick layer of material would be enough to absorb about 90% of the incoming radiation.

Considering our production process, it is mandatory to reduce the thickness of the CdTe layer without losing the overall performance of the device, such as efficiency and long-term stability.

To assess the extent of this problem, an attempt was made to deposit a CdTe film of only about (3

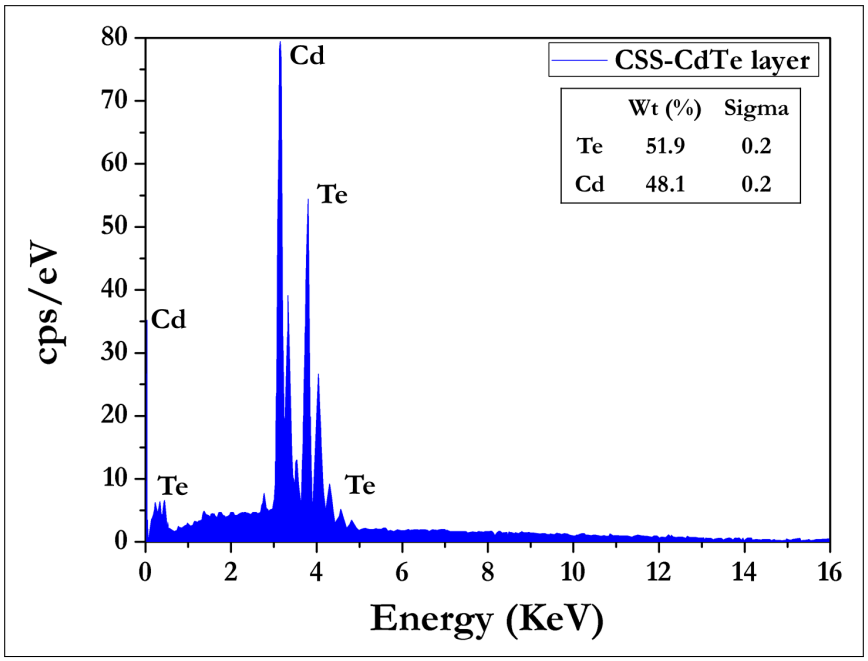

Figure 4.12: An EDX measurement of the CSS CdTe-film stoichiometry shows that tellurium is 51.9 wt% and cadmium is 48.1 wt%.

÷ 4) µm and the film was found to show, as expected, cavities (Figure 4.11). In particular, the crystalline grains exhibit a reduction in their size with the presence of some voids, which can favour the formation of shunt-paths and, as consequence, weak *p-n* junctions.

Despite showing that there is a difference in morphology between thicker and thinner CSS-deposited CdTe films, we have found out that there is no difference in stoichiometry between them. In both the 3 µm- and 6 µm-thick CSS CdTe films, the CdTe layer was found to have a Te-rich surface. Figure 4.12 shows the SEM-EDX measurements performed on a 3 µm-thick film.

Furthermore, our chlorine treatment (Ar containing 4% HCl + CHF_3) offers an additional advantage in terms of film surface composition: the CdTe surface remains Te-rich also after the treatment. This is only possible because our treatment does not introduce Cd in the deposited CdTe film. In the following section 4.2.2, we will analyse the importance of this feature to make the back contact directly on the CdTe surface. The characterisation that was carried out with SIMS on a CdTe film shows that there is an excess of Te in the CSS-deposited films (Figure 4.13).

After attesting that it was not possible to deposit compact films with a thickness of (2 ÷ 3) µm using the CSS technique, we investigated the following novel approach, consisting a (100 ÷ 200) nm-thick sputter-deposited CdTe layer on top of the first inhomogeneous CSS-deposited CdTe film.

This second CdTe layer is deposited by sputtering in an atmosphere of pure Ar at a temperature around 570 K, using a stoichiometric CdTe target with a purity of 99.999%. An SEM image of the sputtered CdTe film morphology (Figure 4.14) shows that the resulting film surface is very compact, being characterised by an excellent coverage already at very low thicknesses and it is completely pinhole-free.

Moreover, it exhibits a Cd-rich stoichiometry and it features a resistivity of about 1×10^6 Ω cm with a *n*-type behaviour. These qualities are presumably ascribable to the Te vacancies as the Cd/Te ratio suggests (see Figure 4.15).

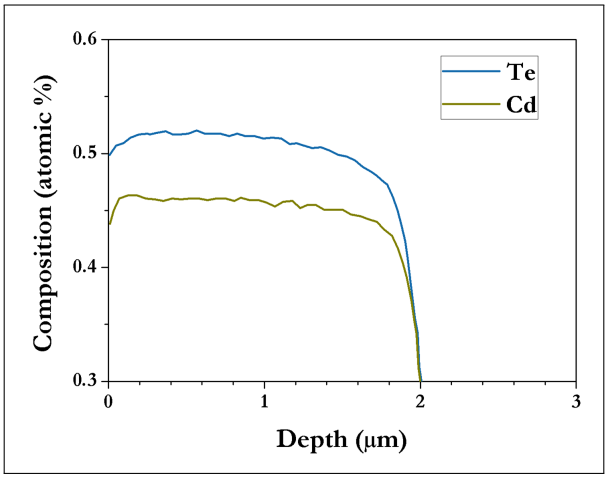

Figure 4.13: SIMS measurement performed within a depth of 2 μm from the surface of the CSS CdTe film.

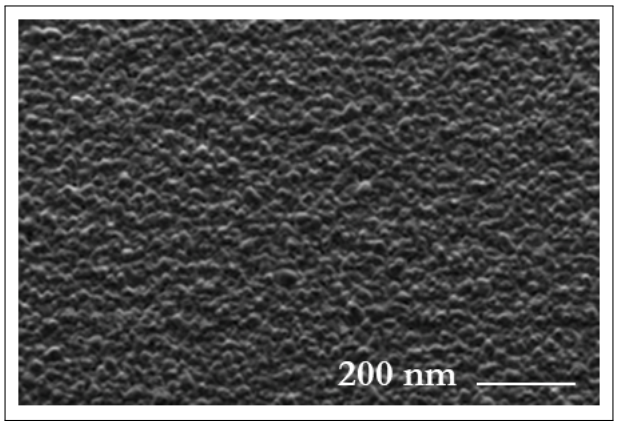

Figure 4.14: SEM image of the CdTe bi-layer (CSS + Sputtering) before the treatment.

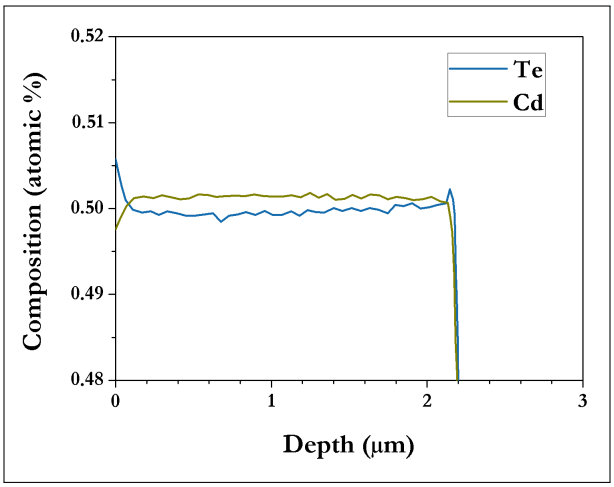

Figure 4.15: SIMS measurement that shows the Cd-rich nature of the CdTe sputtered film also after the Cl-treatment.

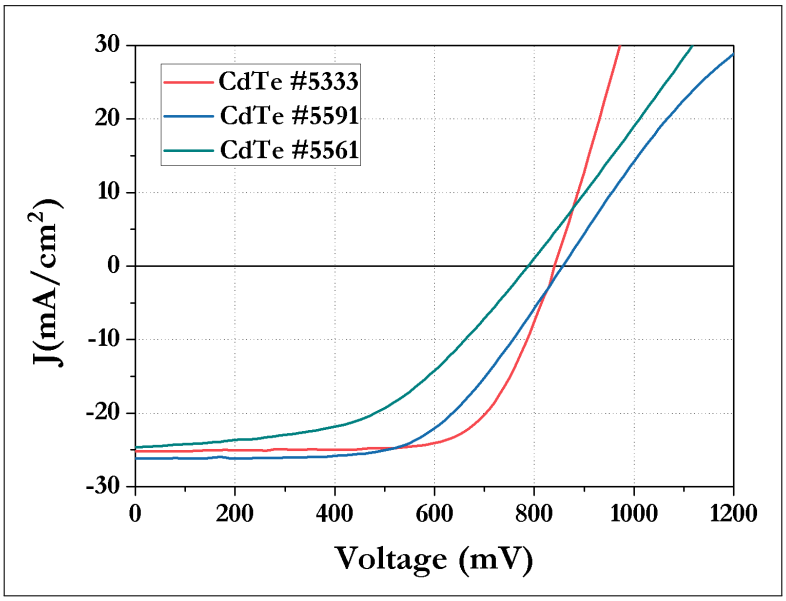

Figure 4.16: Comparison between the J-V characteristic of three CdTe-based solar cells.

This resulting CdTe bi-layer was subsequently heat-treated at 670 K under a controlled chlorine atmosphere and the solar cell was completed with a Bi_2Te_3-Cu-Mo back-contact.

To understand if our novel approach can reduce the thickness of the CdTe layer without affecting the performance of the device, we tested the finished solar cells. The main results are summarised in Table 4.2 and Figure 4.16.

Table 4.2: Comparison between the PV parameters of three CdTe-based solar cells.

Sample (#)	**V_{OC} (mV)**	**J_{SC} (mA/cm^2)**	**FF (%)**	**Eff. (%)**	**R_S * (Ω)**	**R_{Sh} * (Ω)**
5333	830	25.2	70.0	14.9	5.60 ± 0.02	1428 ± 20
5591	860	26.1	59.2	9.4	10.61 ± 0.04	1250 ± 9
5561	786	24.5	50.4	9.4	14.20 ± 0.01	227 ± 5

Note: * R_S and R_{Sh}, referred to solar cells with an area of 1 cm^2, have been extrapolated from the under-light J-V characteristics.

In particular, a comparison between the PV parameters of various solar cells is reported. Sample #5333 is produced using the novel method described above, while sample #5991 and sample #5561 are the result of a single CSS deposition of an 8 µm-thick and a 3 µm-thick CdTe layer, respectively. The CdTe bi-layer solar cell exhibits: $V_{OC} \approx 830$ mV, $J_{SC} \approx 25$ mA/cm^2, FF around 0.72 and an efficiency of about 15%.

Since these useful results cannot be simply justified by a filling of the cavities performed by the sputtered CdTe layer, we have formulated an ad-hoc hypothesis in order to explain this outcome. Our hypothesis is that, after the chlorine treatment, the sputtered CdTe layer, which is characterised by a Cd-rich (*n*-type) stoichiometry, can segregate within the grain boundaries. In this way, it may form a *p-n-p* junction across each grain boundary. This junction generates a built-in electric field in the

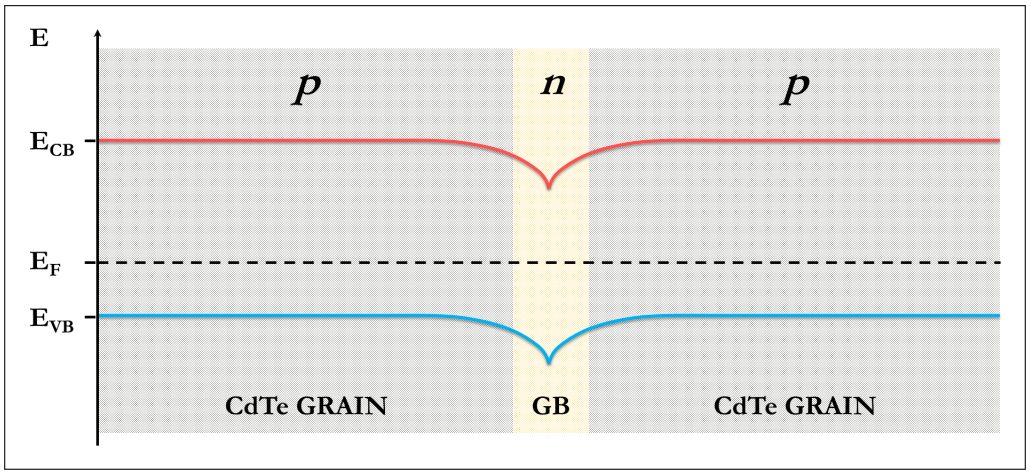

Figure 4.17: Basic representation of a band diagram in the case of a *p*-*n*-*p* junction across each grain boundary.

region between the grain edge and its interior, which acts as a mirror for the minority carriers and leads to an increase of their average lifetime. It then facilitates the separation of the photo-generated carriers, and consequently it reduces the carrier recombination rate. It should be highlighted that under this hypothesis, the holes are attracted by the grain boundaries, while the electrons are repulsed away from them. This effect is already known in the literature [9, 17] and it is schematically represented in Figure 4.17.

In order to verify this hypothesis, we performed an STEM-EDX analysis on a CdTe bi-layer after the chlorine treatment along a grain boundary and within the grain interior, and this is shown in Figure 4.18 and Table 4.3. The STEM-EDX analysis validates our idea as it detects an excess of Cd along the grain boundaries and an excess of Te within the grains.

This new type of active grain boundary passivation can also be useful against the formation of shunt paths. This is possible if the bottom of the cavities does not leave the CdS layer completely exposed. We have proved that it is necessary a CSS-CdTe layer with a thickness ≥ 2 µm to obtain these results.

In conclusion, we were successful in our aim to develop a new approach to reduce the thickness of the CdTe absorber layer down below 3 µm. This was achieved by creating a compact bi-layer where the interplay between these two CdTe layers with different stoichiometry gives rise to an active grain boundary passivation that preserves the cell performance.

4.2.2 Back-contact ohmicity and stability

A barrier-free and stable back contact is fundamental to improve the efficiency of CdTe/CdS-based solar cells. Since CdTe has a high electron affinity (χ = 4.5 eV) and a wide energy band gap (1.49 eV), it is required a material with a high work function (above 5.5 eV) to form a good ohmic contact (as demonstrate in Appendix C - Metal-semiconductor junction).
Unfortunately, materials with such values of work function are rare, as shown in Table 4.4 where some of the most common metal used as back contact with their work function are pointed out. It is evident, that most metals do not exhibit a work function large enough to form an ohmic contact with the *p*-type CdTe and therefore they form a Schottky-barrier with the absorber layers.

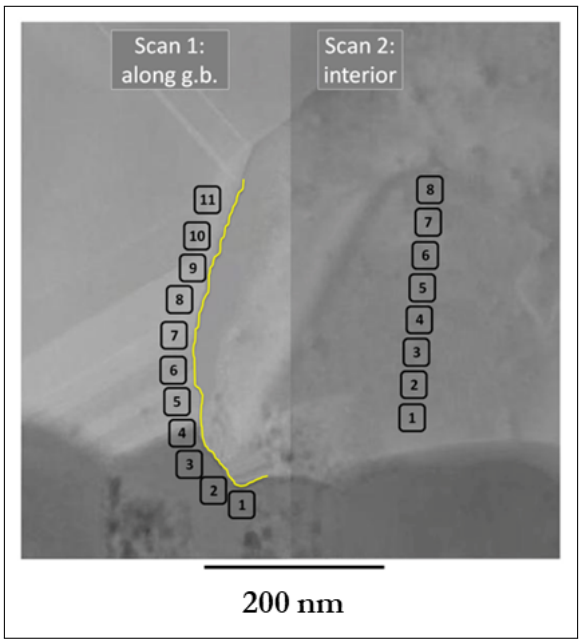

Figure 4.18: EDX scan of both a grain boundary on the left and a grain on the right of a CdTe bi-layer after treatment. The data are reported in Table 4.3.

Table 4.3: Atomic % concentrations data of S, Cl, Cd, and Te, associated to the Figure 4.18.

EDX scan along the grain boundary					**EDX scan inside the grain**			
Scan #	**S (at.%)**	**Cl (at.%)**	**Cd (at.%)**	**Te (at.%)**	**Scan #**	**S (at.%)**	**Cd (at.%)**	**Te (at.%)**
1	29.3	4.9	42.4	23.4	1	4.4	46.2	49.4
2	16.1	4.8	35.0	44.1	2	3.2	47.3	49.5
3	24.4	4.0	45.4	26.2	3	2.1	48.2	49.7
4	17.1	5.1	44.7	33.1	4	3.0	47.3	49.7
5	3.2	––	47.7	49.1	5	2.3	47.8	49.8
6	2.9	––	50.7	46.4	6	––	48.5	51.5
7	2.9	––	49.3	47.8	7	––	51.2	48.8
8	2.5	––	49.4	48.1	8	––	51.3	48.7
9	2.8	––	49.7	47.5				
10	3.0	––	49.2	47.8				
11	2.7	––	50.8	46.5				

Table 4.4: List of the most common metal used as back contact with their work function. Data from [18].

Metal	Work function (eV)
Ag	4.26
Al	4.28
Mo	4.49
Cu	4.65
Co	4.97
Au	5.10
Ge	5.15
Ni	5.15
Pd	5.40
Pt	5.63

Moreover, when the Fermi level at the metal/CdTe interface is pinned, also a metal with high work function might not form an ohmic contact. The presence of a back-contact barrier negatively influences the final performance of the device, because this barrier limits the hole collection. This is one of the main causes of the roll-over effect (current-limiting effect) in the J-V characteristics.
Furthermore, the deposition of these metals directly on the CdTe surface layer shows another important disadvantage: the diffusion of metal into the grain boundaries of the absorber layer, compromises also the long-term stability of the solar cell.

To overcome these problems, an alternative contacting technique makes use of a thin buffer layer between the *p*-type CdTe and the metal contact [19, 20, 21]. This buffer layer must have the following characteristics:

- Chemical stability.
- A suitable band alignment with CdTe, to enable an easy hole transport.
- A high acceptor level doping to facilitate the formation of a tunnel junction with a metal layer.

When a buffer layer between CdTe and metal contact is used, another aspect have to be considered: the use of copper in the back contact in order to form a thin film of Cu_xTe on the surface of the CdTe layer, is needed [22, 23, 24, 25].
It is well-known that copper is one of the most frequently used materials for improving the CdTe solar cell performances because it contributes to the creation of an ideal back contact by increasing the carrier concentration and consequently decreasing the potential barrier. As a result, a reduction of series resistance and an increase of open-circuit voltage is observed.
However, it is also well known that copper is a fast diffuser in to many materials and it diffuses more quickly along the polycrystalline grain boundaries. For these reason, an excessive presence of copper can lead to an over-time solar cell degradation. In particular, it causes a reduction of carrier lifetime, negatively affecting the creation of deep level defects into the CdTe energy band gap that reduces both J_{SC} and V_{OC}.

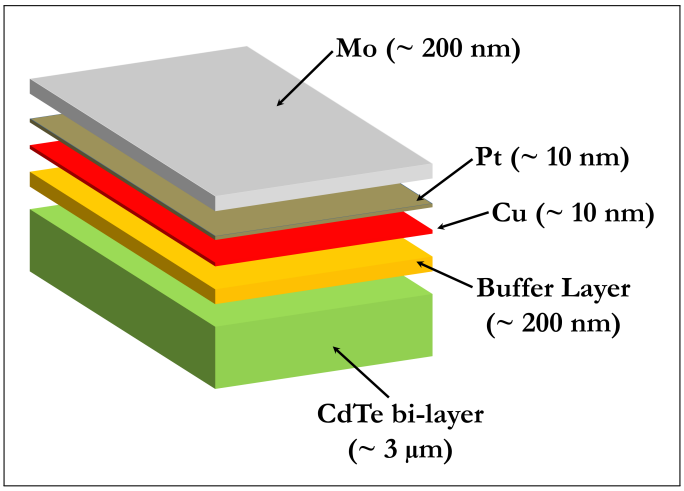

Figure 4.19: Structure of the back contact for CdTe solar cells.

It is therefore necessary to control the Cu-diffusion. Literature shows that if x in the Cu_xTe compound is less than 1.4, the contact is quite stable over time. On the contrary, if x is higher than 1.4, the Cu_xTe compound is not stable and, as a consequence, copper penetrates into the CdTe layer.

At ThiFiLab, several attempts were made and different buffer materials such as As_2Te_3, Bi_2Te_3 and ZnTe were tested [26, 27]. These layers are deposited directly onto the Te-rich CdTe surface without any chemical etching.
As_2Te_3 films are deposited by rf magnetron sputtering with a deposition rate between 10 and 20 Å/sec. Bi_2Te_3 films are deposited by electron gun at a substrate temperature in the range of (470 ÷ 520) K. Finally, ZnTe films are deposited by rf magnetron sputtering at 300 K substrate temperature and then annealed at 520 K for 20 minutes. We deposited these buffer layers with a thickness that can vary between 100 nm and 200 nm.
The resulting As_2Te_3 and Bi_2Te_3 thin films exhibit a low resistivity in the range of $(10^{-2} \div 10^{-3})$ Ω cm; on the contrary the ZnTe films exhibit a high resistivity (measurements performed with the four point probes method). The lowest resistivity measured on a ZnTe film is about 10^5 Ω cm, when films are deposited by rf magnetron sputtering at room temperature. It should be underlined that a 20 minutes vacuum annealing at 520 K is enough to reduce the resistivity to 2 Ω cm. In this last condition, ZnTe is suitable to be used as a back contact when coupled with p-type CdTe.
Each buffer layer was covered with about 10 nm of copper deposited by dc magnetron sputtering at a substrate temperature of 520 K in order to form, through Cu-diffusion, a Cu_xTe layer at the CdTe surface. Each contact was finished by adding a thin layer of platinum (∼ 10 nm) and then a thicker layer of molybdenum (∼ 200 nm) to form an ohmic contact with the buffer layer and both these layers are deposited by dc magnetron sputtering. We chose to add a platinum layer because Pt is known for its high work function (5.8 eV) making it a suitable material for connecting p-type high-conductivity buffer layers. The resulting structure of the back-contact is summarised in Figure 4.19. The resulting solar cells are then exposed to a post deposition annealing in air at 400 K for 30 minutes.

The results for As_2Te_3, Bi_2Te_3 and ZnTe are very similar and cell efficiencies are on the order of (15 ÷ 16)% with a fill factor of 0.7 ÷ 0.72. What makes a difference is the presence of platinum, which was confirmed to be fundamental. Figure 4.20 (which refers to a ZnTe back contact) shows that, when

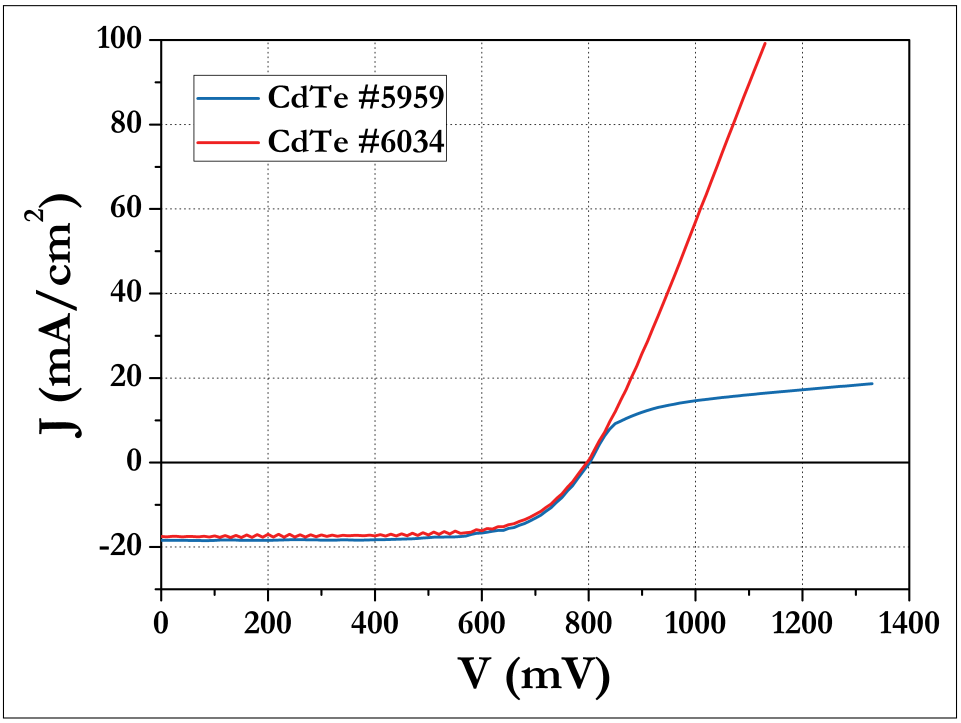

Figure 4.20: Comparison between sample CdTe #5959 (external contact is made without platinum) and sample CdTe #6034 (external contact is made with platinum). J-V characteristics were measured under STC – namely, incident power density of 1000 W/m^2, a temperature of 298.15 K, under AM 1.5 filtered solar light spectrum.

platinum is not used in the external contact, a roll-over appears in the J-V characteristic, causing a significant deviation from the high-voltage ideal profile.

From these results, we can remark that to obtain a CdS/CdTe solar cells with high efficiency without any roll-over effect the following characteristics are needed:

1. The presence of copper is fundamental to form a Cu_xTe layer on top of CdTe and at the same time, the diffusion of copper has to be controlled. In particular, x needs to be lower than 1.4.

2. A suitable buffer layer to control the Cu-diffusion is needed.

3. A metal with a high work function, such as platinum, is needed in order to make an ohmic contact with the buffer layer.

Since the back contact affects both the performances and the long-term stability of the devices, it is important to analyse also the long-term stability of our CdTe solar cells. Figure 4.21 shows a detailed analysis of the time-stability in the case of Bi_2Te_3 buffer layer. In particular, we compared air-annealed and not air-annealed back-contacts. The tests are made by keeping the solar cells in a metal box in dark at room temperature and under one sun at 350 K. During these tests, the devices are exposed to one sun light for about 1300 hours.

The data show that the device annealed in air and tested in dark at room temperature, is very stable. In particular, it exhibits an efficiency of more than 90% of the initial performance after 1300 hours (red line). Moreover, the comparison between the air-annealed back-contact (blu line) and the not air-annealed one (purple line) shows that after 1000 hours of accelerated lifetime test there is a great difference in stability. The air-annealed back-contact exhibits the 80% of the starting efficiency against

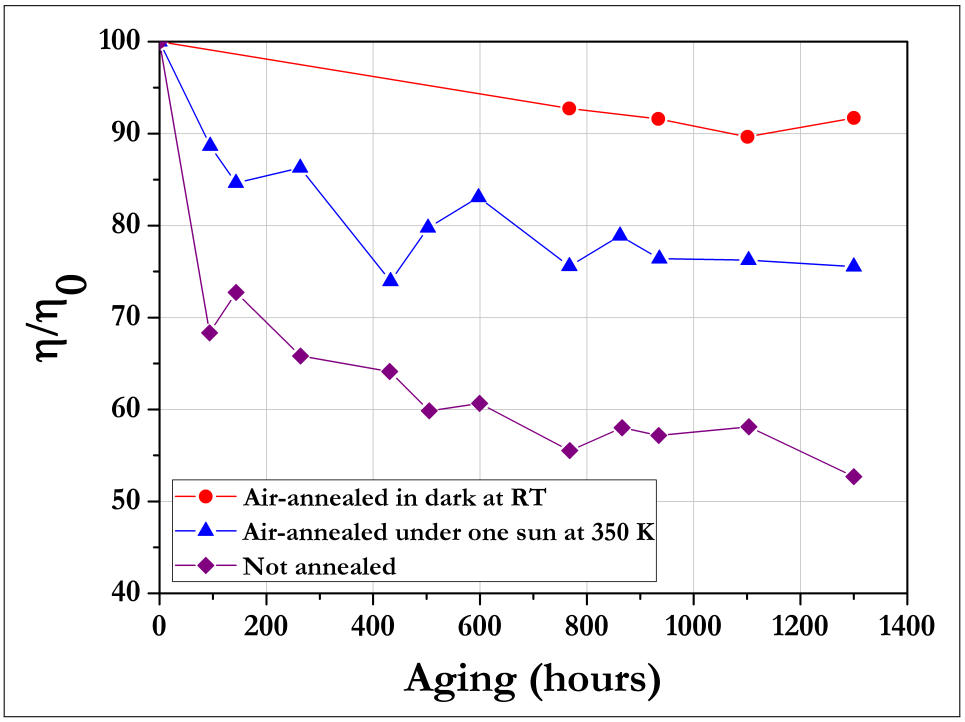

Figure 4.21: Comparison between the lifetime stability test of tree different CdTe-based solar cells with Bi_2Te_3 as buffer layer. In particular, red line: a device air-annealed and tested in dark at room temperature; blu curve: a device air-annealed and tested under one sun at 350 K. Finally, purple curve: a device not annealed and tested under one sun at 350 K.

60% of not air-annealed one. We can observe that the heat treatment in air of the back-contact is not really enhancing the diffusion of foreign atoms into the CdTe film, but it favours a change of the back contact structure.

At this time, we are also analysing the stability of the devices with ZnTe as buffer layer. The first data show only a little efficiency degradation, which stabilise at values close to the initial value.

In conclusion, we found out a method for making a stable non-rectifying back contact in CdTe-based solar cells. We noted that copper is fundamental for a suitable back contact but its diffusion must be controlled by a buffer layer. Finally, we detected the importance to make the contact on buffer layer with a high work function metal (e.g. platinum) to avoid any roll over in the J-V characteristic.

References

[1] Wikipedia. (Accessed September 22, 2017).
https://en.wikipedia.org/wiki/Soda-lime_glass

[2] L. Kranz, J. Perrenoud, F. Pianezzi, C. Gretener, P. Rossbach, S. Buecheler and A.N. Tiwari. *Effect of sodium on recrystallization and photovoltaic properties of CdTe solar cells.* Solar Energy Materials and Solar Cells. Elsevier. 2012, Volume 105, Pages: 213-219.

[3] N. Romeo, A. Bosio, V. Canevari, M. Terheggen and L. Vaillant Roca. *Comparison of different conducting oxides as substrates for CdS/CdTe thin film solar cells.* Thin Solid Films. Elsevier. 2003, Volume 431, Pages: 364-368.

[4] A. Bosio, N. Romeo, S. Mazzamuto and V. Canevari. *Polycrystalline CdTe thin films for photovoltaic applications.* Progress in Crystal Growth and Characterization of Materials. Elsevier. 2006, Volume 52, Number 4, Pages: 247-279.

[5] O. Madelung, U. Rössler and M. Schulz. *Cadmium telluride (CdTe) crystal structure, modifications.* II-VI and I-VII Compounds; Semimagnetic Compounds. Springer Berlin Heidelberg. 1999, Volume 41, Pages: 1-7.

[6] N. Amin and K.S. Rahman. *Close-spaced sublimation (CSS): A low-cost, high-yield deposition system for cadmium telluride (CdTe) thin film solar cells.* Book: Modern Technologies for Creating the Thin-film Systems and Coatings. Chapter 18. InTech. 2017.

[7] D. Wang, Z. Hou and Z. Bai. *Study of interdiffusion reaction at the CdS/CdTe interface.* Journal of Materials Research. Cambridge University Press. 2011, Volume 26, Number 5, Pages: 697-705.

[8] S. Mazzamuto, L. Vaillant, A. Bosio, N. Romeo, N. Armani and G. Salviati. *A study of the CdTe treatment with a Freon gas such as CHF_2Cl.* Thin Solid Films. Elsevier. 2008, Volume 516, Number 20, Pages: 7079-7083.

[9] J.D. Major. *Grain boundaries in CdTe thin film solar cells: a review.* Semiconductor Science and Technology. IOP Publishing. 2016, Volume 31, Number 9, Page: 093001.

[10] J. Hiie. *CdTe:$CdCl_2$:O_2 annealing process.* Thin Solid Films. Elsevier. 2003, Volume 431, Pages: 90-93.

[11] J. Hiie. *Effects of $CdCl_2$ treatment on deep levels in CdTe and their implications on thin film solar cells: A comprehensive photoluminescence study.* Journal of Materials Science: Materials in Electronics. Springer. 2015, Volume 26, Number 7, Pages: 4571-4583.

[12] A. Abbas, G.D. West, J.W. Bowers, P. Isherwood, P.M. Kaminski, B. Maniscalco, P. Rowley, J.M. Walls, K. Barricklow and W.S Sampath. *The effect of cadmium chloride treatment on close-spaced sublimated cadmium telluride thin-film solar cells.* IEEE Journal of Photovoltaics. IEEE. 2013, Volume 3, Number 4, Pages: 1361-1366.

[13] L. Vaillant, N. Armani, L. Nasi, G. Salviati, A. Bosio, S. Mazzamuto and N. Romeo. *Interface properties of HCF_2Cl annealed CdTe thin films for solar cells applications.* Thin Solid Films. Elsevier. 2008, Volume 516, Number 20, Pages: 7075-7078.

[14] T.X. Zhou, N. Reiter, R.C. Powell, R. Sasala and P.V. Meyers. *Vapor chloride treatment of polycrystalline CdTe/CdS films.* Photovoltaic Energy Conversion, 1994, Conference Record of the Twenty Fourth. IEEE. 1994, Volume 1, Pages: 103-106.

[15] A. Bosio, G. Rosa, D. Menossi and N. Romeo. *How the chlorine treatment and the stoichiometry influences the grain boundary passivation in polycrystalline CdTe thin films.* Energies. Multidisciplinary Digital Publishing Institute. 2016, Volume 9, Number 4, Page: 254.

[16] N. Armani, G. Salviati, L. Nasi, A. Bosio, S. Mazzamuto and N. Romeo. *Role of thermal treatment on the luminescence properties of CdTe thin films for photovoltaic applications.* Thin Solid Films. Elsevier. 2007, Volume 515, Number 15, Pages: 6184-6187.

[17] C. Li, Y. Wu, J. Poplawsky, T. Pennycook, N. Paudel, W. Yin, S. Haigh, M.P. Oxley, A.R. Lupini, M. Al-Jassim, S.J. Pennycook and Y. Yan. *Grain-boundary-enhanced carrier collection in CdTe solar cells.* Physical review letters. APS. 2014, Volume 112, Number 15, Page: 156103.

[18] National Physical Laboratory. (Accessed September 28, 2017). `http://www.kayelaby.npl.co.uk/atomic_and_nuclear_physics/4_3/4_3.html`

[19] C. Narayanswamy, T.A. Gessert and S.E. Asher. *Analysis of Cu diffusion in ZnTe-based contacts for thin-film CdS/CdTe solar cells.* AIP Conference Proceedings. AIP. 1999, Volume 462, Number 1, Pages: 248-253.

[20] S.H. Demtsu and J.R. Sites. *Effect of back-contact barrier on thin-film CdTe solar cells.* Thin Solid Films. Elsevier. 2006, Volume 510, Number 1, Pages: 320-324.

[21] S. Uličná, P.J.M. Isherwood, P.M. Kaminski, J.M. Walls, J. Li and C.A. Wolden. *Development of ZnTe as a back contact material for thin film cadmium telluride solar cells.* Vacuum. Elsevier. 2017, Volume 139, Pages: 159-163.

[22] X. Wu, J. Zhou, A. Duda, Y. Yan, G. Teeter, S. Asher, W.K. Metzger, S. Demtsu, S.H. Wei and R. Noufi. *Phase control of Cu_xTe film and its effects on CdS/CdTe solar cell.* Thin Solid Films. Elsevier. 2007, Volume 515, Number 15, Pages: 5798-5803.

[23] J. Zhou, X. Wu, A. Duda, G. Teeter and S.H. Demtsu. *The formation of different phases of Cu_xTe and their effects on CdTe/CdS solar cells.* Thin Solid Films. Elsevier. 2007, Volume 515, Number 18, Pages: 7364-7369.

[24] T.A. Gessert, W.K. Metzger, P. Dippo, S.E. Asher, R.G. Dhere and M.R. Young. *Dependence of carrier lifetime on Cu-contacting temperature and ZnTe:Cu thickness in CdS/CdTe thin film solar cells.* Thin Solid Films. Elsevier. 2009, Volume 517, Number 7, Pages: 2370-2373.

[25] N. Romeo, A. Bosio, S. Mazzamuto, A. Romeo and L. Vaillant-Roca. *High efficiency CdTe/CdS thin film solar cells with a novel back-contact.* Proceedings of 22nd European Photovoltaic Solar Energy Conference. 2007, Pages: 1919-1921.

[26] A. Bosio, N. Romeo, D. Menossi, G. Rosa, P.P. Lottici, A. Romeo, I. Rimmaudo and A. Salavei. *Key developments in CdTe thin film solar cell back-contact.* Proceedings of 28th European Photovoltaic Solar Energy Conference. 2013, Pages: 2357-2361.

[27] N. Romeo, G. Rosa and A. Bosio. *The back contact in CdTe/CdS thin film solar cells.* Submitted to Solar World Congress 2017. 2017.

Chapter

5

Enhancements in CIGS solar cells

In this chapter, a description of the structure of CIGS-based solar cells fabricated by using sputtering technique at ThiFiLab is given.
Then, I will focus on the two main aspects investigated during my PhD research project: the inspection of the process requirements that must be met to obtain high-quality precursors on a soda-lime glass and the extension of this standard process to flexible thin metal foil substrates. I will report the main experimental results achieved in order to enhance these two aspects.

5.1 Experimental details of CIGS-based solar cells structure

The $CuInGaSe_2$ (CIGS) solar cell realised at ThiFiLab consists of the sequence of layers illustrated in Figure 5.1. As shown, our device is fabricated in substrate configuration. First of all there is the substrate (SLG, ceramic or thin metal foil); then, there is the back contact and the junction formed by the absorber layer and the window material; finally, the front contact. All these layers are deposited by using only the sputtering technique. In the next paragraphs, we will examine the different layers that form the solar device produced at ThiFiLab and how it is manufactured.

Since the front contact (ITO + ZnO) and the window layer (CdS) are made in the same way as CdTe-based solar cells, descriptions of the deposition processes will not be repeated (see Sections 4.1.2 and 4.1.3, respectively).

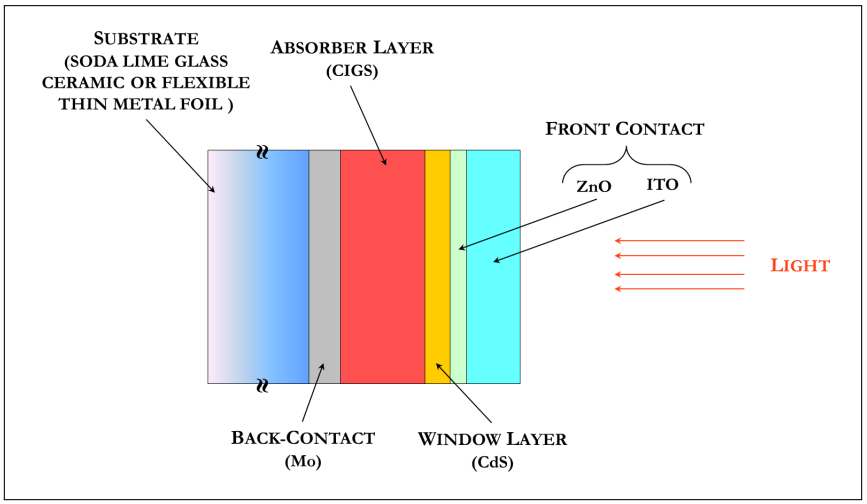

Figure 5.1: Structure of the CIGS-based solar cell fabricated at ThiFiLab in substrate configuration.

5.1.1 Substrate

As shown in the case of CdTe-based solar cell, the substrate is the base on which all the solar cell layers are deposited. Therefore, the choice of a suitable substrate represents an important part in the production of a thin-film solar cell. It has to exhibit chemical stability, mechanical robustness, low lattice mismatch between substrate and deposited film as well as low costs. In this case, substrate transparency is not required, because in substrate configuration, the light enters the absorbing material crossing only the front contact.

Usually, at ThiFiLab two different types of substrates are used for the production of CIGS-based solar cells: SLG and ceramic substrate (for BIPV applications). During my PhD, we try to extend this standard process also to flexible thin metal foil substrates.

The properties of SLG substrate have already been described in section 4.1.1 but, on the contrary of CdTe-based solar cells, sodium plays an important role in the electrical performance of CIGS devices. In literature, it is well known that the presence of Na promotes [1, 2, 3, 4]:

- Preferred orientation and grain size enhancement.
- Resistivity decrease.
- V_{OC} increase.

Indeed, a moderate diffusion of Na into the growing film (typical concentrations are on the order of 0.1 at.%) can improve the *p*-type doping of CIGS, increasing the number of acceptors and promoting a consequent increase in holes density of about 1 - 2 orders of magnitude. This phenomenon can be explained considering that Na replaces the anti-site defects (like In_{Cu}) and then inhibits its formation.

In the next section we will analyse the main properties of the ceramic substrate used in ThiFiLab, while the characteristics of flexible metallic substrate will be shown in detail in the next section 5.2.2.

5.1.1.1 Ceramic substrate

Starting from the observation that ceramic tiles currently present on the market are characterised by a large number of surface defects and, among them, the best ones are produced from finely granu-

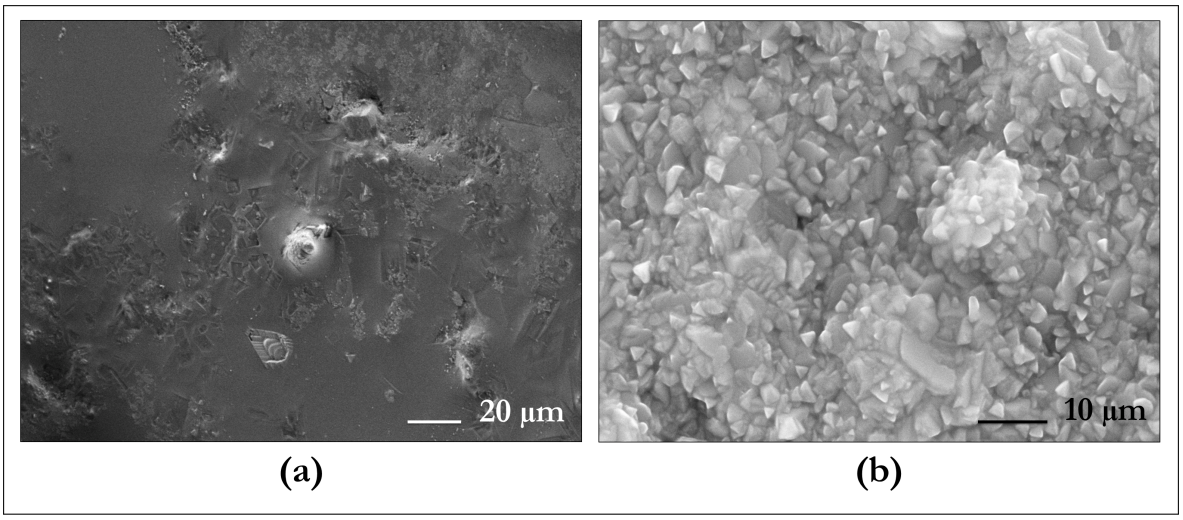

Figure 5.2: SEM images of the morphology of: (a) raw commercial ceramic tile, (b) CIGS layer deposited by sputtering and selenisation on top of this ceramic substrate [5].

Table 5.1: EDX measure on SLG substrate and on an enamelled ceramic tile surface after a vacuum heat treatment at 750 K [5].

Element (at.%)	Si	Na	K	Ca	Mg	Al	B	Fe	Ti
SLG	73.3	13.4	< 1	12.2	< 1	< 1	< 1	< 1	< 1
Enamelled ceramic	72.0	7.8	4.6	11.9	2.5	< 1	< 1	< 1	< 1

lated powder (granules with size of about 10 µm) [5]. It should be noted that more the starting powder is fine and more the surface of tile will be smooth. However, even the best commercial ceramic tiles exhibit a high surface unevenness and roughness. As an example, Figure 5.2a shows the surface morphology of a raw ceramic tile. It is very difficult to deposit uniform thin films on such a substrate because, in many case, the surface defects (voids or protuberances) are greater than the thickness of the deposited thin film. As shown in Figure 5.2b, deposited thin films cannot properly cover the entire surface of the substrate and thus there is a high probability of having pin-holes or electrical shunting problems.

This problem can be overcome by covering the surface of the ceramic substrate with a thin layer of a glassy enamel. In particular, a glassy enamel with a composition similar to that of SLG substrate was chosen (Table 5.1). As shown in Figure 5.3a, the substrate surface is much smoother and therefore, this type of ceramic substrate is suitable for deposition of thin films (Figure 5.3b).

The enamel described above has usually a thickness in the range from 300 µm to 1000 µm. It is deposited starting from wet powders, which are then processed directly on the ceramic surface at a temperature between 1210 K and 1250 K.

Therefore, enamelled ceramic can be a good alternative to SLG substrate because it does not suffer of either chemical or physical problems at process conditions. Finally, the technique for cleaning the ceramics substrates is quite similar to that used for SLG glasses, as reported in the Appendix B - Cleaning of substrate surface.

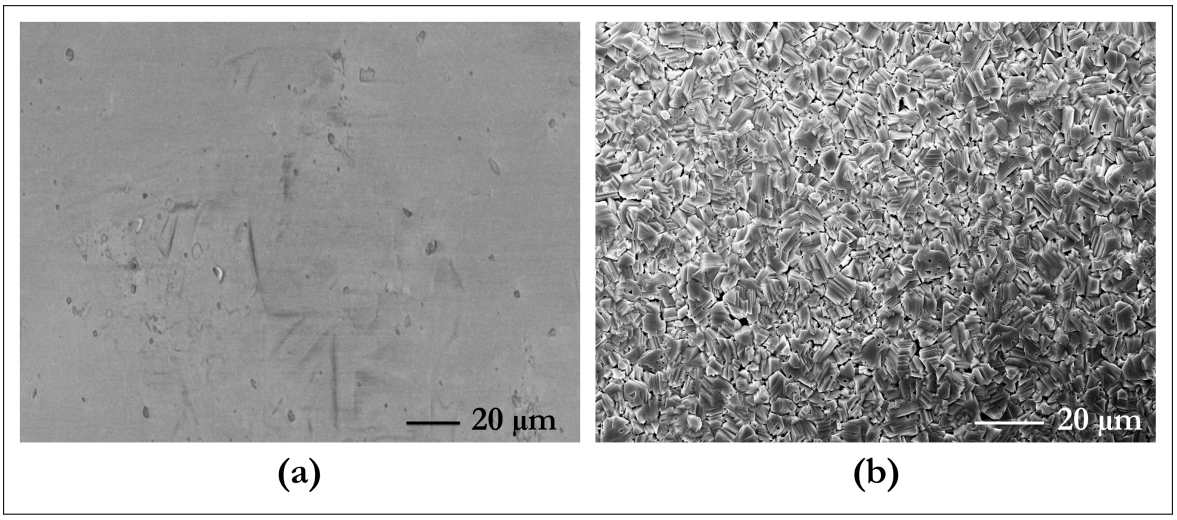

Figure 5.3: SEM images of the morphology of: (a) ceramic tile covered with a glassy enamel realised by the fabrication production process, (b) CIGS layer deposited by sputtering on top of this ceramic substrate [5].

5.1.2 Back contact

To produce a suitable back contact for CIGS-based solar cells, a high conductivity together with good chemical stability is needed and molybdenum is the most common metal used. It should be noted that many other back-contact materials were investigated (such as platinum, gold, silver or copper), but Mo is currently the most widely used [6, 7]. In fact, it presents the following advantages:

- Stability at the typical process temperatures.
- Resistance to form alloy with Cu and In.
- Low contact resistance with CIGS layer.

Mo typical electrical resistivity is about 5×10^{-5} Ω cm and the suitable value for CIGS-based solar cells is ≤ 0.3 Ω cm. Then, the total series resistance of the device can be easily limited with this type of back contact.

Furthermore, to produce a proper ohmic contact between a metal and a *p*-type semiconductor, it is fundamental for the metal to exhibit a working function higher than the electronic affinity of the semiconductor (Appendix C - Metal-semiconductor junction). In this case, it is required a work function close to 5 eV. Although Mo has a work function of about 4.6 eV (slightly lower than the required one), there is still a discrete ohmic behaviour for the Mo-CIGS contact. Moreover, Mo is a metal with a high melting point (2896 K) and with low coefficient of thermal expansion (4.8 µm/(m K) at 298.15 K) [8]. These properties make Mo suitable as a back contact in CIGS solar cells, because the production of these devices require process temperatures greater than 750 K. At these temperatures, if CIGS thin film is grown on a metal with high coefficient of thermal expansion, it is possible to introduce a large number of defects at the CIGS-Mo interface. These defects are made by the mechanical stress generated during the heating and cooling phases of the process.

When Mo is contacted with CIGS layer, some lattice defects are introduced into the interface region and this is due to the difference in the lattice parameter between the two materials.
However, during the deposition of CIGS layer, a $MoSe_2$ thin layer is usually formed at the CIGS/Mo

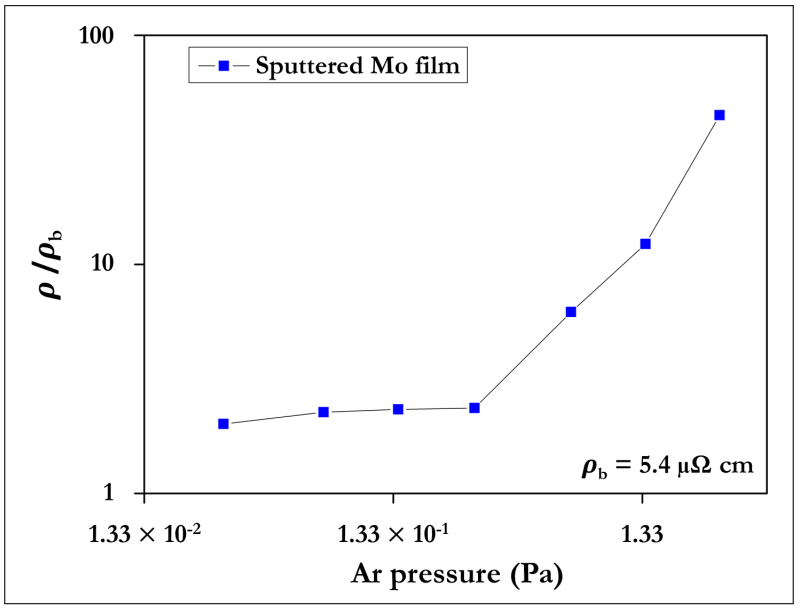

Figure 5.4: Normalised Mo film resistivity as a function of Ar pressure into the deposition sputtering chamber. ρ_b is the room-temperature Mo bulk resistivity, equal to 5.4 μΩ cm. Data from [9].

interface. This layer changes the CIGS/Mo contact from Schottky to ohmic-type contact since it has a high *p*-type conductivity with a proper electron affinity.
Furthermore, the presence of $MoSe_2$ allows a more gradual variation of the lattice mismatch between Mo and CIGS. It also improves the CIGS adhesion and limits the formation of interface defects.

5.1.2.1 Sputtering deposition of molybdenum layer

At ThiFiLab, molybdenum is typically deposited by dc magnetron sputtering. The sputtering deposition conditions influence the structural, morphological and electrical properties of the Mo layer.

During deposition, molybdenum, such as other refractory material (e.g. Cr, W, Nb, Ta or V), exhibits a correlation between the sputtering gas pressure and the mechanical stress of the deposited film [9]. In particular, when Mo is deposited in presence of a high argon pressure (about 1 Pa), Mo thin film grows with a porous columnar structure. These films exhibit a tensile stress and this allows good adhesion to the substrate. Unfortunately, the presence of pores increases the resistivity of the Mo thin film (Figure 5.4).
On the contrary, when Mo is deposited in presence of a low argon pressure (about 10^{-1} Pa), the Mo thin film results less porous, more and more tightly packed and then, with a low resistivity (Figure 5.4). Unfortunately, these films are found to be under a compressive stress. Therefore, mismatch between substrate and Mo film increases to a limit value beyond which the Mo layer does not have a proper adhesion to the substrate. This is the main cause of delamination of Mo thin film.

In order to obtain a Mo layer with good adhesion to the SLG substrate and at the same time, with a small electrical resistance, it is necessary to deposit a Mo bi-layer structure. The first Mo layer is deposited at high pressure to facilitate adhesion, while the second Mo layer is deposited at low pressure to achieve good electrical conductivity.

For these reasons, we usually deposited Mo by dc magnetron sputtering in a bi-layer configuration

at room temperature. The first layer of Mo is very thin (thickness of about 30 nm) and it is deposited in an Ar flow of 45 sccm (corresponding to a chamber pressure of 4.5×10^{-1} Pa). Then, the second Mo layer is deposited in an Ar flow of 15 sccm (corresponding to a chamber pressure of 1.5×10^{-1} Pa) and the typical thickness is about 800 nm.

5.1.3 Absorber layer

Copper indium gallium diselenide (CIGS) is a I-III-VI_2 semiconductor material with a chalcopyrite crystal structure (space group $I\bar{4}_{2d}$) [10, 11, 12, 13]. The typical chemical formula is $CuIn_xGa_{(1-x)}Se_2$, where X represents the content of gallium:

$$X = \frac{[Ga]}{[In + Ga]} \tag{5.1}$$

CIGS is a *p*-type direct energy band gap semiconductor with an energy band gap that varies continuously with x from about 1.04 eV for $x = 0$ (namely $CuInSe_2$) to about 1.68 eV for $x = 1$ (namely $CuGaSe_2$). It has also a large optical absorption coefficient on the order of 10^4 cm^{-1}. For this reason, it is a suitable material for thin-film PV applications as absorber layer.

Currently, several deposition techniques are used to realise the CIGS absorber layer, such as: co-evaporation and chalcogenization of metallic layers, rapid thermal annealing of elemental layers, CVD, pulsed electron deposition and sputtering. Each of this methods can provide a final good quality crystalline thin film but, in order to obtain a low-cost fully automated in-line production processes, we chose to deposit the precursors by sputtering and to selenise them immediately afterward. The selenisation step is performed in a pure Se atmosphere, which makes this technique environmentally sustainable.

5.1.3.1 Process description

Now, I will review the latest development in CIGS production at our laboratory [14]. In particular, I will show the comparison between devices obtained with different starting precursors, namely, In_2Se_3, Ga_2Se_3 and Cu against InSe, GaSe and Cu.

5.1.3.1.1 The In_2Se_3, Ga_2Se_3, and Cu system

An In_2Se_3, Ga_2Se_3, and Cu sequence is deposited on top of the Mo back-contact film in the same sputtering chamber without breaking the vacuum. Figures 5.5 and 5.6 display the sputtering system, where one can see the sequence of the four targets used.

The precursor deposition process involves the following sequence (see Figure 5.7):

1. A 1000-nm-thick In_2Se_3 film is deposited by rf magnetron sputtering, at a substrate temperature of about 670 K, with a 3.3 W/cm^2 power density at a deposition rate of 1 nm/s under a 0.5 Pa argon pressure[1].

2. A rf magnetron sputtering deposition of a 330-nm-thick Ga_2Se_3 film at a substrate temperature of about 720 K, with 1.8 W/cm^2 power density at a deposition rate of 0.4 nm/s under a 0.2 Pa

[1]The deposition rate was measured with a quartz micro-balance and the film thickness was measured with a profilometer.

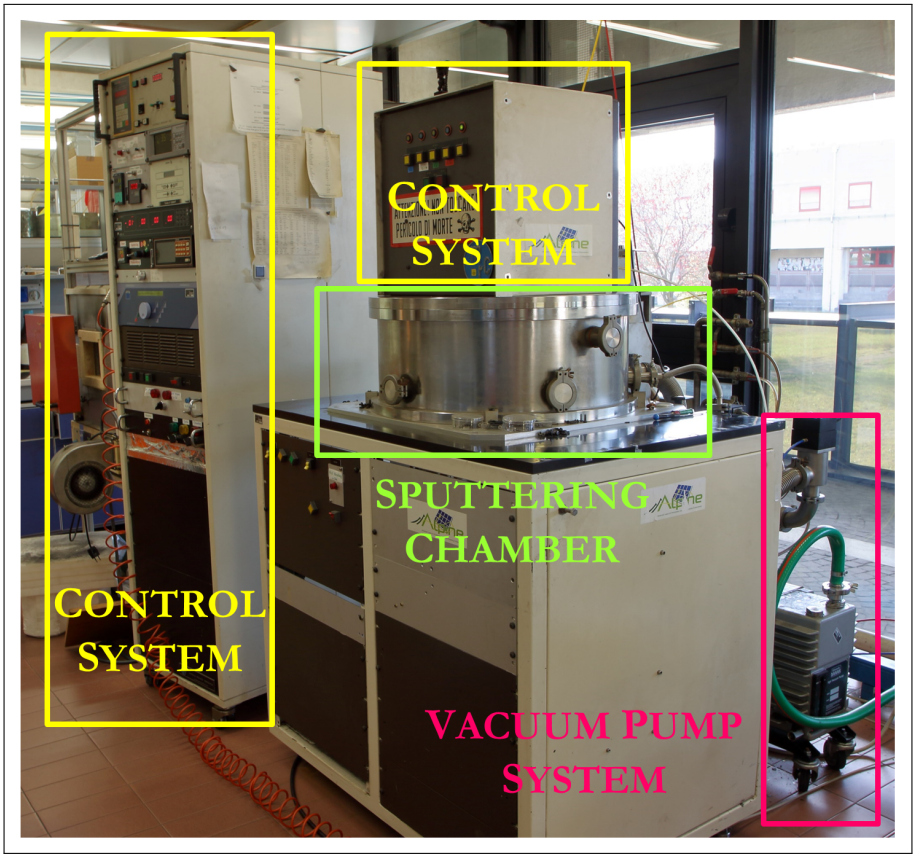

Figure 5.5: Photo of the sputtering system used to deposit CIGS layers at ThiFiLab.

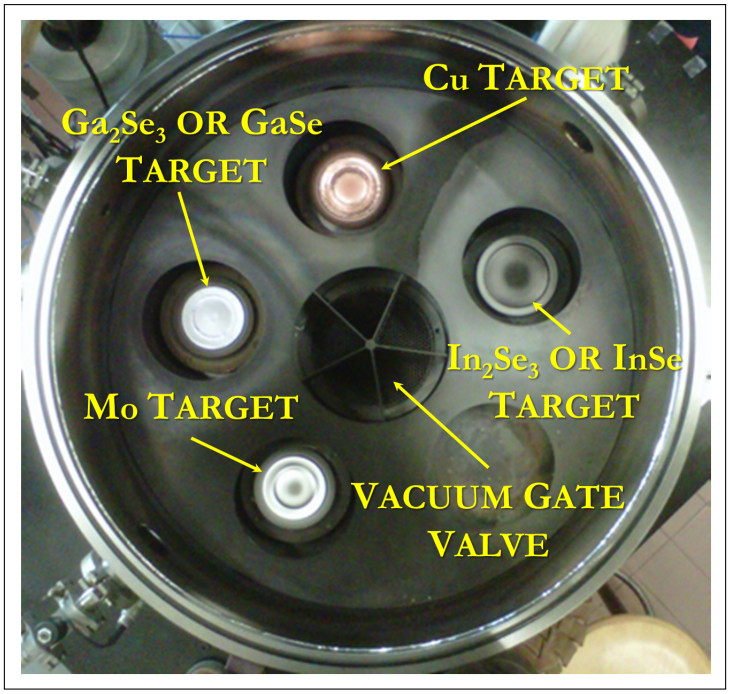

Figure 5.6: Inside of the ThiFiLab sputtering chamber. It is possible to see the four different targets and the vacuum gate valve.

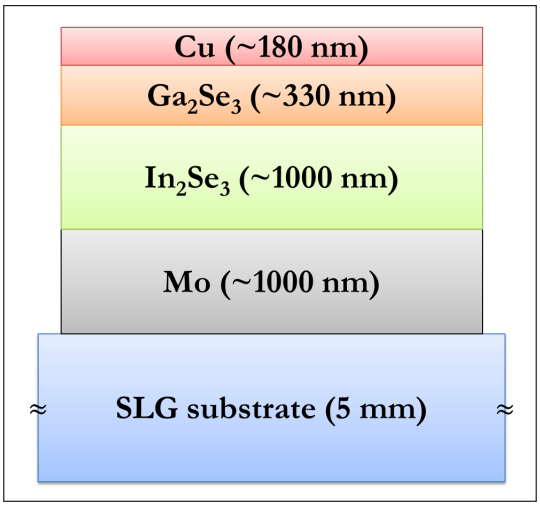

Figure 5.7: Sequence of deposited layers used to obtain the CIGS absorber material starting from In_2Se_3, Ga_2Se_3 and Cu targets.

argon pressure.

3. A dc magnetron sputtering deposition of a 180-nm-thick Cu film at a substrate temperature of about 620 K, with 1.8 W/cm^2 power density at a deposition rate of 0.6 nm/s under a 0.2 Pa argon pressure.

The difference between the deposition temperatures for each layer is due to the high reactivity and diffusivity of copper. It is known, from literature, that diffusion increases with temperature. The two main negative effects of a strong Cu reactivity are that Cu induces surface segregation of Cu-based secondary phases and partial separation of the crystalline grains. As a consequence, the film uniformity is negatively affected.
It is possible to avoid this problem by depositing Cu on top of the Ga_2Se_3 film at low substrate temperature (620 K). Immediately after, it is made a further annealing in vacuum at a temperature of 670 K. In this way, a uniform film is obtained with enhanced single-phase crystallisation. Finally, the precursor material is subjected to the selenisation process, which is performed in a pure-selenium atmosphere for 10 min at a temperature of about 800 K.

In Figures 5.8 and 5.9 are reported the SEM images of the morphology and XRD spectrum of the CIGS absorber layer deposited according to this method. The surface morphology is uniform throughout the whole substrate area.

The highest photovoltaic parameters obtained with this absorber material are the following: V_{OC} = 530 mV, J_{SC} = 35.16 mA/cm^2, FF = 58%, and efficiency equal to 10.81%. Measurements were performed at 298 K under 100 mW/cm^2 A.M. 1.5 filtered light (standard conditions).

In these thermodynamic conditions, a CIS crystalline material with a more ideal structure can form as demonstrated by the above PV parameters. Therefore, it is possible to prevent the lattice defects, letting the photo-generated carriers to be collected and transported more effectively through the junction.

To improve the efficiency of the CIGS-based solar cells, it is necessary a proper distribution of the Ga concentration within the absorber material. As literature reports [15, 16, 17, 18], an accurately

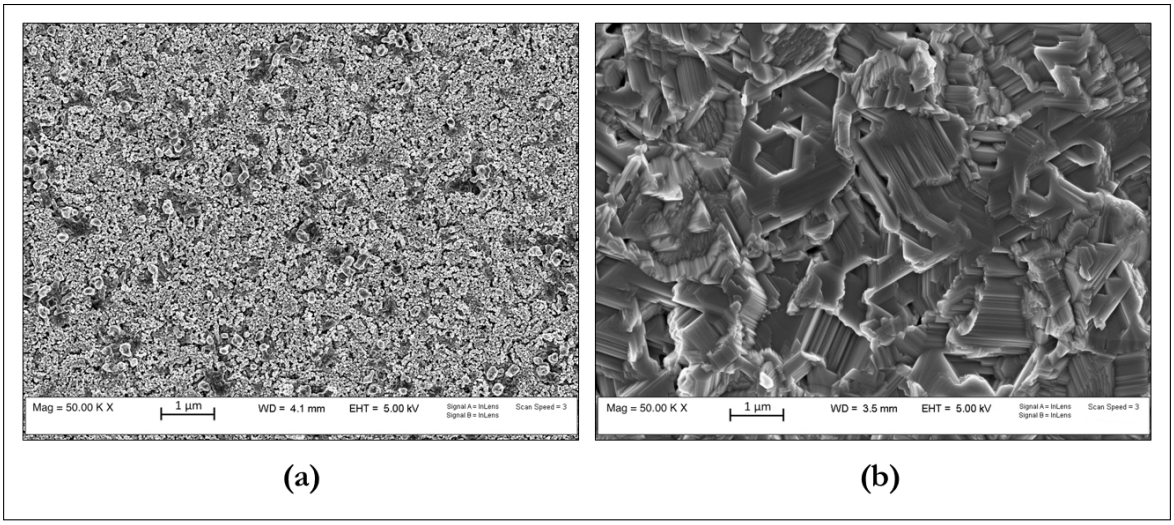

Figure 5.8: SEM morphology image of (a) the as-deposited In_2Se_3-Ga_2Se_3-Cu precursor and (b) the resulting CIGS absorber layer after the selenisation process.

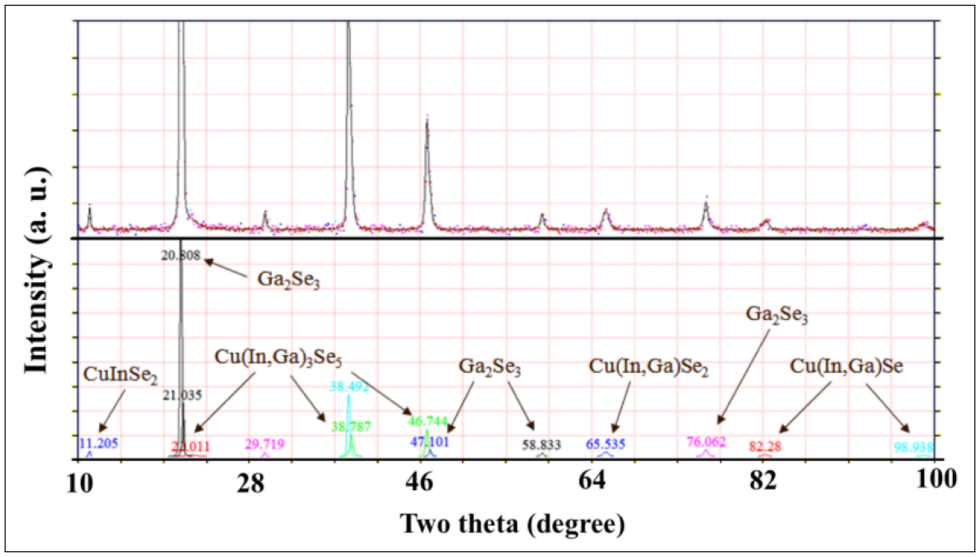

Figure 5.9: XRD spectrum of the CIGS absorber layer obtained starting from In_2Se_3, Ga_2Se_3 and Cu target.

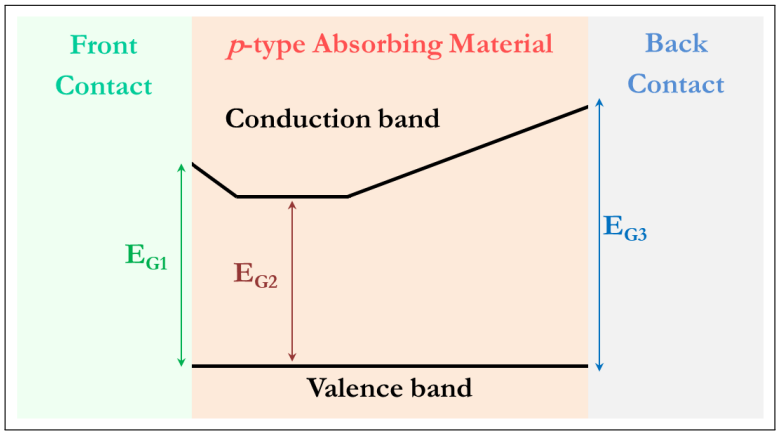

Figure 5.10: Scheme of the band diagram of an optimized Ga double-graded CIGS absorber layer (E_{G3} > E_{G1} > E_{G2}). Adapted from [16]

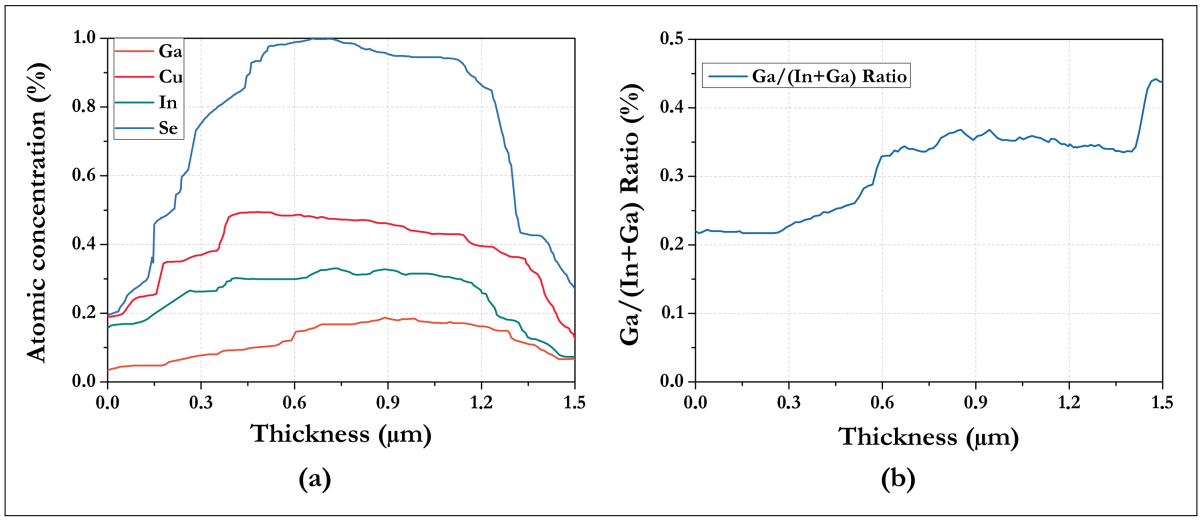

Figure 5.11: (a) SIMS in-depth profile spectrum of the CIGS absorber layer produced starting from In_2Se_3, Ga_2Se_3 and Cu target. The Mo signal was removed in order to make the spectrum more readable. (b) The Ga/(In + Ga) ration along the CIGS absorber layer thickness.

tailored double-graded Ga concentration (Figure 5.10) can lead to a graded energy band gap of CIGS absorber layer and this can increase the efficiency of the device.
The reasons, why it is important to follow this double-graded Ga concentration, can be outlined as follows:

1. The back grading (E_{G3}) will provide an additional drift field for the minority electrons. In this way, there will be an improve of carrier collection and a reduction of back-contact recombination.

2. The front grading at CIGS/CdS interface (E_{G1}) requires to be thin enough (well below 20 nm) in order to let carriers overcome this barrier or pass through it by a tunnel mechanism. In this way, there will be an increase in V_{OC}.

3. A lower energy gap layer (E_{G2}) has to be produced inside the absorber material. This layer, with a thickness of about 1000 nm, can increase the long wavelength absorption and thus supply a higher amount of photo-generated carriers. In this way, it is possible to increase the amount of solar photons absorbed inside the space charge region.

Unfortunately, the precursors prepared with the aforementioned procedure do not produce the desired double graded Ga concentration, as can be seen in the SIMS in-depth profile analysis (Figure 5.11).

Ga_2Se_3 is not the ideal starting material, since gallium is not correctly supplied for a proper reaction with other elements. In particular, Ga_2Se_3 does not release enough Ga during the Cu and In reaction with selenium. The result is an In-rich absorber layer instead of a Ga-rich surface layer. Then, the reactivity of the starting materials has to be adjusted in order to obtain an improved Ga distribution within the absorber layer.

With the aim to achieve this condition, we replaced In_2Se_3 and Ga_2Se_3 precursors with other materials, which can interact more effectively one with each other. By using the process conditions already optimised for the method described above, In_2Se_3 was replaced with InSe, whereas Ga_2Se_3 was substituted with GaSe.

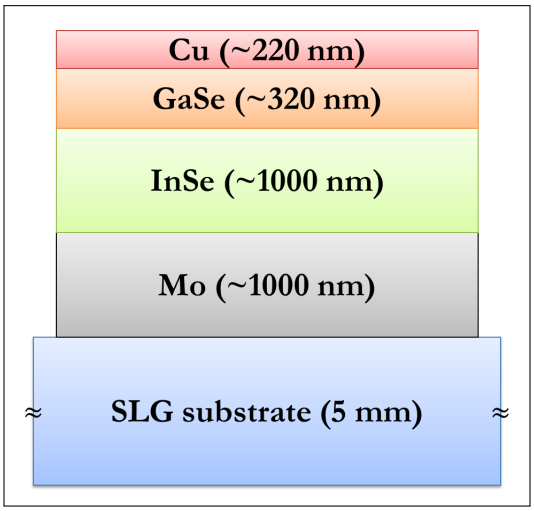

Figure 5.12: Sequence of deposited layers used to obtain the CIGS absorber material starting from InSe, GaSe and Cu target.

5.1.3.1.2 The InSe, GaSe, and Cu system

We chose InSe because it is more reactive than In_2Se_3 and it can probably release In into the absorber material in a more uniform way. InSe allows for the formation of a better CIS crystal structure with correct stoichiometry on a larger portion of the absorber, enhancing both its optical and electronic properties. The InSe film is deposited at a 670 K substrate temperature, by rf magnetron sputtering with a 3.3 W/cm^2 power density, with 0.5 Pa argon pressure (1.2 nm/s deposition rate).

On the other hand, Ga_2Se_3 was replaced with GaSe. GaSe exhibits a lower melting point and decomposes at a lower temperature with respect to Ga_2Se_3. It could release Ga atoms more easily, allowing for a better interaction with other elements, especially with copper. Furthermore, GaSe was found to have a thermal stability similar to that of Ga_2Se_3, and uniform and homogeneous polycrystalline GaSe films can be successfully obtained at deposition temperatures as low as 670 K. GaSe is deposited by rf magnetron sputtering, with a 1.8 W/cm^2 power density with a 0.5 Pa argon pressure (0.3 nm/s deposition rate).

Figure 5.12 displays the InSe, GaSe, and Cu deposition sequence. Cu can be sputtered onto GaSe at the same deposition temperature (about 670 K) without causing any collateral issues inside the precursor, while it improves the surface uniformity. Figure 5.13a and 5.13b show the XRD spectra of the as-deposited precursor layers and of the same film after the selenisation process. Furthermore, the superficial uniformity of the precursor stack and of the absorber layer immediately after the selenisation step are respectively shown in Figure 5.14a and 5.14b.

If we compare this CIGS absorber layer with the prepared one starting with In_2Se_3 and Ga_2Se_3, it results more compact and dense exhibiting an average grain size larger than 1 μm.

The highest photovoltaic parameters obtained with this absorber material are as follows: V_{OC} = 560 mV, J_{SC} = 34.92 mA/cm^2, FF = 64%, and efficiency equal to 12.51%. Measurements were performed at standard conditions. This data exhibit unexpectedly low values of V_{OC} and FF. These limitations were attributed to the fact that gallium, which is less reactive than indium, tends to diffuse towards the bottom and ends up being drained away from the film surface.

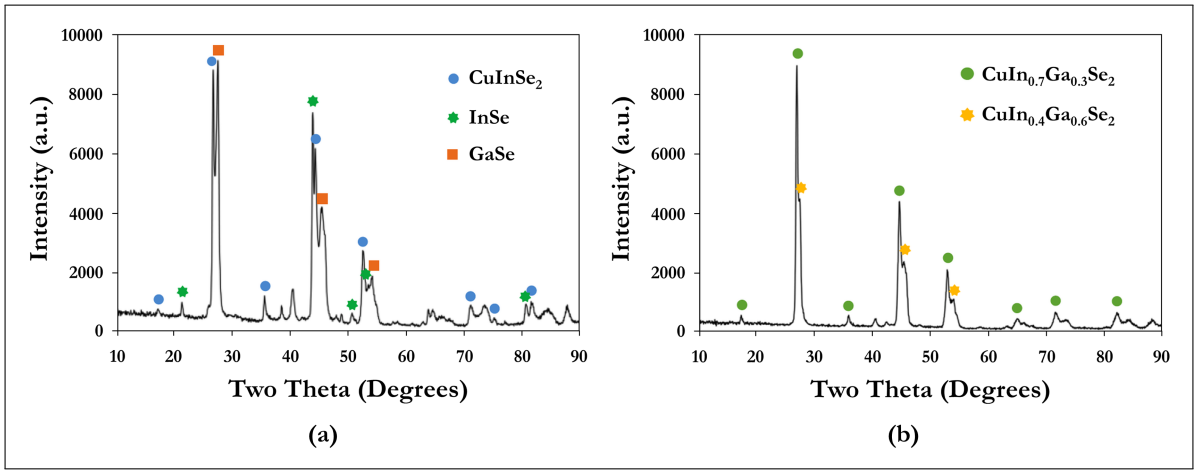

Figure 5.13: Grazing incidence XRD spectra of (a) InSe–GaSe–Cu-based precursor layers and (b) the same sample after selenisation.

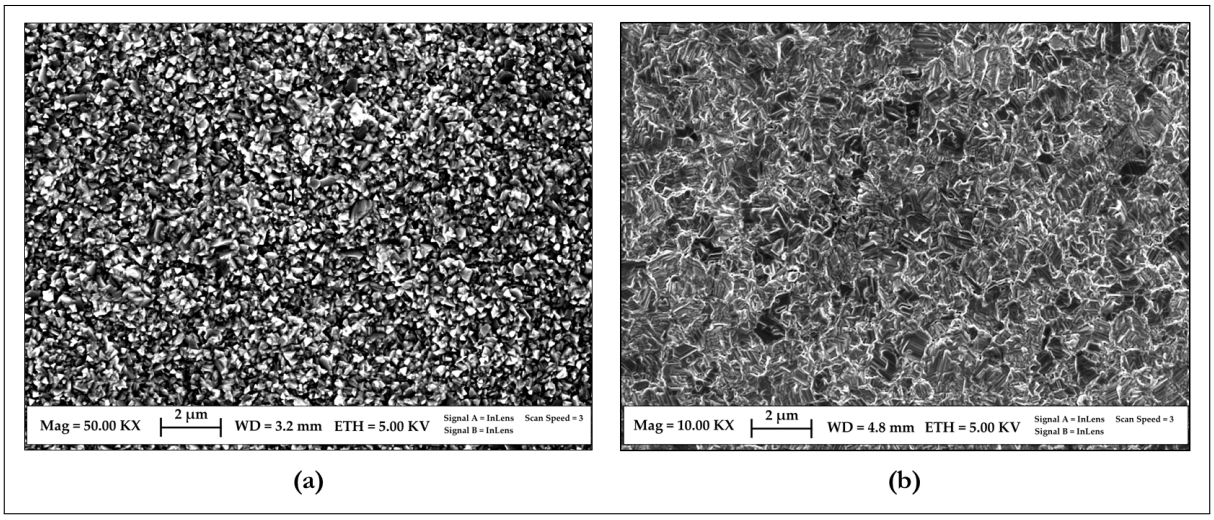

Figure 5.14: SEM morphology image of (a) the as-deposited InSe-GaSe-Cu precursor and (b) the resulting CIGS absorber layer after the selenisation process.

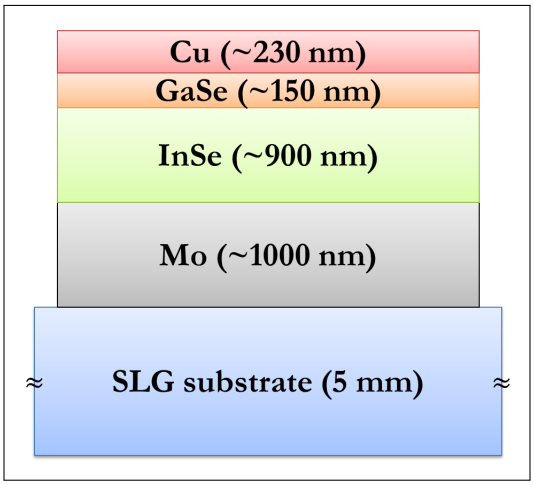

Figure 5.15: InSe-GaSe-Cu-GaSe sequence of deposited layers, in order to obtain the CIGS absorber.

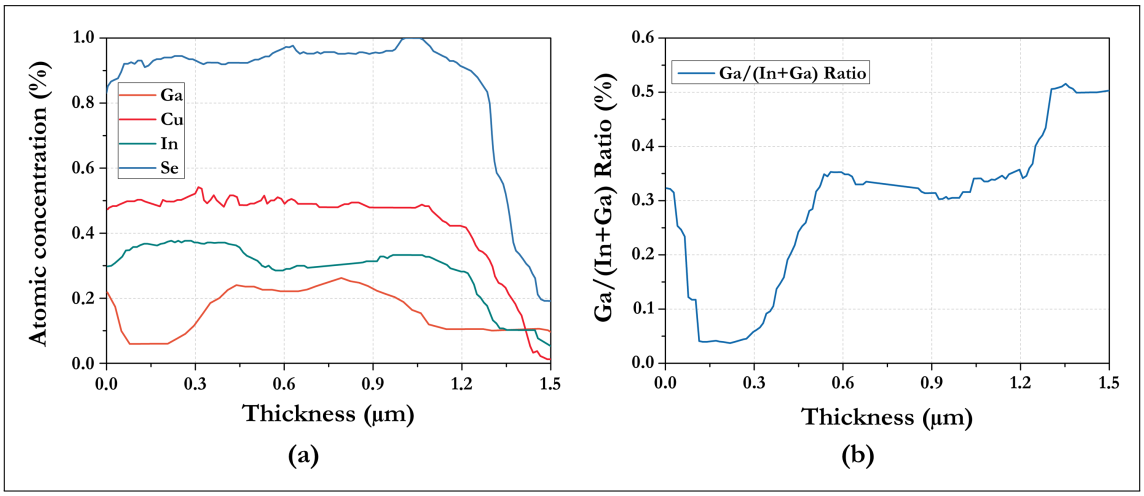

Figure 5.16: (a) SIMS in-depth profile spectrum of the CIGS absorber layer produced with InSe-GaSe-Cu-GaSe stacked layers. The Mo signal was removed in order to make the spectrum more legible. (b) The Ga/(In + Ga) ratio along the CIGS absorber layer thickness.

5.1.3.1.3 The InSe-GaSe-Cu-GaSe layer sequence

With the aim to realise a CIGS layer exhibiting more gallium near the surface, a change, in the sequence of the layer deposition, was carried out.
The new process consists in the following deposition sequence: 900-nm-thick InSe film, 150-nm-thick GaSe film, 230-nm-thick Cu film and 250-nm-thick GaSe film on top of the initial Mo layer (see Figure 5.15).
In the section 5.2.1, we will investigate the deposition parameters that must be met in order to obtain reproducible CIGS absorber layer for obtaining high efficiency solar cells.

The SIMS analysis (Figure 5.16) shows that this new absorber layer includes more gallium in proximity of the surface. Moving away from the surface, the Ga concentration decreases and then increases again when approaching the back contact.

The highest photovoltaic parameters obtained with this method yielded the following parameters: V_{OC} = 576 mV, J_{SC} = 38.13 mA/cm^2, FF = 74%, and efficiency equal to 16.25%. Measurements were performed at standard conditions.

With this last method, an enhancement in the performance of solar cells was observed, exhibiting energy conversion efficiencies above (15 ÷ 16)%. This is probably due to the V-shaped Ga distribution, which helps to maximize both the photovoltage and the photocurrent of the solar cell. A good control of the Ga concentration is the key to engineer the profile of the energy band gap of the absorbing material, which in turn plays a fundamental role in the operation of the solar cell.

We applied this fabrication process to ceramic substrates, and the resulting precursor seemed to maintain a morphology of the same quality (Figure 5.17). The highest performing solar cells obtained

[2]All parameters refer to an area of around 1 cm^2 (if not expressly stated otherwise). The photovoltaic parameters were collected over 20 samples for every method. Each sample included 4 cells; therefore, we tested about 80 cells for each method to make sure that the whole fabrication process was indeed reproducible (as the standard deviation indicates). At any rate, we here reported the PV parameters of solar cells representative of each method. Generally, we have chosen to show the photovoltaic parameters of devices made with layers on which morphological, structural, and compositional investigations were carried out.

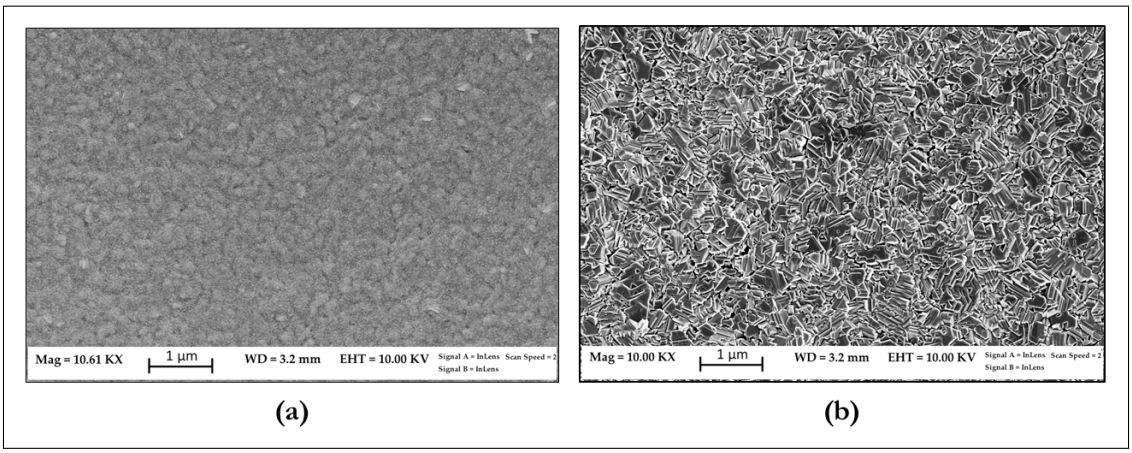

Figure 5.17: SEM morphology image of (a) the as-deposited InSe-GaSe-Cu-GaSe precursor on ceramic and (b) the resulting CIGS absorber layer after the selenisation process.

Table 5.2: Comparison between the photovoltaic parameters of 1 cm^2 CIGS-based solar cells, fabricated with the different methods on glass and ceramic substrates at the ThiFiLab. The data are referred to the J-V characteristics of Figure 5.18.

Sequence of layer thickness (nm)				**Sample (#)**	**Substrate (Material)**	**V_{OC} (mV)**	**J_{SC} (mA/cm^2)**	**FF (%)**	**Eff. (%)**
In_2Se_3 (1000)	Ga_2Se_3 (330)	Cu (180)	––	2012	SLG	530	35.16	0.58	10.81
InSe (1000)	GaSe (320)	Cu (220)	––	3097	SLG	560	34.92	0.64	12.51
InSe (900)	GaSe (150)	Cu (230)	GaSe (250)	4025	SLG	576	38.13	0.74	16.25
InSe (1000)	GaSe (250)	Cu (350)	GaSe (450)	1113	Ceramic	610	36.79	0.61	13.79

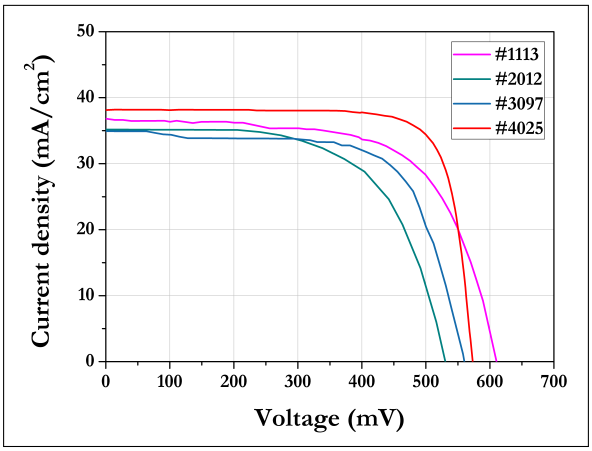

Figure 5.18: Comparison between J-V characteristics of four different solar cells reported in Table 5.2. (a) #2012: first method — (In_2Se_3–Ga_2Se_3–Cu) on SLG. (b) #3097: second method — (InSe–GaSe–Cu) on SLG. (c) #4025: third method — (InSe–GaSe–Cu–GaSe) on SLG. (d) #1113: third method — (InSe–GaSe–Cu–GaSe) on ceramic. All Measurements performed at 298 K under 100 mW/cm^2 A.M. 1.5 filtered light (standard conditions).

with this method displayed the following parameters: V_{OC} = 610 mV, J_{SC} = 36.79 mA/cm^2, FF = 61%, and efficiency equal to 13.69%. Measurements were performed at standard conditions.

As one can see from the data[2] in Table 5.2 and in Figure 5.18, there is a reduction in the photocurrent of solar cells deposited on ceramic tiles compared to the solar cell grown on SLG.
A possible explanation is that commercially available ceramic tiles are characterised by a high number of macroscopic surface defects. Voids and prominences are larger than the combined thickness of all the deposited films, which cannot fill or cover them completely. If the ceramic surface is covered by glassy enamel, with a composition similar to the SLG, the surface is much smoother, making the ceramic a suitable substrate for a thin-film deposition. The residual defectiveness requires the use of a material poorer in Cu, as compared with CIGS grown on SLG, to avoid a deleterious segregation of Cu-rich binary phases, such as Cu_2Se, inside the non-uniformities of the ceramic substrates surface. A Cu-poor material is obtained by increasing the In concentration. However, this has a negative influence on the Ga-concentration profile as more indium makes it flatter, inevitably leading to a loss of the benefits that come from a V-shape distribution.

5.2 Research work

By following the last described method, a fine-tuning of the absorber material energy band gap is achieved, and devices with an efficiency of (15 ÷ 16)% were assembled on SLG.
For this reason, in my PhD research project I have investigated the process requirements that must be met to obtain high-quality precursors on a soda-lime glass substrate needed for the preparation of reproducible high-efficiency CIGS solar cells [19].
Moreover, we tried to export the fabrication process developed on soda-lime glass and ceramic tiles to flexible substrates, such as thin metal foils.

In the following two sections, I will exhibit the main experimental results obtained to develop these two aspects.

5.2.1 Analysis of the deposition requirements

The requirements that we have found to be essential to obtain a reproducible CIGS absorber layer for solar cells with an efficiency greater than 16%, starting from InSe, GaSe and Cu targets and using sputtering and selenisation techniques, can be summarised as follows.

1. **Quality of starting materials**
   The targets should be very compact, with a density higher than 97% to avoid cracking or damage problems during the sputtering deposition. To obtain such a high density, it is necessary to produce the targets by vacuum hot-pressing at 670 K and 200 Kbar pressures. Furthermore, the minimum purity of the targets need to be 99.999%.
   In our sputtering system, we typically use target with a diameter of 7.62 cm, thickness of 0.635 cm and 99.999% purity prepared by vacuum hot-pressing. Figure 5.19 shows some of our targets bonded to the target holder.

2. **Tuning of sputtering power density**
   In order to analyse the influence of sputtering power on deposited films, we deposited a series of

Figure 5.19: Targets typically used in our laboratory.

Table 5.3: Deposition parameters and the corresponding atomic compositions of the InSe films.

InSe sample #	[1]SP (W/cm^2)	[2]T_S (K)	In (at.%)	Se (at.%)	Ar (at.%)
1	3.8	470	51.9	45.1	3.0
2	3.8	670	50.9	49.1	––
3	3.8	730	50.8	49.2	––
4	3.2	670	47.8	52.2	––

Note:

[1] SP = Sputtering Power Density

[2] T_S = Substrate Temperature

films with different power density.

The strategy followed for InSe was to deposit by rf magnetron sputtering 1 µm-thick InSe films on Mo-covered SLG substrate with different sputtering power density.

These films were characterised by SEM on a Tescan combined with an Oxford Instruments Energy Dispersive X-ray (EDX) Spectroscopy System in order to measure the elemental compositions of the samples. EDX was carried out using an accelerating voltage of 20kV. The main results are summarised in Table 5.3.

We have observed that, when the rf sputtering power density is less than 3.2 W/cm^2, the InSe target surface becomes dark and this indicate that some Se is sputtered back onto the target surface. In the case of sputtering power density higher than 3.8 W/cm^2, there are some In little droplets segregated on top of the target surface. In order to obtain stoichiometric InSe films, it is fundamental that the target surface does not change its color and does not segregate any In-drops. The most uniform and stoichiometric InSe films are obtained by using 3.8 W/cm^2 power

Table 5.4: Deposition parameters and the corresponding atomic compositions of the GaSe films.

GaSe sample #	[1]SP (W/cm^2)	[2]T_S (K)	Ga (at.%)	Se (at.%)
5	3.4	670	50.0	50.0
6	2.2	670	50.1	49.9

Note:

[1] SP = Sputtering Power Density

[2] T_S = Substrate Temperature

density.

Also in the case of GaSe films, the same strategy was followed. We deposited by rf magnetron sputtering 500 nm-thick GaSe on Mo-covered SLG substrates by using different sputtering power density.

It was noted that GaSe thin films composition does not depend on the power density variation, as shown in Table 5.3. We have chosen to deposit GaSe at low deposition rate to prevent overheating of the target surface.

3. **Substrate temperature**

To analyse the influence of substrate temperature on deposited films, we deposited a series of films at different substrate temperature.

Being the most critical layer, InSe was deposited at three different temperatures, namely 470 K, 670 K and 730 K. At low temperature (namely 470 K), the film morphology results uniform and smooth (Figure 5.20a). Unfortunately, the microprobe analysis evidences some Ar- and Se-excesses are incorporated. The presence of argon and Se-excess can cause sticking problems when the InSe film reacts with GaSe and Cu. Furthermore, the lack of peaks in X-rays analysis can indicate that the InSe films deposited at low temperature are amorphous (Figure 5.20b). This measurement was made using a powder diffractometer operating with $CuK_{\alpha 1}$ (λ = 1.5418 Å) in the theta-2theta configuration.

Considering the InSe films deposited at 670 K, they appear uniform and smooth but at the electron microscope they exhibit some rods (see Figure 5.21a). From the X-ray analysis (Figure 5.21b), it is clear that these films are well crystallised but they contain several In-Se phases. In particular, they exhibit diffraction peaks corresponding to both InSe and In_2Se_3 polycrystalline phases. Peaks at 10.63° and 21.34°, are related to the (003) and (006) orientations of the InSe phase (R-3m space group). Instead, the 27.62°, 29.4°, 31.37°, 44.13°, 67.3° peaks are associated to the γ-In_2Se_3 polycrystalline phase. The substrate shows the 40.21°, 73.1°, and 86.85° reflections, which correspond to the Mo cubic phase.

Finally, when the InSe deposition is made at a higher substrate temperature (namely 730 K), even though they contain almost the only InSe phase (Figure 5.22b) they present some unevenness, like voids or ridges (Figure 5.22a). In particular, from the XRD pattern, the peaks located at around 10.6°, 21.3°, 44.7°, 45.3° and 50.6° reflections show a better oriented InSe material. Instead,

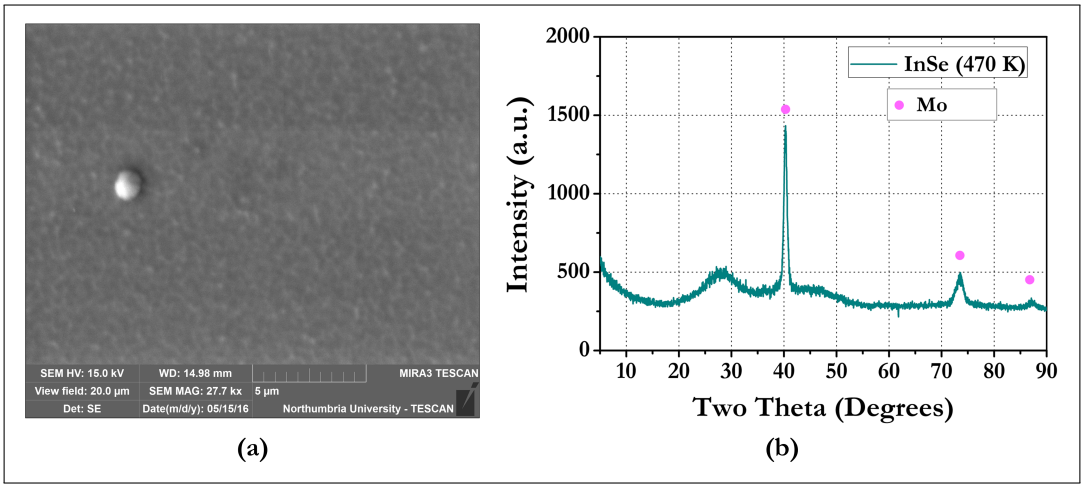

Figure 5.20: Plan-view SEM image (a) and X-ray diffraction pattern (b) of an InSe film deposited at a substrate temperature of 470 K (sample #1) on Mo-covered soda-lime glass.

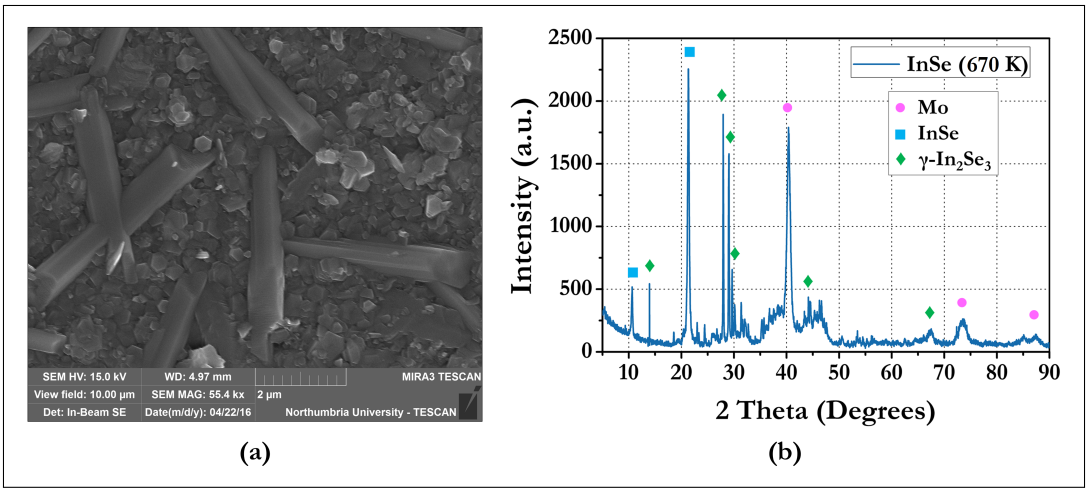

Figure 5.21: Plan-view SEM image (a) and X-ray diffraction pattern (b) of an InSe film deposited at a substrate temperature of 670 K (sample #2) on Mo-covered soda-lime glass. The presence of InSe roads are clearly evident.

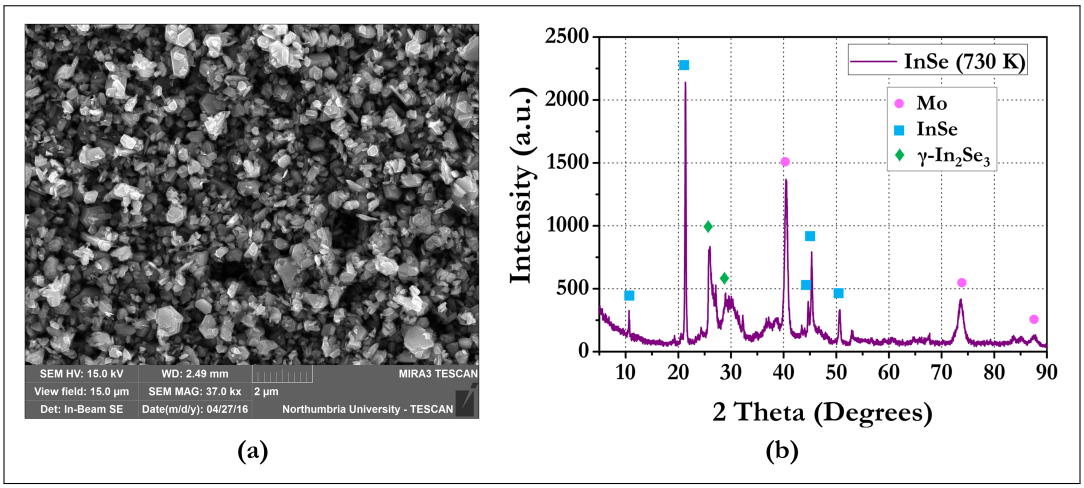

Figure 5.22: Plan-view SEM image (a) and X-ray diffraction pattern (b) of an InSe film deposited at a substrate temperature of 730 K (sample #2) on Mo-covered soda-lime glass. The black regions in the SEM image correspond to holes that are probably due to a separation of crystalline phases.

Table 5.5: Sequence of deposited layers to obtain the precursor for CIGS, with its deposition parameters and deposited thicknesses.

Step sequence	Film deposited	Sputtering technique	Argon flux (sccm)	Deposition rate (nm/sec)	[1]T_S (K)	[2]SP (W/cm^2)	Thickness (nm)
1	InSe	rf magnetron	20	1.9	670	3.8	900
2	GaSe	rf magnetron	20	0.6	670	3.4	150
3	Cu	dc magnetron	15	0.8	670	2.0	230
4	GaSe	rf magnetron	20	0.6	670	3.4	250

Note:

[1] T_S = Substrate Temperature

[2] SP = Sputtering Power Density

the peaks at 26.7° and 27,3° are related to the In_2Se_3 hexagonal phase.

The uniformity and smoothness of each single films are very important in order to have a good mixing between InSe, GaSe and Cu layers.

Moreover, the chemical and physical stability of the InSe layer is of primary importance when the reactivity with Cu is taken into consideration. The grain size of the InSe crystallites controls the speed at which In, Cu and Se react. If the grain size is too small (less than 1 μm) then the elements react quickly producing local not uniformities such as spatially separated binary phases, such as In_2Se_3 and Cu_2Se.

Consequently, the InSe film deposited at 670 K is the best suited as In supplier because it presents a lot of crystallites (1 ÷ 2) μm large and (6 ÷ 8) μm long. This crystallites are bigger if compared with the average dimension of the crystalline grains of the InSe film deposited at 730 K.

4. **Se evaporation rate during selenisation**

The influence of selenium evaporation rate during the selenisation treatment was investigated by the realisation of precursors following the optimum deposition conditions previously analysed and summarised in Table 5.5. These precursors are then selenised by using different Se evaporation rate. In particular, the selenisation is carried out evaporating pure Se from a graphite crucible placed in a vacuum chamber. The substrate is heated up by Halogen lamps able to reach 770 K in less than 4 min. Figure 5.23 and 5.24 show a chart and a photography of our selenisator system, respectively.

The characterisation of the samples indicates that a suitable evaporation rate for Selenium is on the order of 1 μm/s, since higher evaporation rates produce $Cu(In,Ga)Se_2$ thin films with bigger grains interspersed with a lot of voids, as it is shown in Figure 5.25a and 5.25b. This is probably due to the reaction that is too fast when a high evaporation rate of Se is used. As a result, a chaotic growth is obtained.

We can conclude that the critical parameters are: targets quality, sputtering power density, substrate temperature and Se evaporation rate and we have put in evidence how they can influence the quality of the resulting absorber layers. Therefore, the use of these precautions is fundamental in order to obtain high quality and reproducible $Cu(In,Ga)Se_2$ film with the V-shaped Ga distribution for PV applications.

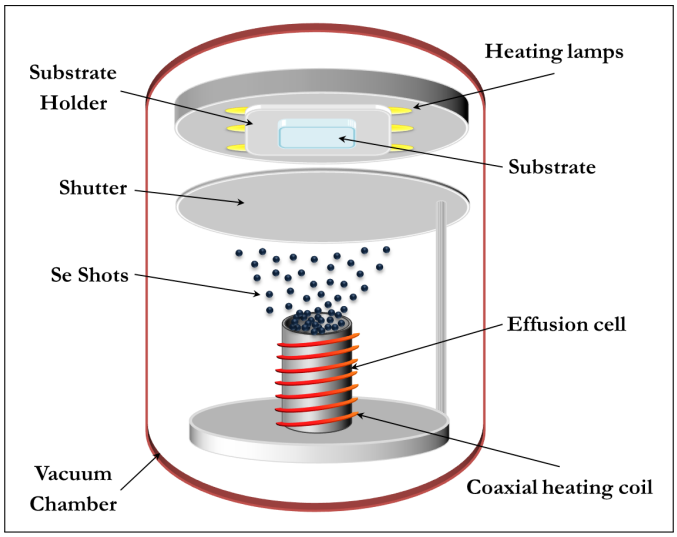

Figure 5.23: Basic chart of the selenisator system.

Figure 5.24: Photography of our selenisator system.

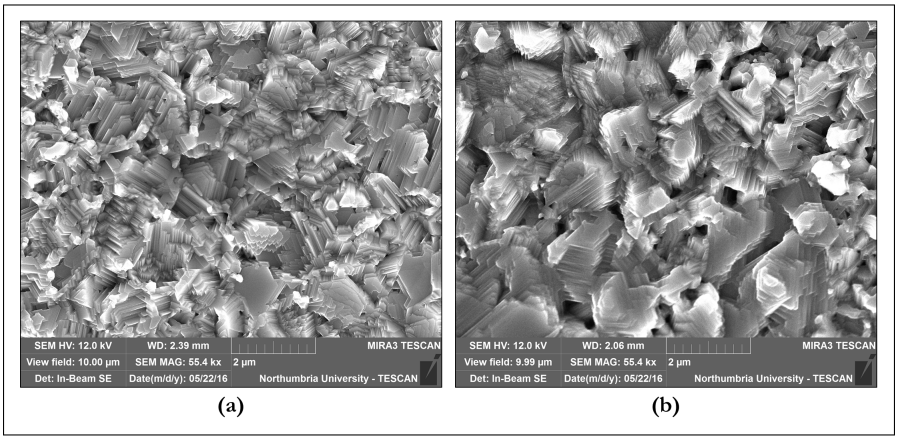

Figure 5.25: SEM images of the morphology of two different CIGS absorber layer after the selenisation process. In Figure (a), the Se evaporation rate is on the order of 1 µm/s. In Figure (b), the Se evaporation rate is higher than 1 µm/s an the black points correspond to holes, which are not present in the (a) case.

In fact, when this films are used as absorber in a Cu(In,Ga)Se_2/CdS solar cells, the devices have given an efficiency higher than 16%.

5.2.2 CIGS on flexible substrate

Flexible thin-films solar cells represent new frontier in PV technology, since it can be used for novel applications due to their low cost and light weight. In particular, they can be used in BIPV on curved surfaces or in textiles and automotive integrations to charge most of the electronic devices.

In this section, I will present the research done with the aim of exporting our fabrication process developed for soda-lime glass and ceramic substrates to flexible substrates, such as thin metal foils.

The use of a flexible substrate introduced new technological challenges, which we can summarise as follows.

1. **Choice of thin metal foil substrate**
   The selection of a proper substrate for our solar cell represents a fundamental challenge. The substrate needs to be:

   - Vacuum compatible, because it must not out-gassing during the deposition processes.
   - Thermally stable, as it has to withstand process temperatures (also over 700 K).
   - Suitable thermal expansion coefficient to avoid problem of film adhesion or creaking.
   - Chemical stability, for example, it does not have to react with selenium during the selenisation or with other elements during the fabrication process. Furthermore, the substrate does not have to release impurity, that can diffuse into the absorber layer.
   - Smooth surface, as the surface roughness can cause electrical shunting problems.
   - Low cost in order to produce low cost devices.

   Due to the process temperatures, the only substrates available are thin-metal foils. We have tested both nickel foils and stainless steel foils, which are both vacuum compatible.
   Stainless steel foil is one of the most attractive candidate for use as a flexible substrate material for CIGS solar cells, because it is stable at the high process temperatures and it is also commercially available. On the other hand, nickel foils are a little more expensive than stainless steel sheets, but it has low thermal expansion coefficient ($\alpha = 13.0 \times 10^{-6}\ K^{-1}$) and then it is potentially a better choice to have a good film adhesion.
   The main problem that arise here is the diffusion of impurities from the substrate surface into the absorber layer, then there is the necessity of a barrier layer.

2. **Barrier layer between the metallic substrates and the active layer**
   If the metallic substrates allow to deposit all the layers at the high process temperatures with the advantageous of proper deposition of the CIGS thin film, unfortunately, they present the great disadvantage of the diffusion of substrate constituent elements into the absorber layer. This diffusion obviously adversely affects the solar cells performances, then it is necessary to separate the substrate from the solar cell device with a barrier layer.
   It should be highlighted that the use of a barrier layer is crucial also in order to provide an electrical insulation between the conductive substrate and the monolithically interconnected solar

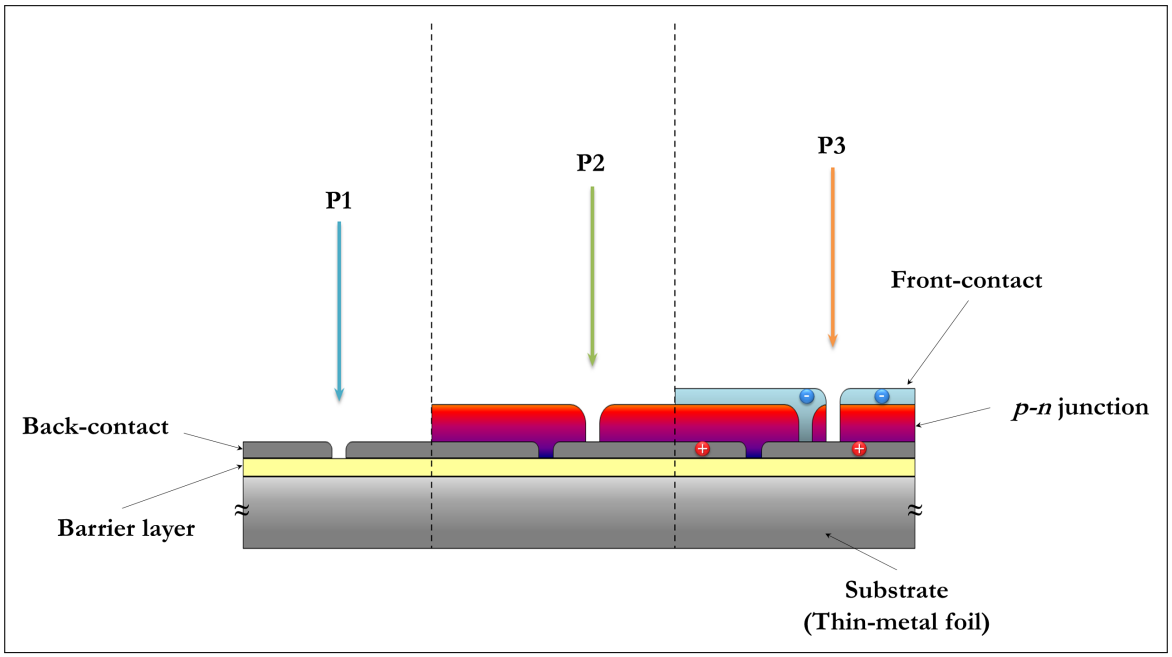

Figure 5.26: Scheme of scribing sequences for monolithically interconnected solar modules on flexible thin metal foil.

cells, as shown in Figure 5.26. Therefore, we need to use barrier layer materials that are both good insulator, good diffusion barrier and above all, they have to survive at the process temperatures without forming cracks or losing their insulating properties.

From literature [20, 21, 22, 23], SiO_2 and Al_2O_3 are two suitable materials and we have tested both.

We deposited 500 nm-thick of SiO_2 film by rf reactive magnetron sputtering on a nickel foils after the substrate surface cleaning (Appendix B - Cleaning of substrate surface). The deposition was made in an argon plus oxygen atmosphere (20 sccm of Ar + 2 sccm of O_2) with a process total pressure of 1 Pa. Unfortunately, the resulting film is not uniform and moreover does not prevent the diffusion of nickel from the substrate surface, as shown in SEM images (Figure 5.27) and EDS data (Table 5.6).

For these reasons, we chose to deposit 500 nm-thick of Al_2O_3 film by electron-beam evaporation at 470 K and in this way, we obtain a uniform film.

Table 5.6: EDS analysis of 500 nm of SiO_2 deposited by rf reactive magnetron sputtering on a Nickel foil. The film was covered with 50 Å of gold deposited by dc magnetron sputtering. The SEM images are reported in Figure 5.27.

Sample region	O (at.%)	Si (at.%)	Ca (at.%)	Ni (at.%)	Au (at.%)
Black part	63.13	32.62	––	––	4.26
White part	65.77	10.84	1.70	5.86	15.85
Grey part	50.66	42.10	––	5.29	1.97

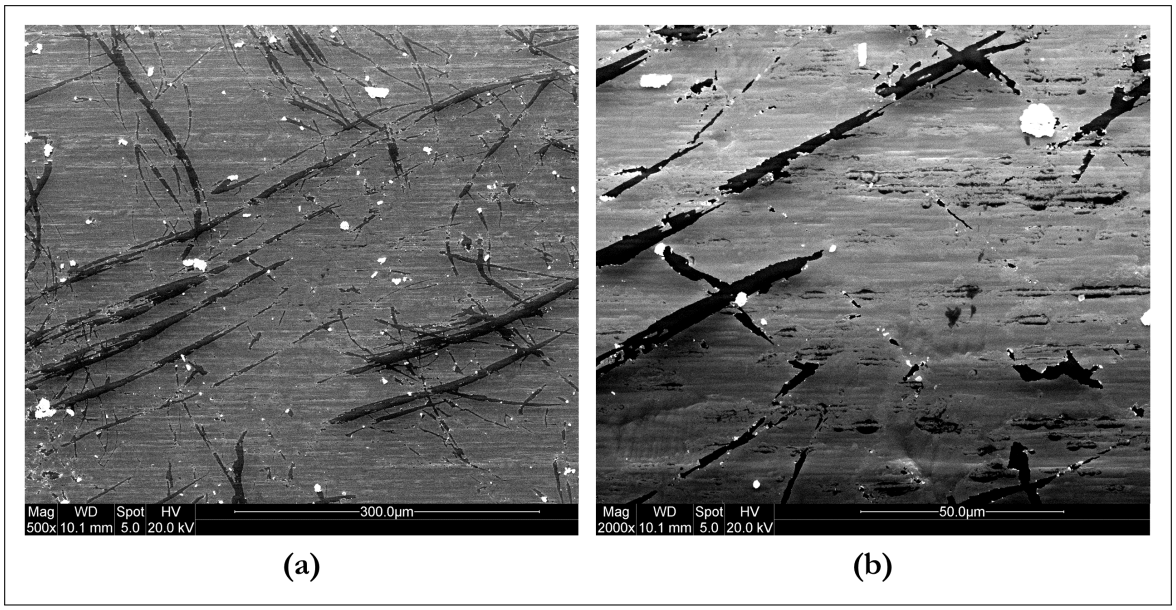

Figure 5.27: SEM images of 500 nm of SiO_2 deposited by rf reactive magnetron sputtering on a Nickel foil. The film was covered with 50 Å of gold deposited by dc magnetron sputtering. The EDS data are reported in Table 5.6.

3. **Absence of sodium**

   Using a sodium-free substrate, there is not the possibility to take advantage of sodium diffusion from the substrate. The absence of Na reduces mainly V_{OC} and F.F.

   We have tested two way to incorporate Na in our CIGS absorber layer with the deposition of a 100 Å of NaF by electron-beam evaporation at 370 K:

   (a) The direct deposition of NaF before the selenisation process, as shown in Figure 5.28a.

   (b) A two selenisation method, in which the NaF was introduced immediately after the first selenisation, as shown in Figure 5.28b.

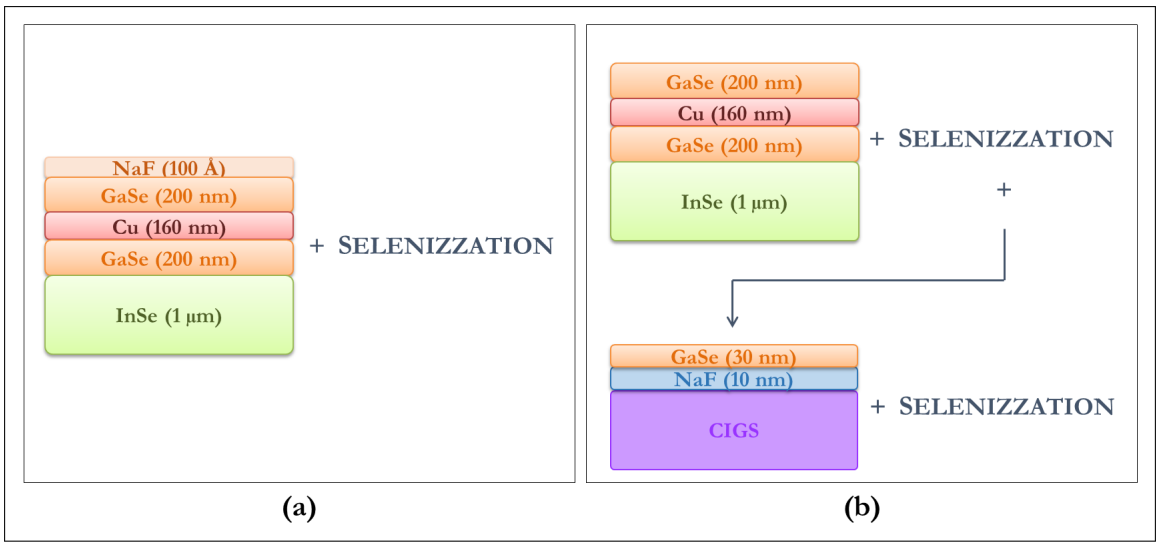

Figure 5.28: Scheme of the two different process used to incorporate sodium into the CIGS absorber layer.

Unfortunately, the photovoltaic parameters obtained for devices realised on nickel substrate are

considerably lower (efficiency in the range of (2 ÷ 3)%) than those commonly obtained on glass and on ceramic. The possible causes are represented by two factors: the growth and selenisation temperature and the buffer layer. In order to understand the origin of these negative results, we have characterised the CIGS thin film by SEM and EDS in four different steps of our process:

1. Sample a: the precursor (InSe-GaSe-Cu-GaSe) as deposited (Figure 5.29a).

2. Sample b: the precursor after selenisation (Figure 5.29b).

3. Sample c: the precursor after the deposition of NaF and after selenisation (Figure 5.29c).

4. Sample d: the absorber layer obtained with the two steps selenisation process (Figure 5.29d)

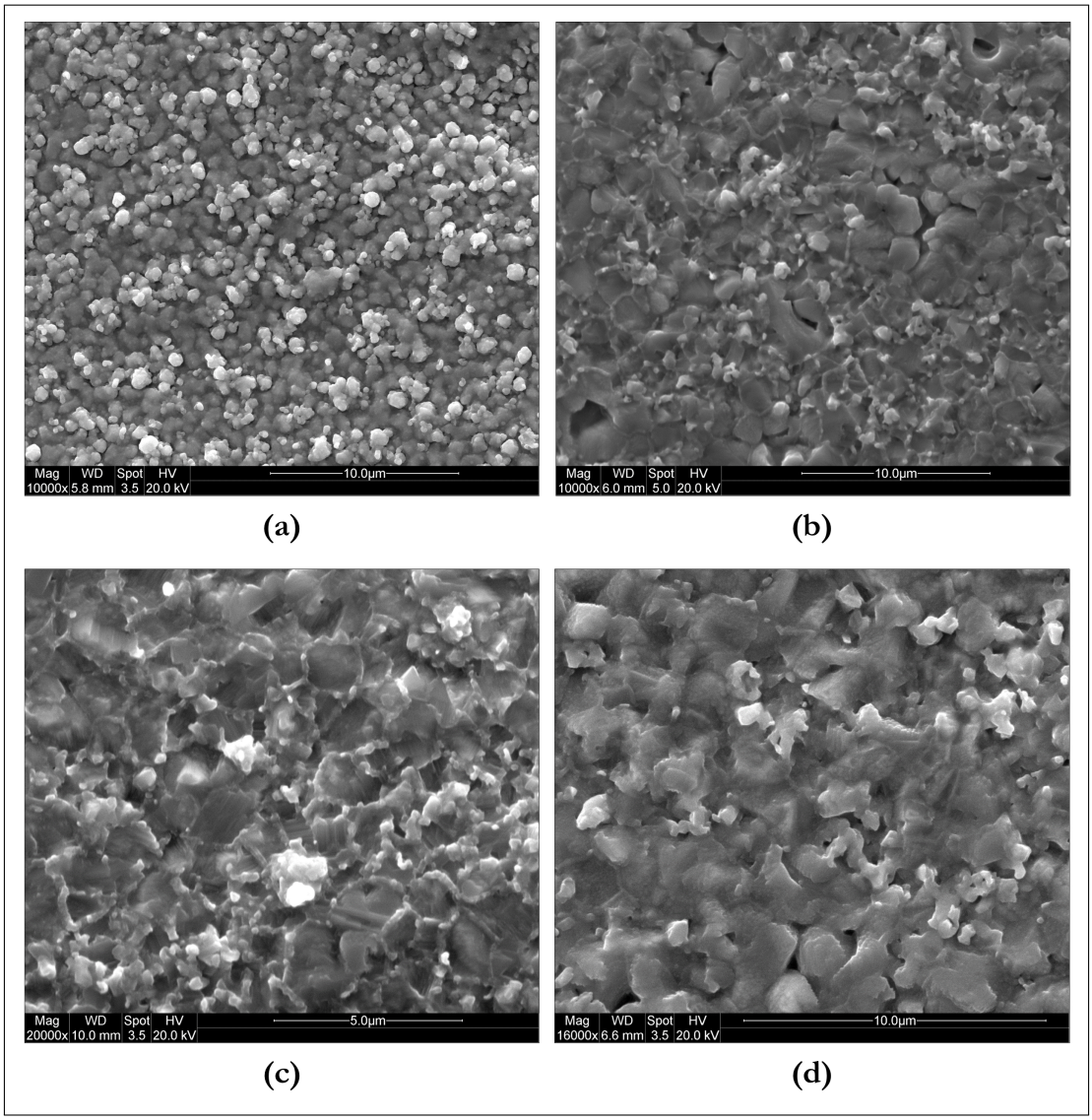

Figure 5.29: SEM images of: (a) a precursor (InSe-GaSe-Cu-GaSe) as deposited (Sample a), (b) the same precursor after the selenisation (Sample b), (c) a precursor after the deposition of NaF and the selenisation (Sample c) and finally (d) the absorber layer obtained with the two steps selenisation process (Sample d). The EDS data are reported in Table 5.7.

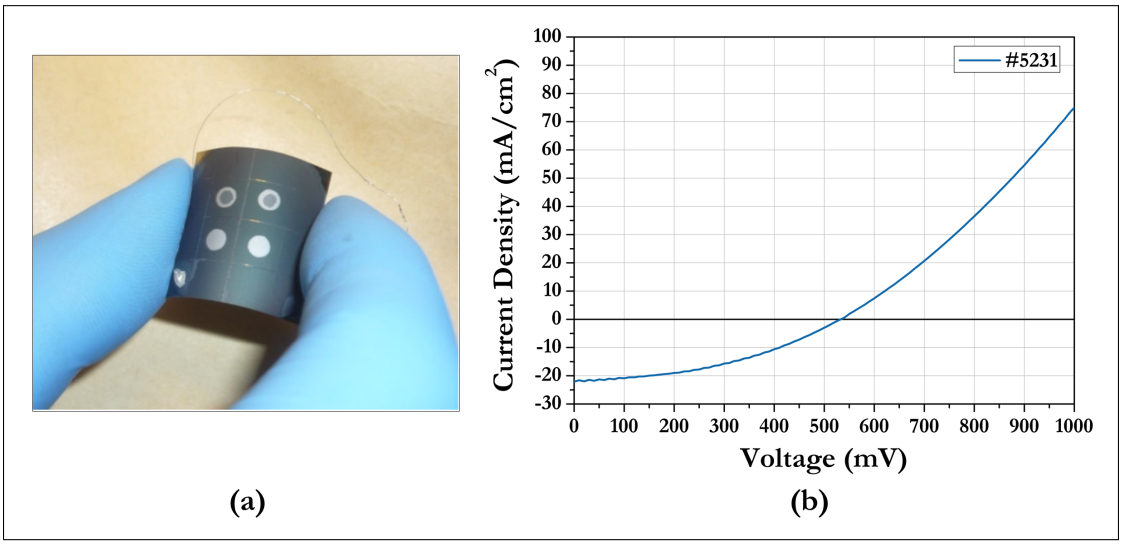

Figure 5.30: (a) Photograph of our CIGS solar cell on stainless steel substrate. (b) J-V characteristic of our best device. Measurement performed at 298 K under 1000 mW/cm^2, A.M. 1.5 filtered light.

As shown in Table 5.7, a presence of (2 ÷ 3) at.% of nickel was detected into the absorber layer in all the samples prepared as described above. We think that the presence of nickel within the *p*-type absorber

Table 5.7: EDS analysis of the films reported in Figure 5.29.

Sample	**Ni** (at.%)	**Cu** (at.%)	**Ga** (at.%)	**Se** (at.%)	**In** (at.%)
a	2.61	31.41	20.35	33.59	12.04
b	2.94	22.85	3.47	48.19	22.55
c	2.62	23.06	4.03	47.47	22.83
d	2.59	23.40	6.41	47.13	20.46

layer represents a *n*-type doping. Furthermore, it drastically change the reaction during the selenisation process. These factors significantly damage the operation of the device.

Also the results obtained on stainless steel substrate have not met our expectations: measurements on the most promising sample yielded a V_{OC} of 540 mV, a J_{SC} of 22.09 mA/cm^2, FF of 40% with an efficiency of only 6.2% (see Figure 5.30). In this case, the main reasons why these values are lower to those commonly obtained with a glass/ceramic substrate can be:

- A problem of film adhesion because of the thermal expansion coefficient of stainless steel at our process temperatures.
- The diffusion of Fe into the absorber layer. We observed the presence of about 1% of Fe into the absorber layer, then the necessity to improve again the barrier layer.
- The need of using optimised sputtering conditions as we have done for SLG and ceramic substrate; in particular, the substrate temperature and the sputtering power density.

Table 5.8: Deposition parameters and corresponding atomic compositions of the InSe films deposited on stainless steel.

InSe sample #	[1]SP (W/cm^2)	[2]T_S (K)	In (at.%)	Se (at.%)	Ar (at.%)	Fe (at.%)
7	3.8	470	51.3	43.8	3.9	1.0
8	3.8	670	52.7	46.1	––	1.2
9	3.8	730	52.2	46.8	––	1.0
10	3.2	670	52.2	44.5	2.3	1.0

Note:

[1] SP = Sputtering Power Density

[2] T_S = Substrate Temperature

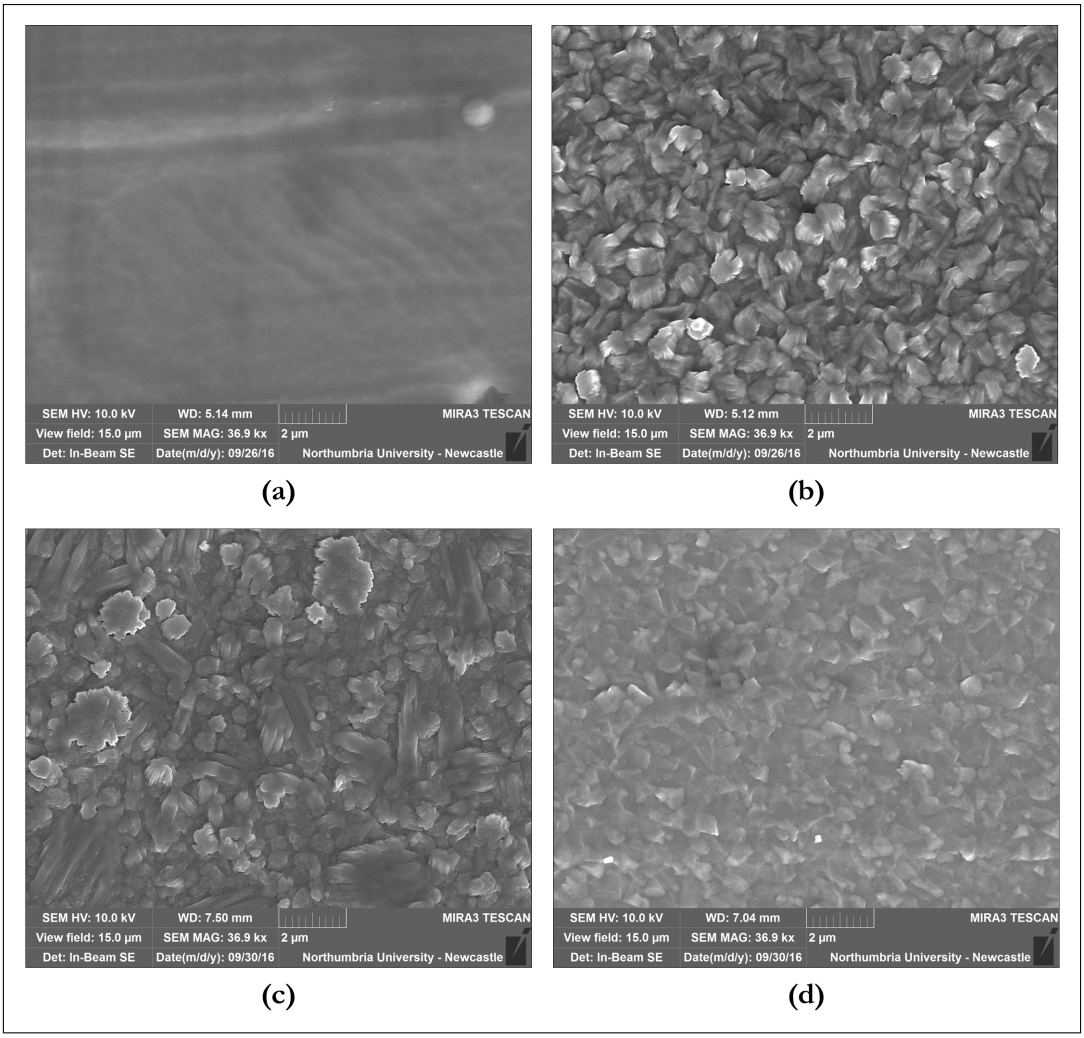

Figure 5.31: Plan-view of SEM images of the sample described in Table 5.8. In particular, (a) correspond to Sample #7, (b) to Sample #8, (c) to Sample #9 and (d) to Sample #10.

For these reason, we begin to analyse the influence of the sputtering condition for the deposition of the critical InSe film. We deposited four InSe thin-film in the same way on SLG and then we

characterised them by SEM and EDS (as shown in Table 5.8 and in Figure 5.31). The data suggest that the effect of substrate temperature on the resulting InSe film is different compared to the same film deposited on SLG, then this aspect needs to be thoroughly investigated.

We should conclude that the main aspects to be considered in order to export our fabrication process developed for SLG and ceramic substrates on flexible substrates are:

- The necessity of a barrier layer between the metallic substrates and the active layer.
- The necessity of incorporate a small amount (about 0.1 at.%) of sodium.
- The need of using optimised sputtering conditions, different from those used for SLG.

References

[1] T. Nakada, D. Iga, H. Ohbo and A. Kunioka. *Effects of sodium on Cu(In,Ga)Se_2-based thin films and solar cells.* Japanese journal of applied physics. IOP Publishing. 1997, Volume 36, Number 2R, Page: 732.

[2] M.A. Contreras, B. Egaas, P. Dippo, J. Webb, J. Granata, K. Ramanathan, S. Asher, A. Swartzlander and R. Noufi. *On the role of Na and modifications to Cu(In,Ga)Se_2 absorber materials using thin-MF (M = Na, K, Cs) precursor layers.* Photovoltaic Specialists Conference. IEEE. 1997, Pages: 359-362.

[3] L.M. Mansfield, I.L. Repins, S. Glynn, M.D. Carducci, D.M Honecker, J.W. Pankow, M.R. Young, C. DeHart, R. Sundaramoorthy and C.L. Beall. *Sodium-doped molybdenum targets for controllable sodium incorporation in CIGS solar cells.* JPhotovoltaic Specialists Conference. IEEE. 2011, Pages: 003636-003641.

[4] P. Salomè, V. Fjällström, A. Hultqvist and M. Edoff. *Na doping of CIGS solar cells using low sodium-doped Mo layer.* IEEE Journal of Photovoltaics. IEEE. 2013, Volume 3, Number 1, Pages: 509-513.

[5] A. Bosio, D. Menossi, G. Rosa and N. Romeo. *Key developments in CIGS thin film solar cells on ceramic substrates.* Crystal Research and Technology. Wiley Online Library. 2014, Volume 49, Number 8, Pages: 620-627.

[6] U.P. Singh and S.P. Patra. *Progress in polycrystalline thin-film Cu(In,Ga)Se_2 solar cells.* International Journal of Photoenergy. Hindawi Publishing Corporation. 2010, Volume 2010. DOI: 10.1155/2010/468147.

[7] T. Wada, N. Kohara, S. Nishiwaki and T. Negami. *Characterization of the Cu(In,Ga)Se_2/Mo interface in CIGS solar cells.* Thin Solid Films. Elsevier. 2001, Volume 387, Number 1, Pages: 118-122.

[8] Wikipedia. (Accessed October 9, 2017).
`https://en.wikipedia.org/wiki/Molybdenum`

[9] J.H. Scofield, A. Duda, D. Albin, B.L. Ballard and P.K. Predecki. *Sputtered molybdenum bilayer back contact for copper indium diselenide-based polycrystalline thin-film solar cells.* Thin Solid Films. Elsevier. 1995, Volume 260, Number 1, Pages: 26-31.

[10] J.L. Shay and J.H. Wernick. *Ternary chalcopyrite semiconductors: growth, electronic properties, and applications: International series of monographs in the science of the solid state.* Elsevier. 2013, Volume 7.

[11] J.L. Shay and J.H. Wernick. *Effects of Ga addition to $CuInSe_2$ on its electronic, structural, and defect properties.* Applied physics letters. API. 1998, Volume 72, Number 24, Pages: 3199-3201.

[12] R.H. Bube. *Photovoltaic materials.* Volume 1, Publisher World Scientific Publishing Company. 1998.

[13] D. Menossi, A. Bosio and N. Romeo. *Fabrication of a Cu(In, Ga)Se_2/CdS thin-film solar cell. In key developments in $CuInGaSe_2$ thin film solar cell.* LAP Lambert Academic Publishing. 1st ed. 2014.

[14] G. Rosa, A. Bosio, D. Menossi and N. Romeo. *How the starting precursor influences the properties of polycrystalline $CuInGaSe_2$ thin films prepared by sputtering and selenization.* Energies. Multidisciplinary Digital Publishing Institute. 2016, Volume 9, Number 5, Page: 354.

[15] M. Gloeckler and J.R. Sites. *Band-gap grading in Cu(In, Ga)Se_2 solar cells.* Journal of Physics and Chemistry of Solids. Elsevier. 2005, Volume 66, Number 11, Pages: 1891-1894.

[16] M.A. Contreras, J. Tuttle and A. Gabor. *High efficiency Cu(In, Ga)Se_2-based solar cells: processing of novel absorber structures.* IEEE Photovoltaic Specialists Conference-1994. IEEE. 1994, Volume 1, Pages: 68-75.

[17] N.E. Gorji and M. Perez, U. Reggiani and L. Sandrolini. *A new approach to valence and conduction band grading in CIGS thin film solar cells.* International Journal of Engineering and Technology. IACSIT Press. 2012, Volume 4, Number 5, Page: 573.

[18] T. Dullweber, U. Rau, M.A. Contreras, R. Noufi and H.W. Schock. *Photogeneration and carrier recombination in graded gap Cu(In, Ga)Se_2 solar cells.* IEEE Transactions on Electron Devices. IEEE. 2000, Volume 47, Number 12, Pages: 2249-2254.

[19] A. Bosio, G. Rosa, S. Mazzamuto, A. Romeo, F. Piccinelli and N. Romeo. *The influence of compound target preparation, sputtering power and substrate temperature on the achievement of Cu(In,Ga)Se_2 precursors suitable to get high efficiency solar cells.* Proceedings of 32th European Photovoltaic Solar Energy Conference. 2016, Pages: 1233-1236.

[20] F. Kessler and D. Rudmann. *Technological aspects of flexible CIGS solar cells and modules.* Solar Energy. Elsevier. 2004, Volume 77, Number 6, Pages: 685-695.

[21] F. Kessler, D. Herrmann and M. Powalla. *Approaches to flexible CIGS thin-film solar cells.* Thin Solid Films. Elsevier. 2005, Volume 480, Pages: 491-498.

[22] R. Wuerz, A. Eicke, M. Frankenfeld, F. Kessler, M. Powalla, P. Rogin and O. Yazdani-Assl. *CIGS thin-film solar cells on steel substrates.* Thin Solid Films. Elsevier. 2009, Volume 517, Number 7, Pages: 2415-2418.

[23] J.M. Delgado-Sanchez, N. Guilera, L. Francesch, M.D. Alba, L. Lopez and E. Sanchez. *Ce-*

ramic barrier layers for flexible thin film solar cells on metallic substrates: a laboratory scale study for process optimization and barrier layer properties. ACS applied materials & interfaces. ACS Publications. 2014, Volume 6, Number 21, Pages: 18543-18549.

Chapter

6

Cu-based delafossite as a new material for photovoltaics

In this chapter, I will present the last part of my PhD project research: a study of new rare earth-free materials for photovoltaic applications.
This research is the result of a collaboration between our laboratory and the CNR Institute of Materials for Electronics and Magnetism (IMEM), in Parma. We tried to obtain novel p-type transparent conducting oxides (TCOs) to be used as transparent back contacts in bifacial CIGS- and CdTe-based solar cells.
I will focus on the reasons why we chose copper-based delafossite as a p-type TCO and on the sputtering deposition process. Finally, I will report on the main experimental results.

6.1 Transparent conducting oxides

In recent decades, the development of transparent electronics is a goal in the field of advanced electronics and therefore TCOs are fundamental materials for this purpose.
TCOs are compounds that combine both high electrical conductivity (carrier concentrations higher than 10^{20} cm^{-3}) and transparency to visible light (optical energy band gap greater than 3 eV) in a single material [1, 2]. The main approach to obtain these two antagonist properties is to use oxides with a wide energy band gap, which favours the transparency, doped with a significant amount of charge carriers, that can be either holes (*p*-type) or electrons (*n*-type). As TCOs can be produced with either *n*-type or *p*-type conductivity, they can be used in many different applications including solar cells, transparent transistors, organic light-emitting diodes and liquid-crystal displays, as shown in Figure 6.1.

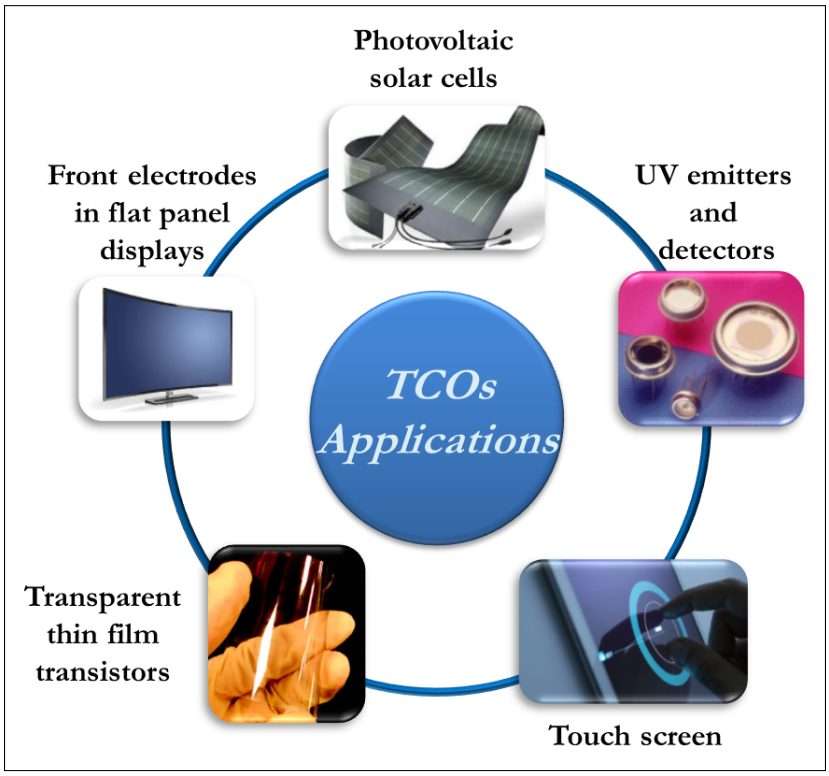

Figure 6.1: Some of the main applications of the transparent conductive oxides.

While the *n*-type TCOs (such as: In_2O_3, SnO_2 and ZnO) have currently reached high performances and their production process have become routinely common, the *p*-type TCOs are more difficult to develop. Therefore, many potential applications of TCOs are still limited by the absence of *p*-type TCOs materials (Figure 6.2) [3, 4].

The difficulty to realise *p*-type TCOs materials is due to the intrinsic electronic structure of metal oxides [5, 6, 7]. The top of the valence band of most oxide materials is usually dominated by strongly localized O 2p states, which when doped *p*-type, results in deep, strongly localized O 2p levels. These acceptor levels have a high probability to be localised around the oxygen atoms and then, they need to have a high energy to overcome the wide barrier height to reach the conduction band. These aspects limit the electrical conductivity.

A possible way to overcome this problem is to modify the valence band edge with the introduction of appropriate cations characterised by energy levels comparable to the oxygen 2p level. In this way, it is possible to reduce the strong coulombian force due to oxygen ions and then the holes can be more delocalised. This approach, to obtain *p*-type TCO is called 'Chemical modulation of the valence band' (CMVB) and it is schematically represented in Figure 6.3, where both the atomic orbitals are occupied by electron pairs and then the anti-bonding level is the highest occupied level. As a consequence, it becomes the valence band edge. It should be mentioned that the $3d^{10}$-closed shell of Cu^+ ions and $4d^{10}$-closed shell of Ag^+ ions are suitable cationic species for the CMVB technique.

Literature shows that another important requirement to obtain *p*-type TCOs is represented by the tetrahedral coordination of the oxide ions as it increase the *p*-type conductivity by an increment of delocalised acceptor states close to the valence band edge. For this reason, Cu_2O was the first *p*-type TCO material studied. Unfortunately, Cu_2O exhibits a small energy band gap (about 2.17 eV) probably due to

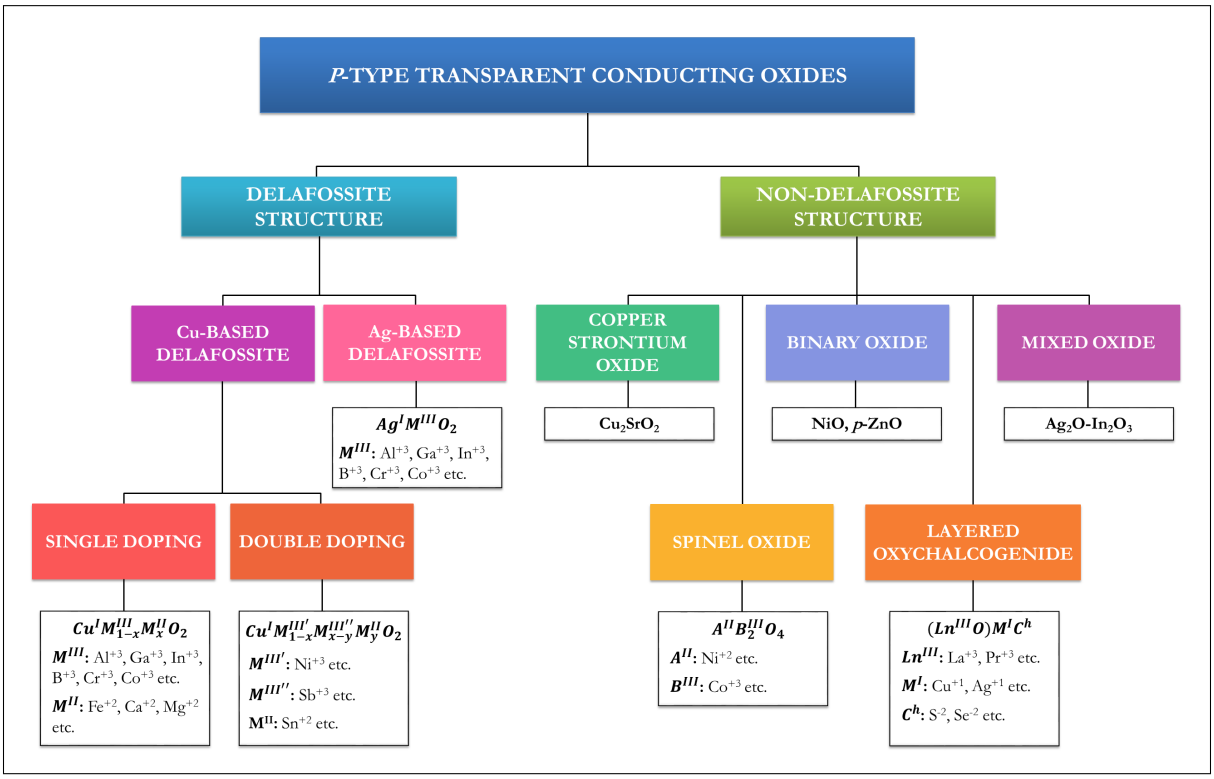

Figure 6.2: Flow-chart of main *p*-type transparent conducting oxide materials, adapted from [3, 4].

the strong Cu–Cu interaction in a cuprite structure, which limit the use of Cu_2O thin films in fully transparent electronics. For this reason, we studied *p*-type TCO exhibiting energy band gap higher than 3 eV.

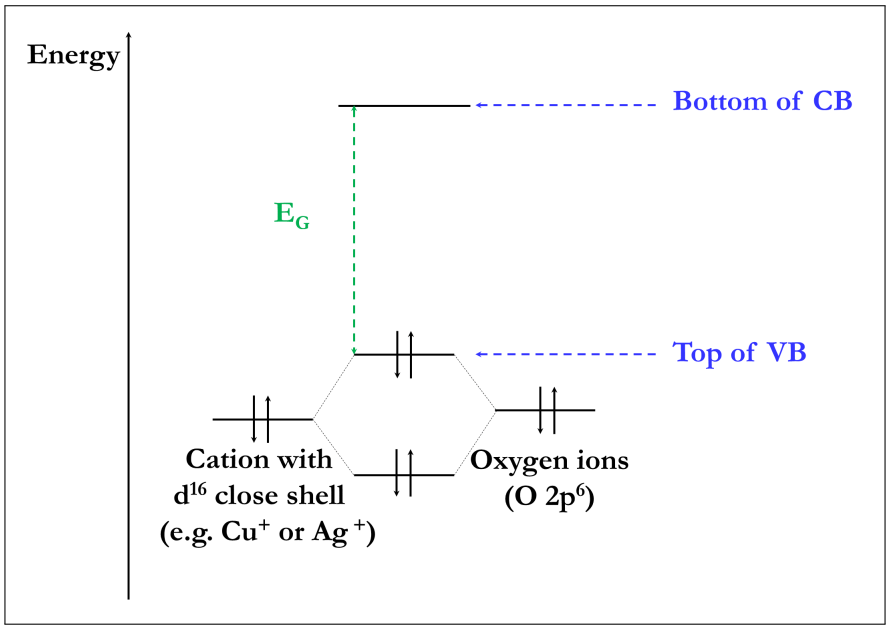

Figure 6.3: Schematic representation of the CMVB method, adapted from [6].

Therefore, the copper-based delafossite family represents the best candidate materials for *p*-type TCO since they are composed of non-toxic and abundant materials and they present a suitable solar

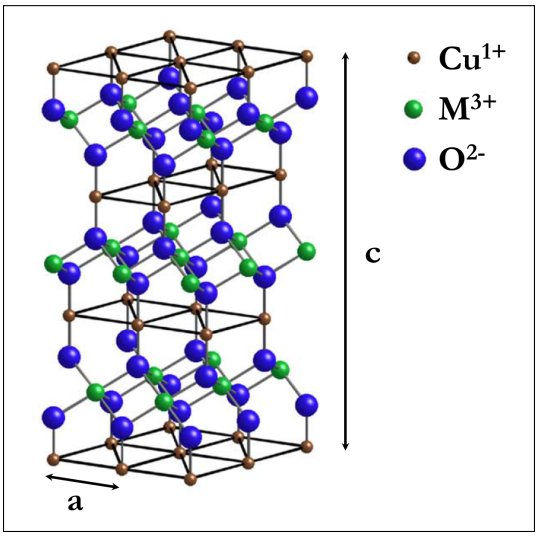

Figure 6.4: The Cu-based delafossite structure (space group $R\bar{3}m$), adapted from [8].

spectral transparency in the visible range. In the following section, we will explain in detail their main properties.

6.2 Copper-based delafossite

The copper-based delafossite family is the group of ternary oxides compounds with the general formula $CuMO_2$, where M indicates a trivalent ions such as B^{+3}, Al^{+3}, Ga^{+3}, In^{+3}, Fe^{+3}, Co^{+3} and Cr^{+3} [8]. In the typical structure, each Cu^{+1} cation is linearly coordinated with two oxygen ions and their interatomic distance is quite small (between 2.8 Å to 3.0 Å for many compounds). Each M^{+3} cation is located in distorted edge-shared MO_6 octahedra. Finally, the oxygen ions are located in a pseudo-tetrahedral coordination with one Cu^{+1} cation and three M^{+3} cations. The structure of $CuMO_2$ can be summarised as alternating layers of Cu^{+} and MO_6 octahedral, stacked along the c axis (as shown in Figure 6.4).
The Cu-based delafossites display both the hexagonal 2H structure with the P63/mmc space group and rhombohedral 3R structure with the $R\bar{3}m$ space group, according to the orientation of the planar layer.

It should be highlighted that the $CuMO_2$ crystal structure presents two unique advantages for the electronic configuration, that are crucial for the CMVB technique:

1. The reduction of Coulomb force induced by oxygen atoms and as a consequence, the delocalisation of the hole states at the valence band edge.

2. Since the O–Cu–O units are isolated by the MO_2 layers into two-dimensional sheet, there is a reduction of the Cu–Cu interactions that is crucial in order to enlarge the energy band gap.

Among the $CuMO_2$ delafossites, $CuAlO_2$, $CuGaO_2$, $CuInO_2$ and $CuBO_2$ have been reported to exhibit a wide optical direct energy band gap and *p*-type behaviour.

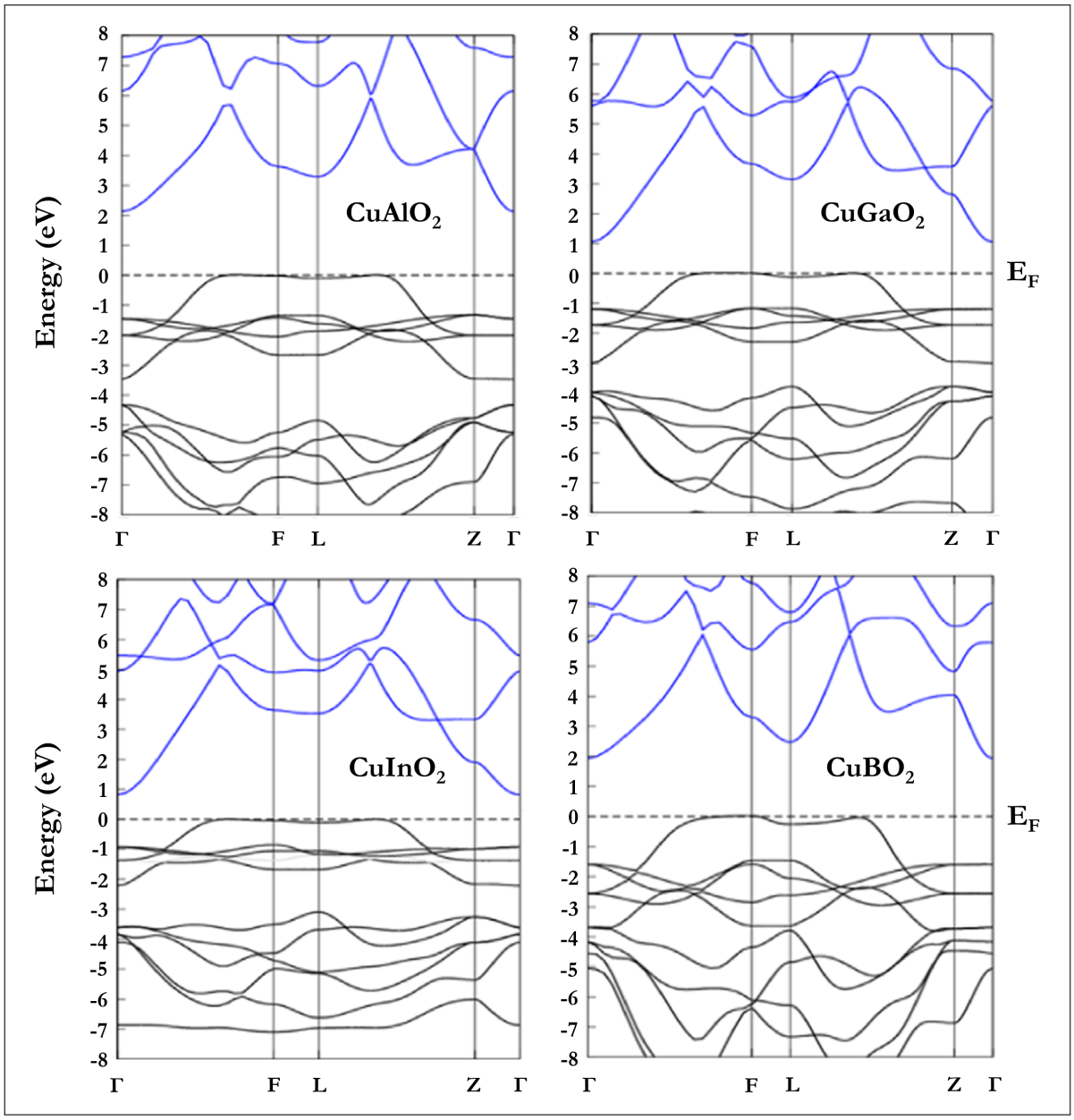

Figure 6.5: The calculate band structure of $CuAlO_2$, $CuGaO_2$, $CuInO_2$ and $CuBO_2$ using the Tran-Blaha modified Becke-Johnson approximation, adapted from [9].

In Table 6.1 are summarised the structural data, the optical and electrical properties of the principal Cu-based delafossite materials reported in literature and Figure 6.5 shows their calculate band structure [7, 9]. It should be noted that, at wavelengths greater than 500 nm, the reported transmittance values for $CuAlO_2$, $CuGaO_2$, $CuInO_2$ and $CuBO_2$ are 70%, 80%, 70% and 75%, respectively. These values are lower than that of the *n*-type TCO, which show typical transmission value around 90% over the entire visible spectrum.

However, these *p*-type TCO materials present a critical aspect. Their solid state synthesis must occur at high temperatures (above 1200) and with an oxygen pressure of about 1 Pa. It is then obvious that the deposition technique of these thin films plays a crucial role on the properties of the resulting films. Literature reports that, even using the same deposition technique, a slight variation of the

Table 6.1: Comparison between the structural data and the optical and electrical properties of the principal Cu-based delafossite. Data from [7, 9]

	$CuAlO_2$	$CuGaO_2$	$CuInO_2$	$CuBO_2$
Structural data				
a (Å)	2.858	2.980	3.292	2.840
c (Å)	16.96	17.10	17.39	16.52
M^{3+} size (Å)	0.67	0.76	0.94	0.41
Cu–O (Å)	1.86	1.85	1.84	––
M–O (Å)	1.91	1.99	2.17	––
Cu–Cu (Å)	2.86	2.98	3.92	2.85
Optical properties				
Transmittance (%)	70	80	70	75
Direct E_g (eV)	3.5	3.6	3.9	4.5
Indirect E_g (eV)	1.8	––	1.4	2.2
Electrical properties				
Conductivity (S cm^{-1})	0.34	0.02	––	1.65
Carrier concentration (cm^{-3})	2.7×10^{19}	1.7×10^{18}	––	1×10^{17}
Hall mobility (cm^2/V s)	0.13	0.23	––	100

deposition parameters can produce films with different properties. Currently, the $CuMO_2$ delafossites thin films are deposited using various techniques, that include pulsed laser deposition, rf magnetron sputtering, chemical vapor deposition, e-beam evaporation, rapid thermal annealing, spray technique, sol-gel technique etc [3, 10, 11, 12, 13].
In the next section, we will report the work done in order to investigate a deposition process of Cu-based delafossite that was simple, reproducible and suitable to be used for photovoltaic applications.

6.3 Research work

During my PhD project, we focused on polycrystalline $CuGaO_2$ and $CuBO_2$ thin films. We tried to sputter-deposit these materials to assess their effectiveness as back contact in bifacial CIGS- and in CdTe-based solar cells (where they would replace the metal and buffer layer). In the next two sections, I will present the main results that were obtained for both materials.

6.3.1 $CuGaO_2$

Our aim was to deposit $CuGaO_2$ on an SLG substrate by using a simple and reproducible process based on rf reactive magnetron sputtering.

Our fist attempt to obtain $CuGaO_2$ delafossite was made by using a sputtering target with a Cu/Ga ratio of 1 and a purity of 99.99%. Several films were deposited under different conditions of sputtering power density and oxygen partial pressure (reactive gas). The main obtained results are summarised in Table 6.2.

Table 6.2: Deposition parameters and resulting atomic compositions of the films that were sputtered from a Cu-Ga target (Cu/Ga = 1). All films, 1 μm thick, were deposited on soda-lime glass substrates.

Sample (CGO #)	[1]T_S (K)	[2]SP (W/cm^2)	[3]Pressure ratio (%)	Deposition rate (Å/sec)	Cu (at.%)	Ga (at.%)
04	750	1.8	2	14.5	76 ± 1	24 ± 1
01	750	1.8	5	5.0	76 ± 1	24 ± 1
05	750	2.2	1	4.5	76 ± 1	24 ± 1
02	750	2.7	9	6.9	77 ± 1	23 ± 1
03	750	3.1	13	5.8	76 ± 1	24 ± 1

Note:

[1] T_S = Substrate Temperature

[2] SP = Sputtering Power Density

[3] Pressure ratio = $P_{O_2}/(P_{Ar}+P_{O_2})$

These data show that, despite the target original composition, copper is 3 times more abundant than gallium in the resulting films. They also rule out any dependence of the Cu/Ga ratio on either sputtering power or oxygen partial pressure. The difference between the Cu/Ga ratio in the starting target and in the deposited films could be explained by considering the difference between the enthalpies of formation of Cu_2O and Ga_2O_3 (-1.68 eV/mol and -10.9 eV/mol, respectively). In addition, the resulting films are completely amorphous, as evidenced by X-ray analysis, and exhibit very high resistivity ($> 10^8$ Ω cm).

To overcome this problem, we replaced the CuGa target with a $CuGa_2$ one (Cu/Ga ratio = 0.5), by taking advantage of the ε phase of the Cu-Ga phase diagram (reported in Figure 6.6). By using this target, several films were deposited at different values of sputtering power, oxygen partial pressure and substrate temperature; main results are summarised in Table 6.3. The data exhibit that the Cu/Ga ratio in the resulting films is about 1. There are not any appreciable variations of the Cu/Ga ratio as a function of sputtering power and partial oxygen pressure.
These films were characterised by X-ray diffraction and, unfortunately, the films that were deposited on SLG substrates were found to be almost exclusively amorphous.
For this reason, taking into account the thermodynamic stability of the delafossite and spinel phases (as shown in Figure 6.7), it became necessary to increase the substrate temperature. This decision had two consequences: the first one, entirely practical, was the need to create a new substrate holder capable of reaching higher temperatures, while the second one was the need to abandon soda-lime glass as a substrate, due to the high requested temperatures, well above 770 K.
We tested alkali-free glass and quartz substrates and they allowed us to make a film at a substrate temperature of 850 K with a sputtering power density of 3.3 W/cm^2 and a partial oxygen pressure of 55% with respect to the Ar + O_2 total pressure. This film exhibits both $CuGaO_2$ with rhombohedral crystal structure (space group $R\bar{3}m$) and $CuGaO_2$ with hexagonal crystal structure (P63/mmc) (as shown in Figure 6.8). The morphology of this film is displayed in Figure 6.9. The film features a direct energy band gap of 3.95 eV (see Tauc plot in Figure 6.10).

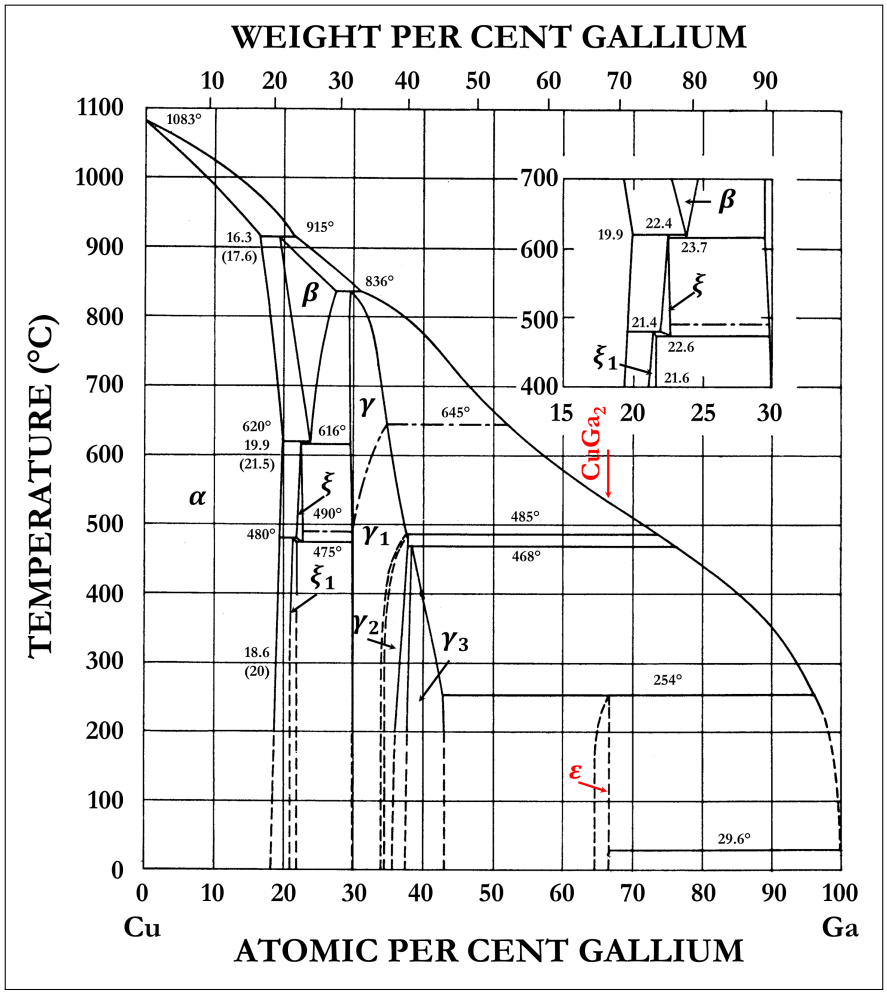

Figure 6.6: Cu-Ga phase diagram, adapted from [14].

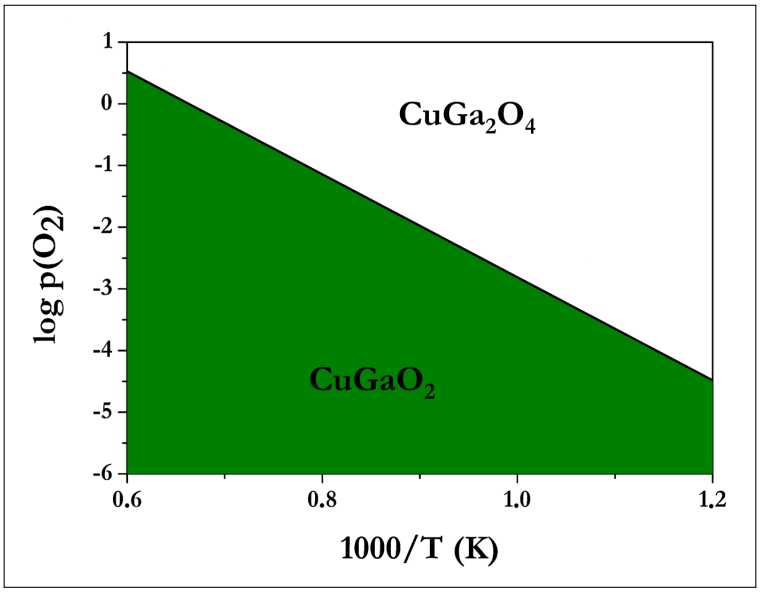

Figure 6.7: The thermodynamic stability of $CuGaO_2$ delafossite and spinel phases as a function of temperature and of oxygen partial pressure. Adapted from [15].

Table 6.3: Deposition parameters and resulting atomic compositions of the films that were sputtered from a $CuGa_2$ target (Cu/Ga = 0.5). All films are 1 µm thick.

Sample (CGO #)	Type of Substrate	[1]T_S (K)	[2]SP (W/cm^2)	[3]Pressure ratio (%)	Deposition rate (Å/sec)	Cu (at.%)	Ga (at.%)
08	SLG	750	1.8	5	10.5	50 ± 1	50 ± 1
12	SLG	750	1.8	13	2.0	50 ± 1	50 ± 1
13	SLG	750	2.2	13	4.5	50 ± 1	50 ± 1
18	SLG	800	2.2	13	3.4	51 ± 1	49 ± 1
21	SLG	800	2.7	50	2.0	50 ± 1	50 ± 1
24	SLG	800	3.3	52	2.9	51 ± 1	49 ± 1
33	Alkali free	850	3.3	55	3.0	51 ± 1	49 ± 1

Note:

[1] T_S = Substrate Temperature

[2] SP = Sputtering Power Density

[3] Pressure ratio = $P_{O_2}/(P_{Ar}+P_{O_2})$

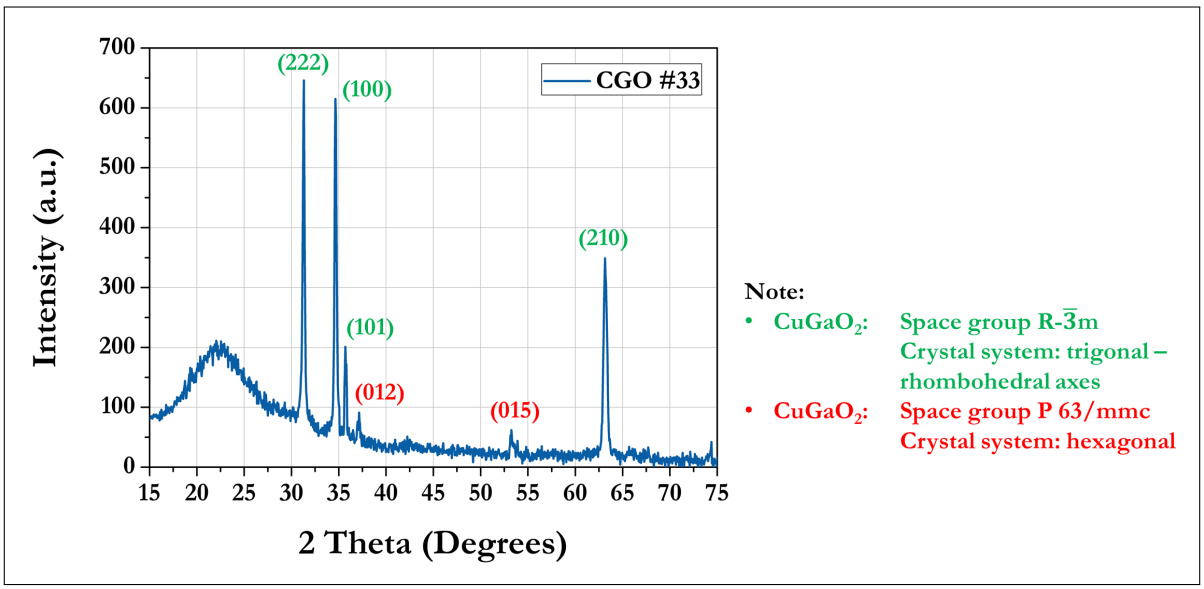

Figure 6.8: X-ray diffraction pattern of sample CGO #33, which was deposited on alkali-free glass at a substrate temperature of 850 K.

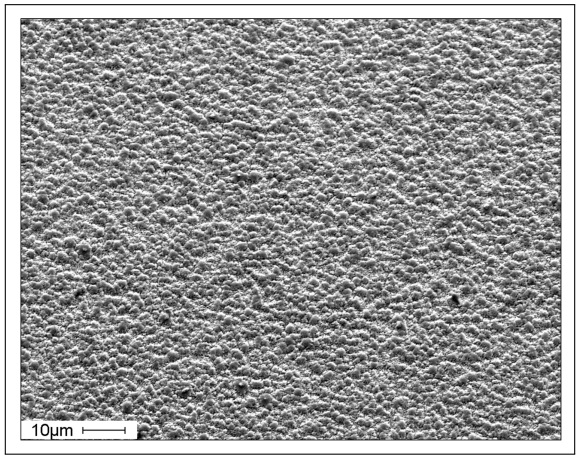

Figure 6.9: SEM image of sample CGO #33 morphology.

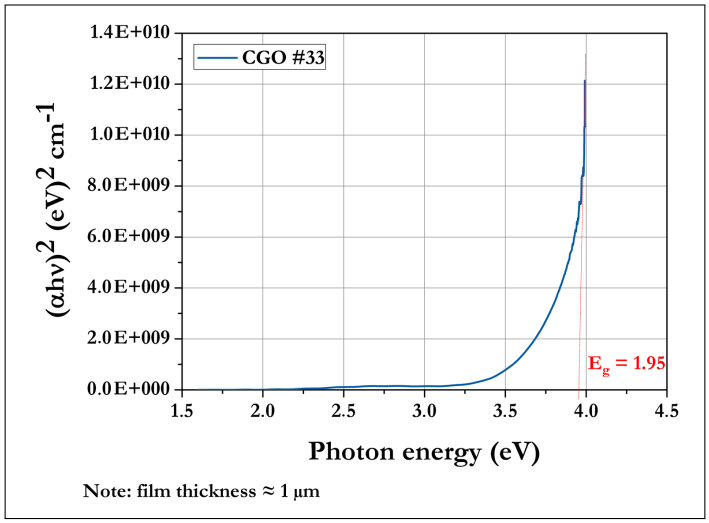

Figure 6.10: Tauc plot of a $CuGaO_2$ film showing the extrapolation of its energy band gap.

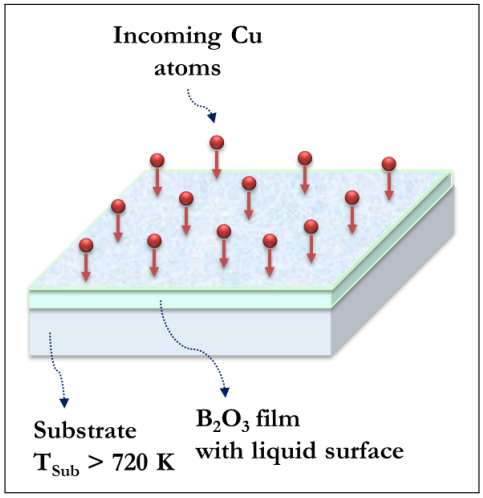

Figure 6.11: Schematic representation of a novel approach using quasi-reothaxy technique for the deposition of $CuBO_2$ films.

Table 6.4: Deposition parameters of the $CuBO_2$ films.

Sample (CBO #)	B_2O_3 (nm)	[1]T_S (Cu) (K)	Cu (nm)	[2]Pressure ratio (%)	[3]T_{Treat} (K)	Gas treatment
01	400	770	360	10	770	Dry air
04	400	720	150	––	––	––
22	400	720	150	––	720	Argon

Note:

[1] T_S (Cu) = Substrate Temperature during the deposition of copper

[2] Pressure ratio = $P_{O_2}/(P_{Ar}+P_{O_2})$

[3] T_{Treat} = Treatment temperature

6.3.2 $CuBO_2$

$CuBO_2$ is currently considered one of the most promising Cu-based delafossite materials because of a recent theoretical analysis, which indicates that the energy band gaps of $CuMO_2$ compounds should increase as the ionic radius of M decreases [16, 17, 18, 19, 20]. $CuBO_2$ should have the largest energy band gap and also the best transmittance in visible spectrum.

To obtain $CuBO_2$ films, we though to an innovative process. In particular, $CuBO_2$ films were obtained by using a two-stage deposition process: an electron beam assisted deposition of a B_2O_3 layer followed by a sputtering deposition of a Cu film. B_2O_3 films were deposited at a substrate temperature of 470 K. Since B_2O_3 films can be treated as a glassy systems, we took advantage of the material softening point at about 720 K to perform the Cu deposition under quasi-rheotaxial conditions (as shown in Figure 6.11). In particular, copper was deposited by dc magnetron sputtering at a substrate temperature of 720 K. After the deposition, the films were exposed to an annealing treatment. We tested three different types of annealing treatment: in vacuum, in air and in argon atmosphere. The main results are summarised in Table 6.4. X-ray investigations confirmed the crystalline nature of these films (see Figure 6.12). However, we have also detected a reproducibility problem, which is probably due to the

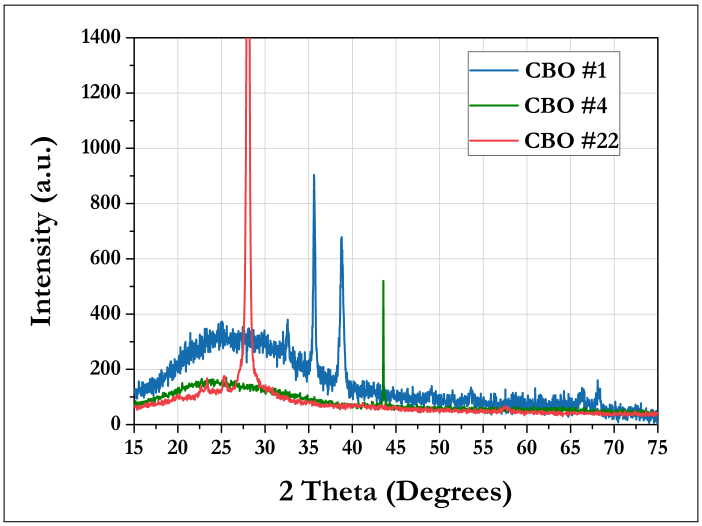

Figure 6.12: X-ray diffraction pattern of the sample reported in Table 6.4.

highly hygroscopic nature of the B_2O_3 film.

Finally, we have to mention that in both cases ($CuGaO_2$ and $CuBO_2$) the search of a method to dope these films with II-group elements of the periodic table to make them conductive is still currently in progress.

References

[1] A. Stadler. *Transparent conducting oxides—an up-to-date overview.* Materials. Molecular Diversity Preservation International. 2012, Volume 5, Number 4, Pages: 661-683.

[2] G. Hautier, A. Miglio, G. Ceder, G.M. Rignanese and X. Gonze. *Low hole effective mass p-type transparent conducting oxides: identification and design principles.* Nature communications. Nature Publishing Group. 2013, Volume 4, Page: 2292.

[3] A.N. Banarjee and K.K. Chattopadhyay. *P-type transparent semiconducting delafossite $CuAlO_{2+x}$ thin film: promising material for optoelectronic devices and field emission displays.* Materials science research trends. 2008, Chapter 1, Pages: 17-132.

[4] S. Nandy, A. Banerjee, E. Fortunato and R. Martins. *A review on Cu_2O and Cu^I-based p-type semiconducting transparent oxide materials: promising candidates for new generation oxide based electronics.* Reviews in Advanced Sciences and Engineering. American Scientific Publishers. 2013, Volume 2, Number 4, Pages: 273-304.

[5] H. Kawazoe, H. Yanagi, K. Ueda and H. Hosono. *Transparent p-type conducting oxides: design and fabrication of pn heterojunctions.* Mrs Bulletin. Cambridge University Press. 2000, Volume 25, Number 8, Pages: 28-36.

[6] A.N. Banerjee and K.K. Chattopadhyay. *Recent developments in the emerging field of crystalline p-type transparent conducting oxide thin films.* Progress in Crystal Growth and Characterization of Materials. Elsevier. 2005, Volume 1, Pages: 52-105.

[7] K.H.L. Zhang, K. Xi, M.G. Blamire and R.G. Egdell. *P-type transparent conducting oxides.* Journal of Physics: Condensed Matter. IOP Publishing. 2016, Volume 28, Number 38, Page: 383002.

[8] M. Marquardt, N. Ashmore and D.P. Cann. *Crystal chemistry and electrical properties of the delafossite structure.* Thin Solid Films. Elsevier. 2006, Volume 496, Number 1, Pages: 146-156.

[9] M.A. Ali, A. Khan, S.H. Khan, T. Ouahrani, G. Murtaza, R. Khenata and S.B. Omran. *First principles study of Cu based Delafossite transparent conducting oxides $CuXO_2$ (X= Al, Ga, In, B, La, Sc, Y).* Materials Science in Semiconductor Processing. Elsevier. 2015, Volume 38, Pages: 57-66.

[10] M.H. Bakar, L.M. Li, K.A. Mohamad, S. Sulaiman, S. Salleh and A. Alias. *Effect of annealing temperature on $CuGaO_2$ thin films deposited by RF sputtering technique.* Journal of Advanced Research in Applied Mechanics. 2015, Volume 14, Number 1, Pages: 12-17.

[11] V. Varadarajan and D.P. Norton. *$CuGaO_2$ thin film synthesis using hydrogen-assisted pulsed laser deposition.* Applied Physics A: Materials Science & Processing. Springer. 2006, Volume 85, Number 2, Pages: 117-120.

[12] M. Neumann-Spallart, S.P. Pai and R. Pinto. *PLD growth of $CuAlO_2$.* Thin Solid Films. Elsevier. 2007, Volume 515, Number 24, Pages: 8641-8644.

[13] S. Santra, N.S. Das, B. Das, D. Banerjee and K.K. Chattopadhyay. *Synthesis of $CuBO_2$ nano/microrods via easy molten salt route and study of its field emission properties.* Crystal Growth & Design. ACS Publications. 2015, Volume 15, Number 3, Pages: 1518-1525.

[14] M.H. Anderko and M. Hansen. *Constitittion of Binary Alloys McGraw-Hill.* New York. 1958.

[15] A.P. Amrute, Z. Lodziana, C. Mondelli, F. Krumeich and J. Perez-Ramirez. *Solid-state chemistry of cuprous delafossites: Synthesis and stability aspects.* Chemistry of Materials. ACS Publications. 2013, Volume 25, Number 21, Pages: 4423-4435.

[16] M. Snure and A. Tiwari. *$CuBO_2$: A p-type transparent oxide.* Applied physics letters. AIP. 2007, Volume 91, Number 9, Page: 092123.

[17] C. Ruttanapun. *Optical and electronic properties of delafossite $CuBO_2$ p-type transparent conducting oxide.* Journal of Applied Physics. AIP. 2013, Volume 114, Number 11, Page: 113108.

[18] M.F. Iozzi, P. Vajeeston, R. Vidya, P. Ravindran and H. Fjellvåg. *Structural and electronic properties of transparent conducting delafossite: a comparison between the $AgBO_2$ and $CuBO_2$ families (B= Al, Ga, In and Sc, Y).* RSC Advances. Royal Society of Chemistry. 2015, Volume 5, Number 2, Pages: 1366-1377.

[19] D. Scanlon, A. Walsh and G.W. Watson. *Understanding the p-type conduction properties of the transparent conducting oxide $CuBO_2$: a density functional theory analysis.* Chemistry of Materials. American Chemical Society. 2009, Volume 21, Number 19, Pages: 4568-4576.

[20] S. Santra, N.S. Das, D. Sen and K.K. Chattopadhyay. *$CuBO_2$: a new highly transparent p-type wide band gap electron field emitter.* Journal of Physics D: Applied Physics. IOP Publishing. 2014, Volume 47, Number 50, Page: 505301.

Chapter

7

Conclusion

In this last part, I finish by providing a brief summary of the main addressed issues in my PhD research project. In particular, I will focus on the results achieved pursuing the three main favoured aspects during this research: the implementation of CdTe- and CIGS- based solar cells and the investigation of sputter-deposited delafossite materials as a new p-type transparent conducting oxide for photovoltaic applications.
I will also give an outlook on the possible future activity.

7.1 Improvements in CdTe solar cells

Cadmium telluride is one of the most promising material to be used as absorber layer for thin-film solar cells. It has a direct energy band gap of 1.49 eV, very close to the theoretical limit of the maximum conversion efficiency, and it can be easily deposited in the form of thin film through highly scalable industrial techniques.

At ThiFiLab, a fully scalable process to produce high-efficiency CdTe-based solar cells has been developed. This production process requires the use of only two deposition techniques: close-spaced sublimation and sputtering.

As described in Chapter 4, the resulting CdTe-based device presents some critical features, such as: grain boundary passivation, CdS-CdTe interface, necessity of a chlorine treatment, presence of sodium in the substrate and back contact ohmicity and stability. In the wider context of implementing this device, my PhD project research has privileged two main aspects of the cell manufacturing:

1. Grain boundary passivation.

2. Back-contact ohmicity and stability.

Concerning the grain boundary passivation, we have discovered a new approach to reduce the thickness of the CdTe absorber layer well below 3 μm. This was achieved by creating a compact bi-layer where the interplay between two CdTe layers with different stoichiometry gives rise to an active grain boundary passivation that preserves the cell performance.

Regarding the back-contact ohmicity and stability, we have found a method to obtain a stable non-rectifying back contact for CdTe-based solar cells. In particular, to obtain a CdTe-based solar cell with high efficiency and without any roll-over effect, it is fundamental to have:

- Copper to form a Cu_xTe layer on top of CdTe and at the same time, the diffusion of copper has to be controlled (x needs to be lower than 1.4).
- A suitable buffer layer to control the Cu-diffusion.
- A metal with a high work function (e.g. platinum) to make an ohmic contact with the buffer layer.

Despite the promising results, some aspects are still open and a further investigation of the back-contact interface is still necessary.

In order to further improve the solar cell performance, an open circuit voltage well over 0.95 V could be reached, by managing the absorber energy band gap, improving the carrier lifetime and CdTe doping level. One possible solution is to use a larger gap material to form a junction with CdS e.g. by adding a small amount of Zn to CdTe. The thickness of this layer must be sufficiently thin (10 nm) to allow tunneling of electrons generated by light inside the absorber.
On the contrary, in order to better absorb the solar light, an absorbing material with a smaller energy band gap than that of CdTe would be desirable. In this way, near-infrared photons produce electron-hole pairs which would otherwise be lost, consequently increasing solar cell photo-current. A suitable material for this purpose is $CdTe_xSe_{(1-x)}$ with x between 0 and 0.5 [1, 2]. Depending on the value of x, the most appropriate energy band gap material for better absorbing a wide part of solar light spectrum is easy to find. Moreover, parasitic light absorption in CdS could be reduced by introducing materials with larger energy band gap and/or smaller absorption coefficient such as Cd(O, S) or $Cd_xZn_{(1-x)}S$. Fill factor could be improved from 75% towards 80% by engineering the *p-n* junction in a passivated polycrystalline thin CdTe layer (2 μm thick) putting together the new concepts described before concerning grain boundary smart passivation and minority carriers mirror, preventing recombination at back contact and negligible internal resistance.

These are only two of the innovations which can lead to device efficiency greater than 20%, which is, nowadays, the minimum goal to be considered as a promising device for industrial production.

7.2 Enhancements in CIGS solar cells

CIGS solar cells are currently the main alternative to silicon-based solar cells for large-scale applications. CIGS shows excellent properties as absorber layer for photovoltaic applications. It is a direct energy band gap semiconductor and as well as for CdTe, 1 μm thick of CIGS is enough to absorb about 90% of the incident radiation.

At ThiFiLab a fully scalable process to produce high efficiency CIGS-based solar cells has been developed. This production process requires only sputtering technique and selenisation treatment. By following this production process, a fine-tuning of the absorber material energy band gap is achieved, and devices with an efficiency of (15 ÷ 16)% were assembled on SLG.

In my PhD research project, I have investigated the process requirements that must be met to obtain high-quality precursors on soda-lime glass substrate needed for the preparation of reproducible high-efficiency CIGS solar cells, as described in Chapter 5. This investigation has led to the following conclusions:

- InSe and GaSe targets should have a density higher than 97% to avoid damage during the sputtering deposition.
- Sputtering power requires tuning, especially for InSe. We have found out that the correct setting for sputtering power is about 3.8 W/cm^2. By using this value, we were able to prevent both indium segregation on the target surface and the peeling effect of the film from the substrate that occurs during selenisation when an incorrect (too low or high, respectively) sputtering power is used.
- The substrate temperature must be carefully chosen, as well, especially for InSe. If the temperature of the substrate is higher than 670 K, the InSe film will contain an excess of In, whereas, if the temperature is lower than 470 K, it will contain an excess of Se.
- The deposition rate of Se during selenisation also plays an important role. It has been found that the average grain size of the finished CIGS film is larger when the evaporation rate of Se is around 1 μm/s.

Moreover, we tried to export the fabrication process developed on soda-lime glass and ceramic tiles to flexible substrates, such as thin metal foils. The results we obtained, however, have not met our expectations, the device performances are lower to those commonly obtained on glass/ceramic substrate. The main new technological challenges that must be overcome to export our fabrication process to flexible substrate are:

- To improve the barrier layer between the metallic substrates and the active layer in order to prevent the diffusion of impurities.
- To control the sodium incorporation.
- To use a optimised sputtering conditions; in particular, the substrate temperature and the sputtering power density.

7.3 Cu-based delafossite as a new material for photovoltaics

The copper-based delafossite family represents one of the most promising materials for *p*-type transparent conductive oxide. We tried to sputter-deposit $CuGaO_2$ and $CuBO_2$ materials with simple and reproducible method. Our aim was to test their effectiveness as back contacts in bifacial CIGS solar

cells and in CdTe cells. In particular, in CdTe-based solar cells, Cu-based delafossite would replace both the metal and buffer layer of the back contact.

As described in Chapter 6, for the deposition of polycrystalline $CuGaO_2$ thin films, we used a sputtering target with a Cu/Ga ratio of 0.5 and the deposition was made in presence of oxygen as a reactive gas. Unfortunately, we found out that an excessively high substrate temperature (850 K) was required for the deposition of these films. In the case of $CuBO_2$, the films were obtained using a two-stage deposition process: an electron beam assisted deposition of a B_2O_3 layer followed by sputtering deposition of a Cu film. In particular, we took advantage of the B_2O_3 softening point at about 720 K to perform the Cu deposition under quasi-rheotaxial conditions. In this case, an annealing treatment is necessary after the deposition. However, we have detected a reproducibility problem, which is probably due to the highly hygroscopic nature of the B_2O_3 film.

The obtained $CuGaO_2$ and $CuBO_2$ films need to be doped with II-group elements of the periodic table to make them conductive.

References

[1] S. Meng and Y. Yan. *Band gap optimization of CdTeSe thin-film solar cells.* Journal of Advances in Physics. 2016, Volume 12, Number 2, Pages: 4213-4218.

[2] J.D. Poplawsky. *Cadmium telluride solar cells: Record-breaking voltages.* Nature Energy. Nature Publishing Group. 2016, Volume 1, Page: 16021.

Appendix A - Energy units

The energy units can be fall into two categories [2]:

1. *Basic units*
   This term refers to the energy units definitions that are not related to a particular fuel;

2. *Source-based units*
   This term refers to the energy units definitions that are related to idealized properties of a specific fuel.

Let us now examine the main energy units and conversions for both these categories [3, 4].

Basic units

The main basic units for energy are: joules, calories, British thermal units and watt-hours.

Joule (J) is the official, internationally accepted energy unit for scientific work and it takes the name from the English physicist James Prescott Joule. One Joule is equal to the energy transferred to an object when a force of one newton acts on that object in the direction of its motion through a distance of one meter. One Joule is also the energy dissipated in form of heat when an electric current of one ampere passes through a resistance of one ohm for one second.

$$J \quad = \quad N \cdot m \quad = \quad \frac{kg \cdot m^2}{s^2}$$

Calorie (cal) is a more familiar energy unit. In the traditional definition, one calorie is the amount of thermal energy required to raise the temperature of one gram of water by one degree Celsius, from 14.5 °C to 15.5 °C.

$$1\,cal \quad = \quad 4.1868\,J$$

Calorie is still a small amount of energy, and therefore commonly referred to kilo-calorie (kcal). The calorie is mainly used to measure chemical energy that our bodies can extract from food.

British thermal unit (Btu) is the analogue of calorie in the British system of units. In the traditional definition, one Btu is the amount of thermal energy required to rise the temperature of one pound of water by one degree Fahrenheit (°F), from 39 °F to 40 °F.

$$1\,Btu \quad = \quad 251.9958\,cal \quad = \quad 1055.06\,J$$

Also Btu is still a small amount of energy, and so it is common to see thermal energies measured in millions of Btu's (MBtu). It is important to underline that Btu unit is the one used in EIA publications.

Watt-hour (Wh) is the standard unit of electrical energy. Commonly, electricity production and consumption is measured by kilowatt-hour (kWh).

$$1\,kWh \quad = \quad 3,600,000\,J \quad = \quad 860\,kcal \quad = \quad 3,413\,Btu$$

Source-based units

When we discuss about production and use of energy, it is often convenient to speak in terms of a bulk amount of fuel, typically a barrel of oil or a ton of coal. So, barrels or tonnes of oil do not exclusively denote a volume or a mass, but they can also be used to represent an amount of energy in physical measure.
It is important to emphasize that all these conversion factors are approximate. In fact, the conversion of a specific quantity of solid, liquid or gaseous fuel into its equivalent energy may depend upon a range of factors such as the specific gravity of the fluid, the amount of water entrained in the mixture, the temperature and pressure at which the measurements are taken, and other factors. Consequently, in many cases there is no single factor that can be used for conversion, and there is an intrinsic inaccuracy in this approach. We then review the main conversion factors for oil, coal and natural gas.

Oil conversion factors

The energy corresponding to the heat content of crude oil from different countries varies from about 5.6 MBtu per barrel to about 6.3 MBtu. The nominal conversion factor for a barrel of crude oil, which is close to its actual average energy content, is:

$$1\,boe \quad = \quad 5.80\,MBtu$$

Another type of equivalence is given by the tonnes of oil equivalent (toe) measurement across different fuels. In fact, for oil, unlike coal, mass is commonly specified in tonnes. The tonnes of oil equivalent generally refers to the energy content of one metric ton of crude oil. Unfortunately, there are a lot of different definitions in literature for a tonne of oil equivalent. By definition it is set equal to 10.0×10^7 kcal (IT) in OECD/IEA publications, but in other cases it is equal to 10.7×10^7 kcal (thermochemical). These conversion factors correspond, respectively, to:

$$1\,toe \quad = \quad 1.00 \times 10^{10}\,cal(IT) \quad = \quad 41.868\,GJ \quad = \quad 39.68\,MBtu(IT)$$

and

$$1\,toe \quad = \quad 1.07 \times 10^{10}\,cal(Thermochemical) \quad = \quad 44.769\,GJ \quad =$$

$$= \quad 42.46\,MBtu(Thermochemical).$$

Coal conversion factors

Also the energy corresponding to the heat content of coal from different countries varies from about 10 MBtu/ton to about 30 MBtu/ton. The regions, in which there is a low heat content, correspond to a large lignite fraction. The amounts of coal can be described both in short tons and metric tons. By definition the energy content of one tonne of coal equivalent (tce) is set equal to 7×10^9 cal:

$$1\,tce \quad = \quad 29.3\,GJ \quad = \quad 27.8\,MBtu.$$

Natural gas conversion factors

In contrast to oil and coal, natural gas is made up largely of methane (CH_4) and, so its energy content data is much more uniform. The heat content of natural gas can vary from about 900 Btu/ft^3 to about 1100 Btu/ft^3. Moreover, it is common use the "therm" unit in publications concerning natural gas production and consumption, where:

$$1\,therm \quad = \quad 100,000\,Btu.$$

References

[1] Daniel Schroeder. *Energy, entropy, and everything.* Chapter 1. Weber State University. (Accessed May 31, 2017).
http://physics.weber.edu/schroeder/eee/chapter1.pdf

[2] American Physical Society. *Energy units.* (Accessed May 31, 2017).
https://www.aps.org/policy/reports/popa-reports/energy/units.cfm

[3] Sohbet Karbuz. *Conversion factors and oil statistics.* Energy Policy, 32, 2004, Pages: 41–45.

[4] Ilika Mohan. *Teri energy & environment data directory and yearbook. 2013/2014.* Chapter 3. TERI Press. ISBN : 9788179935446.

Appendix B - Cleaning of substrate surface

The function of a surface cleaning is to remove all the impurities that may prevent the adhesion of the films to the substrate. In particular, the term 'clean surface' means that the surface need to have a degree of cleanliness to allow the realization of all the subsequent phases of a process. Therefore, substrate surface cleaning plays a central role in the production of thin-film solar cells and it is also a very specific process that depends on the substrate nature.

The substrates currently used at ThiFiLab are:

- For CdTe-based solar cells: soda-lime glass with an area of 2.5 $\times$ 2.5 cm^2 and a thickness of 1 mm.
- For CIGS-based solar cells:
  - soda-lime glass with an area of 2.5 $\times$ 2.5 cm^2 and a thickness of 3.3 mm.
  - ceramic with an area of 2.5 $\times$ 2.5 cm^2 and a thickness of 3.3 mm.
  - nickel and stainless steel sheets with 2.5 $\times$ 2.5 area and 0.05 mm thickness;

The cleaning process developed at ThiFiLab for soda-lime glass substrates can be divided in the following steps.

1. First step
   The substrate is placed in a solution of 60% acetone (CH_3COCH_3) and 40% isopropyl alcohol ($CH_3CH(OH)CH_3$) and then, it is cleaned with absorbent paper to remove any macroscopic impurities present on the glass surface.

2. Second step
   The substrate is located into a plasma-etching system in order to remove any residual organic material. In particular, the plasma-etching process consist in bombing the surface with ionized molecules. The combination of heat produced during bombing and the presence of oxygen ions cause the oxidation of organic compounds, namely their combustion and transformation into volatile phases. They then leave the glass surface and can be pumped out thanks to the vacuum system.
   It should be underlined that no additional gas supplies are required. Our machine uses ambient air as the source of the ionized molecules. The RF magnetron generator operates with a power of 96 W and DC bias voltage of 390 V at room temperature. The plasma chamber reaches a vacuum of 50 Pa and this cleaning process takes only 10 minutes.

Ceramics and flexible metal substrates need a third cleaning step. They are then annealed in vacuum at temperature of about 750 K for 60 minutes. In this way, the substrates tend to expel the gases probably adsorbed during its previous cleaning phases. This stage is also called out-gassing step. If these gases would remain into the substrate, they could provoke problem of film adhesion.

It should be highlighted that our cleaning method does not need dangerous chemical reactions and it is easy scalable at industrial level.

Appendix C - Metal-semiconductor junction

Metal-semiconductor contacts are of great importance, because they are present in every semiconductor device. When a metal and a semiconductor are joined, there are two kinds of contact that depend on the combination of materials used [1, 2, 3]. The two possible contacts can be:

1. Rectifying, when it allows current to pass in one direction. This type of contact is also called Schottky barrier.

2. Ohmic, when it allows current to pass in either direction.

Before discussing the behaviour of a metal-semiconductor junction, it is first necessary to introduce two concepts:

- Work function (φ): the energy required to bring an electron (e^-) from the Fermi level (E_F) to the vacuum level (E_0)[1]:

$$\varphi = \frac{E_0 - E_F}{q} \tag{7.1}$$

- Electron affinity (χ): the energy required to bring an e^- from the conduction band (E_{CB}) to the vacuum level (E_0) if the semiconductor is *n*-type, otherwise it correspond to the difference between E_0 and the valence band (E_{VB}) for a *p*-type semiconductor:

$$\chi = \frac{E_0 - E_{CB}}{q} \quad [n - type\, semiconductor] \tag{7.2}$$

$$\chi = \frac{E_0 - E_{VB}}{q} \quad [p - type\, semiconductor] \tag{7.3}$$

Rectifying contact

The Figure 7.1 shows the band diagram for metal-semiconductor. The work functions of the metal and semiconductor have been indicated as φ_m and φ_s, respectively.

When a contact between metal and an *n*-type semiconductor ($\varphi_m > \varphi_s$) is made, the electrons can lower their energy by moving from the semiconductor conduction band into the metal. This build up of charge on the metal-semiconductor interface causes a deformation of band profile. This process continues until the chemical potential in the semiconductor arrives at the equilibrium with E_F of the

[1] **E_0** (Vacuum energy) is the reference energy that a free electron of the material would have in vacuum.

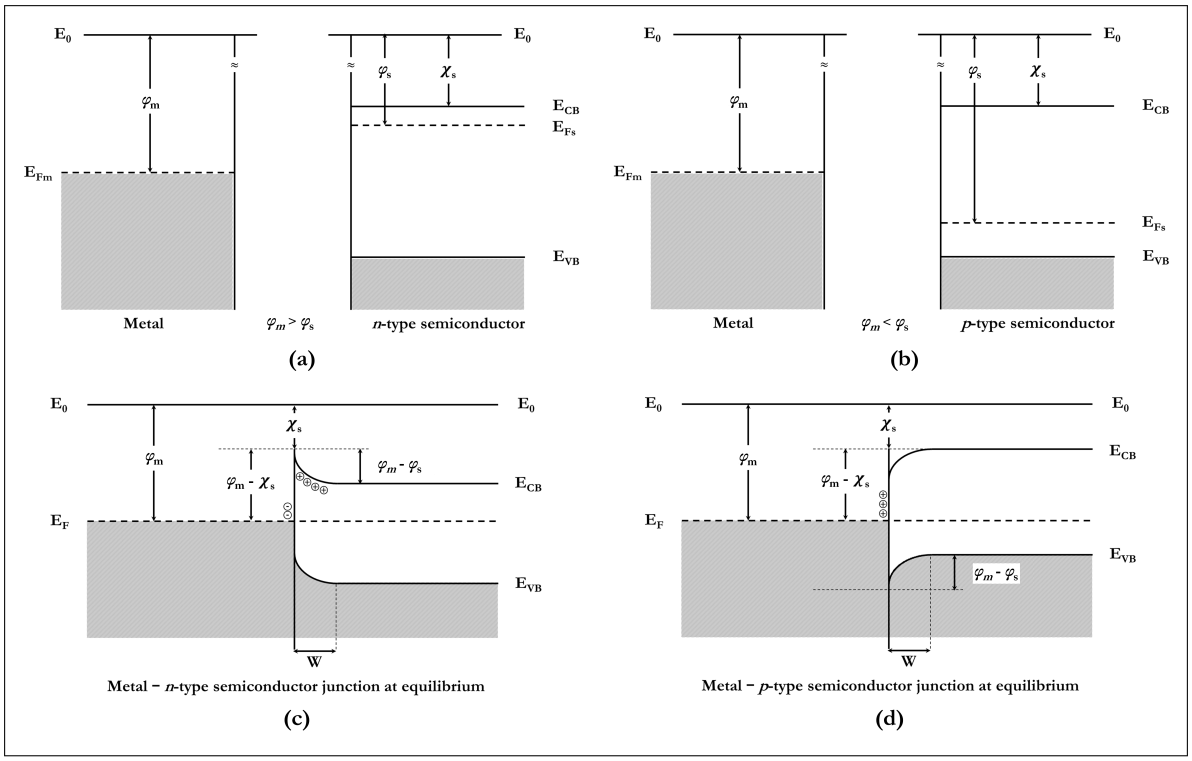

Figure 7.1: Band profiles of disconnected metal and semiconductor *n*-type (a) and *p*-type (b), respectively. Formation of a Schottky junction in the case of a *n*-type (c) and *p*-type (d) semiconductor, respectively.

metal. However, far from the junction, the structure of the bands remains almost the same, except for an overall displacement down in energy.

An immediate consequence of making a metal-semiconductor contact is that a region near to the junction interface is produced in the semiconductor, which has no conducting electrons. Then, this corresponds to an electron depleted region of electrons and therefore it is called depletion layer or space charge region (typically indicated with W). It acts as a potential barrier, which has an height of:

- $\varphi_m > \chi_s$ for the electrons that moves from the metal to the semiconductor.
- $\varphi_m > \varphi_s$ for the electrons that moves from the semiconductor to the metal.

At a certain temperature, there will be electrons in the metal that will have enough thermal power to overcome the potential barrier and spread to the semiconductor conduction band. At the same time, there will be electrons that will have enough heat energy to spread from the semiconductor into the metal. At the equilibrium, these two currents have to be equal. If they do not reach the same level, the band structure would fold up to create this condition.

In addition to the diffusion current, there is also a drift current. This is generally very small and independent from the potential barrier height. It is generated by the formation of electron-hole pairs in the depletion layer as a result of thermal excitation. Electrons are accelerated into the semiconductor, on the contrary, holes into the metal.

The total current trough the junction is the sum of both diffusion and drift current. At equilibrium (namely without any voltage applied), this sum is equal to zero.

If the junction is now polarised by connecting the metal to the negative terminal of a battery

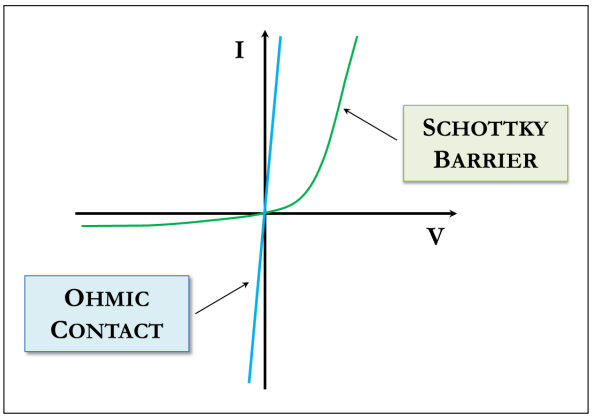

Figure 7.2: Comparison between the I-V characteristic for a metal-semiconductor junction in the case of ohmic and rectifying contact.

and the semiconductor to the positive one, the bands in the semiconductor will be further deformed. The height of the potential barrier and the width of the depletion region increase so much to make impossible a diffusion current in both directions. The drift current remains, producing a slight constant flow of electrons from the metal to the semiconductor and this phenomenon is called reverse bias.

On the other hand, when the metal is connected to the positive terminal of a battery, the negative charge in the metal decreases, limiting the deformation of the bands. The lower potential barrier for electrons results in net current flow of charges from the semiconductor to the metal. This phenomenon is called forward bias. Figure 7.1 (green line) shows the I-V characteristic in the case of a rectifying contact.

A similar rectifying behaviour can be described in the case of a junction between a *p*-type semiconductor and a metal ($\varphi_m < \varphi_s$).

When contact is made, the electrons move from the metal to the empty states of the valence band. Also this build up of charge on the metal-semiconductor interface causes a deformation of band profile, opposed to the previous one. When equilibrium is reached, a hole-free region is created and, near the interface, a potential barrier for holes.

If the junction is now inverse polarised by connecting the metal to the positive terminal of a battery and the semiconductor to the negative one, the bands will be deformed further in the semiconductor (holes are repelled from the interface). The height of the potential barrier and the width of the depletion region increase so much for the holes to make impossible a diffusion current in both directions. The resulting net current is very low. On the contrary, if the junction is directly polarised, holes are attracted to the interface and both the potential barrier and depletion region are reduced.

Ohmic contact

It is possible to crate a contact between a metal and a semiconductor that have a linear (non-rectifying) relationship between the voltage applied and the current that flows across the junction. Figure 7.1 (blue line) shows the I-V characteristic of this type of junction, which is also called ohmic contact.

There are two ways to obtain a metal-semiconductor ohmic contact:

- Heavy semiconductor doping in order to create at the interface a high and narrow potential

barrier that can be crossed by tunnelling.

- Introducing a high density of states at the interface by surface treatment in order to create a potential barrier for cross-tunneling effect.

In particular, a metal-semiconductor junction results in an Ohmic contact only if the Schottky barrier height is equal to zero or negative. Then, the carriers are free to flow and there is a minimal resistance across the junction.

This means that the work function of the metal have to be close to or smaller than the electron affinity of the semiconductor in the case of an *n*-type semiconductor ($\varphi_m < \varphi_s$). On the contrary, in the case of a *p*-type semiconductor, the work function of the metal have to be close to or higher than the electron affinity of the semiconductor ($\varphi_m > \varphi_s$).

It should be highlighted that since the work function of most metals is lower than 5 eV and the typical electron affinity of semiconductor is about 4 V, it can be difficult to find a metal that makes an ohmic contact to *p*-type semiconductors with a large energy band gap such as CdTe.

References

[1] C. Ghezzi. *Fisica dei semiconduttori.* Monte Università Ed., Parma. 2013.

[2] J. Mishra and J. Singh. *Semiconductor device physics and design.* Springer Science & Business Media. 2007.

[3] University of Cambridge. *Metal–semiconductor junction – Rectifying contact.* (Accessed October 9, 2017).
https://www.doitpoms.ac.uk/tlplib/semiconductors/junction_rectifying.php

Publications

1. A. Bosio, N. Romeo, D. Menossi, **G. Rosa**, P.P. Lottici, A. Romeo, I. Rimmaudo and A. Salavei.

   "Key developments in CdTe thin film solar cell back-contact"

   Proceedings of 28th European Photovoltaic Solar Energy Conference and Exhibition (EU-PVSEC). 2013, Pages: 2357-2361.

2. A. Bosio, D. Menossi, **G. Rosa** and N. Romeo.

   "Key developments in CIGS thin film solar cells on ceramic substrates"

   Proceedings of 28th European Photovoltaic Solar Energy Conference and Exhibition Crystal Research and Technology. 2014, Volume 49, Number 8, Pages: 620-627.

3. N. Romeo, A. Bosio, D. Menossi, **G. Rosa**, A. Salavei and A. Romeo.

   "Improvement in processing CdTe/CdS thin film solar cells"

   Proceedings of 29th European Photovoltaic Solar Energy Conference and Exhibition (EU-PVSEC). 2014, Pages: 1709-1712.

4. A. Bosio, D. Menossi and **G. Rosa**.

   "Il fotovoltaico di seconda generazione diventa competitivo"

   1st ed., Publisher: Aracne Editrice, Italy. 2015.

5. A. Bosio, **G. Rosa**, D. Menossi and N. Romeo.

   "Influence of stoichiometry on grain boundary passivation in polycrystalline CdTe thin films"

   Energies. 2016, Volume 9, Page: 254.

6. **G. Rosa**, A. Bosio, D. Menossi and N. Romeo.

   "How the starting precursor influences the properties of polycrystalline $CuInGaSe_2$ thin films prepared by sputtering and selenization"

   Energies. 2016, Volume 9, Page: 354.

7. A. Bosio, **G. Rosa**, S. Mazzamuto, A. Romeo, F. Piccinelli and N. Romeo.

   "The influence of compound target preparation, sputtering power and substrate temperature on the achievement of $Cu(In,Ga)Se_2$ precursors suitable to get high efficiency solar cells"

   Proceedings of 32th European Photovoltaic Solar Energy Conference and Exhibition (EU-PVSEC) 2016, Pages: 1233-1236.

8. N. Romeo, **G. Rosa** and A. Bosio.

   "The back contact in CdTe/CdS thin film solar cells"

   Submitted to Solar World Congress 2017.

9. A. Bosio, **G. Rosa** and N. Romeo.

   "Past, present and future of the thin film CdTe/CdS solar cells"

   Solar Energy - Special issue: "Recent Progress in Photovoltaics, Part 1", to be submitted.

Acknowledgements

And finally here I am, at the very end of my PhD thesis. This is also the end of a personal academic adventure.

This adventure has been made possible thanks to the support of many people. I would like to spend a few words to say 'Thank you' to those who accompanied me during these years. Some of them did so by outright joining forces with me, some by sharing their advice, their tips or even just a word of encouragement.

Hopefully, I will not leave anyone out of these few lines, but I want to start by saying 'Thank you so much' to all of you!

First of all, I would like to express my deepest gratitude to my supervisor, Prof. Alessio Bosio, for his helpfulness and irreplaceable guidance throughout the last three years. It has been him and his vast knowledge of photovoltaics that allowed me to freely experiment in person on the various aspects of PV technology research.

I also wish to thank Prof. Nicola Romeo for proving a capable and experienced instructor, always so keen on guiding me and mentoring me in the development of custom deposition processes.

I am extremely grateful to Dr Samantha Mazzamuto at Northumbria University, Newcastle for her supportiveness in performing XRD and SEM measurements and for all the clarifications she was able to provide about data analysis.

I wish to thank Prof. Alessandro Romeo and Dr Daniele Menossi at the University of Verona for their helpfulness in performing lifetime stability test on my solar devices and for their pertinent comments on CdTe solar cells.

Special thanks go to the IMEM-CNR group for sharing their ideas about the project on delafossites. In particular, I would like to thank Prof. Roberto Fornari, Prof. Edmondo Gilioli, Dr Francesco Pattini and Dr Nicholas Cavallari for our fruitful collaboration in the study of delafossites and for their readiness to discuss our results.

Many thanks also go to the coordinator of doctoral course, Prof. Cristiano Viappiani, for his obliging support and all his clear answers. Likewise, while I have the chance, I would like to extend my gratitude to the technical, administrative and academic staff of the Mathematical, Physical and Computer Science Department for their invaluable assistance.

Now the reader will have to excuse me as I feel the urge to retreat to my native language to say 'Thank you' to the people that, yes, travelled with me along this doctoral journey, but also supported me outside of it in my everyday life. These are people who I have put through a lot...

Finalmente qualche parola in italiano e soprattutto un grande respiro a pieni polmoni… Sono davvero arrivata all'ultima pagina di questa tesi!

Fino a qualche giorno fa mi sembrava proprio un traguardo impossibile e devo ammettere che, quando domenica 15 ottobre il mio computer ha deciso di abbandonarmi, ho proprio pensato: "non riuscirò mai a finire in tempo…". Invece, grazie alla mia super squadra del cuore, capitanata da Simone e composta da amici, colleghi e famiglia, sono riuscita a recuperare un computer, i programmi e tutti i dati per concludere questa tesi. Grazie davvero alla mia squadra del cuore!

In questo elenco di ringraziamenti, non può assolutamente mancare un immenso grazie mille al mio super English Teacher per l'infinita pazienza nelle nostre divertentissime lezioni del sabato pomeriggio. Grazie mille per aver cercato in tutti i modi possibili di migliorare il mio inglese!

Non cito uno ad uno tutti gli amici e colleghi, perché sono talmente tanti che mi servirebbe un'altra tesi per ringraziarli tutti singolarmente, ma sappiate che siete tutti qui. Grazie mille per avermi sostenuto, incoraggiato e aiutato durante questo percorso!

Non credo ci siano abbastanza parole per ringraziare la mia famiglia e soprattutto i miei genitori… Mamma, papà vorrei che questo mio traguardo, per quanto possibile, possa essere un premio anche per voi, per tutta la pazienza, il sostegno e i sacrifici che avete fatto per farmi arrivare qui. Grazie mille per essere i genitori speciali che siete!

E infine, last but not least, colui che mi ha insegnato a volare… Simone, a te un immenso Grazie e un infinito Scusa! Grazie per essere accanto a me anche quando esserci è davvero complicato! Scusa se il mio orgoglio è andato troppo forte per poterti dire scusa!

E adesso? Un nuovo inizio tutto da scoprire, una nuova pagina bianca da colorare, una nuova avventura da vivere! Si parte!

Grazie mille a tutti!
Thank you so much!

Parma, Monday 30th October 2017.

Greta Rosa